Erste Messung der Ladungsasymmetrie und Suche nach schweren Resonanzen in der Top-Quark-Paarproduktion mit dem CMS-Experiment

Zur Erlangung des akademischen Grades eines
DOKTORS DER NATURWISSENSCHAFTEN
von der Fakultät für Physik des
Karlsruher Institut für Technologie (KIT)

genehmigte

Dissertation

von

Dipl.-Phys. Thomas Peiffer
aus Fritzlar

Tag der mündlichen Prüfung: 17.06.2011

Referent: Prof. Dr. Th. Müller, Institut für Experimentelle Kernphysik

Korreferent: Prof. Dr. G. Quast, Institut für Experimentelle Kernphysik

Zusammenfassung

Eine der wesentlichen Fragen, welche die Physik in den vergangenen Jahrzehnten bis zum heutigen Tage nicht endgültig zu klären vermochte, ist diejenige, ob eine grundlegendene mathematischen Beschreibung aller in der Natur beobachtbaren Vorgänge existiert. Die erfolgreichste Theorie zur Erklärung der Wechselwirkungen als fundamental angesehener Teilchen ist das so genannte Standardmodell (SM) der Elementarteilchenphysik [1–11]. Das SM basiert auf bestimmten Symmetrieprinzipien. Unter der Voraussetzung, dass die mathematische Beschreibung aller Vorgänge im Rahmen des SM invariant ist unter bestimmten Symmetrietransformationen, kann diese Theorie die Existenz dreier fundamentaler Kräfte erklären. Dieses sind die elektromagnetische Kraft sowie die schwache und starke Kernkraft. Die fundamentalen Bausteine der Materie werden im SM in drei Familien geordnet, von denen nur die Teilchen der ersten Familie als stabil gelten, während die schwereren Teilchen der zweiten und dritten Familie in ihre leichteren Partner der ersten Generation zerfallen und somit nicht zum Aufbau der alltäglich beobachtbaren Natur beitragen. Solche schweren und instabilen Teilchen können nur kurzzeitig in hochenergetischen Kollisionen anderer Teilchen erzeugt werden. Die bekannten Elementarteilchen umfassen zum einen die sechs Quarks und zum anderen genauso viele Leptonen, die drei elektrisch geladenen Leptonen Elektron, Myon und Tauon sowie die ungeladenen Neutrinos. Des Weiteren beschreibt das SM die Wirkung der drei Kräfte durch Austauschteilchen. Das Photon vermittelt die elektromagnetische Wechselwirkung, die Gluonen sind für die starke Wechselwirkung verantwortlich und die W- und Z-Bosonen sind die Austauschteilchen der schwachen Kernkraft.

Das Standardmodell in seiner heutigen Form wurde bereits um das Jahr 1970 entwickelt und bis heute haben fast alle Messungen die Vorhersagen dieses Modells mit eindrucksvoller Genauigkeit bestätigt. Dennoch wird erwartet, dass das SM keine fundamentale und vollständige Theorie der Natur sein kann. Ein offensichtliches Problem des SM ist die Inkompatibilität mit der allgemeinen Relativitätstheorie [12]. Bis heute ist es nicht gelungen, die Beschreibung der Gravitation in das SM zu integrieren. Ebenso gibt das SM keine Antwort darauf, wieso gerade die beobachteten Teilchen existieren. Obwohl es die Erzeugung der Teilchenmassen mit Hilfe des Higgs-Mechanismus [13–15] erklären kann, liefert es keinerlei Begründung für die beobachteten Massen. Auch das im Rahmen des Higgs-Mechanismus vorhergesagte Higgs-Boson konnte experimentell noch nicht nachgewiesen werden und bleibt somit der letzte fehlende Baustein des SM. Weitere Beobachtungen, die durch das SM weder vorhergesagt noch erklärt werden können, betreffen Dunkle Materie und Dunkle Energie, welche einen Großteil des Energiegehalts des Universums zu tragen

scheinen, aber durch keine im SM beschriebene Teilchenart erklärt werden können. Es gibt daher eine Vielzahl an theoretischen Modellen, welche diese Probleme des SM zu lösen versuchen. Experimentell konnte allerdings noch keiner dieser Ansätze bestätigt werden. Ob eine Beschreibung der Natur, die sämtliche beobachtbaren Phänomene einschließt, in einer für den Menschen verständlichen Form überhaupt möglich ist und wie solch eine fundamentale Theorie aussieht, ist eine der ungelösten Fragestellungen der modernen Physik.

Die Suche nach neuen, unbekannten Effekten in Elementarteilchenreaktionen kann dazu dienen, Hinweise auf eine dieser neuen Theorien zu geben. Besonders in hohen Energiebereichen, die in früheren Experimenten noch nicht zugänglich waren, wird erwartet, dass der Einfluss unbekannter Effekte sichtbar werden sollte. Dazu wurde im Jahr 2010 der Large Hadron Collider (LHC) [16], der Protonen bei einer Schwerpunktsenergie von 7 TeV kollidieren lässt, erstmals bei dieser Energie in Betrieb genommen. Teilchenkollisionen mit hohen Energien sind zum Beispiel eine Voraussetzung dafür, das schwerste bekannte Elementarteilchen – das Top-Quark – zu erzeugen. Das Top-Quark nimmt im Standardmodell eine Sonderstellung ein. Es ist rund vierzig mal schwerer als das b-Quark, das zweitschwerste bekannte Quark. Aufgrund seiner hohen Masse zerfällt das Top-Quark unverzüglich, bevor es einen gebunden Zustand einnehmen kann. Diese Eigenschaft unterscheidet es von allen anderen Quarks, so dass eine Untersuchung des Top-Quarks Messungen an einem quasi-freien Quark zulässt. Ebenso ist das Top-Quark dasjenige Teilchen, das gemäß des SM die stärkste Kopplung an das Higgs-Feld haben sollte. Daher erlauben Untersuchungen von Top-Quarks indirekt die Eigenschaften des Higgs-Teilchens zu bestimmen. Viele theoretische Erweiterungen des SM sagen aufgrund dieser Besonderheit des Top-Quarks neue Phänomene vorher, die sich bevorzugt im Bereich der Top-Quark-Produktion zeigen sollten.

Die denkbar einfachste Art und Weise nach neuen Austauschteilchen, die in Top-Antitop-Quark-Paare zerfallen, zu suchen ist, das Spektrum der invarianten Masse $m_{\mathrm{t\bar{t}}}$ zu untersuchen. Falls das Top-Quark-Paar über den Austausch eines schwereren, noch unbekannten Teilchens erzeugt würde, sollte sich dieses Teilchen als eine Erhöhung im Spektrum der invarianten Top-Quark-Paar-Masse im Bereich solcher $m_{\mathrm{t\bar{t}}}$-Werte zeigen, welche der Masse des neuen Austauschteilchens entsprechen. Die Suche nach Resonanzen im $m_{\mathrm{t\bar{t}}}$-Spektrum erlaubt vorrangig solche Austauschteilchen zu identifizieren, welche eine schmale Zerfallsbreite besitzen, was dazu führt, dass ihr Einfluss nur in einem schmalen Bereich von $m_{\mathrm{t\bar{t}}}$ sichtbar sein sollte. Es gibt aber auch theoretische Modelle, welche hypothetische Austauschteilchen vorhersagen, die sich aufgrund einer größeren Zerfallsbreite nicht als eine eindeutige Signatur im Spektrum der invarianten Masse des Top-Quark-Paars erkennen lassen. Eine alternative Methode nach Einflüssen unbekannter Effekte in der Top-Quark-Paarproduktion zu suchen, ist die Messung von Asymmetrien zwischen Top- und Antitop-Quarks. Solche Asymmetrien können durch neue Austauschteilchen hervorgerufen werden, die unterschiedlich an Top- und Antitop-Quarks koppeln. Bisherige Messungen zu diesem Thema wurden allesamt mit den Experimenten am Tevatron-Beschleuniger durchgeführt [17–21]. Am Tevatron-Beschleuniger lässt man Protonen mit Antiprotonen kollidieren, diese so genannte Ladungsasymmetrie in der Top-Quark-Paarpro-

duktion äußert sich daher als eine Vorwärts-Rückwärts-Asymmetrie, bei der Top-Quarks bevorzugt in Richtung der einlaufenden Protonen, Antitop-Quarks hingegen in die entgegengesetzte Richtung emittiert werden. Mehrere Messungen einer solchen Vorwärts-Rückwärts-Asymmetrie in verschiedenen Messgrößen zeigen teils deutliche Abweichungen von mehr als drei Standardabweichungen zur Vorhersage des Standardmodells, welches nur kleine Asymmetrien zwischen Top- und Antitop-Quarks zulässt. Eine direkte Übertragung der Messmethode vom Tevatron auf den LHC ist nicht möglich, da am LHC mit Proton-Proton-Kollisionen ein symmetrischer Ausgangszustand vorliegt und somit keine Möglichkeit besteht, eine Vorwärts-Rückwärts-Asymmetrie zu erzeugen. Um auch in Proton-Proton-Kollisionen eine Ladungsasymmetrie messen zu können, können die Pseudorapiditätsverteilungen von Top- und Antitop-Quarks untersucht werden. Die Pseudorapidität η eines in einer Teilchenkollision erzeugten Teilchens ist definiert als

$$\eta := -\ln\left(\tan\frac{\theta}{2}\right),$$

wobei θ der Winkel zwischen dem Impulsvektor des emittierten Teilchens und der Protonstrahlachse ist. Die Verteilungen der Pseudorapidität von Top- und Antitop-Quarks, η_{t} beziehungsweise $\eta_{\bar{\mathrm{t}}}$, werden im symmetrischen Proton-Proton-Anfangszustand zwar symmetrisch um Null verteilt sein, ein neues Austauschteilchen mit unterschiedlichen Kopplungen an Top- und Antitop-Quarks würde allerdings dazu führen, dass die Pseudorapiditätsverteilungen unterschiedliche Breiten aufweisen. Eine Ladungsasymmetrie für den LHC lässt sich daher als Zentral-Dezentral-Asymmetrie auffassen. Für die in dieser Arbeit durchgeführte Messung wird die Ladungsasymmetrie A_C als Asymmetrie der Verteilung $|\eta_{\mathrm{t}}| - |\eta_{\bar{\mathrm{t}}}|$ definiert:

$$A_C := \frac{N^+ - N^-}{N^+ + N^-}.$$

Hierbei bezeichnen N^+ und N^- die Anzahl an beobachteten Top-Quark-Paarproduktionsereignissen, bei denen positive bzw. negative Werte für $|\eta_{\mathrm{t}}| - |\eta_{\bar{\mathrm{t}}}|$ gemessen werden.

Die vorgenommenen Messungen zur Suche nach neuen Austauschteilchen in der Top-Quark-Paarproduktion basieren auf Daten, die im Jahr 2010 mit dem Compact Muon Solenoid (CMS) Experiment [22] gesammelt wurden. Das CMS-Experiment ist einer von mehreren Detektoren, welche die Teilchenkollisionen des LHC aufzeichnen. Der CMS-Detektor ist ein Vielzweckdetektor, der dazu gebaut wurde, eine Vielzahl möglicher Teilchenreaktionen zu identifizieren. Dazu besitzt der CMS-Detektor mehrere Subsysteme, die zylinderförmig um den Kollisionspunkt der beiden Protonstrahlen angeordnet sind. Es befinden sich im zentralen Bereich Siliziumdetektoren, welche eine präzise Bestimmung von Flugbahnen geladener Teilchen erlauben. Des Weiteren besitzt der CMS-Detektor elektromagnetische und hadronische Kalorimeter zur Messung der Energie von Photonen und Elektronen beziehungsweise von Hadronen wie zum Beispiel Protonen, Neutronen oder Pionen. Den äußeren Bereich des Detektors bilden Myon-Kammern, welche die Signale von Myonen aufzeichnen, die als einzige Teilchen aufgrund ihrer nur geringen Wechselwirkung mit dem Detektormaterial den äußeren Bereich des Detektors erreichen können. Den gesamten

CMS-Detektor durchdringt ein von einem supraleitenden Magneten erzeugtes Magnetfeld, welches geladene Teilchen auf Kreisbahnen zwingt, was eine Impulsbestimmung dieser Teilchen aufgrund der Krümmung ihrer Spuren erlaubt. Insgesamt steht für die durchgeführten Analysen ein mit dem CMS-Experiment aufgenommener Datensatz mit einer integrierten Luminosität von 36 pb^{-1} zur Verfügung.

Von den aufgezeichneten Detektorsignalen lässt sich nicht unmittelbar auf den Prozess zurückschließen, welcher eine bestimmte Signatur im Detektor hervorruft. Um einen Vergleich zwischen Vorhersagen für Kollisionsprozesse, welche entweder durch das Standardmodell oder auch durch Erweiterungen desselben erklärt werden, durchzuführen, sind verschiedene Schritte zur Simulation von Kollisionsereignissen sowie zur Rekonstruktion von beobachtbaren Signalen im Detektor nötig. Mit Hilfe computergestützter Simulationsrechnungen können gezielt Ereignisse zu bestimmten Prozessen, wie sie in Proton-Proton-Kollisionen auftreten können, generiert werden. Diese so genannten Monte-Carlo-Ereignisgeneratoren werden verwendet, um sowohl den Signalprozess der Top-Quark-Paarproduktion als auch verschiedene Untergrundprozesse, die eine ähnliche Ereignissignatur aufweisen, zu modellieren. Des Weiteren werden auch generierte Datensätze verwendet, welche die Produktion von Top-Quark-Paaren über den Austausch eines schweren Z′-Bosons simulieren. Für alle Monte-Carlo-Datensätze werden in einem Simulationsprozess die im Detektor durch das jeweilige Ereignis erzeugten Signale generiert. Da die unmittelbaren Detektorsignale meist noch keine eindeutige Identifizierung erlauben, werden verschiedene Rekonstruktionsalgorithmen sowohl für die simulierten Datensätze als auch für die vom Detektor aufgezeichneten Daten angewendet. Zu diesen Rekonstruktionsalgorithmen gehören unter anderem Erkennungsmethoden für Spuren geladener Teilchen anhand der gemessenen Einzelsignale im Spurdetektor. Spuren bilden die Grundlage für die Rekonstruktion weiterer Detektorsignaturen. Eine Kombination aus Spuren im inneren Spurdetektor und in den äußeren Myon-Kammern erlaubt zum Beispiel, Myonen zu identifizieren. Eine Spur in der inneren Spurkammer, die zu einer Energiemessung im elektromagnetischen Kalorimeter assoziiert werden kann, dient zum Auffinden von Elektronen. In der harten Proton-Proton-Wechselwirkung erzeugte Gluonen oder Quarks können nicht direkt im Detektor nachgewiesen werden. Sie unterliegen aufgrund der Struktur der starken Wechselwirkung einem Schauer- und Hadronisierungsprozess, an deren Ende ein Bündel an Hadronen erzeugt wird. Diese Teilchenbündel – so genannte Jets – lassen sich mit geeigneten Algorithmen zur Gruppierung von Energiemessungen in den Kalorimetern und Spuren rekonstruieren. Mit den rekonstruierten Jets lassen sich die Impulse der sie erzeugenden Quarks oder Gluonen abschätzen. Einen Spezialfall stellen solche Jets dar, die durch ein b-Quark erzeugt wurden. Hadronen, die b-Quarks beinhalten, haben eine Lebensdauer, in der diese Hadronen eine messbare Distanz zurücklegen können, was eine Unterscheidung von b-Quark-Jets von anderen Jets ermöglicht. Einzig die nur schwach wechselwirkenden Neutrinos können nicht direkt mit dem CMS-Experiment nachgewiesen werden. Kollisionsereignisse mit Neutrinos sind aber aufgrund von fehlender Transversalenergie erkennbar.

Die Messung der Ladungsasymmetrie in Top-Quark-Paarproduktion sowie die Suche nach Resonanzen im $m_{\mathrm{t\bar{t}}}$-Spektrum verwenden beide den so genannten Lepton-

+Jets-Zerfallskanal des Top-Quark-Paares. Ein Top-Quark zerfällt fast immer in ein b-Quark und ein W-Boson, das W-Boson kann dann entweder hadronisch in zwei Quarks oder ein Leptonpaar zerfallen. Wenn eines der beiden W-Bosonen aus dem Top-Quark-Zerfall leptonisch, das andere hadronisch zerfällt, so spricht man von einem Lepton+Jets-Zerfall. Die Signatur eines solchen Zerfalls besteht somit aus vier Jets aus den beiden b-Quarks und den zwei weiteren Quarks eines W-Boson-Zerfalls, aus einem geladenen Lepton und einem Neutrino aus dem Zerfall des anderen W-Bosons. Für die Messung der Ladungsasymmetrie wird eine auf die erwartete Signatur abgestimmte Ereignisselektion verwendet, um einen an Top-Quark-Paarereignissen angereicherten Datensatz zu gewinnen. Dazu wird verlangt, dass im Wesentlichen alle ausgewählten Ereignisse mindestens vier Jets mit gewissen kinematischen Bedingungen aufweisen sowie dass in jedem Ereignis, das selektiert wird, genau ein hochenergetisches Elektron oder Myon nachweisbar ist. Die wesentlichen nach der Selektion verbleibenden Untergünde, welche den Top-Quark-Datensatz verunreinigen, sind die Produktionsprozesse von leptonisch zerfallenden W- und Z-Bosonen in Assoziation mit Jets, die elektroschwache Produktion einzelner Top-Quarks sowie QCD-Multi-Jet-Prozesse, in denen Leptonen in speziellen Hadronzerfällen auftreten können. Eine Abschätzung der Untergrundbeiträge liefert die Wirkungsquerschnittsmessung der Top-Quark-Paarproduktion [23]. Um in jedem selektierten Ereignis eine Abschätzung für die sensitive Messgröße $|\eta_\mathrm{t}| - |\eta_{\bar{\mathrm{t}}}|$ zu erlangen, ist eine Rekonstruktion der Impulsvektoren der Top-Quarks notwendig, welche, da nur ihre Zerfallsprodukte detektierbar sind, nicht unmittelbar gemessen werden können. Dazu werden zunächts die einzelnen Zerfallsprodukte des Top-Quark-Paares rekonstruiert, indem Jets den jeweiligen Quarks aus den Top-Quark-Zerfällen zugeordnet werden und der Impuls des Neutrinos anhand der fehlenden Transversalenergie ermittelt wird. Die Impulsvektoren der Top-Quarks ergeben sich dann aus der Addition der einzelnen Zerfallsproduktimpulse. Da die Zuordnung von gemessenen Objekten zu Top-Quark-Zerfallsprodukten nicht eindeutig ist, ergibt sich eine Vielzahl an Rekonstruktionshypothesen, von denen diejenige ausgewählt wird, welche am besten die erwarteten Massen der Top-Quarks und des hadronisch zerfallenden W-Bosons wiedergibt sowie als b-Jets identifizierte Jets möglichst den b-Quarks zuordnet. Abbildung 1(a) zeigt die rekonstruierte $|\eta_\mathrm{t}| - |\eta_{\bar{\mathrm{t}}}|$-Verteilung für die CMS-Daten in der ausgewählten Hypothese, woraus sich eine Ladungsasymmetrie von $A_C^\mathrm{rek} = 0.018 \pm 0.034$ ergibt. Die gemessene Verteilung von $|\eta_\mathrm{t}| - |\eta_{\bar{\mathrm{t}}}|$ wird durch verschiedene Einflüsse gestört, welche einen direkten Vergleich der rekonstruierten Ladungsasymmetrie mit Theorievorhesagen und anderen Experimenten unmöglich macht. Erstens rührt fast die Hälfte aller selektierten Ereignisse von Untergründen und nicht von Top-Quark-Paarproduktion her und zweitens ist die rekonstruierte $|\eta_\mathrm{t}| - |\eta_{\bar{\mathrm{t}}}|$-Verteilung durch die Unvollkommenheit der Rekonstruktionsmethode verschmiert gegenüber der wahren Verteilung. Da auch die Selektionseffizienz von Top-Quark-Paarereignissen nicht unabhängig vom jeweiligen $|\eta_\mathrm{t}| - |\eta_{\bar{\mathrm{t}}}|$-Wert ist, kann sich die rekonstruierte Ladungsasymmetrie im Vergleich zur wahren Größe verschieben. Um die gemessene Verteilung bezüglich dieser Effekte zu korrigieren, wird ein regularisiertes Entfaltungsverfahren verwendet. Dabei werden zunächst die Beiträge von Untergrundprozessen subtrahiert und anschließend die verbleibende $|\eta_\mathrm{t}| - |\eta_{\bar{\mathrm{t}}}|$-

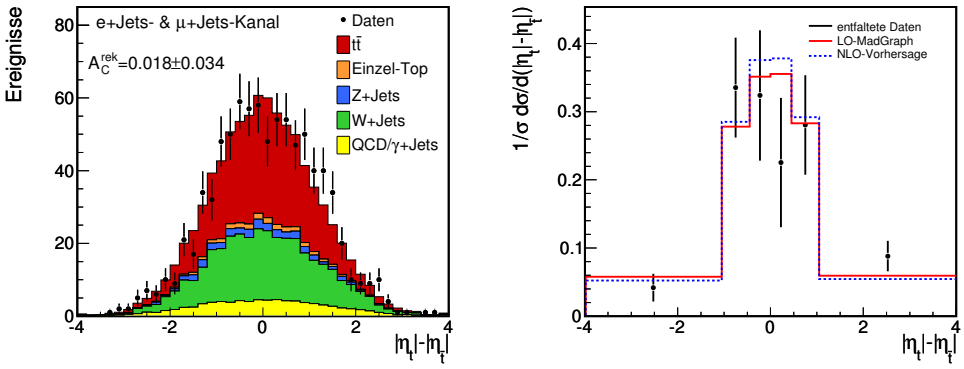

(a) (b)

Abbildung 1: Datenverteilung der rekonstruierten $|\eta_t| - |\eta_{\bar{t}}|$-Variablen im Vergleich zur Simulation von Signal- und Untergrundprozessen (a) und korrigierte $|\eta_t| - |\eta_{\bar{t}}|$-Verteilung im Vergleich zur MadGraph-Monte-Carlo-Simulation und zur Theorievorhersage gemäß [24–26] (b).

Verteilung mit einer verallgemeinerten Matrixinvertierungsmethode, die Regularisierungsbedingungen auf die Form der erwarteten Verteilung beinhaltet, entfaltet. Das Entfaltungsverfahren wird getestet in Zufallsexperimenten, in welchen mögliche Datensätze anhand der Monte-Carlo-Simulation erzeugt werden. Nachdem sich die Entfaltungsmethode in diesen Tests als stabil erwiesen hat und auch der Einfluss systematischer Unsicherheiten mit demselben Verfahren getestet wurde, ergibt sich für den CMS-Datensatz die korrigierte $|\eta_t| - |\eta_{\bar{t}}|$-Verteilung, wie sie in Abbildung 1(b) gezeigt ist, und daraus eine Ladungsasymmetrie von

$$A_C = 0.060 \pm 0.134(\text{stat.}) \pm 0.026(\text{syst.}).$$

Diese Messung stellt die erste Bestimmung der Ladungsasymmetrie in Proton-Proton-Kollisionen dar und ist aufgrund der statistischen Unsicherheit konsistent mit der Theorievorhersage für die Asymmetrie von $A_C^{\text{theo}} = 0.0130 \pm 0.0011$ [24–26].

In einer weiteren Messung, welche in dieser Arbeit durchgeführt wurde, wird das Spektrum der invarianten Masse des Top-Quark-Paares auf mögliche Resonanzen untersucht. Neue Austauschteilchen mit einer Masse von mehr als einem TeV/c^2, welche in Top-Quark-Paare zerfallen, führen zu einer grundlegend anderen Ereigniskinematik im Vergleich zur Kinematik von Top-Quarks, welche in vom Standardmodell beschriebenen Prozessen erzeugt werden. Die Top-Quarks, welche durch den Austausch eines schweren Teilchens produziert werden, sollten durchschnittlich sehr hohe Impulse haben, weshalb erwartet wird, dass die einzelnen Zerfallsprodukte dieser Top-Quarks oft eng beieinander liegen. Dies führt dazu, dass Jets oft nicht mehr als getrennte Objekte im Detektor nachweisbar sind und auch geladene Leptonen aus Top-Quark-Zerfällen oft dicht an oder sogar in einem Jet liegen. Daher müssen die Ereignisselektion angepasst und die Rekonstruktion von Top-Quark-Impulsen modifiziert werden. Für die hier vorgestellte Analyse werden Ereignisse des Myon+Jets-Zerfallskanals untersucht. Selektiert werden nun Ereignisse mit mindestens zwei statt vier Jets und auch die Myonidentifikationskriterien wurden

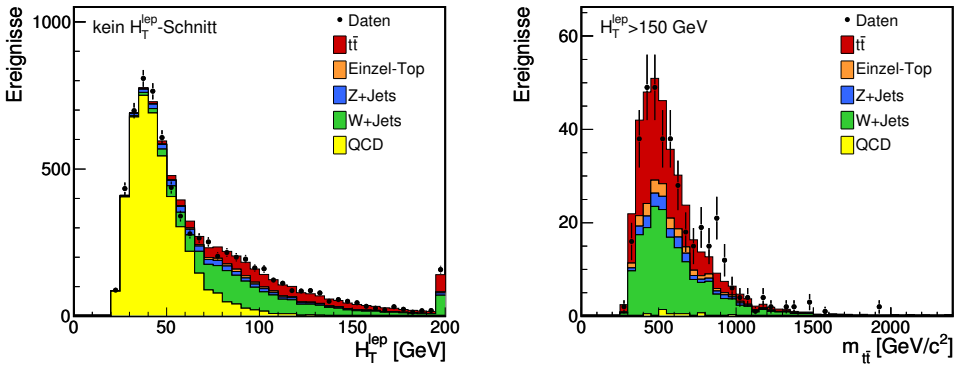

(a) (b)

Abbildung 2: Datenverteilung der beiden untersuchten Vraiablen $H_{\mathrm{T}}^{\mathrm{lep}}$(a) und $m_{\mathrm{t\bar{t}}}$(b) im Vergleich zur Untergrundsimulation für den 2010 von CMS aufgenommenen Datensatz mit einer integrierten Luminosität von 36 pb^{-1}. Die Raten der Untergrundprozesse ergeben sich aus einem Likelihood-Fit an die beiden gezeigten Verteilungen.

entsprechend der erwarteten Ereigniskinematik verändert. Der nach dieser Selektion noch recht große Untergrund, der zum überwiegenden Teil aus QCD-Multi-Jet-Ereignissen besteht, kann durch einen Schnitt von $H_{\mathrm{T}}^{\mathrm{lep}} > 150$ GeV reduziert werden, wobei die Variable $H_{\mathrm{T}}^{\mathrm{lep}}$ definiert ist als skalare Summe des transversalen Myonimpulses und der fehlenden Transversalenergie. Für den besagten Untergrund aus QCD-Multi-Jet-Ereignissen wird eine auf Daten basierende Modellierung vorgenommen, indem Ereignisse mit weniger klar identifizierten Myonkandidaten selektiert werden. Um mögliche Resonanzen in der Top-Quark-Paarproduktion zu finden, ist eine Rekonstruktion der invarianten Masse $m_{\mathrm{t\bar{t}}}$ und somit der Impulse der einzelnen Top-Quarks notwendig. Die hier verwendete Rekonstruktionsmethode ähnelt derjenigen, welche für die Messung der Ladungsasymmetrie verwendet wurde. Allerdings ist aufgrund der geänderten Kinematik eine gezielte Zuordnung von gemessenen Jets zu Quarks in der Zerfallskette der Top-Quarks nicht mehr möglich, weshalb Jets direkt entweder dem Top- oder dem Antitop-Quark zugeordnet werden. Ausgewählt wird dann eine Rekonstruktionshypothese, welche am besten die erwartete Kinematik von hochenergetischen Top-Quarks widerspiegelt. Zur Berechnung von Ausschlussgrenzen auf den Wirkungsquerschnitt von Resonanzen im $m_{\mathrm{t\bar{t}}}$-Spektrum wird eine statistische Auswertung einer Likelihood-Funktion, welche die Ereignisraten für Signal- und Untergrundprozesse berücksichtigt, vorgenommen. Zur Berechnung der Likelihood-Funktion werden die erwarteten Verteilungen von Signal und Untergrund für die $m_{\mathrm{t\bar{t}}}$-Verteilung verwendet, welche bis auf das QCD-Multi-Jet-Modell aus Monte-Carlo-Simulationen gewonnen werden. Als Signalprozess dient die Monte-Carlo-Simulation eines schweren Z′-Bosons, welches in Top-Quark-Paare zerfällt. Um eine präzisere Abschätzung der einzelnen Untergrundbeiträge zu erlangen, geht gleichzeitig auch die $H_{\mathrm{T}}^{\mathrm{lep}}$-Verteilung im Bereich $H_{\mathrm{T}}^{\mathrm{lep}} < 150$ GeV in die Likelihood-Funktion ein. Die Likelihood-Funktion erlaubt einen quantitativen Vergleich der gemessenen Verteilungen mit der Erwartung. In einem Likelihood-Fit, in dem zunächst kein Signalprozess berücksichtigt wird, können

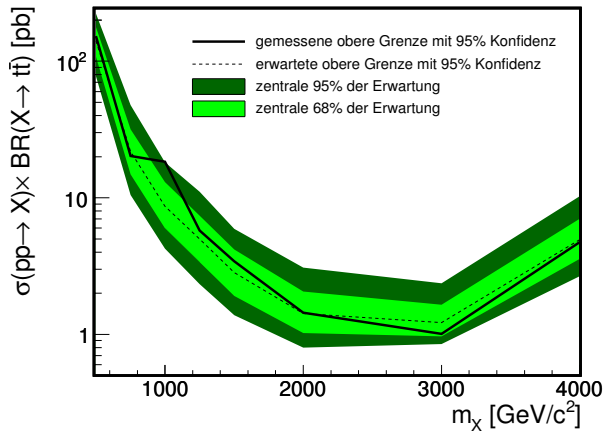

Abbildung 3: Erwartete und gemessene Ausschlussgrenzen mit einer Konfidenz von 95% für den Wirkungsquerschnitt des Prozesses $pp \to X \to t\bar{t}$ mit einem hypothetischen Austauschteilchen X als Funktion der Masse dieses Teilchens.

die erwarteten Beiträge der einzelnen Untergründe bestimmt werden. Das Ergebnis dieses Likelihood-Fits ist in Abbildung 2 gezeigt und ergibt eine gute Beschreibung der beiden benutzten Verteilungen durch die Untergrundmodelle. Des Weiteren werden zusätzliche Parameter zur Beschreibung systematischer Unsicherheiten in die Likelihood-Funktion aufgenommen. Mit einer Marginalisierungsmethode werden alle Parameter der Likelihood-Funktion, bis auf den Parameter, der den Signalanteil beschreibt, ausintegriert. Mit diesem Verfahren lässt sich der im Rahmen der gemessenen Daten erlaubte Bereich für den Signalanteil bestimmen, aus welchem dann Ausschlussgrenzen mit 95% Konfidenz auf den Wirkungsquerschnitt für schwere Resonanzen mit unterschiedlichen Massen bestimmt werden können. Die gemessenen Ausschlussgrenzen sind in Abbildung 3 gezeigt und werden mit den erwarteten Ausschlussgrenzen verglichen, welche man anhand von Simulationsstudien, in denen die statistische Methode auf zufallsgenerierte Verteilungen ohne irgendeinen Signalanteil angewendet wird, erhält. Die gemessenen Ausschlussgrenzen stimmen im Rahmen von statistischen Fluktuationen mit der Erwartung überein, die man unter der Annahme erhält, dass die untersuchten Verteilungen durch Prozesse des Standardmodells erklärt werden können.

Zusammenfassend lässt sich sagen, dass in den vorgenommenen Untersuchungen der Top-Quark-Paarproduktion keine Abweichungen vom Standardmodell gesehen wurden. Es kann erwartetet werden, dass insbesondere die statistischen Unsicherheiten der Messungen mit einem größeren Datensatz erheblich reduziert werden können. Die durchgeführten Messungen zeigen allerdings bereits, welche Verfahren zur Untersuchung von Top-Quark-Paaren mit dem CMS-Experiment prinzipiell möglich sind. Insbesondere die Messung der Ladungsasymmetrie belegt, dass derartige Messungen in Zukunft nicht den Tevatron-Experimenten vorbehalten bleiben werden. Die erwartete Datennahme am LHC in den Jahren 2011 und 2012 wird die Sensitivität der vorgestellten Analysen erhöhen und zeigen, ob die Top-Quark-Paarproduktion auch mit höherer Präzision noch im Rahmen des Standardmodells beschrieben wird.

First Measurement of the Charge Asymmetry and Search for Heavy Resonances in Top Quark Pair Production with the CMS Experiment

Zur Erlangung des akademischen Grades eines
DOKTORS DER NATURWISSENSCHAFTEN
von der Fakultät für Physik des
Karlsruher Institut für Technologie (KIT)

genehmigte

Dissertation

von

Dipl.-Phys. Thomas Peiffer
aus Fritzlar

Tag der mündlichen Prüfung: 17.06.2011

Referent: Prof. Dr. Th. Müller, Institut für Experimentelle Kernphysik

Korreferent: Prof. Dr. G. Quast, Institut für Experimentelle Kernphysik

Introduction

Aim of modern particle physics is to provide a fundamental mathematical model which can basically describe all observable processes in nature. The most accurate and well-established theory known today is the Standard Model of elementary particles. The Standard Model is a quantum field theory describing all known fundamental particles as point-like objects and grouping them into three generations. Basic idea of the Standard Model is to introduce local gauge symmetries and to demand all physical processes to be invariant under these symmetry transformations. With this concept, the Standard Model can describe all elementary particle reactions mediated by either the strong, the weak, or the electromagnetic force over a large range of energy scales. Although the Standard Model provides a precise description of those interactions, it cannot be a fundamental theory of nature. For instance, it cannot explain the origin of gravity and gives no answers to questions, why exactly three generations of particles exist and why these particles have exactly the masses as they are observed. It can also not explain the unknown origin of Dark Energy and Dark Matter which seem to carry the largest amount of energy in the universe.

One possibility to test the properties of the Standard Model and to search for influences of undiscovered processes is to analyse particle interactions at high energy scales. The Large Hadron Collider (LHC) has been launched in 2010 to provide proton-proton collisions with a centre-of-mass energy of 7 TeV. For the first time, particle collisions with such a high energy are provided under laboratory conditions. To analyse the result of these collisions, detector devices are required recording as precisely as possible all products emerging from the proton-proton interactions. One of these detectors is the Compact Muon Solenoid (CMS) experiment. The CMS detector has been designed to study a broad spectrum of physics processes. Therefore, it comprises several detection devices to record all kinds of particles emitted in the primary interaction such as muons, electrons, photons, and hadrons.

One aspect of high-energy particle physics which can be studied at the LHC is the production of top quarks. The top quark is the heaviest elementary particle known today. Due to its extraordinary high mass it can only be produced in particle collisions with sufficiently high energy. It also plays a unique role in the Standard Model since it decays nearly instantaneously before the formation of bound states and offers therefore the opportunity to observe a quasi-free quark. Since the top quark has the largest mass of all particles in the Standard Model, it is also predicted to couple strongly to the Higgs boson, the only predicted particle of the Standard Model which has not been discovered so far. Due to this remarkable role of the top quark in the Standard Model, it is assumed that influences of unknown physical processes could

first be observed in the top quark sector. In this thesis, analyses focussing on the search for not yet discovered exchange particles in the pair production of top quarks in proton-proton collisions detected with the CMS experiment are presented. Such new particles decaying to top-antitop quark pairs are predicted by various theories extending the Standard Model. The most direct way to search for undiscovered exchange particles is the examination of the invariant mass of the top quark pair $m_{\mathrm{t\bar{t}}}$. If the top quarks were produced via the exchange of a heavy particle, their invariant mass $m_{\mathrm{t\bar{t}}}$ should be equal to the mass of the resonance particle. This effect would be visible as a peak in a specific mass region of the differential cross section of top quark pair production as function of $m_{\mathrm{t\bar{t}}}$. Hence, an analysis of the $m_{\mathrm{t\bar{t}}}$ spectrum enables to find such new particles or to set limits on their production rate.

An alternative way to search for new top quark pair production mechanisms is the study of asymmetries between top and antitop quarks. In the Standard Model, top and antitop quarks are predicted to be produced with nearly symmetric kinematic behaviour. In case of new production mechanisms, top quark pairs might be produced via the exchange of a particle which couples differently to top and antitop quarks. If such mechanisms were realised in nature, top quarks would be produced with a different angular distribution compared to antitop quarks. The search for such asymmetries between top and antitop quarks is in so far interesting as recent observations at the Tevatron collider show deviations from Standard Model predictions in such angular distributions. A measure for the angular direction of a particle produced in collisions is the pseudorapidity η. A pseudorapidity of $\eta = 0$ indicates a particle emission perpendicular to the direction of the colliding proton beams, whereas $\eta = \pm\infty$ would correspond to an emission in the direction of the incoming particles. Since the proton-proton collisions at the LHC are completely symmetric, also the pseudorapidity distributions of top and antitop quarks will be distributed symmetrically around zero. Only differences in the width of their η distributions can be an indication for asymmetric production mechanisms. To comprise possible asymmetric effects between top and antitop quarks into a single measurable quantity, the charge asymmetry between positively charged top and negatively charged antitop quarks can be defined as the asymmetry of the distribution of $|\eta_{\mathrm{t}}| - |\eta_{\bar{\mathrm{t}}}|$. The measurement of the charge asymmetry is also sensitive to new production mechanisms of top quarks which cannot be seen in the $m_{\mathrm{t\bar{t}}}$ spectrum.

In this thesis, two analyses are developed focussing on the measurement of new effects in top quark pair production using the data sample collected with the CMS detector during the year 2010. In the analysis presented first, the charge asymmetry in top quark pair production is measured. The search for narrow resonances in the $m_{\mathrm{t\bar{t}}}$ spectrum with masses of several TeV/c^2 is the topic of the second performed study. For both analyses, a selection of candidate events is applied exploiting the specific detector signatures of top quark pair decays. Furthermore, reconstruction techniques are developed to estimate the momenta of top quarks. Due to their short lifetime, top quarks are not directly accessible with the detector. Therefore, the momenta of top quarks have to be reconstructed from their measurable decay products. Selection and reconstruction methods have to be different for the study of $\mathrm{t\bar{t}}$ production processes with high invariant masses $m_{\mathrm{t\bar{t}}}$ compared to the analysis

techniques used for the measurement of the charge asymmetry in which basically a Standard-Model-like event kinematic is expected. In the Standard Model, top quark pairs are mainly produced with relatively low momenta. This leads to a more or less isotropic distribution of the top quark decay products in the detector. Hadron jets and leptons produced in such decays are usually well separated from each other. In contrast to this event topology, top quarks produced in the decay of a new massive resonance particle are expected to carry relatively large boost factors. This effect would lead to an emission of all decay products of a top quark into the same flight direction. The individual top quark decay products would therefore not be well distinguishable since they would often overlap and merge together in the detector. Hence, new selection and reconstruction techniques have to be developed for the study of such boosted top quark decays.

For the measurement of the charge asymmetry, the reconstructed $|\eta_{\mathrm{t}}| - |\eta_{\bar{\mathrm{t}}}|$ spectrum has to be corrected for smearing effects arising from the reconstruction and selection efficiencies as well as from the detector resolution in order to compare the measured spectrum with theory predictions or other experiments. Therefore, unfolding algorithms are utilised correcting the reconstructed $|\eta_{\mathrm{t}}| - |\eta_{\bar{\mathrm{t}}}|$ distribution back to the true kinematics of the produced top quark pair. Having optimised and tested the performance of the unfolding technique in computer simulation based studies, it is applied to determine the $\mathrm{t\bar{t}}$ charge asymmetry in the measured CMS data sample.

For the search for heavy resonances in the $m_{\mathrm{t\bar{t}}}$ spectrum, a statistical inference of the reconstructed $m_{\mathrm{t\bar{t}}}$ distribution is used to obtain upper limits on the cross section of possible heavy particles decaying into top quark pairs. Performing the statistical method with the CMS data sample, the obtained upper limits on resonance cross sections can be compared to the expected ones obtained under the hypothesis that the $m_{\mathrm{t\bar{t}}}$ spectrum is described by Standard Model processes only. Deviations from the expectation could then be an indication for the presence of a new particle decaying to top quark pairs.

Both analyses presented in this thesis are sensitive to new production mechanisms of top quark pair events which might cause the observed deviation from the Standard Model at the Tevatron. Since both analyses focus on different aspects of possible new influences of not yet discovered physical processes, they will provide complementary information on the question whether the production of top quarks in proton-proton collisions at the LHC is fully described within the Standard Model or new theoretical models have to be considered.

Contents

Chapter 1

Top Quarks in the Standard Model and Beyond

Aim of all theories in physics is to provide a mathematical description of processes observed in nature. The search for fundamental theories, from which all other mathematical descriptions can be derived in principle, is a challenge for theoretical physicists. The most fundamental theories existing today are the theory of general relativity [12] and the Standard Model of particle physics (SM) developed by several physicists about 40 years ago [1–11]. General relativity is a description of the gravitational force as a geometrical property of space-time, the unification of space and time in a four dimensional geometry. However, the general relativity gives no description of the fundamental building blocks of matter and the other forces. There exist also no theory which successfully unifies general relativity with quantum mechanics. The best theory known today, which mathematically describes all known elementary particles and their interactions except the gravitational force, is the Standard Model. It provides a quantum mechanical description of particle interactions consistent with the theory of special relativity. Although predictions of the SM have been tested very accurately over several orders of magnitude of length and energy scales in the last years, it cannot be the fundamental theory of nature, since gravitation is not integrated into the SM.

In the following sections, a short overview of the particles and interactions of the SM is given. The top quark, the heaviest known elementary particle, plays an important role to test the properties of the SM. How the top quark is produced in high energetic particle interactions and how the SM predicts its decays will be shown. Alternative theories extending the SM can affect the production of top quarks. Observable effects in top quark production which can proof these theories are presented in the last sections of this chapter.

1.1 The Standard Model

The Standard Model of elementary particle physics is a theory describing fundamental particles as quantum mechanical fields. It contains all known fermions and three forces mediated between the fermions. Fermions are particles with half-integer spin.

All building blocks of matter are fermions with spin $\frac{1}{2}\hbar$. The three forces described by the SM are the strong force, the weak force, and the electromagnetic force. The forces are mediated by spin $1\hbar$ particles, so-called bosons. The SM contains also the Higgs mechanism, which allows a unification of the weak and the electromagnetic forces.

All three SM forces are introduced with the principle of local gauge invariance under certain transformations. The gauge principle says, that physical laws are invariant under these symmetry operations. The concept of symmetries is a very successful way to describe laws of nature. Noether's theorem [27] says, that every symmetry transformation which keeps a physical system unchanged leads to a conserved quantity. For example, the time invariance of a physical system leads to the conservation of energy and the invariance under translation leads to the conservation of momentum. Also Einstein's theory of relativity is mainly driven by this concept. All rules of general relativity – besides the equivalence principle of mass and inertia – are based on the assumption, that physical laws are invariant under general space-time coordinate transformations. In a similar way, the SM employs the principle of local gauge symmetry to explain the interactions between the particle fields.

The standard way to illustrate the gauge invariance of a quantum mechanical system is the Lagrangian formalism. The Lagrangian of a single particle field ψ is a function of the space-time vector x_μ, the field ψ and its derivatives $\partial^\mu\psi := \frac{\partial\psi}{\partial x_\mu}$. For example, the Lagrange function of a free fermion field with mass m is given by:

$$\mathcal{L} = i\bar{\psi}\gamma_\mu\partial^\mu\psi - m\bar{\psi}\psi. \tag{1.1}$$

In here and in all following formulas within this chapter, the natural constants c and $\hbar$ are set to unity. The equation of motion, which fully describes the kinematics of the field ψ, can be calculated from $\mathcal{L}$ using the Euler-Lagrange equation:

$$\frac{\partial}{\partial x_\mu}\left(\frac{\partial\mathcal{L}}{\partial\left(\frac{\partial\psi}{\partial x_\mu}\right)}\right) - \frac{\partial\mathcal{L}}{\partial\psi} = 0. \tag{1.2}$$

In the SM, the Lagrangian is required to be invariant under local $SU(N)$ transformations. The $SU(N)$ is the group of unitary $N \times N$ matrices with determinant 1. A matrix $U \in SU(N)$ transforms the field ψ via:

$$\psi \to U(x)\psi. \tag{1.3}$$

The Lagrangian and therefore the equation of motion derived from the Euler-Lagrange equation 1.2 should be invariant under the transformation 1.3 of the field ψ. *Local* gauge invariance means, that the transformation matrix U can be a function of space-time x. Every $SU(N)$ matrix U can be decomposed as follows:

$$U(x) = e^{i\lambda_a(x)T_a}, \tag{1.4}$$

where the $\lambda_a(x)$ are real parameters and the T_a are the N^2-1 linearly independent, traceless generators of the $SU(N)$ group. They form the corresponding Lie algebra of $SU(N)$ with the commutation relation

$$[T_a, T_b] = if_{abc}T_c, \tag{1.5}$$

where the real constants f_{abc} are the so-called structure constants.

Requiring gauge invariance of the theory leads to the prediction of conserved currents due to Noether's theorem. These Noether charges are quantum numbers which are conserved quantities in each particle reaction described within the gauge invariant theory. However, the Lagrange equation for fermions given in equation 1.1 is not invariant under the local gauge transformation from equation 1.3 since terms proportional to $\partial_\mu \lambda_a(x)$ occur when replacing ψ with the transformed field $e^{i\lambda_a(x)T_a}\psi$. To keep the Lagrangian invariant under the $SU(N)$ transformation, new fields can be introduced. The gauge fields G^a_μ, with $a = 1 \dots N^2 - 1$, appear in the covariant derivatives D_μ replacing the standard derivatives ∂_μ in the Lagrangian:

$$\partial_\mu \rightarrow D_\mu = \partial_\mu + igT_a G^a_\mu. \tag{1.6}$$

The covariant derivative transforms as $D_\mu \rightarrow U D_\mu U^+$, the gauge fields itself transform with

$$G^a_\mu \rightarrow G^a_\mu - \frac{1}{g}\partial_\mu \lambda_a(x) - f_{abc}\lambda_b(x) G^c_\mu. \tag{1.7}$$

The kinetic term $\bar{\psi}\gamma_\mu D^\mu \psi$ in the Lagrangian with the covariant derivative D_μ is now invariant under the local gauge transformation. In the definition of the covariant derivative the coupling constant g was introduced which is a free parameter of the theory. The introduction of the covariant derivative leads to additional terms in the Lagrangian which correspond to couplings of the fermion field ψ to the gauge fields G^a_μ. These terms are given by $g\left(\bar{\psi}\gamma^\mu T_a \psi\right) G^a_\mu$, the constant g therefore parametrises the strength of these couplings.

To obtain a fully gauge invariant Lagrangian the term $-\frac{1}{4} G^a_{\mu\nu} G^{\mu\nu}_a$ is added taking the kinetic energy of the gauge fields into account. Here, the field strength tensor $G^a_{\mu\nu}$ is defined as:

$$G^a_{\mu\nu} := \partial_\mu G^a_\nu - \partial_\nu G^a_\mu - g f_{abc} G^b_\mu G^c_\nu. \tag{1.8}$$

The term $-g f_{abc} G^b_\mu G^c_\nu$ leads to coupling terms of the gauge bosons between themselves. Gauge interactions with structure constants $f_{abc} \neq 0$ are called non-Abelian. The final Lagrange function for a single fermion field ψ, invariant under an arbitrary $SU(N)$ transformation, is:

$$\mathcal{L} = i\bar{\psi}\gamma_\mu \partial^\mu \psi - m\bar{\psi}\psi - g\left(\bar{\psi}\gamma^\mu T_a \psi\right) G^a_\mu - \frac{1}{4} G^a_{\mu\nu} G^{\mu\nu}_a. \tag{1.9}$$

The formalism of local gauge invariance allows to explain interactions between elementary particles in an elegant way. Just by demanding that the theory should be invariant under certain symmetry operations, a description of mediating particles – the gauge fields – is obtained. The corresponding Noether currents are the quantum numbers, which are conserved in every particle interaction described within this model.

1.1.1 Gauge Bosons of the Standard Model

The SM contains three types of interactions which can all be introduced with the principle of local gauge invariance. In the theory of quantum electrodynamic

(QED) [28–34], electromagnetic interactions can be deduced from the invariance of the Lagrangian under $U(1)$ phase transformations of the field ψ:

$$\psi \rightarrow \psi e^{i\lambda(x)}. \tag{1.10}$$

The $U(1)$ transformation is just a multiplication with a complex phase, because the group $U(1)$ has only one generator $T_1 = 1$. Here, all physical observables depend on the absolute square of wave functions only. Since the number of gauge fields introduced by an $SU(N)$ symmetry is equal to the number of linearly independent generators, only one field $G^1_\mu = A_\mu$ belongs to the $U(1)$ symmetry. This field A_μ can be related to the photon field. The corresponding conserved Noether current is the electric charge, it is measured in units of the elementary charge $e = 1.602 \cdot 10^{-19}$ C. The coupling strength of the electromagnetic interaction is parametrised with the fine structure constant $\alpha = \frac{e^2}{4\pi\epsilon_0}$. The fine structure constant is a free parameter of the SM. The value of α is experimentally found to be $7.297{\cdot}10^{-3}$ [35]. The range of the electromagnetic force is infinite, since the $U(1)$ has no structure constants. Therefore, there are no self-interactions between two photons and the photon can freely propagate to infinity.

In a similar way, the weak interaction is explained in the SM. For the modelling of the weak interaction an $SU(2)$ symmetry is introduced. The group $SU(2)$ has three generators, thus, also three gauge bosons are predicted. There are two bosons, the W bosons which carry electric charges of $\pm 1e$ and the electrically neutral Z boson. Most weak interactions like the β-decay can only be explained by the existence of electrically charged exchange bosons. The first neutral current interaction mediated by the Z boson were observed in 1973 [36]. Finally, the direct discovery of the two W bosons [37, 38] and the Z boson [39, 40] in 1983 was a great success to proof the validity of the SM. The conserved charge of the weak interaction is the so-called weak isospin. It is called isospin, since it behaves algebraically identical to an ordinary spin. The standard representation of the three generators of $SU(2)$ is $T_i = i\sigma_i$, with σ_i being the Pauli matrices and $i = 1 \ldots 3$. Although the coupling constant of the weak interaction is larger than the electroweak coupling constant, interactions including weak couplings are usually rarer at low energy scales. This can be explained by the fact that the W and Z bosons are massive. The mass of the W boson is 80.4 GeV/c^2, the Z boson has a mass of 91.2 GeV/c^2 [35]. The high boson masses suppress the interchange of these bosons at scales below their masses. At energy scales above the W and Z boson mass the strength of the weak interaction is of the same order as the strength of the electromagnetic force.

The W boson couples only to fermions which have left-handed chirality and to anti-fermions with right-handed chirality. Right- and left-handed fermion states are given by the following projections:

$$\psi_R = \frac{1+\gamma_5}{2}\psi, \qquad \psi_L = \frac{1-\gamma_5}{2}\psi, \tag{1.11}$$

where $\gamma_5 = i\gamma_0\gamma_1\gamma_2\gamma_3$ is the combination of the four Dirac matrices $\gamma_0, \ldots, \gamma_3$. For massless particles, its chirality is equal to its helicity, the projection of the spin to the momentum vector. Therefore, the charged weak interactions are maximally

parity violating. The Z boson also couples differently to both chirality states but not uniquely to left-handed fermions.

The third interaction described with a gauge symmetry within the SM is the strong force which is explained with the gauge group $SU(3)$. The corresponding gauge fields are the gluons. Experimental evidence for the existence of gluons as the gauge fields of the strong force was claimed in 1979 by four experiments [41–44]. The Noether charges of the strong interactions are called colours, the theory of strong interactions is therefore named quantum chromodynamics (QCD) [8–11]. There are three Noether charges which are called red, green, and blue colour charges. The $SU(3)$ is a non-Abelian gauge group, the gluons can therefore interact among themselves. This self-interactions reduce the range of the strong force. If two particles carrying a colour charge are separated, the gluon field strength in between the separated objects increases with their distance. If the distance of the two charged particles exceeds a certain value, the energy of the gluon field becomes large enough that new particle-antiparticle pairs can be created. These newly created particles also carry colour charges and form bound states with the originally separated particles. Therefore, only neutral colour charged objects bound by the strong force can be observed freely, a property which is called confinement. Strong interactions are responsible for the formation of stable nucleons.

In summary, the full gauge group of the SM is $SU(3) \times SU(2) \times U(1)$, representing the strong, the weak and the electromagnetic forces. Although the concept of gauge invariance is very successful to describe three elementary forces, the gravitational force can not be integrated into the same formalism within the SM.

1.1.2 Fermions of the Standard Model

All observed fundamental constituents of matter are fermions. As fermions are spin-$\frac{1}{2}$ particles they follow the Fermi-Dirac statistic and underlie the Pauli exclusion principle [45]. Two fermions of the same type with exactly the same quantum numbers are not allowed to occupy the same position in space-time. In the SM, there are two classes of elementary fermions which are called leptons and quarks. In both classes, three families of particles exist. Fermions of two different families are completely identical in their quantum numbers except their mass. All observable matter is made up of fermions of the first family. Particles with higher masses of the second and third family are unstable and subsequently decay into the particles of the first family which have the lowest masses. The list of fermions of the SM is completed by their antiparticles. To every particle explained above exists an antiparticle with the same mass but conjugated charges.

Each lepton family consists of two particles, a charged lepton carrying an electric charge of $-1e$ and a corresponding neutrino, which is electrically neutral. The leptons of the first family are the electron and the electron-neutrino. The charged leptons of the second and third family are the muon and the tau, the corresponding neutral leptons are the muon- and the tau-neutrino. Leptons do not carry any colour charges, they can therefore only participate in weak and electromagnetic interactions. The left-handed leptons which participate in weak interactions can be

arranged in weak isospin doublets. Each doublet consists of a charged left-handed lepton and its left-handed neutrino partner. Right-handed charged leptons carry no weak isospin and are therefore isospin singlets. The existence of a right-handed neutrino is only hypothetical in the SM since a right-handed neutrino would have no weak, electromagnetic, nor strong charge. Therefore, it could not interact with any other particle of the SM and would be unobservable.

The quarks are the particles of the SM which participate not only in electromagnetic and weak but also in strong interactions. Each quark has a red, green, or blue colour charge. Overall, there are six quarks, two in each of the three families. The two quarks of the first family are the up and the down quark. The quarks of the second generation are called charm and strange quark, the quarks of the third family are the top and the bottom quark. The up-type quarks carry an electric charge of $+\frac{2}{3}e$, the down type-quarks have electric charges of $-\frac{1}{3}e$. Again, the left-handed up- and down-type quarks are arranged in weak isospin doublets. The right-handed quarks are weak isospin singlets and do not participate in weak interactions. As explained above, quarks cannot be observed as free particles since they are colour charged. The observable bound states which are colour neutral are called hadrons. Bound hadrons with a quark and an antiquark are called mesons. They are unstable because the quark can annihilate with the antiquark. Hadrons formed out of three quarks are called baryons. The most prominent baryons are proton and neutron which form nuclei. The only stable hadron is the proton. Although quarks have fractional electric charges, in all baryon and meson bound states the electric charges add up to integer values. All quarks and leptons described within the SM and their quantum numbers are summarised in table 1.1.

1.1.3 Higgs Mechanism and Electroweak Unification

The Higgs mechanism is a theory to explain the masses of the weak gauge bosons [13–15]. It also facilitates a unified description of the weak and the electromagnetic forces. As has been explained, the weak interaction is described by requiring the Lagrangian to be invariant under $SU(2)$ transformations. Unfortunately, the observation of the massive $\mathrm{W}^{\pm}$ and Z gauge boson stands in contradiction to the gauge invariance. To explain massive gauge bosons an additional term has to be introduced to the Lagrangian which is of the form $m^2 G_\mu G^\mu$. Inserting these mass terms into the transformation relation for the gauge fields given in equation 1.7 the Lagrangian is no longer invariant under the gauge transformation.

The idea of the Higgs mechanism is to introduce a new field Φ with a potential energy $V(\Phi)$. In the following it will be shown that the couplings of this field to the gauge bosons can generate their masses. The Lagrangian including the field Φ is assumed to be invariant under certain group transformations but the potential $V(\Phi)$ is formed such that the vacuum ground state $|0\rangle$ of Φ does not follow this invariance. In this case the vacuum expectation value $\langle 0|\Phi|0\rangle$ is not equal to 0. This phenomenon is called spontaneous symmetry breaking. The Goldstone theorem [47, 48] predicts that in every spontaneously broken symmetry massless boson fields occur. However, these massless Goldstone bosons have not been observed in nature. In the Higgs

type	name	Q[e]	I	I_3	colour	m in GeV/c^2
Leptons	e_R	-1	0	0	0	$(510.998910 \pm 0.000013) \cdot 10^{-6}$
	e_L	-1	$\frac{1}{2}$	$-\frac{1}{2}$	0	
	ν_e	0	$\frac{1}{2}$	$+\frac{1}{2}$	0	~ 0
	μ_R	-1	0	0	0	$(105.658367 \pm 0.000004) \cdot 10^{-3}$
	μ_L	-1	$\frac{1}{2}$	$-\frac{1}{2}$	0	
	ν_μ	0	$\frac{1}{2}$	$+\frac{1}{2}$	0	~ 0
	τ_R	-1	0	0	0	1.77682 ± 0.00016
	τ_L	-1	$\frac{1}{2}$	$-\frac{1}{2}$	0	
	ν_τ	0	$\frac{1}{2}$	$+\frac{1}{2}$	0	~ 0
Quarks	u_R	$+\frac{2}{3}$	0	0	r, g or b	$\sim 2 \cdot 10^{-3}$
	u_L	$+\frac{2}{3}$	$\frac{1}{2}$	$+\frac{1}{2}$		
	d_R	$-\frac{1}{3}$	0	0		$\sim 5 \cdot 10^{-3}$
	d_L	$-\frac{1}{3}$	$\frac{1}{2}$	$-\frac{1}{2}$		
	c_R	$+\frac{2}{3}$	0	0	r, g or b	~ 0.1
	c_L	$+\frac{2}{3}$	$\frac{1}{2}$	$+\frac{1}{2}$		
	s_R	$-\frac{1}{3}$	0	0		$1.27^{+0.07}_{-0.09}$
	s_L	$-\frac{1}{3}$	$\frac{1}{2}$	$-\frac{1}{2}$		
	t_R	$+\frac{2}{3}$	0	0	r, g or b	173.3 ± 1.1
	t_L	$+\frac{2}{3}$	$\frac{1}{2}$	$+\frac{1}{2}$		
	b_R	$-\frac{1}{3}$	0	0		$4.67^{+0.18}_{-0.06}$
	b_L	$-\frac{1}{3}$	$\frac{1}{2}$	$-\frac{1}{2}$		

Table 1.1: List of all fermions of the Standard Model and their quantum numbers. Q is the electric charge, I and I_3 are the weak isospin and its third component, m is the particle's mass. The content of SM fermions is completed by the antiparticles. Each antiparticle has the same mass but opposite charges compared the respective particles [35, 46].

mechanism an elegant way is introduced to parametrise the Goldstone bosons into unobservable objects and simultaneously generate mass terms for the $W^\pm$ and Z gauge bosons.

In the SM, the Lagrangian including the field Φ is assumed to be invariant under transformations of the group $SU(2)_L \times U(1)_Y$. The first group $SU(2)_L$ is the gauge group used to describe the weak interactions with the W boson as gauge boson. The index L indicates that only left-handed fields in the SM Lagrangian participate in weak interactions. The gauge group $SU(2)_L \times U(1)_Y$ contains a new $U(1)$ group with a conserved quantum number Y called hypercharge. The hypercharge Y and the weak isospin I are related to the electric charge Q via the Gell-Mann-Nishijima formula:

$$Q = I_3 + \frac{Y}{2}. \tag{1.12}$$

The ground state of Φ breaks the $SU(2)_L \times U(1)_Y$ symmetry spontaneously to the previously mentioned $U(1)_{\text{e.m.}}$ symmetry of the electromagnetic force. The minimal way to define a field Φ which fulfils the requirements to break the $SU(2)_L \times U(1)_Y$ with a non-vanishing vacuum expectation value is a complex doublet:

$$\Phi = \sqrt{\frac{1}{2}} \begin{pmatrix} \phi_1 \\ \phi_2 \end{pmatrix}, \tag{1.13}$$

with two complex scalar fields ϕ_1 and ϕ_2. The Lagrangian of the field Φ is

$$\mathcal{L}_{\text{Higgs}} = (\partial_\mu \Phi^\dagger)(\partial^\mu \Phi) - V(\Phi), \tag{1.14}$$

with the potential $V(\Phi)$ which is parametrised with two parameters μ and λ as follows:

$$V(\Phi) = \mu^2 \Phi^\dagger \Phi + \lambda (\Phi^\dagger \Phi)^2. \tag{1.15}$$

For $\mu^2 < 0$ and $\lambda > 0$ the potential $V(\Phi)$ has a finite minimum at $|\Phi_0|^2 = -\frac{\mu^2}{2\lambda}$. Therefore, the ground state of Φ has a vacuum expectation value $v = \sqrt{-\frac{\mu^2}{\lambda}}$ which does not vanish. The manifold of points where $V(\Phi)$ is minimal is invariant under $SU(2)$ which is illustrated in a schematic view in figure 1.1. Making a particular choice for the minimum breaks the symmetry spontaneously, but leaves the Lagrangian invariant under $SU(2)_L \times U(1)_Y$ transformations.

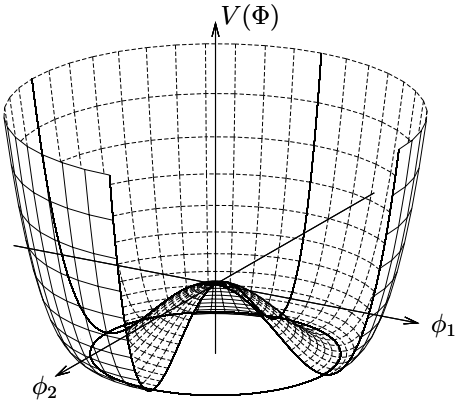

Figure 1.1: The potential of the field Φ [49]: The set of minima of the potential is a circle in the complex plane. By choosing one minimum to be the vacuum expectation value the symmetry of Φ is broken spontaneously.

In the standard parametrisation the particular vacuum field $\Phi_0 := \sqrt{\frac{1}{2}} \begin{pmatrix} 0 \\ v \end{pmatrix}$ is chosen. The field Φ can be expanded around the ground state Φ_0 using four real scalar fields $\theta_1(x)$, $\theta_2(x)$, $\theta_3(x)$ and $h(x)$. With this parametrisation Φ is given by:

$$\Phi(x) = e^{\frac{i}{v}\theta_a(x)\tau_a} \begin{pmatrix} 0 \\ \frac{v+h(x)}{\sqrt{2}} \end{pmatrix}, \tag{1.16}$$

where τ_a are the generators of an $SU(2)$ transformation. The fields $\theta_a(x)$ are the predicted massless Goldstone bosons. If the Lagrangian $\mathcal{L}_{\text{Higgs}}$ in equation 1.14

is required to be invariant under $SU(2)_L \times U(1)_Y$, the Goldstone bosons can be absorbed in an $SU(2)$ phase. Since $e^{\frac{i}{v}\theta_a(x)\tau_a}$ is just an $SU(2)$ transformation and the $SU(2)$ phase can be chosen arbitrarily without changing the physics described by the Lagrangian, the Goldstone bosons disappear in $\mathcal{L}_{\text{Higgs}}$ when choosing a specific gauge. The only remaining field is $h(x)$, which represents the Higgs field. The possibility to parametrise the new field Φ in the form of equation 1.16 is therefore the crucial point of the Higgs mechanism.

For a gauge invariant formalism the standard derivatives in the Lagrangian 1.14 have to be replaced by the covariant derivatives from equation 1.6:

$$D_\mu = \partial_\mu + \frac{ig}{2}\tau_a W_\mu^a + \frac{ig'}{2}B_\mu, \tag{1.17}$$

where W_μ^a are the three gauge fields for the $SU(2)_L$, B_μ is the gauge field of the $U(1)_Y$ group, and g and g' are the respective coupling constants. Inserting all these ingredients into the Lagrangian 1.14 together with the field $\Phi(x)$ in the parametrisation $\Phi(x) = \sqrt{\frac{1}{2}}\begin{pmatrix} 0 \\ v + h(x) \end{pmatrix}$, couplings of the Higgs field $h(x)$ to the four gauge fields W_μ^a and B_μ are found which are of the form of the needed mass terms for gauge bosons. In the potential energy term $V(\Phi)$ also a mass term for the Higgs field $h(x)$ occurs. The Higgs boson mass is $m_h = \sqrt{2\lambda}v$.

The $SU(2)_L$ and $U(1)_Y$ eigenstates, W_μ^a and B_μ, are not directly mass eigenstates. Corresponding mass eigenstates are the fields of the physically observed W bosons W_μ^+ and W_μ^-, the Z boson Z_μ, and the photon A_μ. The charged W boson fields are linear combinations of W_μ^1 and W_μ^2:

$$W_\mu^\pm = \frac{1}{\sqrt{2}}\left(W_\mu^1 \mp W_\mu^2\right). \tag{1.18}$$

Their mass is $m_W = \frac{1}{2}vg$. The two remaining fields for the Z boson and the photon are given by linear combinations of the fields W_μ^3 and B_μ:

$$\begin{aligned} A_\mu &= \cos\theta_W B_\mu + \sin\theta_W W_\mu^3, \\ Z_\mu &= -\sin\theta_W B_\mu + \cos\theta_W W_\mu^3. \end{aligned} \tag{1.19}$$

The angle θ_W is called Weinberg or weak mixing angle and is given by $\tan\theta_W = \frac{g'}{g}$. The rotation with θ_W is chosen such, that the mass of the photon field is $m_A = 0$. Then, the mass of the Z boson is $m_Z = \frac{v}{2}\sqrt{g^2 + g'^2}$. With the masses of W and Z bosons the weak mixing angle is given by $\cos\theta_W = \frac{m_W}{m_Z}$. Since the Z boson is a linear combination of the fields W_μ^3 and B_μ it becomes clear, why the couplings in neutral currents of the weak interaction mediated by the Z boson are not completely left-handed. By construction, only the gauge bosons of the $SU(2)_L$ group, which are the three fields W_μ^a, are coupling exclusively to left-handed fermions, whereas the B_μ has equal right- and left-handed couplings. Due to its B_μ admixture, the Z boson couples also to right-handed fermions.

In summary, the Higgs mechanism is a construction to describe the masses of the heavy gauge bosons W and Z in a unified picture of weak and electromagnetic interactions, the so-called electroweak theory. A new field with four degrees of freedom

is introduced. Three degrees of freedom are absorbed in a phase transformation and thus generate mass terms for the three weak gauge bosons keeping the photon massless. The only missing piece of the electroweak unification is the experimental observation of the Higgs boson itself. It is the only particle predicted in the SM which could not be observed so far. The mass of the Higgs boson is a free parameter of the theory. Direct searches at the LEP experiments [50] and at the Tevatron [51] have excluded a Higgs boson mass of

$$m_h < 114.4 \text{ GeV}/c^2 \quad \text{and} \quad 158 \text{ GeV}/c^2 < m_h < 175 \text{ GeV}/c^2 \tag{1.20}$$

at 95% confidence level. Global fits to electroweak precision measurements [52] give an upper limit of 186 GeV/c^2 at 95% confidence level on the Higgs boson mass. This limit holds only under the assumption that there is no influence from effects not described by the SM on the electroweak measurements going into these fits.

Yukawa Sector

The same field Φ which was introduced to explain the masses of the weak gauge bosons can be used to describe the masses of the SM fermions. Additional couplings of Φ to the fermions are added to the SM Lagrangian. These couplings generate mass terms of the form $-m\bar{\psi}\psi$. For the lepton sector, these couplings are given by

$$\mathcal{L}_Y^l = -\sum_{j=e,\mu,\tau} y_j \bar{L}_j \Phi l_j + h.c., \tag{1.21}$$

where L_j are the three isospin doublets of the left-handed leptons and l_j are the isospin singlets of the charged right-handed leptons:

$$\begin{aligned} L_j &= \begin{pmatrix} \nu_e \\ e_L \end{pmatrix}, \begin{pmatrix} \nu_\mu \\ \mu_L \end{pmatrix}, \begin{pmatrix} \nu_\tau \\ \tau_L \end{pmatrix} \\ l_j &= e_R, \mu_R, \tau_R. \end{aligned} \tag{1.22}$$

Using the parametrisation $\Phi(x) = \sqrt{\frac{1}{2}} \begin{pmatrix} 0 \\ v + h(x) \end{pmatrix}$, only couplings of charged leptons to the Higgs field are introduced. The neutrinos in the isospin doublets remain massless. The masses of left- and right-handed charged leptons are equal and given by $m_j = \frac{v}{\sqrt{2}} y_j$. The constants y_j are the Yukawa coupling parameters which define the strength of the coupling of the leptons to the Higgs field and therewith the lepton masses. They are free parameters within the theory. The SM gives no prediction on the strengths of these couplings.

In a similar way, the masses of quarks are described in the SM. However, the Yukawa mechanism for the quarks is a bit more complicated than in the lepton sector since additionally masses for the right-handed particles have to be generated. The mass eigenstates of quarks are not identical to the $SU(2)_L$ eigenstates of the weak interaction. By convention, the weak eigenstates of down-type quarks, denoted as d′, s′, and b′, are rotated with respect to the mass eigenstates by the unitary

Cabibbo-Kobayashi-Maskawa (CKM) matrix [53]:

$$\begin{pmatrix} \mathrm{d} \\ \mathrm{s} \\ \mathrm{b} \end{pmatrix} = V^{\mathrm{CKM}} \begin{pmatrix} \mathrm{d}' \\ \mathrm{s}' \\ \mathrm{b}' \end{pmatrix} = \begin{pmatrix} V_{\mathrm{ud}} & V_{\mathrm{us}} & V_{\mathrm{ub}} \\ V_{\mathrm{cd}} & V_{\mathrm{cs}} & V_{\mathrm{cb}} \\ V_{\mathrm{td}} & V_{\mathrm{ts}} & V_{\mathrm{tb}} \end{pmatrix} \begin{pmatrix} \mathrm{d}' \\ \mathrm{s}' \\ \mathrm{b}' \end{pmatrix}. \tag{1.23}$$

The weak eigenstates can again be arranged in isospin singlets and doublets:

$$\begin{aligned} Q_j &= \begin{pmatrix} \mathrm{u}_L \\ \mathrm{d}'_L \end{pmatrix}, \begin{pmatrix} \mathrm{c}_L \\ \mathrm{s}'_L \end{pmatrix}, \begin{pmatrix} \mathrm{t}_L \\ \mathrm{b}'_L \end{pmatrix} \\ \mathrm{u}_{Rj} &= \mathrm{u}_R, \mathrm{c}_R, \mathrm{t}_R \\ \mathrm{d}'_{Rj} &= \mathrm{d}'_R, \mathrm{s}'_R, \mathrm{b}'_R. \end{aligned} \tag{1.24}$$

With this abbreviations the mass terms of the quarks can be written as couplings of the quark fields to the Higgs field:

$$\mathcal{L}_Y^q = -\sum_{j,k=1}^{3} \bar{Q}_j \Phi^c Y^{\mathrm{u}}_{jk} \mathrm{u}_{Rk} - \sum_{j,k=1}^{3} \bar{Q}_j \Phi Y^{\mathrm{d}}_{jk} \mathrm{d}'_{Rk} + h.c., \tag{1.25}$$

where a summation over all three quark generation is performed. In equation 1.25, the conjugated field Φ^c is defined as $\Phi^c = \sqrt{\frac{1}{2}} \begin{pmatrix} v + h(x) \\ 0 \end{pmatrix}$. The Yukawa couplings are given as matrices for the up- and down-type quarks separately. The mass matrix Y^{u} defines the masses of the up-type quarks via $M^{\mathrm{u}}_{jk} = \frac{v}{\sqrt{2}} Y^{\mathrm{u}}_{jk}$. The mass matrix M^{u} can be chosen in a diagonal form and contains the masses of the up, the charm, and the top quark, $M^{\mathrm{u}} = \mathrm{diag}(m_{\mathrm{u}}, m_{\mathrm{c}}, m_{\mathrm{t}})$. The mass matrix of the down-type quarks $M^{\mathrm{d}} = \frac{v}{\sqrt{2}} Y^{\mathrm{d}}_{jk}$ cannot be diagonalised simultaneously to M^{u}, hence – as already mentioned – the mass eigenstates of the down-type quarks are equal to rotated weak eigenstates which is described by the CKM matrix. The strength of the Yukawa couplings parametrised with the matrices Y^{u} and Y^{d} defines the masses of the quarks. The fermion masses are translated into couplings of the Higgs field to the quark and lepton fields. The strengths of these couplings are free parameters within the SM. Thus, the SM cannot give any explanation for the absolute mass values.

In addition to the free mass parameters, the CKM matrix was introduced in the Yukawa sector of the SM. The CKM matrix is a unitary 3×3 matrix which has four independent free parameters, three mixing angles and one complex phase. Also the CKM parameters are not predicted by any mechanism of the SM. They can only be measured experimentally. The absolute values of the CKM matrix elements are measured in a global fit to several observables [35]. The result of this fit is:

$$\begin{pmatrix} |V_{\mathrm{ud}}| & |V_{\mathrm{us}}| & |V_{\mathrm{ub}}| \\ |V_{\mathrm{cd}}| & |V_{\mathrm{cs}}| & |V_{\mathrm{cb}}| \\ |V_{\mathrm{td}}| & |V_{\mathrm{ts}}| & |V_{\mathrm{tb}}| \end{pmatrix} = \begin{pmatrix} 0.97428 \pm 0.00015 & 0.2253 \pm 0.0007 & 0.00347^{+0.00016}_{-0.00012} \\ 0.2252 \pm 0.0007 & 0.97345^{+0.00015}_{-0.00016} & 0.0410^{+0.0011}_{-0.0007} \\ 0.00862^{+0.00026}_{-0.00020} & 0.0403 \pm^{+0.0011}_{-0.0007} & 0.999152^{+0.000030}_{-0.000045} \end{pmatrix}. \tag{1.26}$$

The off-diagonal elements of V^{CKM} specify the probability for transitions from one quark generation to another family in electroweak interactions. The numbers of quarks in each family are therefore not conserved in the SM. Only the overall number of quarks is conserved in each particle interaction. This stays in contrast to the lepton sector of the SM. The SM knows no lepton number violation. In every reaction the number of leptons in each generation is predicted to be conserved.

1.1.4 Feynman Rules

Having constructed the complete Lagrangian of the SM it is in principle possible to calculate cross sections for particle interactions. However, the SM is a quantum field theory, hence, for a specific particle interaction with a certain initial state the final state of this interaction is not deterministic. Only probabilities can be calculated to find a certain final state in a specific reaction. The S-matrix gives the probability amplitude for a transition from an initial state $|i\rangle$ to a final state $|f\rangle$ via $\langle f|S|i\rangle$. Following Fermi's Rule [54], the transition rate is proportional to the absolute square of the matrix element. To calculate a transition rate into all possible phase-space configurations of the final state an integration over the entire phase-space has to be performed. To calculate the S-matrix in the SM, a time dependant perturbation series has to be performed. This series is called Dyson series [55]. The Dyson series coherently sums up all possible interactions leading from the initial state $|i\rangle$ to the final state $|f\rangle$. Feynman diagrams are a graphical representations of the processes going into the Dyson series. To each interaction term from the Lagrangian between different boson or fermion fields a vertex is associated. In addition, for each field there exists a propagator term describing the free propagation of this particle in space-time. For a given process with initial state $|i\rangle$ and final state $|f\rangle$ one can determine the terms of the Dyson series by drawing the Feynman diagrams consisting of propagator lines and vertices leading from $|i\rangle$ to $|f\rangle$. For each line and vertex a rule exists to translate the Feynman diagrams into formulas in the Dyson series. A multiplication with a coupling constant arises from each vertex in a Feynman diagram. The leading order (LO) term of the perturbation series is defined by the sum of all Feynman diagrams with minimal number of powers of coupling constants. As an example, the LO diagrams for the QED process $e^+e^- \to e^+e^-$ including the exchange of one photon are shown in figure 1.2.

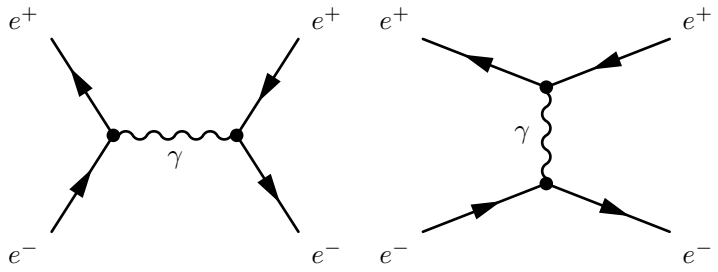

Figure 1.2: The leading order Feynman diagrams for the QED process $e^+e^- \to e^+e^-$.

Diagrams with one more vertex contribute to the next-to-leading order (NLO) terms. These diagrams usually contain loops where an integration over internal momenta of particles running in these loops has to be performed. The integrals over these loop diagrams do not necessarily have to be finite. Since observed reactions in nature do not show infinities, one has to solve the problem of divergent terms in the perturbation series. The solution to this problem is called renormalisation. The idea behind renormalisation takes into account that the masses, charges, and coupling constants written into the Lagrangian are actually no constants but functions of

the energy scale an interaction takes place at. The same problem already occurs in classical electrodynamics. For instance, a constant elementary charge carried by a point-like electron would lead to an infinite field strength at distances $d \to 0$ to the electron. In real nature, the increasing field strength close to the electron leads to the production of virtual pairs of particles and antiparticles. The charges of these virtual particles effectively shield the charge of the bare electron. Therefore, at small distances the effective electron charge decreases. To describe this effect without introducing virtual corrections – which correspond to higher order loops in quantum field theory – the electron charge is defined as a function of the distance to the electron. The introduction of running parameters with distances corresponding to certain energy scales is the main idea behind renormalisation. All measured parameters like charges and masses are therefore not constant but functions of an energy scale. The SM turns out to be a fully renormalisable theory, which means that all loop divergencies can be absorbed by introducing energy-scale dependent parameters.

1.1.5 Open Questions

The Standard Model successfully describes nearly all observed phenomenas in particle interactions. Although many predictions of this theory were confirmed very precisely in many measurements in the past, some open questions remain which are not addressed or can not be answered by the SM. First of all, the SM does not include the gravitational force. Every attempt to formulate a gravitational theory which is consistent with quantum field theories like the SM failed.

A first deviation from the SM was the observation that neutrinos are massive particles [56, 57]. Neutrinos travelling over large distances are found to change their flavour. This stands in contradiction with the SM where the number of leptons in each generation is predicted to be conserved. This observation can be explained by introducing neutrino masses and mass eigenstates which are different from the flavour eigenstates. The neutrino masses could not be measured directly so far, only upper limits of about 1 eV/c^2 can be concluded from the observed oscillations. Several approaches to incorporate neutrino mass terms into the SM exist. Yet the question which mechanism of neutrino mass generation is realised in nature is still not answered.

Another open question deals with the electric charges of elementary particles. Atoms are known to be uncharged. This implies that the electron has to carry exactly the opposite charge of the proton. In the SM this effect occurred as an unexpected fine tuning. There is no obvious reason why the charges of quarks forming the proton have to add up to the electron charge.

Other limitations of the validity come from astrophysical observations. Only 5% of the observed energy density of the universe is made out of the known fermions of the SM. The dominant part of the universe seems to consist of so-called Dark Matter and Dark Energy. The existence of Dark Matter and Energy cannot be explained by the SM. However, only matter and no antimatter is observed in the universe. The existence of matter and the absence of antimatter can only be explained by an

asymmetric behaviour of particles and antiparticles. The only source of such a CP asymmetry in the SM is the complex phase of the CKM matrix. But the symmetry violating processes induced by this phase have a much too small effect to explain the observed non-existence of antimatter in our universe.

The SM gives also no explanation for the actual values of the free parameters in the theory. These unpredictable parameters of the SM are for instance the Yukawa couplings and therefore the masses of the fermions. It exists no explanation for the large difference of mass values which are observed. The heaviest quark, the top quark, has a mass which is several orders of magnitude larger than the masses of the quarks of the first generation.

Also in the Higgs sector of the SM some questions remain unsolved. First of all, the Higgs boson has not been observed so far. But even the observation of the Higgs boson would not solve all related questions. The Higgs mechanism unifies the weak and electromagnetic forces at a relatively low energy scale which is given by the mass of the Higgs boson ($\sim 10^3$ GeV). Most theories extending the SM assume a unification of all four forces at least at the Planck scale which is of the order of 10^{19} GeV. If the SM would be valid even for scales several times larger than the scale of the electroweak unification, the question arises why the mass of the Higgs boson is so much smaller than the assumed unification at much higher scales. The Higgs boson mass has to be corrected for contributions arising from fermion loops in the Higgs propagator. If these loops contain contributions up to the scale where the next unification of forces takes place, a fine-tuning is needed to cancel divergent loop corrections to the Higgs boson mass in order to keep this mass finite. The question why such a fine-tuning should exist is named the hierarchy problem.

Although the SM does not answer all these open questions, it is the best theory known describing almost all elementary particle interactions with great accuracy.

1.2 The Top Quark

The top quark is the heaviest elementary particle known today. Its high mass of (173.3 ± 1.1) GeV/c^2 [46] made it difficult to find the top quark. It took until 1995, nearly 20 years after the bottom quark was observed, to discover the top quark at the Tevatron collider by the CDF [58] and D0 [59] experiments in proton-antiproton collisions at a centre-of-mass energy of 1.8 TeV. The centre-of-mass energy of all previous colliders has been too low to produce top quarks. Until the start of data taking at the Large Hadron Collider (LHC) at a centre-of-mass energy of 7 TeV in 2010, the Tevatron was the only collider facilitating the production of top quarks and to study their properties.

Since the top quark is by far the heaviest quark, it plays an important role in probing the properties of the SM. It is the only quark which decays before it can form bound hadron states. Quark decays are mediated by W bosons. The masses of all other quarks are far below the mass of the W boson, so their decays are suppressed by the weakness of the weak interaction at low energy scales. At the scale of the top quark mass which is larger than the W boson mass the weak interaction becomes apparently much stronger since the W boson can be emitted on-shell. Thus, the

top quark decays nearly instantaneously. The lifetime of the top quark is $\sim 10^{-25}$ s which is much smaller than the usual timescale of QCD interactions of $\sim 10^{-23}$ s. The top quark is therefore a quasi-free quark which does not form any bound state. This makes the top quark an interesting candidate to study quark properties which are not distorted by QCD interaction in the formation of bound states. The top quark mass is of the same order as the Higgs vacuum expectation value v. The top quark has therefore not only the largest Yukawa coupling of all fermions but also a Yukawa coupling which is close to unity. The precise measurement of the top quark mass together with the determination of mass and width of the W boson allows to constrain the mass of the Higgs boson since both, top quark and Higgs boson, contribute to the W propagator via loop corrections. Due to the large coupling of the top quark to the Higgs boson the top quark plays also the most prominent role in the hierarchy problem. The loop contributions for which the Higgs boson mass has to be corrected are mainly influenced by loops containing top-antitop quark pairs.

1.2.1 Top Quark Production

Top quarks can be produced in high-energetic particle collisions where the centre-of-mass energy of the colliding particles exceeds the mass of the produced particles. In the following discussion of top quark production only proton-proton collisions are considered, as these collisions are performed experimentally at the LHC. Protons are composed bound states made out of quarks and gluons. In deep inelastic scattering processes of protons effectively their constituents are colliding. From these collisions, top quarks can either be produced in pairs of top and antitop quarks, or as single top quarks. The top quark pair production is dominated by strong interactions. The leading order Feynman diagrams contributing to the top quark pair production are shown in figure 1.3. The top quarks are either produced in gluon-gluon fusion or in quark-antiquark annihilation. In quark-antiquark annihilation there exists also the possibility to produce top quark pairs in an electroweak reaction via the exchange of a Z boson or a photon, but the amplitude of this process is negligible compared to the amplitude for the strong interactions. Taking also NLO Feynman diagrams into account, the top quark pair can also be produced in processes with quark-gluon initial states. Some examples for NLO Feynman diagrams of $\mathrm{t\bar{t}}$ production are depicted in figure 1.4. Single top quarks can only be produced in electroweak interactions. The production rate of single top quarks is two to three times smaller than the rate of top quark pair production. The first observation of single top quark production in proton-antiproton collisions was made at the Tevatron in 2009 [60,61].

To calculate the total cross section of top quark pair production in proton-proton collisions several ingredients are required. The partonic cross section $\hat{\sigma}(ij \to \mathrm{t\bar{t}})$ can be calculated with Feynman rules of perturbative QCD. It provides the cross section for a transition of the initial state which consists either of a quark-antiquark or a gluon-gluon pair to the final state with top and antitop quark. Since in experiments as the LHC, only composed hadrons like protons are collided, a description of quarks and gluons as parts of the hadron carrying only a certain fraction of the total hadron momentum is required. For this purpose, the concept of Parton Distribution

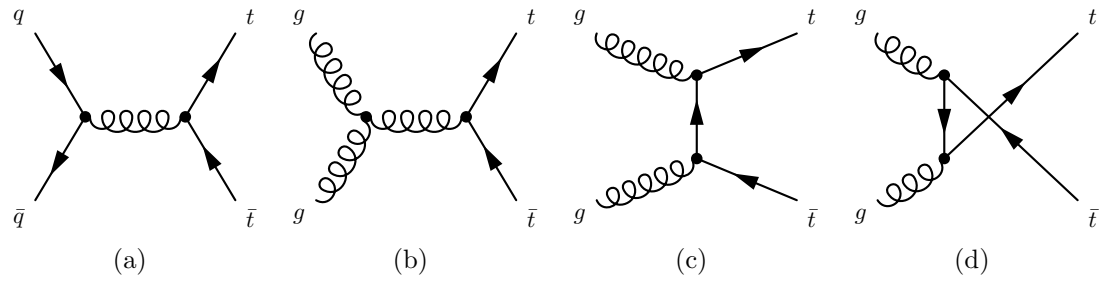

Figure 1.3: All leading order Feynman diagrams for top quark pair production in hadron-hadron collisions: quark-antiquark annihilation (a) and gluon-gluon fusion (b)-(d).

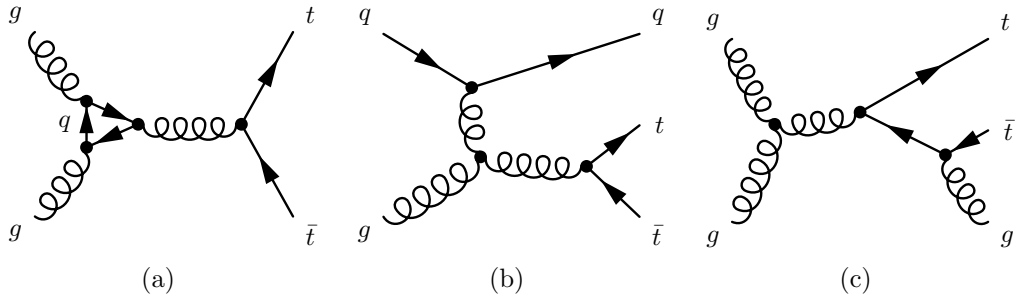

Figure 1.4: Examples for NLO Feynman diagrams of top quark pair production with loops (a) or initial (b) or final state radiations (c). In NLO diagrams, also processes with quark-gluon initial states can occur.

Functions (PDF) is introduced. The PDF describes the probability to find a parton i in a hadron A carrying a momentum fraction $x_i = \frac{p_i}{p_\mathrm{A}}$ of the entire hadron. The PDF $f_{i,\mathrm{A}}(x_i, Q^2)$ is not only a function of the momentum fraction x_i, but also depends on an energy scale Q. The total hadronic cross section of top quark pair production in proton-proton collisions can then be calculated with a factorisation ansatz [62]. In this ansatz, the scale parameter Q is set to the so-called factorisation scale μ_F. This scale is introduced to separate short and long range interactions. For the study of top quark pair production, the scale parameter μ_F is usually set to the mass of the top quark, $\mu_F = m_\mathrm{t} \cdot c^2$. In figure 1.5, the PDFs of the constituents of the proton in the CTEQ6L [63, 64] parametrisation are shown. In the factorisation ansatz the cross section is calculating by integrating the partonic cross section $\hat{\sigma}(ij \to \mathrm{t\bar{t}})$ with the PDF for the initial partons i, j and summing over all possible initial states:

$$\sigma(\mathrm{pp} \to \mathrm{t\bar{t}}) = \sum_{i,j} \int dx_i dx_j f_{i,\mathrm{p}}(x_i, \mu_F^2) f_{j,\mathrm{p}}(x_j, \mu_F^2) \hat{\sigma}(ij \to \mathrm{t\bar{t}}, \hat{s}, \mu_F^2, \mu_R^2). \qquad (1.27)$$

The summation is performed over are all possible initial states of $\mathrm{t\bar{t}}$ production. The partonic cross section depends on the effective centre-of-mass energy of the colliding partons which is given by $\hat{s} = (p_i + p_j)^2 = x_i x_j (p_{\mathrm{p}_1} + p_{\mathrm{p}_2})^2$, where p_{p_1} and p_{p_2} are the momenta of the incoming protons. Top quark pairs can only be produced, if the momenta of the initial partons p_i and p_j lead to a partonic centre-of-mass energy

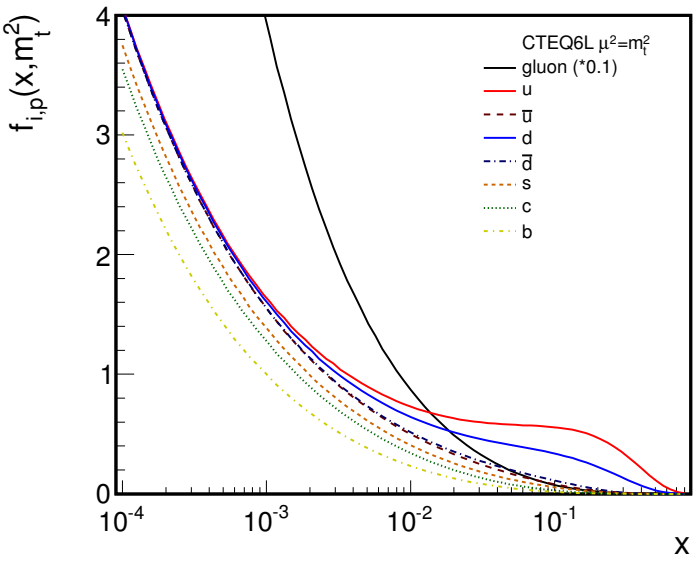

Figure 1.5: The parton distribution functions (PDF) of the proton in the CTEQ6L parametrisation [64]. The scale parameter μ_F is set to the top quark mass. At high momentum fraction x, the PDF $f_{i,\mathrm{p}}(x_i, \mu_F^2)$ of the valence quarks, up and down, are dominant. The gluon PDF is largest for smaller x values.

$\hat{s} \geq (2m_\mathrm{t})^2$. The partonic cross section depends on the factorisation and renormalisation scale parameters μ_F and μ_R. The renormalisation scale μ_R describes the running of the strong coupling constant. The factorisation scale separates between the description of high-energetic processes going into the partonic cross section and low-energetic effects parametrised with the PDF. In an exact calculation it should make no difference, whether an effect is described by the partonic matrix element or by the PDF. But since processes can only be calculated in a finite order of a perturbative series, the final result on the total cross section has a residual dependency on the choice of the scale parameters. In the absence of infinite order calculations the variation of the scale parameters leads to changes in the total cross section which have to be treated as uncertainties on the result. Since both scale parameters are more or less arbitrary, they are usually set to the same value, $\mu_F = \mu_R$. A recent approximate next-to-next-to-leading order calculation of the total cross section of top quark pair production in proton-proton collisions at a centre-of-mass energy of 7 TeV yields $\sigma_{\mathrm{t\bar{t}}} = (165 \pm 10)$ pb assuming a top quark mass of 173 GeV/c^2 [65].

1.2.2 Top Quark Decay Modes

In the SM, the top quark decay is mediated by weak interactions. Due to the CKM matrix elements related to the top quark (see equation 1.26), the top quark decays in almost 100% of all cases into its lighter isospin partner, the b-quark. In this decay a W boson is emitted. Other allowed decay modes contain transitions to the first and second quark families, but the decay of the top quark into d- or s-quarks is suppressed due to the CKM matrix elements: The decay amplitude of a top quark into a b-quark is proportional to $|V_\mathrm{tb}|^2$ which is close to 1, whereas the other decay

channels are proportional to $|V_{\mathrm{td}}|^2$ and $|V_{\mathrm{ts}}|^2$ respectively. Since the off-diagonal elements of the CKM matrix are much smaller, flavour changing top decays are much rarer than t- to b-quark decays.

The top quark decay is classified according to the subsequent decay modes of the emitted W boson. The W boson can either decay into a pair of quark and antiquark or into a pair of charged lepton and neutrino. The allowed decay modes of a positively charged W boson are $\mathrm{W}^+ \to \mathrm{e}^+\nu_{\mathrm{e}}$, $\mathrm{W}^+ \to \mu^+\nu_\mu$, and $\mathrm{W}^+ \to \tau^+\nu_\tau$ for the leptonic decays and $\mathrm{W}^+ \to \mathrm{u}\bar{\mathrm{d}}$, $\mathrm{W}^+ \to \mathrm{u}\bar{\mathrm{s}}$, $\mathrm{W}^+ \to \mathrm{u}\bar{\mathrm{b}}$, $\mathrm{W}^+ \to \mathrm{c}\bar{\mathrm{d}}$, $\mathrm{W}^+ \to \mathrm{c}\bar{\mathrm{s}}$, and $\mathrm{W}^+ \to \mathrm{c}\bar{\mathrm{b}}$ for hadronic decays. The decay modes of a W^- are the same with particles and antiparticles exchanged. A decay into a quark-antiquark pair containing a top quark is kinematically forbidden because the W boson mass is smaller than the top quark mass. The W boson couples universally to all weak isospin doublets, but only the leptonic final states are weak eigenstates. The hadronic final states are no eigenstates of the weak interaction, their weak eigenstates are rotated against the mass eigenstates with the CKM matrix. The decay rate of W bosons into quark-antiquark pairs is therefore proportional to the absolute square of the corresponding CKM matrix element. All other kinematic dependencies on the decay rate are equal for all allowed W boson decays under the assumption that all light quarks and leptons are massless. Since each quark-antiquark pair exists in three different colour charge configurations, the decay rate of hadronic W boson decays is enhanced by a factor of three. Then, the branching ratio of all hadronic decays compared to leptonic decays is:

$$\frac{B(\mathrm{W} \to \mathrm{q}\bar{\mathrm{q}}')}{B(\mathrm{W} \to \mathrm{l}\nu_{\mathrm{l}})} = \frac{3\left(|V_{\mathrm{ud}}|^2 + |V_{\mathrm{us}}|^2 + |V_{\mathrm{ub}}|^2 + |V_{\mathrm{cd}}|^2 + |V_{\mathrm{cs}}|^2 + |V_{\mathrm{cb}}|^2\right)}{3} = 2 \qquad (1.28)$$

since due to the unitarity of the CKM matrix $|V_{\mathrm{ud}}|^2 + |V_{\mathrm{us}}|^2 + |V_{\mathrm{ub}}|^2 = |V_{\mathrm{cd}}|^2 + |V_{\mathrm{cs}}|^2 + |V_{\mathrm{cb}}|^2 = 1$. Two thirds of all W bosons decay to hadrons, one third decays equally into one of the three lepton pairs. The branching ratio into electron, muon, or tau and corresponding neutrino is therefore $\frac{1}{9} \approx 0.111$ each. The measured average branching ratio for leptonic decays is $(10.8 \pm 0.09)\%$ [35] which differs slightly from the expectation found in the consideration above due to kinematic constraints originating from different masses of the decay products.

For top quarks being produced in pairs, each of these two quarks decays into a W boson and a b-quark. The top quark decays into a W^+ and a b-quark, the antitop quark disintegrate into a W^- and an anti-b-quark. This leads to three categories of top quark pair decays. In the all-hadronic decay channel both W bosons decay into quark-antiquark pairs, in the dilepton channel both W bosons decay into leptons, and in the so-called lepton+jets channel one W boson decays into leptons and the other W boson decays into quarks. The all-hadronic category has a LO branching ratio of $\frac{2}{3}\cdot\frac{2}{3} = \frac{4}{9}$. The branching ratio of the di-lepton mode is $\frac{1}{3}\cdot\frac{1}{3} = \frac{1}{9}$. In this thesis, top quark pair production in the lepton+jets decay mode is studied. The lepton+jets channel has also a branching ratio of $\frac{4}{9}$, $\frac{4}{27} \approx 14.8\%$ for each lepton type, electron, muon, or tau. The advantage of the lepton+jets category is its larger branching ratio compared to the dilepton decay channel and its clearer signature containing one charged lepton, a neutrino and four quarks in the final state compared to the all-hadronic decay mode in which the final state consists of six quarks.

1.3 Top Quark Production Beyond the Standard Model

Several models extending the SM exist for the purpose of explaining some of the unanswered questions arising from the theory of the SM discussed in section 1.1.5. In some of these models, hypothetical exchange particles can contribute to the production of top quark pairs in high-energetic particle interactions like proton-proton collisions at the LHC. The top quark offers a unique opportunity to study influences of models extending the SM. Models in which new types of exchange particles influence the top quark production are for instance chiral colour models [66] with axigluons, coloron models [67, 68], or extra dimensional theories, such as Randall-Sumdrum [69] or ADD [70] models in which Kaluza-Klein excitations couple to the top quark. The latter models try to incorporate the gravitation into the SM by introducing additional warped dimensions on small distance scales. Especially in the model of warped extra dimensions, Kaluza-Klein excitations of the gluon would preferably couple to top quarks [71]. Also the Higgs boson of the SM or a Higgs boson in a supersymmetric model [72], like the minimal supersymmetric extension of the SM (MSSM), where at least five Higgs bosons are predicted, can decay into top quark pairs, if $m_h > 2m_\mathrm{t}$. Supersymmetry is thought to solve the hierarchy problem and can also provide Dark Matter candidates. In most of these models, the introduced particles couple preferably to (heavy) quarks. For example, models containing a leptophobic Z′ boson [73] belong to this category of theories. In this thesis, two analyses are presented studying the top quark pair production at the LHC. One analysis focusses on the search for heavy resonances decaying into top quarks utilizing the spectrum of the invariant mass of the top quark pair. In the second analysis, the charge asymmetry in top quark pair production is measured. In the following sections, the theoretical motivation for these measurements and the observables at the LHC will be discussed.

1.3.1 The Invariant Mass Spectrum

The invariant mass of the top quark pair, $m_{\mathrm{t\bar{t}}}$, may show a disturbed spectrum, if some new theory models were realised [74]. In the SM, the differential cross section $\frac{d\sigma}{dm_{\mathrm{t\bar{t}}}}$ is predicted to be a spectrum which starts at a threshold of $2m_\mathrm{t}$. The maximum of this spectrum is reached just above the production threshold and it is steeply falling for higher values of $m_{\mathrm{t\bar{t}}}$. Recent calculations [75] show that already $\mathrm{t\bar{t}}$ production at the threshold may show some interesting effects. Just below the production threshold at $2m_\mathrm{t}$ an additional peak may exist. This peak is predicted to be a remnant of a bound $\mathrm{t\bar{t}}$ state in a colour-singlet S-wave configuration in the gluon-gluon production channel. In figure 1.6, this $1S$ peak is shown as it would look like in proton-proton collisions at a centre-of-mass energy of 7 TeV.

The presence of yet unobserved particles decaying into $\mathrm{t\bar{t}}$ pairs will probably distort the shape of the $m_{\mathrm{t\bar{t}}}$ spectrum. In most theoretical models predicting additional contributions to top quark production, the cross section as function of $m_{\mathrm{t\bar{t}}}$ will show a peak around the mass of a new particle which decays into $\mathrm{t\bar{t}}$. The $\frac{d\sigma}{dm_{\mathrm{t\bar{t}}}}$ spectrum

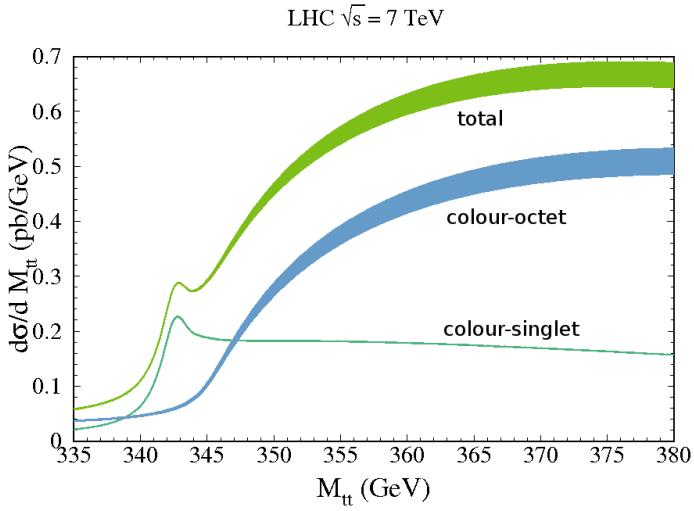

Figure 1.6: Invariant mass distribution of the top quark pair production near the threshold for colour singlet states, colour octet states, and the total sum [75,76]. The bands indicate uncertainties on the scale parametrisation.

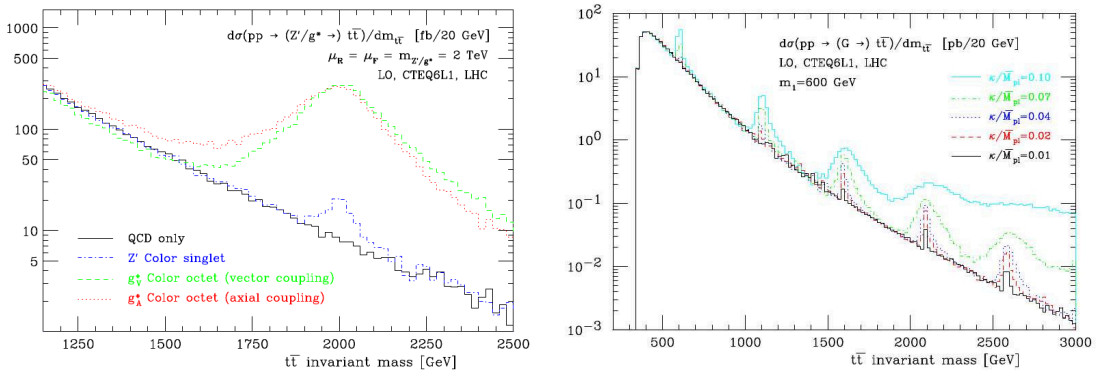

(a) (b)

Figure 1.7: Distribution of $\frac{d\sigma}{dm_{t\bar{t}}}$ in the SM model and several theories extending the SM in proton-proton collisions at the LHC. In (a), the shape of resonances with a mass of 2 TeV/c^2 and various colour structures are shown. The Z′ model is a colour singlet, the lines denoted as colour octets show predictions for resonances with vector couplings (g_V^*, e. g. Kaluza-Klein gluons or colorons) and axial-vector couplings (g_A^*, e. g. axigluons). In (b), Kaluza-Klein excitations of a graviton in a Randall-Sundrum model are shown on top of the SM prediction for different ratios $\kappa/\overline{M}_{\mathrm{pl}}$ which parametrises the size of the extra dimensions. The mass of the first excitation is set to 600 GeV/c^2 [74].

for SM $t\bar{t}$ production and several new models extending the SM is depicted in figure 1.7. Some models predict only single resonances at a certain mass value, whereas in other models, such as the Randall-Sundrum model, a set of several mass peaks in the $m_{t\bar{t}}$ spectrum may be observable [74].

From analyses at the Tevatron experiments, CDF and D0, limits have been set on the existence of resonances in the $t\bar{t}$ mass spectrum [77, 78]. The existing limits

use a leptophobic topcolour Z′ as reference model [67]. In this model, an alternative ansatz is chosen to explain the electroweak symmetry breaking, using a top quark condensate. This model predicts a Z′ boson which preferably couples to quarks of the third generation. Current searches exclude such an additional gauge boson decaying into top quark pairs with masses below 820 GeV/c^2 at 95% confidence level [78]. Since the centre-of-mass energy of the Tevatron collider is limited to 1.96 TeV, these limits will not be extended into the mass region of much more than 1 TeV/c^2 by direct searches.

1.3.2 The $t\bar{t}$ Charge Asymmetry

Another quantity which is sensitive to top quark pair production mechanisms not described within the SM is the $t\bar{t}$ charge asymmetry. The measurement of a sizeable non-vanishing $t\bar{t}$ charge asymmetry can give a hint for the existence of new exchange particles contributing to $t\bar{t}$ production, even if the new particle has a broad decay width or a mass above the current available range in the $m_{t\bar{t}}$ spectrum and will therefore not be visible in the invariant mass distribution.

The charge asymmetry arises, if a hypothetical new exchange particle has different couplings to top quarks than to antitop quarks. In most new theories, the new particle is a gauge boson R_a of a $SU(N)$ group which is added to the gauge group of the SM. A coupling of this gauge boson to the quarks q of the SM is then realised by adding a term to the SM Lagrangian of the form

$$\mathcal{L}_R \sim i\bar{\psi}_q \gamma^\mu \left(g_V^q + g_A^q \gamma_5\right) R_\mu^a T_a \psi_q. \tag{1.29}$$

Here, the coupling parameters g_V^q and g_A^q for vectorial and axial-vectorial couplings can in general be different for each quark flavour q. Different values of g_V^q and g_A^q lead to different couplings to left-handed and right-handed quarks given by the projections in equation 1.11.

The initial state of $t\bar{t}$ production in gluon-gluon fusion is completely symmetric. Therefore, there is no possibility to observe an asymmetry in the behaviour of top and antitop quarks produced in this process. An observable charge asymmetry can only occur in top quark pair events produced with asymmetric initial states such as quark-antiquark annihilation or NLO quark-gluon fusion processes. In $t\bar{t}$ production via quark-antiquark annihilation with asymmetric couplings g_V^q and g_A^q, the outgoing top quark will preferably be emitted in the direction of the incoming quark, the outgoing antitop quark will preferably be emitted in the direction of the antiquark or vice versa, depending on the actual values of the two coupling parameters.

The contributions of quark-antiquark annihilation and gluon-gluon fusion processes can be determined from the PDF at the energy of the colliding partons. The energy of the effectively colliding partons has to exceed the mass of the produced particles, which is $2m_t$ for $t\bar{t}$ production. At the LHC, only about 20% of all $t\bar{t}$ events are produced in quark-antiquark annihilation or in NLO quark-gluon initial processes, while 80% are produced in gluon-gluon fusion processes [79–81]. Hence, only a small momentum fraction of the colliding protons is needed to bring up enough energy for the production of two top quarks. For low momentum fractions,

the gluon PDF is dominating (see figure 1.5). In contrast, for the production of top quark pairs at the Tevatron, a relatively high momentum fraction of the colliding (anti-)protons is required, since the energy of the colliding particles is much lower compared to the LHC. This region of momentum fractions is dominated by the valence quark PDFs. Thus, the ratio of quark-antiquark annihilation is about 85% at the Tevatron.

In proton-antiproton collisions at the Tevatron, the charge asymmetry results in a forward-backward asymmetry. The quarks in the initial state of $\mathrm{t\bar{t}}$ production are mainly valence quarks from the proton, antiquarks in the initial state usually originate from the antiproton. Since the initial state is already asymmetric, a charge asymmetry is visible in opposite flight directions of top and antitop quarks in the laboratory frame. The asymmetry measured at the Tevatron is defined using the rapidities of the top quarks. A particle's rapidity y is defined in the laboratory frame as

$$y := \frac{1}{2} \ln \left(\frac{E + p_z}{E - p_z} \right), \tag{1.30}$$

where E is the energy and p_z the momentum of the particle in the direction of the incoming proton. The rapidity y is Lorentz invariant under boost transformations along the z direction. A useful experimental measurable variable being sensitive to the charge asymmetry which can be generated at the Tevatron is defined in the $p\bar{p}$ rest frame as

$$A_{\mathrm{p\bar{p}}} := \frac{N_{\mathrm{t}}(y \geq 0) - N_{\bar{\mathrm{t}}}(y \geq 0)}{N_{\mathrm{t}}(y \geq 0) + N_{\bar{\mathrm{t}}}(y \geq 0)}, \tag{1.31}$$

where $N_{\mathrm{t}}(y \geq 0)$ and $N_{\bar{\mathrm{t}}}(y \geq 0)$ are the numbers of observed top and antitop quarks, respectively, with positive rapidities. In the SM, a small asymmetry is predicted from NLO QCD corrections to top quark pair production. This small asymmetry arises from interference effects between $\mathrm{t\bar{t}}$ production with additional radiations in initial and final state and loop contributions (see figure 1.4). The predicted value is $A_{\mathrm{p\bar{p}}} = 0.051 \pm 0.006$ [82–84]. A value of $A_{\mathrm{p\bar{p}}} = 0.150 \pm 0.050(\mathrm{stat.}) \pm 0.024(\mathrm{syst.})$ for the charge asymmetry has been found in the most recent measurement with the CDF experiment [17–19]. The measurement shows a visible deviation from the SM prediction which is consistent with the theoretical value only within a 2σ fluctuation. Also the D0 experiment measures a positive charge asymmetry [20, 21]. This measurement is not corrected for detector effects and is therefore not directly comparable with the theory prediction for alternative models. Alternatively, the forward-backward asymmetry at the Tevatron can also be defined in the $\mathrm{t\bar{t}}$ rest frame. In the $\mathrm{t\bar{t}}$ rest frame, the CDF experiment measures an asymmetry of $A_{\mathrm{p\bar{p}}}^{\mathrm{t\bar{t}}} = 0.158 \pm 0.050(\mathrm{stat.}) \pm 0.024(\mathrm{syst.})$ compared to a theory prediction of $A_{\mathrm{p\bar{p}}}^{\mathrm{t\bar{t}}} = 0.078 \pm 0.010$ [24]. The deviation from the SM found in the charge asymmetry by the CDF experiment becomes much more significant when restricting the measurement into a kinematic region with high invariant mass $m_{\mathrm{t\bar{t}}} > 450\ \mathrm{GeV}/c^2$. Here, a charge asymmetry in the $\mathrm{t\bar{t}}$ rest frame of $A_{\mathrm{p\bar{p}}}^{\mathrm{t\bar{t}}} = 0.475 \pm 0.114$ is measured which corresponds to a more than 3σ deviation from the NLO QCD prediction [18].

The most prominent model predicting a charge asymmetry in $\mathrm{t\bar{t}}$ production is the theory of chiral colour [66, 85] which predicts an axigluon. In this model, a new

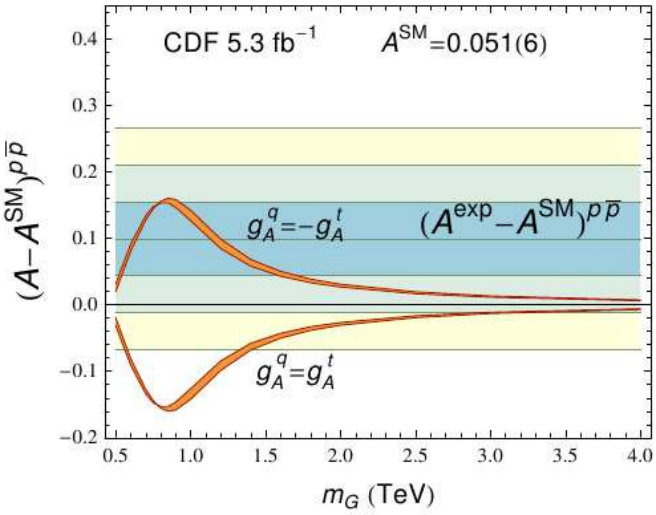

Figure 1.8: Comparison of an axigluon contribution ($g_V^q = g_V^t = 0$, $g_A^q = g_A^t = 1$) to the charge asymmetry observed at CDF as a function of the axigluon mass m_G. Also a hypothetical resonance with $g_A^q = -g_A^t = 1$ is shown. The bands correspond to 1σ, 2σ, and 3σ uncertainties of the measurement [87].

gauge group $SU(3)_1 \times SU(3)_2$ is introduced which is spontaneously broken to the $SU(3)$ of the SM QCD. Similar to the symmetry breaking in the Higgs mechanism in the electroweak theory, a mixing of the two gauge fields G_μ^1 and G_μ^2 corresponding to the groups $SU(3)_1$ and $SU(3)_2$, respectively, leads to an explanation of the gluon field G_μ as superposition of G_μ^1 and G_μ^2:

$$G_\mu = \cos\theta\ G_\mu^1 + \sin\theta\ G_\mu^2. \tag{1.32}$$

The mixing angle θ is a free parameter of these theory. The orthogonal superposition of G_μ^1 and G_μ^2 is a massive axigluon field G'_μ corresponding to the arbitrary gauge field R_μ in equation 1.29:

$$G'_\mu = -\sin\theta\ G_\mu^1 + \cos\theta\ G_\mu^2. \tag{1.33}$$

The pure axigluon has only an axial coupling term, i. e. $g_A^q = 1$ and $g_V^q = 0$ for all quark flavours q. The predicted charge asymmetry for the axigluon model is compared to the measurement in figure 1.8. Since the predicted asymmetry is negative, axigluons with masses up to more than 1 TeV/c^2 can be excluded by the CDF measurement. The measured value would more likely be consistent with a new exchange boson G'_μ which has axial couplings but opposite signs in g_A^q for couplings to the quarks in the initial state and to the top quarks in the final state, i. e. $g_A^t = 1$ and $g_A^q = -1$ for all other flavours q. Combined fits of g_A, g_V, the mass of the new resonance, and the mixing angle θ to the recent measurements of the charge asymmetry and the $\frac{d\sigma}{dm_{t\bar{t}}}$ distribution measured at the Tevatron also including data from direct searches of resonances in di-jet production at the LHC would prefer such a non-flavour universal coupling scheme [86].

The axigluon model is only one candidate for the explanation of the charge asymmetry found at the Tevatron. Many new theories predict an asymmetry already

in LO perturbation theory. Similar to the axigluon model explained above several theoretical approaches try to explain the charge asymmetry with the introduction of a new colour multiplet state [24,85,86,88–92]. In most of these models, the $SU(3)$ of the SM QCD is embedded into a larger group which is spontaneously broken. Also flavour changing couplings of a new vector boson such as a heavy W′ or Z′ [93–95] are introduced in some theoretical explanations of the measured deviation from the SM. Some other theories try to explain the observation of a large charge asymmetry with the exchange of a Kaluza Klein gluon in a Randall-Sundrum model [96, 97]. Models with a coloured exchange particle allow to explain the charge asymmetry already as interference effect of the SM $t\bar{t}$ production with the new gauge boson. Thus, such models are less strongly constrained by measurements of the $\frac{d\sigma}{dm_{t\bar{t}}}$. The listed models are only a few approaches to explain the observed forward-backward asymmetry in top quark pair production at the Tevatron, but there exist many other possible explanations [98–100].

The LHC is a proton-proton collider. Thus, the initial state of all interactions is always symmetric and there is no possibility to observe any forward-backward asymmetry. Also the large fraction of gluon-gluon induced $t\bar{t}$ production processes in the SM makes the search for charge asymmetric effects more complicated. However, other observables exist which are sensitive to the same coupling models which can generate a forward-backward asymmetry in proton-antiproton collisions. At the LHC, effects from a new coupling as described in equation 1.29 can occur in quark-antiquark annihilation. The PDF of quarks and antiquarks as partons of a proton have different spectra (see figure 1.5). Antiquarks can only occur as sea quarks, whereas quarks can either be sea or valence quarks. Therefore, a quark in the initial state carries on average a larger momentum fraction of the proton compared to antiquarks.

As an example, one can assume $t\bar{t}$ production with such couplings g_V^q and g_A^q that the top quark will preferably be emitted in the direction of the incoming quark and the outgoing antitop quark will preferably be emitted in the direction of the antiquark in the centre-of-mass system of the two initial partons. This effect will lead in the laboratory frame to an emission of top quarks more likely into forward or backward directions closer to the incoming proton beams. The antitop quark will be emitted more centrally staying closer to the antiquark in the initial state which has on average a smaller momentum than the initial quark. This situation is illustrated in figure 1.9. Depending on the values of g_V^q and g_A^q, also the opposite situation may occur: if the top quark is preferably be produced in the direction of the inital antiquark, its momentum will be more centrally and the antitop quark will be emitted more likely into the forward and backward directions.

The differences in the centrality of top and antitop quark can then lead to differences in the rapidity spectra. If top quarks are produced more likely in the forward and backward regions of the laboratory frame, their rapidity distributions will be broader than the rapidity spectrum of antitop quarks. This allows the definition of an observable sensitive to the charge asymmetry. One possibility is the definition of a central charge asymmetry using a certain cut-off rapidity y_C [25, 82, 101]. Then, the asymmetry is defined by counting top and antitop quarks in the central region

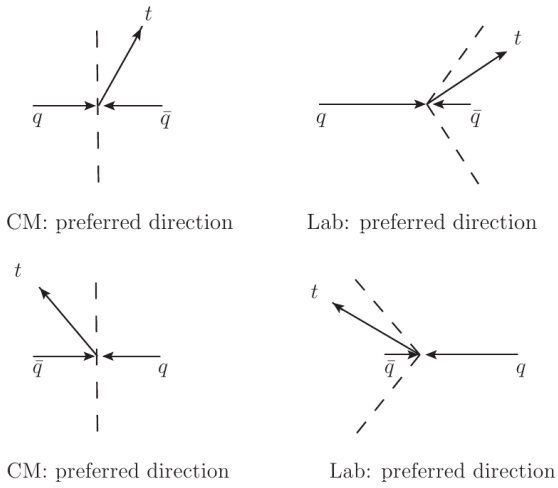

Figure 1.9: If the top quark is preferably produced in the direction of the incoming quark in the centre-of-mass frame due to a $t\bar{t}$ production mechanism with asymmetric couplings, the top quark will be more likely produced in the forward or backward direction when boosting into the laboratory frame [101].

with $|y| < y_C$:

$$A_C(y_C) := \frac{N_t(|y| < y_C) - N_{\bar{t}}(|y| < y_C)}{N_t(|y| < y_C) + N_{\bar{t}}(|y| < y_C)}. \tag{1.34}$$

By introducing the cut-off parameter y_C, the definition of $A_C(y_C)$ in equation 1.34 does not include the full number of available $t\bar{t}$ events. Top quarks with rapidities greater than y_C do not contribute to the determination of the charge asymmetry. Another caveat of this definition is that $A_C(y_C)$ is not defined for individual events but only for a complete set of measured $t\bar{t}$ events. Within this thesis an alternative definition for the charge asymmetry in proton-proton collisions has been invented. An event-by-event defined variable is the difference of absolute pseudorapidity values of the top and the antitop quark, $|\eta_t| - |\eta_{\bar{t}}|$. A particle's pseudorapidity η is defined by:

$$\eta := -\ln\left(\tan\frac{\theta}{2}\right), \tag{1.35}$$

where θ is the angle between the particle's momentum and the direction of the incoming protons. The pseudorapidity η is equal to the rapidity y for massless particles. The advantage of using the pseudorapidity is its definition based on angular measurements only. Using the variable $|\eta_t| - |\eta_{\bar{t}}|$, the charge asymmetry A_C can be definded as a central-decentral asymmetry in this quantity:

$$A_C := \frac{N^+ - N^-}{N^+ + N^-}, \tag{1.36}$$

where N^+ and N^- are the numbers of observed top quark pair events with positive or negative values of $|\eta_t| - |\eta_{\bar{t}}|$ respectively. Compared to the definition of the cut-dependent charge asymmetry in equation 1.34, the definition of the asymmetry in equation 1.36 uses the entire amount of measured $t\bar{t}$ events. As will be discussed

model	Tevatron $A_{\mathrm{p\bar{p}}}^{\mathrm{tt}}$	Tevatron $A_{\mathrm{p\bar{p}}}^{\mathrm{tt}}$ ($m_{\mathrm{t\bar{t}}} > 450$ GeV/c^2)	LHC A_C
SM	0.078±0.010	0.087±0.012	0.0130±0.0011
Octet A	0.129±0.016	0.190±0.014	0.0277±0.0024
Octet B	0.162±0.015	0.235±0.013	0.0294±0.0012
Octet C	0.182±0.016	0.271±0.013	0.0334±0.0012
Octet D	0.118±0.010	0.236±0.016	0.0284±0.0012

Table 1.2: Predicted forward-backward asymmetries at the Tevatron in the $\mathrm{t\bar{t}}$ rest frame and predictions for the corresponding charge asymmetry A_C at the LHC for the SM and several colour-octet models with different parameter sets from an NLO computation [24–26]:
Octet A: Flavour universal axigluon with $g_V = 2$, $g_A = 0.8$, and a mass of $m = 1.6$ TeV/c^2.
Octet B: Flavour non-universal axigluon with $g_V = 0$, $g_A^q = -g_A^t = 3/2$, and $m = 2$ TeV/c^2.
Octet C: Flavour non-universal axigluon with $g_V = 0$, $g_A^q = -g_A^t = 3/2$, and $m = 1.8$ TeV/c^2.
Octet D: Flavour non-universal axigluon in the chiral colour model [85] with a mixing angle of $\theta = 42^\circ$ and $m = 1.45$ GeV/c^2. Vector and axial-vector couplings in this model are given by $g_V^q = g_V^t = 1/\tan 2\theta$ and $g_A^q = -g_A^t = 1/\sin 2\theta$.

later (see chapters 4 and 5), the top quark momenta are not directly accessible in experimental setups. Hence, also the implementation of a cut based on top quark momenta is more complicated from the experimental point of view. The advantage of the definition of the central-decentral asymmetry in equation 1.36 is that it only requires the determination of the $|\eta_{\mathrm{t}}| - |\eta_{\bar{\mathrm{t}}}|$ variable in each event and no further cut variables.

In the SM, only a small asymmetry of $A_C = 0.0130 \pm 0.0011$ is predicted from NLO QCD effects [24–26]. NLO predictions for several axigluon models with various values of g_V and g_A are summarised in table 1.2. The expected deviations from the SM prediction arising from these models are of the order of a few percent.

Although the access to high invariant masses of the $\mathrm{t\bar{t}}$ system is enlarged at higher centre-of-mass energies, the effects induced by the a charge asymmetry in top quark pair production are much smaller at the LHC in proton-proton collisions than at the Tevatron due to the higher fraction of symmetric gluon-gluon initial state processes. Nevertheless, if the asymmetry observed at the Tevatron experiments would be induced by a new physical effect, similar effects should also be observable in top quark pair production at the LHC.

Chapter 2

The Large Hadron Collider and the CMS Experiment

Top quarks are usually unobservable in nature since they can only be produced in high-energetic particle collisions and they decay immediately after their production. To perform precise measurements of particle collisions an experimental setup is required which provides as many as possible reproducible particle collisions under laboratory conditions. The collisions and the particles produced in these interactions have to be recorded by a detector. In a sophisticated way, the recorded information is processed to make it readable and understandable for human beings whose senses are unfortunately not designed to analyse high-energetic particle collisions directly. The data analysed in this thesis were taken with the CMS detector which records proton-proton collisions performed at the Large Hadron Collider. In this chapter, the experimental setup of the accelerator and the detector is described.

2.1 The Large Hadron Collider

The Large Hadron Collider (LHC) [16] is a ring collider which was built by the European Organisation for Nuclear Research (CERN) near Geneva, Switzerland. It is located in an underground tunnel of 26.7 km circumference. The tunnel hosted the former Large Electron Positron collider (LEP) [102] and was constructed in the area of the Swiss-French border. The LHC was originally designed to accelerate protons to an energy of 7 TeV, but up to now only a beam energy of 3.5 TeV has been reached. Two proton beams circulate in opposite directions in the ring and are brought to collisions at four interaction points. The centre-of-mass energy in these proton-proton collisions is 7 TeV. Alternatively, the LHC can also provide collisions of lead ions. The design energy of the lead ion beams is 2.76 TeV per nucleon. At least one detector is placed at each of the four interaction points. The four main experiments directly placed at the interaction points are ALICE (A Large Ion Collider Experiment), ATLAS (A Toroidal LHC ApparatuS), CMS (Compact Muon Solenoid) and LHCb (Large Hadron Collider beauty). They are built in huge underground caverns. Two smaller detectors, the LHCf (Large Hadron Collider forward) experiment and the TOTEM (TOTal Elastic and diffractive cross section

MEasurement) detector, are placed close to the interaction points of ATLAS and CMS, respectively. ALICE [103] is a detector which is designed to study mainly the collisions of lead ions. In this collisions new states of matter such as the quark-gluon plasma [104] may be discovered. The goal of the LHCb experiment [105] is to study mesons consisting of b quarks. In the production and decay of these particles asymmetries between matter and antimatter can be analysed. Since mesons containing b quarks are mainly produced close to one of the colliding proton beams the LHCb detector does not surround the interaction point with sub-detectors in all directions, but covers the forward region of the interaction. ATLAS [106] and CMS [22] are multi-purpose detectors. The sub-detectors of both experiments surround the interaction point hermetically and try to record and to identify all kinds of produced particles. Both detectors are designed to study processes of the SM in detail and especially to search for effects not described by the SM. One goal of ATLAS and CMS is to discover the as yet unobserved Higgs boson. TOTEM [107] is an experiment which studies particles produced very close to the beams. In the measurements performed with TOTEM, for instance the total proton-proton cross section can be measured. The LHCf experiment [108] also uses particles produced in forward direction. The aim of the LHCf experiment is to simulate cosmic rays under laboratory conditions.

General Collider Parameters

The centre-of-mass energy is the most important parameter determining the set of elementary particles which can be produced. In particle collisions, the energy of the colliding particles can be transformed into masses of created particles. From the equivalence of mass and energy, $E = mc^2$, only particles with masses below the centre-of-mass energy can be produced. For searches for new heavy particles, a high centre-of-mass energy is therefore required. The centre-of-mass energy and also the type of colliding particles define the available phase-space and therefore the cross section of a certain physical process.

The performance of a collider is constraint by several conditions. For the centre-of-mass energy of a ring collider mainly the performance of the bending magnets is the limiting factor. A circular accelerator has the advantage that the same acceleration device is crossed by the beam many times. The beam can therefore be brought to relatively high energies without requiring many cavities or high electric field strengths. To keep the beam on a circular orbit, dipole magnets are utilised. At the deflection of charged particles in magnetic fields synchrotron radiation is emitted. A particle's energy loss per turn ΔE due to synchrotron radiation is given by

$$\Delta E = -\frac{4\pi\alpha Z\beta^3\gamma^4}{3R} \tag{2.1}$$

for a particle with Z times the elementary charge. Here, $\beta = \frac{v}{c} \approx 1$ for ultra-relativistic particles; $\gamma = \frac{1}{\sqrt{1-v^2/c^2}}$ is the Lorentz factor of the accelerated particles. To keep the energy loss small the radius R of the accelerator has to be large. Since $\gamma = \frac{E}{m_0c^2}$, the synchrotron radiation is much smaller for particles with high rest mass

m_0. At the LHC where protons are accelerated, the energy loss due to synchrotron radiation does therefore not delimit the beam energy. This is in contrast to electron accelerators, where the synchrotron radiation loss is much larger since the electron rest mass is more than 1,000 times smaller than the proton mass. The main limitation on the beam energy at the LHC arises from the magnetic field strength which is required to keep a proton beam with an energy of several TeV on its circular track. For the LHC design beam energy of 7 TeV a magnetic field strength of 8.33 T is required.

Besides beam energy and centre-of-mass energy, several other parameters describe the performance of a particle collider. The number of observable events N of a physical process of interest is not only proportional to its cross section σ, but also to the integrated luminosity $L_{\text{int}} = \int L dt$:

$$N = \sigma \int L dt. \tag{2.2}$$

In $\int L dt$, the time integral runs over the time range the collider is operating. The instantaneous luminosity L is a measure for the collision rate a collider is delivering. It depends on several machine parameters. In ring colliders like the LHC, two beams are accelerated with oscillating electric fields in radio frequency (RF) cavities. The usage of oscillating fields allows to accelerate charged particles to much higher energies than an acceleration with a static electric field. In a constant field particles can only be brought to an energy equivalent to the applied voltage, whereas a microwave cavity performs an acceleration of a charged particle beam with small voltages but many times, if the frequency is adopted correctly to the particle's flight velocity. As a consequence of this acceleration concept, the particle beams are divided into bunches because only particles flying in-phase with the oscillating field are accelerated correctly. In case of such an acceleration mode, the instantaneous luminosity is a function of the number of bunches per beam N_{b}, the frequency of the colliding bunches f, and the number of particles per beam N_1 and N_2 [16]:

$$L = \frac{f N_{\text{b}} N_1 N_2 \gamma F}{4\pi \epsilon_n \beta^*}. \tag{2.3}$$

In this equation, γ is again the Lorentz factor of the accelerated particles and F, ϵ_n, and β^* are further beam parameters. The geometric luminosity reduction factor F takes into account that the luminosity is reduced, if the two beams collide under a crossing angle which differs from an exact head-on collision. The normalised transverse beam emittance ϵ_n describes the phase space occupied by the beam particles in the transverse plane to the beam direction. β^* is the value of the beta function at the interaction point. The beta function measures the oscillation of the beams around the optimal beam axis. The instantaneous luminosity is measured in units of $\text{cm}^{-2}\text{s}^{-1}$, the integrated luminosity is usually given in pb^{-1}.

The luminosity does mainly depend on the size of the particle bunches, the number of protons per bunch, and the collision rate. For a high luminosity, the diameter of the colliding proton bunches should be kept small, but the number of particles per bunch has to be large. This leads to high densities of protons in the bunches.

Since the protons are all positively charged they repulse each other. Thus, the particle density is mainly limited by this repulsion. Therefore, also the instantaneous luminosity can not be increased to arbitrary high values.

Accelerator Chain

To accelerate protons or heavy ions up to energies of several TeV a chain of accelerators is used before injecting the particles into the LHC. Each pre-accelerator is designed to increase the beam energy to a specific energy level. The accelerator chain is part of the CERN accelerator complex shown in figure 2.1. Most of the pre-accelerators were already built in the last decades at CERN to supply many experiments with particle beams of different energies.

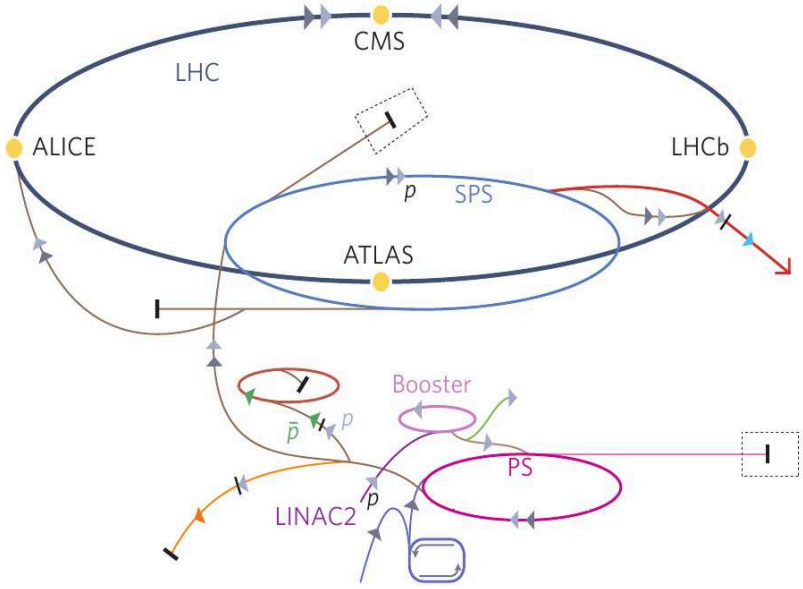

Figure 2.1: Overview of all accelerator devices at CERN [109]. The protons for the LHC are accelerated sequentially by the LINAC 2, the Proton Synchrotron Booster, the Proton Synchrotron (PS), and the Super Proton Synchrotron (SPS) before they are injected into the LHC.

Before protons can be accelerated, they have to be extracted from hydrogen molecules. In a duoplasmatron [110], electrons are injected into a hydrogen plasma. The electrons ionise hydrogen atoms and the free protons are extracted with a high voltage from the duoplasmatron. The first accelerator is a radio frequency quadrupole (RFQ). The injection energy to the RFQ is 92 kV. The electric fields of the RFQ accelerate the protons to an energy of 750 keV and divide the beam into bunches. The next accelerator in the chain is a linear accelerator called LINAC 2 [111]. The LINAC 2 was built in 1978 and accelerates the proton beam to an energy of 50 MeV. The beam is than transferred to the Proton Synchrotron Booster (PSB) [112]. The PSB is a synchrotron with a radius of 25 m which increases the proton beam to an energy of 1.4 GeV. The PSB has four parallel beam pipes to allow higher beam currents. The beam from the PSB is than brought into the Proton Synchrotron

(PS) [113]. The PS is the oldest part of the accelerator chain. It is already operating since 1959. The PS has a circumference of 628 m and accelerates the protons to an energy of about 25 GeV. The last pre-accelerator is the Super Proton Synchrotron (SPS) [114]. Besides the LHC, the SPS is CERN largest accelerator. It is a synchrotron with a circumference of 7 km and was first operating in 1976. The SPS consist of 1,317 magnets to bend and focus the beam. The proton beam coming from the PS is accelerated to 450 GeV by the SPS. From the SPS, two proton beams at this energy are extracted and transferred in opposite directions into the LHC.

The LHC is the world's largest synchrotron. It is divided into eight equally-equipped sections. The LHC consist of two beam pipes for the two circulating beams. The beam pipes are evacuated to a pressure of 10^{-10} atm. A complex system of magnets is used to keep the two beams on their circuits. In total, 1,232 superconducting dipole magnets bend the beams on a circle. Each dipole magnet has a length of 15 m. The effective bending radius of the dipole magnets is 2.8 km which is less than the radius of the LHC tunnel of 4.8 km. In the intersections between the dipole magnets, the beams follow a straight line. This intersection lines are equipped with further focussing magnets. Also the collision points are not equipped with dipole magnets. The magnetic fields in the dipole magnets are arranged such that one dipole magnet can bend both counter-rotating beams simultaneously. The dipoles were originally designed to produce magnetic field strengths of 8.33 T which is required to bend protons with energies of 7 TeV. For the operation with beam energies of 3.5 TeV the field strength is also reduced by a factor of two. To achieve such high field strengths, the magnets have to be superconducting to avoid extremely high energy consumption. The windings of the electromagnets are made of niob-titan (NbTi) and are cooled down for operation to a temperature of 1.9 K by superfluid helium. The cryogenic system consists of eight refrigeration plants, one plant for each LHC sector. A cryogenic distribution line is installed in parallel to the accelerator in the same tunnel to support the magnets with helium. The total cold mass of the LHC is 37,000 t. In addition to the dipole magnets, the LHC comprises 392 superconducting quadrupole magnets. The quadrupoles are the largest focussing magnets. The quadrupole magnets have a lengths of approximately 5 m. Together with a few thousand smaller magnets they focus the beam to their trajectories and bring them to collision at the four interaction points.

In four of the eight insertions between the eight sectors of the LHC, the experiments are placed (see figure 2.2). The ATLAS experiment is placed in insertion 1, ALICE is located at insertion 2, CMS at point 5, and LHCb is placed at point 8. In this insertions, the two beams are crossing each other and can be brought to collisions in the centre of the detectors by further focussing and bending magnets. At insertions 3 and 7, two collimation systems are installed. The collimators are used to clean the beam from its halo and to protect the machine against abnormal beam losses. The beam dump system is placed at point 6. The beams can be vertically ejected from the LHC with kicker and septum magnets. The beam dump system provides a safe extraction of the beam from the LHC to avoid possible destructions caused by the immense beam energy. In the insertion line at point 4, superconducting RF cavities are installed. They are operating at a temperature of 4.5 K with a

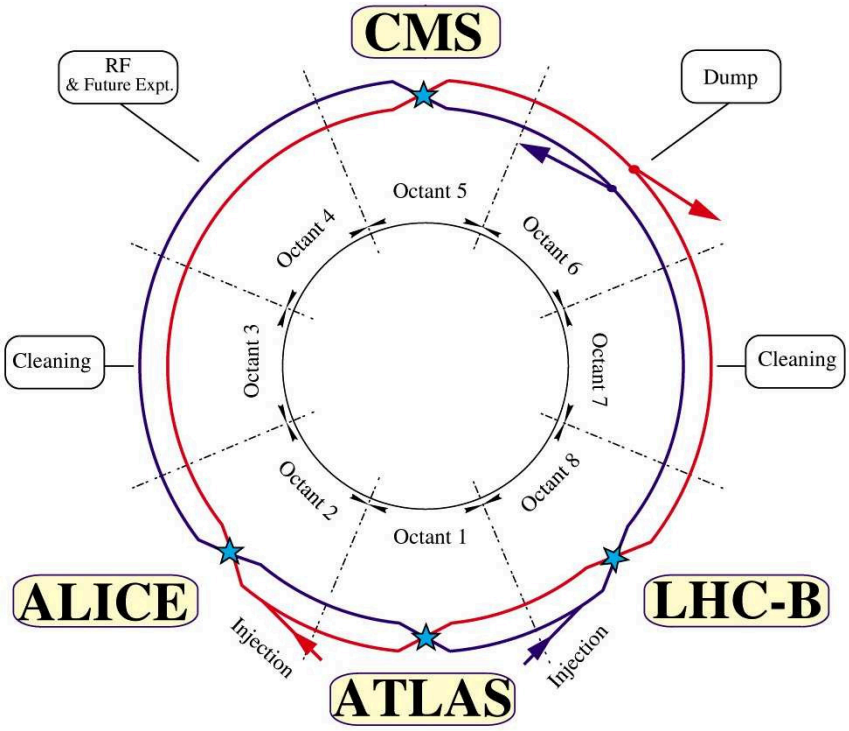

Figure 2.2: Schematic view of the LHC beam trajectories and the position of the four main experiments [16].

frequency of 400 MHz. The RF system is accelerating the beam with electric field strengths of up to 5 MV/m. The RF cavities are also used to focus the proton bunches in longitudinal direction. The frequency of the RF cavities would allow a minimal bunch spacing of a few ns. The maximal bunch spacing time of 25 ns is limited due the RF cavities of the SPS which are running with lower frequencies. This leads to a total number of 2,808 bunches per beam which can be inserted into the LHC. Each bunch can contain up to $1.15{\cdot}10^{11}$ protons.

Protons were circulating in the LHC for the first time in September 2008. Unfortunately, an accident caused by a faulty electrical connection between two magnets only a few days after the first LHC start led to a damage of several magnets in the sector between point 3 and point 4. This accident led to an interruption of the LHC operation until the end of 2009. After the reparation of the damaged sector and the installation of additional safety systems, first proton-proton collisions were performed in November 2009. The beam energy in the proton-proton collisions was increased step-wise from the injection energy to half of the design energy until March 2010. From March until November 2010, the LHC was operating with a centre-of-mass energy of 7 TeV. During this run period an optimisation of the beam parameters was achieved. Some beam parameters could already be brought close to the design values. Design parameters and the parameter values reached at the end of the 2010 run are summarised in table 2.1. During the 2010 proton-proton run, a data set corresponding to an integrated luminosity of 47 pb^{-1} has been delivered by the LHC. Among this data, the CMS detector recorded an integrated luminos-

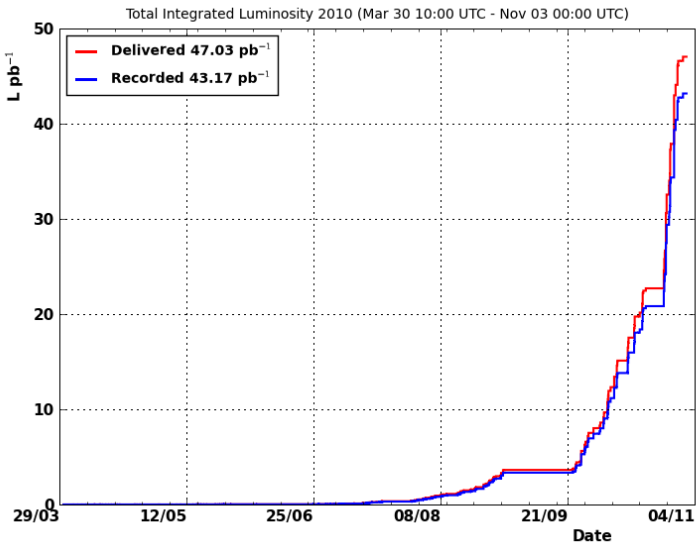

Figure 2.3: Integrated luminosity as function of time delivered by the LHC machine (red curve) and recorded by the CMS detector (blue curve) during 2010 [118].

ity of 43 pb^{-1}. Taking only data taking periods into account where all detector components were running well, a data set corresponding to an integrated luminosity of (36 ± 1) pb^{-1} [115, 116] has been certified to be used for physics analysis. The luminosity has been measured in van der Meer scans [117] by changing the overlap of the colliding beams and determine the total event rate as function of the beam overlap. In figure 2.3, the amount of collected data as a function of time is depicted. As can be seen, the performance of the LHC has been improved continuously during 2010 and most of the data has been collected almost in the last few weeks of data taking.

At the end of 2010, also first collision runs with lead ions were performed for the first time at the LHC. In 2011 the operation of the LHC with proton-proton collisions with a centre-of-mass energy of 7 TeV is continued. The increasing of the beam energy close to the design energy will require a major modification of the LHC machine. This upgrade will probably be performed in the following years during a technical stop which will least more than 12 months.

2.2 The CMS Detector

The Compact Muon Solenoid (CMS) [22, 119] experiment is one of the four main experiments at the LHC. It is placed at the beam interaction point at insertion 5. Besides the ATLAS experiment, CMS is one of the two multi-purpose detectors at the LHC which are designed to cover a broad spectrum of physics analyses. To allow the study of as many as possible processes predicted by the SM or theories extending the SM, the CMS detector allows to detect and identify precisely the emitted particles in proton-proton collisions. Therefore, the CMS detector consists

	design	end of 2010 run
beam energy [TeV]	7	3.5
number of bunches per beam	2,808	368
protons per bunch	$1.15{\cdot}10^{11}$	$1.2{\cdot}10^{11}$
bunch spacing time [ns]	25	150
ϵ_n [µm]	3.75	2.0
β^* [m]	0.55	3.5
instantaneous luminosity [$\mathrm{cm}^{-2}\mathrm{s}^{-1}$]	10^{34}	$2{\cdot}10^{32}$

Table 2.1: List of important LHC beam parameters in design configuration and achieved configuration at the end of 2010 for proton-proton collisions.

of several sub-detectors which surround the interaction point. The sub-detectors are arranged in layers and cover nearly all possible flight directions of particles emitted at the interaction vertex. The sub-detectors are arranged as follows (see also figure 2.4): at the innermost region around the interaction point the tracking system is placed which allows a precise determination of tracks of charged particles; the tracker is surrounded by the calorimetry, an electromagnetic and a hadronic calorimeter for the measurement of energies of electrons, photons, and stable hadrons; the outermost part of the CMS detector consist of muon chambers. One main design element of the CMS experiment is the solenoidal magnet. The magnet is surrounding the complete tracker and the central parts of the calorimetry system. The magnetic field bends charged particles on curved trajectories. From the curvature of the track the particle momentum and its electrical charge can be determined.

The coordinate system to describe position and direction of particles in the CMS detector has its origin in the centre of the collision area. The x direction points radially inwards to the centre of the LHC ring, the z direction points counter-clockwise tangential to the direction of the beam pipe. The CMS coordinate system is a right-system, thus, the y axis is pointing vertically upwards.

2.2.1 Magnet

The magnet is used to penetrate the entire detector with a magnetic field to allow momentum measurements of charged particles. Also the sign of the charge of the particle can be determined from the curvature of its reconstructed track in a magnetic field. A particle with charge q and momentum $p_\perp$ perpendicular to the direction of the magnetic field $\vec{B}$ is bend to a curved track with radius

$$r = \frac{p_\perp}{q|\vec{B}|}. \tag{2.4}$$

At the high centre-of-mass energy provided by the LHC, many produced particles will have momenta up to several TeV/c. To measure these momenta with a track curvature in a magnetic field, a high magnetic field strength is required. Especially for muons this is the only way to measure their momenta since they do nearly not interact with any calorimeter material.

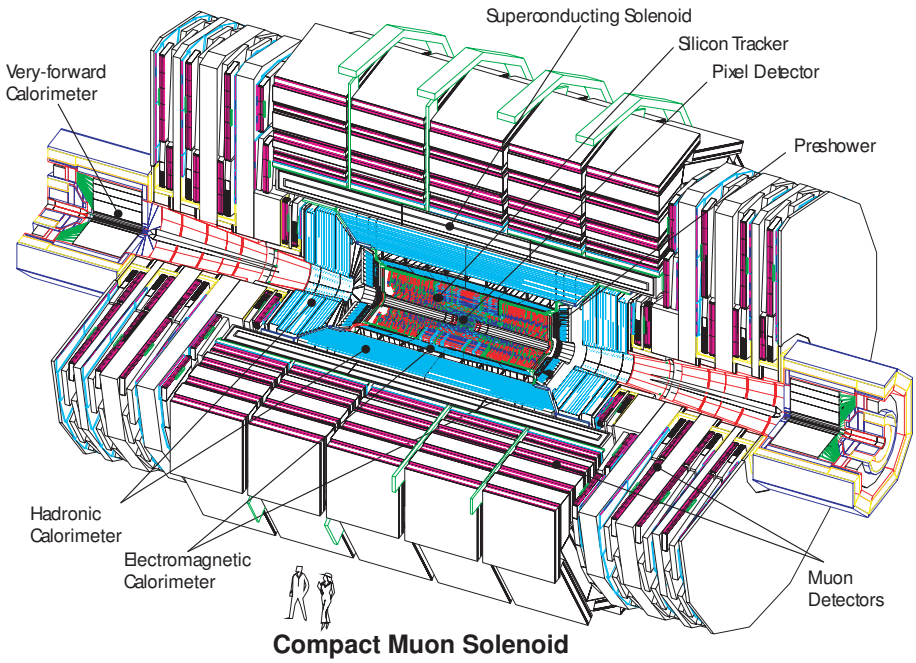

Figure 2.4: Schematic view of the CMS experiment and its sub-detectors [120].

The magnet of the CMS detector is a superconducting solenoid. It has a length of 12.5 m and a diameter of 6.3 m. The windings are made of NbTi which is cooled down to a temperature of 4.6 K. The overall weight of the cold mass is 220 t. The magnet penetrates all detector components in its interior with a homogeneous magnetic field of 3.8 T. The magnetic field outside the solenoid is led back through the muon chambers with an iron return yoke. In the muon chambers, the magnetic field strength is about 2 T. The return yoke is composed of five barrel wheels and six disks at the endcaps. The total mass of the return yoke is about 10,000 t.

2.2.2 Tracking System

The inner tracker of the CMS experiment [121, 122] provides the possibility to measure precisely the trajectories of charged particles emerging from the interaction point. The tracker modules are made of silicon. The usage of semiconducting silicon chips allows a very fine granularity and fast signal read-out which is an essential requirement to identify and to disentangle the tracks of all charged particles produced in proton-proton collisions. The intensive particle flux going through the tracker material also requires radiation-hard sensors. Charged particles passing through a semiconducting silicon detector create electron-hole pairs producing an electric signal which can be read out. The tracking system consist of two parts, the pixel detector closest to the interaction point and the outer part equipped with silicon strip modules. The tracker has an overall lengths of 5.8 m and a diameter of 2.2 m. The active area of all silicon modules is about 200 m^2. The entire tracker is operating at a temperature of $-20°C$. An overview of all modules of the silicon tracker is presented in figure 2.5.

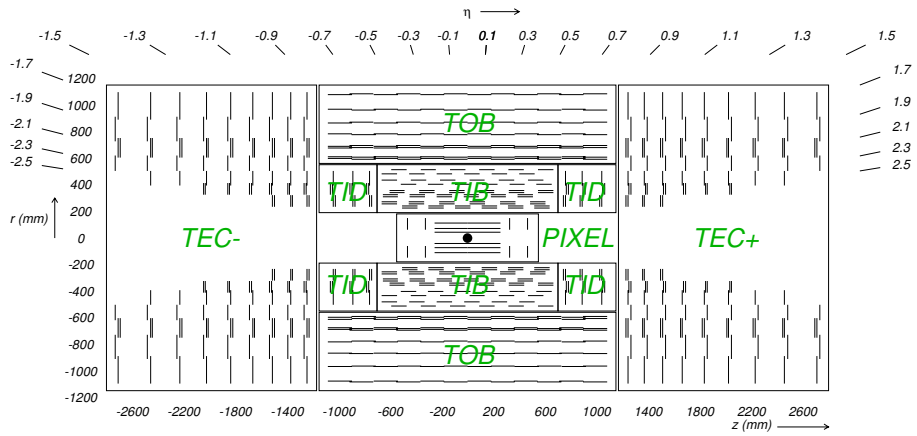

Figure 2.5: View through the CMS inner tracking system [22]. Each line represents a silicon detector module, stereo modules are indicated by a pair of parallel lines.

Pixel Detector

The pixel detector is the innermost detector component of the CMS experiment. It consist of three cylindrical layers of silicon pixel modules surrounding the beam pipe at radii of 4.4 cm, 7.3 cm, and 10.2 cm. The layers consist of 768 pixel modules. In addition to the three barrel layers, two endcap disks equipped with silicon pixel moduls are placed on each side. They have an inner radius of 6 cm and an outer radius of 15 cm. The endcap disks are placed at $z = \pm 34.5$ cm and $z = \pm 46.5$ cm from the centre of the detector. Each disk has a turbine-like geometry of 24 blades rotated by 20°. Each blade consist of 7 pixel modules, in total the endcaps are assembled with 672 modules.

Each module is split into silicon pixel segments of a size of 100 µm× 150 µm. Each of these segments is read out individually. This leads to more than 65 million read-out channels. The arrangement of modules and their overlap provides a nearly full coverage of all directions in which particles can emerge from the interaction point. Most particles pass through three modules which allows a precise determination of a track's direction, origin and curvature. The pixel tracker provides a separation of single hits with distances of the order of 10 µm.

Strip Detector

The silicon strip detector is the outer component of the tracking system. It consist of more than 15,000 modules equipped with single-sided silicon strips. In total, the strip detector has nearly 10 million read-out channels. The strip detector is divided into several subsystems covering different regions in radius and pseudorapidity. The inner part of the strip detector consist of the so-called Tracker Inner Barrel (TIB) and Tracker Inner Disks (TID) systems. The outer region of the tracking device comprises the Tracker Outer Barrel (TOB) and the Tracker EndCaps (TEC). The TIB and the TID cover the detector volume between radii of 20 cm and 55 cm. The outer parts of the strip detector, TOB and TEC, extend the radius of the tracker to 116 cm. The overall strip detector allows to identify tracks with pseudorapidities

$|\eta| < 2.4$.

The TIB covers the inner region with $|z| < 65$ cm. It comprises four layers of modules. For the modules in the inner two layers always two modules are mounted back-to-back with an angle of 100 mrad between their strips. This allows stereo measurements in both r–ϕ and r–z directions. The TID is made of three disks on each side. The inner two disks are equipped with stereo modules. The TOB consists of six concentric layers, the inner two layers also allow a stereo measurement. The forward regions are covered by nine disks of the TEC on each side. Here, the innermost two disks and the fifths disk of the TEC are stereo modules. The strips on the modules of the TID and the TEC point towards the beam pipe, whereas the strips of the barrel modules TIB and TOB run in parallel to the beam direction.

The single hit resolution of the strip detector ranges from 23 µm to 35 µm in the TIB and 35 µm to 53 µm in the TOB over 100 µm to 141 µm in the TID to a resolution between 230 µm and 530 µm in the TEC. The single hit resolution results in a momentum resolution for the measurement of charged particles with a transverse momentum of $p_{\mathrm{T}} \approx 100$ GeV/c of 1–2% [121].

2.2.3 Calorimetry

The calorimetry of the CMS experiment comprises two detector systems: the electromagnetic calorimeter (ECAL) [123] and the hadronic calorimeter (HCAL) [124]. The calorimeters are placed concentrically between the tracker system and the magnet. They provide the measurement of particle energies and a classification of particle types. The inner ECAL is a scintillator detector. Electrons, positrons, and photons mainly deposit their energy in the scintillator material, whereas hadrons are first stopped in the material of the outer HCAL.

Electromagnetic Calorimeter

The energy of electrons, positrons and photons is measured with the ECAL. In the electromagnetic nucleon fields of the scintillator material, electrons and positrons emit bremsstrahlung, photons are converted into electron-positron pairs. The subsequent emission of bremsstrahlung and the creation of conversion pairs produces a shower of electromagnetic particles. The number of particles in this shower is proportional to the initial energy of the incoming electron, positron, or photon. The shower particles excite molecules of the scintillator material which leads to the emission of light. This light can then be detected with photo detectors at the outer end of the scintillator.

The ECAL is made of more than 68,000 lead tungstate ($PbWO_4$) crystals. $PbWO_4$ is a transparent material with a high density of 8.28 g/cm^3 and a short radiation length of $X_0 = 0.89$ cm and a Molière radius of $R_{\mathrm{H}} = 2.2$ cm. $PbWO_4$ can therefore serve as absorber material to produce electromagnetic showers and as scintillator material simultaneously. This allows a compact design with fine granularity. The ECAL consists of a cylindrical barrel (EB) and two endcaps (EE). In front of each endcap a preshower detector (ES) is installed. The ECAL is depicted in figure 2.6.

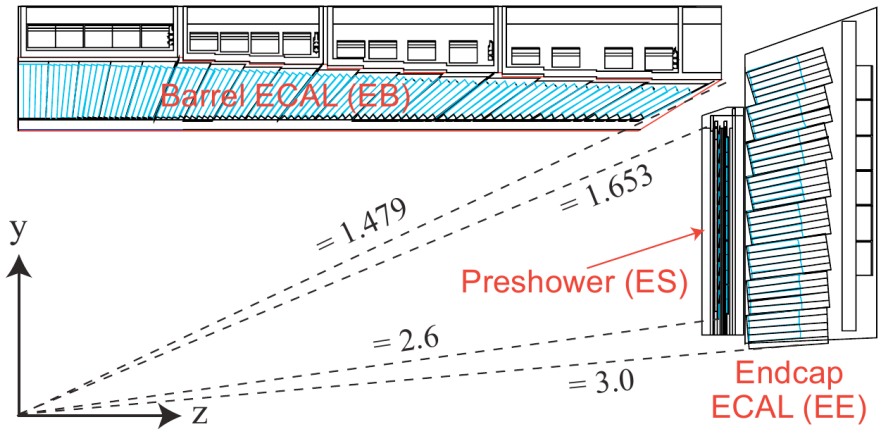

Figure 2.6: Schematic view of one quarter of the CMS ECAL [119].

The EB covers a pseudorapidity region up to $|\eta| = 1.479$ with 61,200 $PbWO_4$ crystals. Each crystal covers an area of 0.0174×0.0174 in the η–ϕ plane. This corresponds to a cross section of 22×22 mm^2 at the front face of the crystals. The inner radius of the EB is 1.29 m. The length of each crystal in the EB is 230 mm, this correspond to 25.8 X_0. All crystals are mounted such that they point toward the interaction point in the centre of the detector. The light emitted due to the electromagnetic showers produced in the crystal – when high-energetic electrons, positrons, or photons pass through – are read out with avalanche photodiodes.

The EE disks cover larger pseudorapidities of $1.479 < |\eta| < 3.0$. Each endcap is divided into two halves, so-called Dees. Each Dee comprises 3,662 crystals. The crystals are grouped into supercrystals of 5×5 crystals. The crystals in the EE have a front face cross section of 28.62×28.62 mm^2 and a length of 220 mm which corresponds to 24.7 X_0. For the read-out vacuum phototriodes are utilised.

The preshower detectors are used to identify charged pions and to improve the identification and localisation of electrons and photons in a pseudorapidity range of $1.653 < |\eta| < 2.6$. Each preshower detector is a sampling calorimeter. Lead radiators are used to produce electromagnetic showers from incoming electrons or photons. The showers are read out by silicon strip detectors placed between the lead layers. The total thickness of the preshower detector is 20 cm.

The energy resolution of the ECAL was measured with electron test beams with electron energies between 20 and 250 GeV [125]. In this calibration study an energy resolution was found for the EB of

$$\left(\frac{\sigma}{E}\right)^2 = \left(\frac{2.8\%}{\sqrt{E}}\right)^2 + (0.30\%)^2, \tag{2.5}$$

where E is the electron energy measured in GeV. The first term is the stochastic term which accounts for fluctuations in the shower containment and statistical fluctuations of the photon showers. The constant term accounts for non-uniformities

and calibration errors of the detector modules. For the EE an energy resolution of

$$\left(\frac{\sigma}{E}\right)^2 = \left(\frac{5.7\%}{\sqrt{E}}\right)^2 + (0.30\%)^2 \tag{2.6}$$

was measured.

Hadronic Calorimeter

The HCAL is used to identify hadrons and to measure their energies. These particles are not stopped by the ECAL and deposit their energy mostly in the HCAL which surrounds the ECAL. The HCAL consist of several parts covering different pseudorapidity regions (see figure 2.7): the HCAL barrel (HB) covers the central region with $|\eta| < 1.3$, the HCAL endcap (HE) extend the coverage of the calorimeter up to $|\eta| = 3$. HB and HE are placed within the solenoid. The HCAL is extended by a module placed outside the solenoid, the outer HCAL (HO). For the detection of hadrons in the most outer region with $|\eta|$ up to 5.2, the forward calorimeters (HF) are placed 11.2 m away from the interaction point.

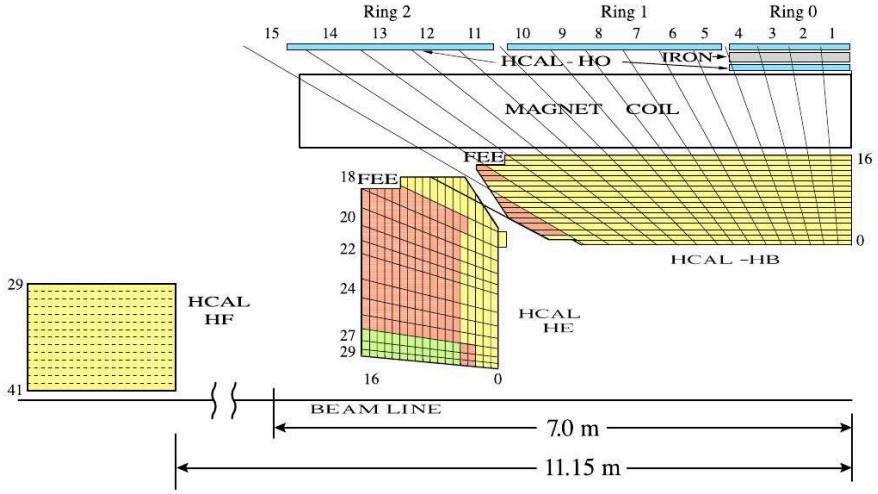

Figure 2.7: Transverse view through one quarter of the CMS HCAL [126] showing the HCAL barrel (HB), the HCAL endcap (HE), and the HCAL forward (HF). The HCAL outer (HO) is placed outside the coil of the CMS solenoid. The label FEE indicates the position of the front-end read-out electronics.

The hadronic calorimeter is a sampling calorimeter utilising brass as absorber material. Since the HCAL is placed in the strong magnetic field inside the solenoid, the non-magnetic absorber material brass was chosen, which additionally features a reasonable hadronic interaction length of $\lambda_I = 16.4$ cm. The absorber is arranged in slices interspersed with plastic scintillators as active material. Hadrons traversing the HCAL react in strong interactions with the absorber material and produce showers of secondary hadrons. These showers lead to excitations of the active material and the emission of light which is transported by wavelength shifting fibres to photo-detectors outside the calorimeter.

The HB comprises 36 identical wedges forming two half-barrels. The absorber plates in the HB are arranged in parallel with the beam axis. The HB wedges are segmented into towers which cover a surface of 0.087×0.087 in the η–ϕ plane. The inner radius of the HB is 1.78 m, the outer radius is 2.88 m. The thickness of the total amount of absorber material in the HB corresponds to 5.8 λ_I for the central towers with $|\eta| < 0.087$ and up to 10.6 λ_I at $|\eta| = 1.3$. The HB is completed by the HO, which increases the effective thickness of the absorber in the barrel region. The HO is divided into five rings following the geometry of the muon chambers in the outer part of the detector. The outer four rings consist of only one scintillator slice using the material of the solenoid as absorber. The coil of the solenoid has a thickness of $\frac{1.4}{\sin\theta} \cdot \lambda_\mathrm{I}$. In the central ring an additional lead plate is placed as absorber between two active layers. This leads to an absorber thickness of at least 10 λ_I over the full barrel region, also including about 1 λ_I from the ECAL. The HE comprises 18 segments arranged in a radial symmetry around the beam pipe. The brass absorber in the HE has a total length of about 10 λ_I. The granularity of the HE is 0.087×0.087 in η–ϕ for $|\eta| < 1.6$ and approximately 0.17×0.17 for rapidities $|\eta| > 1.6$. The HF system is placed outside the solenoid and is used to detect hadron showers in the very forward region of the CMS detector. The HF has to resist high particle fluxes which occur in the forward region of high-energetic particle collisions. Therefore, it comprises steel absorber plates and quartz fibres as active material. Quartz fibres are more radiation-hard compared to plastic scintillators. Hadron showers produce Cherenkov light in the quartz fibres which is detected by photo-multipliers. The HF has a cylindrical structure surrounding the beam pipe with an inner radius of 12.5 cm and an outer radius of 130 cm. The towers of the HF have a granularity of 0.175×0.175 in η–ϕ.

The energy resolution of the HCAL is worse compared to the ECAL. It has been determined in test beams with electrons, pions, protons, and muons and has been confirmed in cosmic muon data [126]. For the barrel and endcap regions an energy resolution of

$$\left(\frac{\sigma}{E}\right)^2 = \left(\frac{84.7\%}{\sqrt{E}}\right)^2 + (7.4\%)^2 \tag{2.7}$$

has been measured. A similar study of the resolution in the HF yields an energy resolution of

$$\left(\frac{\sigma}{E}\right)^2 = \left(\frac{198\%}{\sqrt{E}}\right)^2 + (9\%)^2. \tag{2.8}$$

2.2.4 Muon System

The CMS muon system [127] forms the outer part of the CMS detector. Since muons are minimally ionising particles they loose only a small fraction of their energy in the inner parts of the detector and can also travel nearly undisturbed through the iron layers of the return yoke. Practically, all other electromagnetically or strongly interacting particles are stopped at least in the hadronic calorimeter. Hence, particles which are detected in the outer part of the detector can be identified as muons. The muon system allows the detection of muon tracks. The muon detector

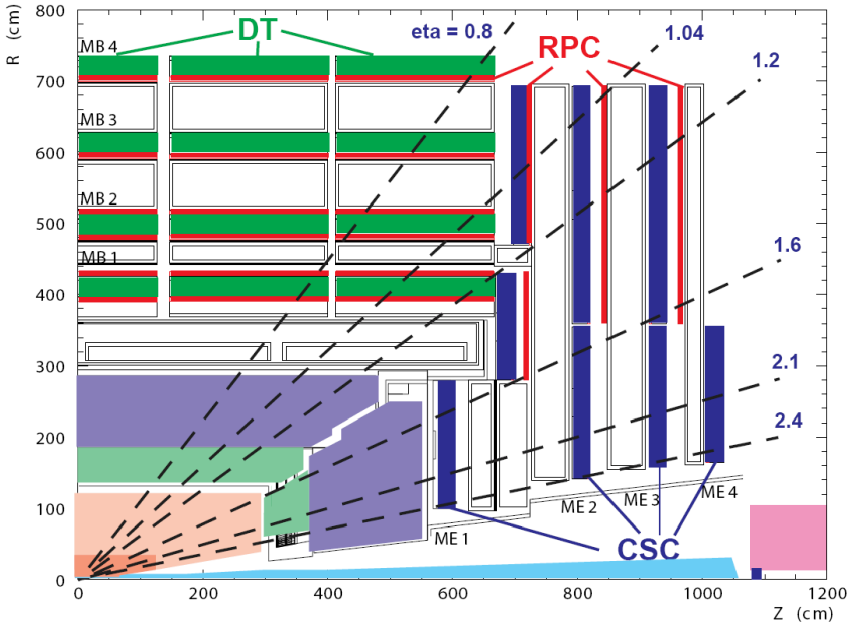

Figure 2.8: Transverse view through one quarter of the CMS muon system [119]. The muon system consist of drift tubes (DT) in the barrel region, cathode strip chambers (CSC) in the endcap region and additional resistive plate chambers (RPC) in both, barrel and endcap.

modules are placed between the iron layers of the return yoke. The magnetic field with a field strength of about 2 T present in the return yoke bend the muon tracks and the muon momenta can therefore be determined from the curvature of their reconstructed tracks. The arrangement of the muon chambers follows mainly the design of the return yoke. In the barrel region, five cylindrical wheels surround the solenoid. The muon system is accomplished by two planar endcaps. The layout of the muon system is shown in figure 2.8. The muon system comprises three kinds of gaseous detector modules. Muons flying through the muon chambers are ionising the gas molecules. The emitted electrons are detected when hitting a positively charged wire in the centre of the gas volume. In the barrel region, the drift tube (DT) chambers cover a pseudorapidity region of $|\eta| < 1.2$. The endcaps are equipped with cathode strip chambers (CSC). In addition to these detector modules, resistive plate chambers (RPC) are placed in both barrel and endcap in the pseudorapidity region with $|\eta| < 1.6$.

The DT chambers are arranged in four concentric layers at radii of approximately 4.0 m, 4.9 m, 5.9 m, and 7 m from the beam axis in the five cylindrical rings of the barrel. The muon chambers are interleaved by iron layers of the return yoke. Each wheel consists of twelve sectors covering 30° in ϕ. The inner three layers of the barrel consist of 60 DT chambers each, the outer layer comprises 70 chambers. The tubes of the DT chambers are filled with a gas mixture of 85% Ar and 15% CO_2. The average drift time in these chambers is about 380 ns. In total, all DT chambers have about 172,000 active wires.

The CSCs in the endcap region cover a pseudorapidity region up to $|\eta| = 2.4$. The CSCs are multi-wire proportional chambers with six gas gaps with planes of

sensitive anode wires. In each endcap four layers of CSC modules are installed. The chambers are trapezoidal and are aligned perpendicular to the beam axis. In each endcap the CSCs are grouped in four layers in between the return plates for the magnetic field at z distances between 5.7 m and 10.6 m away from the interaction point. In total, there are 468 CSCs installed on each side of the detector. The largest CSCs are 3.4 m long and 1.5 m wide. The total number of wires in the CSCs is about 2 million.

The muon system is completed by the RPCs. These gaseous parallel-plate detectors are used to improve the capability to trigger muons with an improved time resolution. Although the spatial resolution of the RPCs is worse compared to the DT chambers and the CSCs, they provide the possibility to identify muons in much shorter time than the design bunch crossing rate of the LHC of 25 ns. The RPCs are mounted in front of all DT chambers in the four layers of the barrel and in parallel to the CSCs in the endcaps.

The muon momentum resolution mainly depends on the ability to measure the curvature of muon tracks. Since muons with a high transverse momentum p_{T} are bent to tracks with a lower curvature the determination of the momentum of high-p_{T} muons is less accurate than the momentum resolution of muons with lower momenta. Muons with a momentum of $p_{\mathrm{T}} < 100$ GeV/c are reconstructed with a momentum resolution better than 10%, whereas the momentum resolution for muons with $p_{\mathrm{T}} = 1$ TeV/c rises up to 40% in the outer pseudorapidity regions. The momentum resolution can significantly be improved by combining the information from the muon chambers with tracking information from the inner tracker.

2.2.5 Trigger, Data Acquisition, and Computing

The LHC delivers proton-proton collisions at a relatively high rate which will reach 40 MHz for the design bunch spacing time of 25 ns. In each bunch crossing up to 20 collision events with a huge number of about 1,000 particles penetrating the detector are expected to occur at an instantaneous luminosity of 10^{34} cm^{-2}s^{-1}. This huge number of events corresponds to a large amount of data which can not be stored without any filtering procedure. Therefore, a trigger system [128, 129] provides a reduction of the collected data on a short time scale by deciding whether an event should be stored or rejected. The data taking rate is decremented by a trigger system which consists of two subsystems called level-1 (L1) trigger and high level trigger (HLT). The data taking rate is lowered to a frequency of several 100 Hz which corresponds to a reduction factor of about 10^7. The decision which events are stored is mainly driven by the signature of processes which are of physical interest. Especially for the search for rare processes it is essential that mostly all events of this certain process are stored. Therefore, the trigger system ensures on a relatively short time scale that the information of events consisting of one or more charged leptons or photons with high momentum, large missing transverse energy, or a high multiplicity of high-energetic hadron jets is recorded.

The L1 trigger is a hardware based trigger system and has local, regional and global components. All components are dedicated programmable electronic devices

using only coarsely segmented data from calorimeter and muon modules. The local components are based on the front-end electronics installed directly inside the detector. Energy deposits in the calorimeters and hit patterns in the muon chambers are stored as so-called trigger primitive generators (TPG) in pipelined memories in the front-end electronics. Regional triggers combine the TPG information in spatial regions to identify, for instance, muon or electron candidates. The global calorimeter and global muon triggers combine information of the entire calorimeter and muon system, respectively. The final L1 decision is taken by the global trigger which is physically based in an underground control room 90 m away from the CMS cavern. The L1 trigger system has a latency time of 3.2 µs and reduces the data rate to about 100 kHz.

The HLT comprises a software based trigger running on a computing farm. The data filtered by the L1 trigger is transferred to the HLT via a network connection which can handle data transfer volumes of 100 GB/s. The HLT uses algorithms combining the L1 trigger objects with the entire information of all detector modules. From the full detector information physical objects such as muons, electrons, or jets are reconstructed with higher accuracy than the objects reconstructed on the level of the L1 trigger. The HLT also provides trigger paths which combine information from several physical objects in one event. These trigger paths are for instance multi-lepton triggers or triggers demanding the existence of a lepton together with jets. All HTL filtering algorithms underlie a continuous adoption to the collision conditions. The overall rate of events stored is reduced by the HLT to several 100 Hz. The full trigger chain of the CMS experiment is schematically shown in figure 2.9.

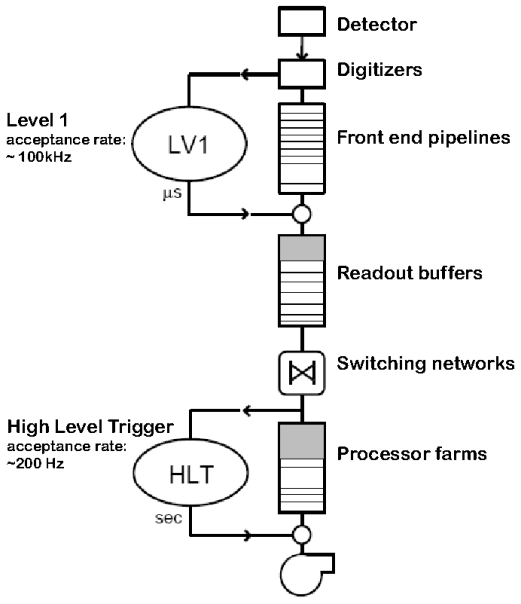

Figure 2.9: Schematic view of the data flow and the trigger system of the CMS experiment.

The data taken by the CMS experiment which have been accepted by the trigger system have to be stored and distributed. Although the amount of data is already

significantly reduced by the trigger, the final data which have to be stored correspond to several petabyte per year. The CMS computing model [130] has been designed to distribute the data as well as simulated events (so-called Monte Carlo samples) and to provide computing resources for data analysis to physicists all over the world. Data distribution and allocation of computing resources is organised within the worldwide LHC computing grid (WLCG) [131], a collaboration of the LHC experiments and several computing centres. The WLCG has a hierarchical structure of computing centres, called Tier-0, Tier-1, and Tier-2. The unique Tier-0 centre is a computing centre directly placed at CERN. All data taken by the LHC experiments is distributed from the Tier-0 to Tier-1 centres. At the Tier-1 computing centres, the data can be reprocessed in case improved reconstruction algorithms are available. They also provide huge storage capacities to store data from the LHC experiments as well as simulated data produced at either the Tier-1 or the smaller Tier-2 centres. The Tier-2 centres are mainly foreseen to keep copies of reduced data sets which can then directly be accessed and analysed by individual physicists or local analysis groups. Local computing devices used for interactive analyses connected to the grid are called Tier-3 sites, although they are not formally part of the WLCG. The grid structure possess each analyser to have access to any data set at one of the Tier-2 sites.

Chapter 3

Generation, Simulation, and Reconstruction

The CMS detector is recording high-energetic proton-proton collisions. Aim of the examination of these collisions is to study the theoretical predictions of the Standard Model or to search for influences of effects which are not described within this theory. The SM is a perturbative theory describing hard scattering processes of fundamental particles such as quarks and gluons. On the other hand the CMS detector allows only for recording of electrical signals produced by secondary particles which emerge from the hard interaction process. For a reasonable comparison of a theory prediction with observed data, a simulation of theoretically expected signals is performed. This simulation consist of several steps. In a first step, hard scattering processes are generated according to theory expectations. For the outcome of the generation step, the formation process of stable particles which would be measurable in the detector is simulated. As last step, the detector response is simulated. For a more comprehensive comparison of real data with simulated events, directly observable signals in the detector undergo a reconstruction procedure. The reconstruction is applied on both, detector signals of real and simulated data, to provide information on more physical objects such as reconstructed charged leptons or jets. In this chapter, the different steps of generation, simulation, and reconstruction are presented and a short description of the used algorithms is given.

3.1 Generation of Events

All processes which can occur in proton-proton collisions are quantum mechanical reactions. Therefore, a deterministic prescription of these processes is not possible, only a probability can be specified for a certain process to take place. This allows a simulation of proton-proton collisions with algorithms based on random number generators. Such algorithms are called Monte Carlo generators, hence, sets of generated collision events are usually called Monte Carlo samples. In most proton-proton collisions no top quark pairs are produced, the signal process which is studied within this thesis. The total inelastic proton-proton cross section is eight to nine orders of magnitude larger than the cross section of $t\bar{t}$ production. Just randomly generating

proton-proton collisions would therefore require a large number of simulated interactions to have at least a few $t\bar{t}$ events generated. Therefore, a dedicated generation of Monte Carlo events containing top quarks is required. Also background processes which do not contain pairs of top quarks but covering the same phase space or leading to the same experimental signature as $t\bar{t}$ production have to be generated in addition to the signal Monte Carlo sample.

The generation of Monte Carlo events consist of several steps. The hard interaction process is generated according to the Feynman diagrams and their probability densities (see section 1.1.4). In this approach, only the interaction of bare quarks, leptons, and gauge bosons is described. The high-energetic partons in the final state of the hard process can further emit radiation. The quarks and gluons simulated in this so-called parton shower finally have to form stable, colour-less hadronic bound states. The different steps contributing to the simulation of proton-proton interactions are depicted in figure 3.1.

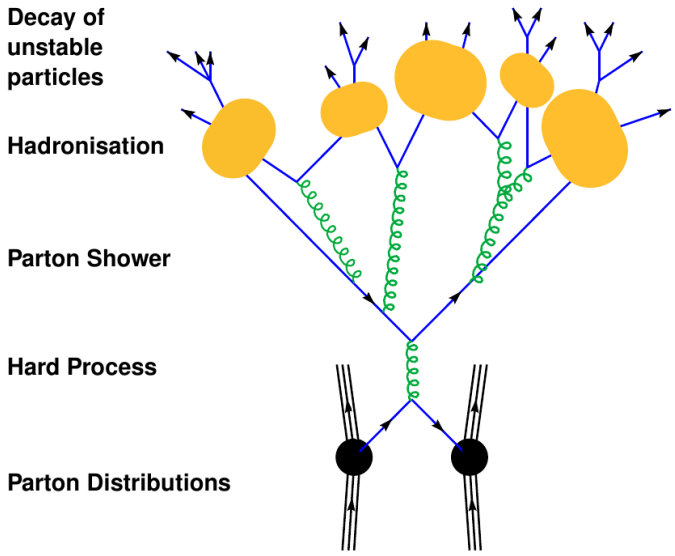

Figure 3.1: Illustration of the different steps of Monte Carlo event generation: partons within the protons are interacting in a hard scattering process [132]. Additional soft radiations from the initial and final state partons in the hard scattering are simulated in the parton shower. The formation of colour-neutral particles is simulated in the hadronisation process. Finally, the decay of unstable particles takes place.

Hard Scattering Process

The simulation of hard scattering processes follows the prediction of perturbative calculations. Events are generated randomly according to the predicted probability densities for a specified process with certain initial- and final-state phase space configuration. These probabilities are taken from the evaluation of the Feynman diagrams of a certain process and the corresponding transition amplitudes. For the simulation of processes in proton-proton collisions, the probability density from the matrix-element calculation has to be folded with the prediction of the parton density

function for the actual initial state configuration (see also section 1.2.1) to determine the probability of a certain process correctly. The simulation of Monte Carlo events via this matrix-element method is the most accurate way to generate events with a high momentum transfer Q. The evaluation of Feynman diagrams accounts for the exact kinematics, spin and helicity structure, and interference effects of several diagrams. At high momentum scales, the perturbative series converges relatively fast. Hence, for most simulations it is often satisfying to include only LO or NLO Feynman diagrams into the calculation.

Parton Shower and Hadronisation

At lower scales, the QCD coupling strength increases and the perturbative series does not converge any more. The simulation of such radiation processes with a matrix-element generator is therefore not an adequate procedure. In a typical $\mathrm{t\bar{t}}$ event, several hundreds of particles with low momenta are emitted which cannot be simulated with a matrix-element generator. Thus, a cut-off energy scale Q_{min} is introduced which defines a minimal momentum to be carried by particles simulated by the generator of the hard scattering. All softer radiations are simulated with algorithms based on other approaches than the perturbative theory. The matching between the simulation of parton radiations by either the matrix element of the hard scattering or the showering process are usually described in the MLM [133] or the CKKW [134] scheme. Soft gluons and photons can in principle be radiated from every parton carrying colour or electric charges in the hard scattering process and emitted gluons can again split up into quark-antiquark pairs. These splitting and radiation processes in the parton shower can be parametrised with the DGLAP evolution equation [135–137]. The showering process starts with partons at the previously defined cut-off scale. A cascade of radiations is simulated according to the splitting probability going forwards in time for particles radiated from the final state particles of the hard interaction. For the ordering of the emission of additional particles in the shower simulation several approaches exist. Usual showering algorithms order the emissions according to the transverse momentum of the emitted parton, the mass of the radiation, or the angle between initial and radiated partons. In the showering simulation, singularities can occur in the calculation of soft collinear radiations. Therefore, usually a soft cut-off parameter Q_0 in the order of 1 GeV/c is introduced to the minimal momentum of radiations. Also the radiations from the initial state partons are described with the DGLAP evolution but with a propagation of the shower backwards in time. In the simulation of initial state radiation, the simulation has to take into account that soft radiations are partially described by the PDF.

All particles simulated by the matrix-element or the parton shower are still elementary fermions or bosons. Coloured objects like bare quarks and gluons cannot exist as free particles in nature due to QCD confinement. Therefore, also a simulation of the formation of hadronic bound states is required for a full and realistic description of elementary particle interactions. For the description of the hadronisation process several models and implementations exist. These algorithms are mainly based on phenomenological descriptions since a detailed explanation of the hadro-

nisation process starting from the QCD Lagrangian is not feasible. Many particles produced in the hadronisation process are unstable. The decays of these particles are simulated randomly according to the known branching ratios of these unstable baryons or mesons. Typically, each quark or gluon in the final state of a hard interaction will lead to a bunch of hadrons observable in the detector after the showering and hadronisation processes. These collections of hadrons are referred to as jets.

Underlying Event and Pile-Up

In the collision of protons, not only one parton within each proton is interacting in a scattering process. Remnants of the protons will also interact with each other and influence the hard interaction, since the remnants are colour-connected to the initial partons and therefore underlie a hadronisation process. There might also occur secondary hard interactions, mostly QCD $2 \to 2$ scattering processes, which take place simultaneously in the interaction of partons in the proton remnants. All these additional processes of the proton remnants are called underlying event.

Since not merely single protons are collided at the LHC, but bunches of protons, several proton-proton collisions can occur in the same bunch crossing. Those additional interactions are called pile-up events. The number of pile-up events is directly proportional to the instantaneous luminosity. For the design operation of the LHC with an instantaneous luminosity of 10^{34} $\mathrm{cm}^{-2}\mathrm{s}^{-1}$, about 20 pile-up events are expected per bunch crossing. In the data set analysed within the context of this thesis, only a few pile-up events are included since the average instantaneous luminosity has been much smaller than the design parameter (see also table 2.1).

3.1.1 Event Generators

For the description of $\mathrm{t\bar{t}}$ signal events as well as for the most important background processes several different Monte Carlo event generators are utilised. Mostly, a combination of different algorithms for the simulation of hard interaction and showering is applied. In this section, a short description of the used algorithms and their main features is given.

Pythia

Pythia [138] is a multi-purpose event generator. It provides many routines to simulate hard interactions as well as showering, hadronisation, and particle decay algorithms. Moreover, the Pythia package allows for the simulation of the underlying event. The showering and hadronisation process can also be applied on hard scattering events produced with an external matrix-element generator. Hard interactions containing SM processes and processes from many other theoretical models can be generated. Emphasis of Pythia is the simulation of strong interactions with multi-hadron final states. The simulation of the hard interaction in Pythia takes into account LO Feynman diagrams only. Pythia matches the hard interaction with the parton shower simulation. The shower evolution in Pythia orders the emitted radiated particles by their transverse momenta, but also angular ordered

showers are implemented. By default, the hadronisation is simulated according to the Lund string model [139] which is based on the parametrisation of the strong field between coloured partons with strings. Along these strings, iteratively the creation of new quark-antiquark pairs is simulated. Decays can also be simulated with Pythia, but there exists the possibility to interface Pythia with external decay programs. The decay of tau leptons for instance is often simulated with the dedicated program Tauola [140]. Tauola explicitly takes into account spin effects and weak corrections which are not considered by Pythia. Pythia contains several free tuning parameters describing the shower, hadronisation, and underlying event processes. The actually used parameter sets are referred to as tunes.

MadGraph and MadEvent

The MadGraph/MadEvent package [141] is designed to simulate nearly all kinds of hard interaction processes in the SM and many extensions of the SM. The program package consists of two parts: MadGraph determines all LO Feynman diagrams contributing to a specified process, MadEvent generates Monte Carlo events according to the MadGraph output. MadGraph can handle nearly all processes of the SM and includes many additional theoretical models like supersymmetric theories and also models containing new resonance particles specifically coupling to top quarks [74]. MadGraph also facilitates to add new particles and couplings easily. MadGraph allows the simulation of all kinds of initial states such as collisions of elementary particles like electrons or positrons, but also collisions of composed objects like protons or antiprotons. For this purpose, some PDF sets are included and additional PDF parametrisations can be linked to MadGraph. Each generated process can contain up to about 10,000 LO Feynman diagrams with up to nine external particles. MadGraph determines the combined LO cross section from these diagrams including their interferences. In this calculation, also spin correlations and colour flows are considered. For the generation of Monte Carlo events, MadEvent draws randomly events with momentum configurations according to the differential cross section found by MadGraph. MadEvent does not include showering and hadronisation algorithms. For the showering, MadEvent is interfaced to Pythia. For the interfacing of different Monte Carlo event generators, the common Les Houches Event (LHE) file [142] format is used. In the LHE files, all generated particles, their momenta, their quantum numbers and their connections to other particles in the corresponding Feynman diagram are listed in a standardised format.

MC@NLO

MC@NLO [79, 80] is a matrix-element generator evaluating LO and NLO Feynman diagrams for the Monte Carlo generation of events. MC@NLO can only simulate events of dedicated SM processes. Available processes are the production of W and Z bosons, lepton pair production, Higgs boson production in the SM and in some extension of the SM, single top quark production, and the production of heavy quark pairs like top quark pair production. A small fraction of events generated with MC@NLO gains negative event weights to avoid a double-counting of processes

which can either simulated by the matrix element or by the showering process. To model distributions of kinematic quantities of the generated process in a physically meaningful way, the distributions of events with negative weights have to be subtracted from the distributions of events with positive weights. This behaviour requires a large number of events to be generated to obtain smooth kinematic distributions. MC@NLO is technically based on the HERWIG/HERWIG++ [143, 144] event generator. Therefore, it is directly interfaced to the HERWIG showering and hadronisation routines. HERWIG offers nearly the same functionality as PYTHIA, but differs mainly in the algorithms implemented for showering, hadronisation, and underlying event simulation.

3.1.2 Signal Generation

For a precise study of top quark pair production in proton-proton collisions, a Monte Carlo simulation of the SM $t\bar{t}$ signal process as well as of possible beyond SM processes in $t\bar{t}$ production is performed.

The emphasise of the presented analyses is the study of $t\bar{t}$ events in the lepton+jets decay channel. Here, the charged lepton is typically an electron or a muon since they produce a cleaner signature in the detector than nearly instantaneously decaying taus. The expected event signature of a lepton+jets $t\bar{t}$ event (see figure 3.2) consists of four jets originating from the four quarks in the final state, a charged lepton, and a neutrino. Although the lepton+jets decay channel plays the most important role in the performed measurements, for the generation of Monte Carlo events all possible decay modes are simulated according to the predicted branching ratios. Especially $t\bar{t}$ events in the dilepton decay channel have a similar event signature as the lepton+jets decay mode. Dilepton $t\bar{t}$ events with one W boson decaying into a tau and the other W boson decaying into an electron or muon have a similar expected event signature as $t\bar{t}$ events in the lepton+jets channel, if the tau is decaying hadronically and can therefore be erroneously identified as a jet originating from a quark. However, lepton+jets events with the charged lepton being a tau can fake the investigated signature of electron+jets or muon+jets events, if the tau decays leptonically.

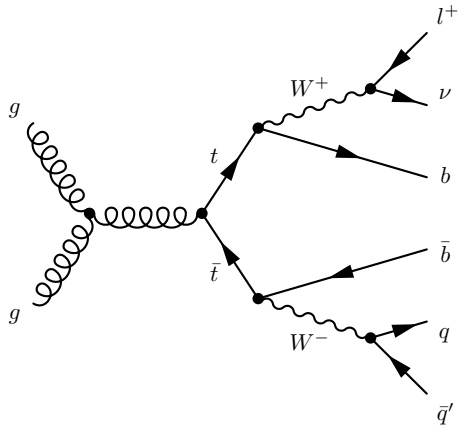

Figure 3.2: Exemplary Feynman diagram of a $t\bar{t}$ event in the lepton+jets decay channel.

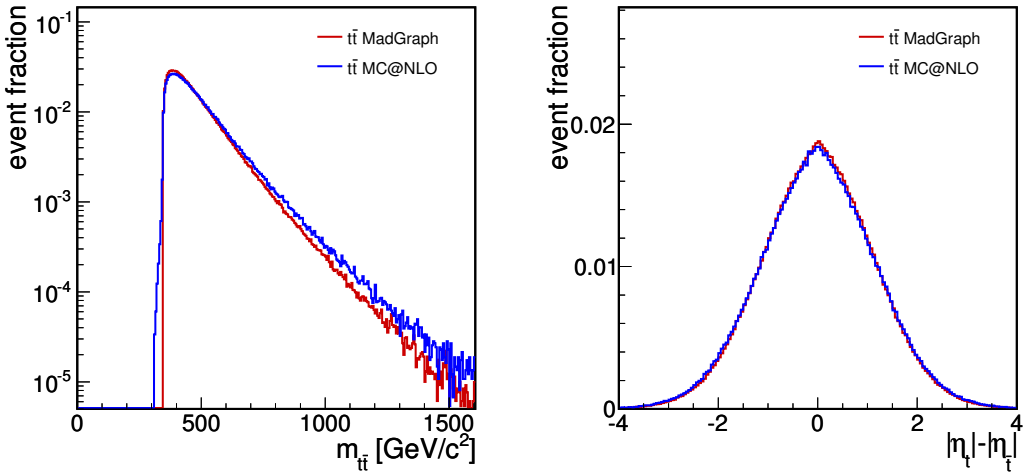

Figure 3.3: Comparison of the distribution of the invariant mass spectrum of the $t\bar{t}$ system (a) and of $|\eta_t| - |\eta_{\bar{t}}|$ (b) in top quark pair events generated with MadGraph/MadEvent and MC@NLO.

The hard interaction of the $t\bar{t}$ signal process is modelled with the MadGraph/MadEvent event generator. For the PDF parametrisation of the colliding protons, the CTEQ6L configuration [63] is used. In the simulation of the hard interaction, all LO Feynman diagrams of the $t\bar{t}$ production including up to three additional hard radiation processes are taken into account. For the $t\bar{t}$ event generation, the mass of the top quark is set to 172.5 GeV/c^2 and the scale factors μ_R and μ_F are set to the top quark mass plus the summed transverse momenta of all additional partons in the final state of the hard process. The shower and the hadronisation is simulated with Pythia using the D6T tune parameter set [145, 146] where the matching between matrix element and showering is performed according to the MLM scheme. As PDF set, the CTEQ6L [63] parametrisation is used. The decay of taus is simulated with Tauola.

An alternative Monte Carlo event generation for the $t\bar{t}$ signal process is performed using MC@NLO. In MC@NLO, all LO and NLO Feynman diagrams are evaluated to simulate top quark pair production taken also loop diagrams into account. From the NLO Feynman diagrams, hard radiation effects are only simulated up to first order in the matrix-element generation. All further radiation effects are simulated in the parton shower. For the simulation of $t\bar{t}$ events with MC@NLO, the top quark mass is set to 172.5 GeV/c^2 and the CTEQ6M [63] parameter set is used.

The two generators used for the simulation of the $t\bar{t}$ process predict slightly different kinematic behaviours of the generated top quarks. A comparison of the two sensitive variables which are studied within this thesis, the invariant mass of the $t\bar{t}$ system, $m_{t\bar{t}}$, and the variable $|\eta_t| - |\eta_{\bar{t}}|$ which is sensitive to the $t\bar{t}$ charge asymmetry, are compared for both generators in figure 3.3. In the distribution of $m_{t\bar{t}}$, the most noticeable differences between MadGraph and MC@NLO are visible in the turn-on region around $2m_t$ and in the tail of the invariant mass spectrum. The

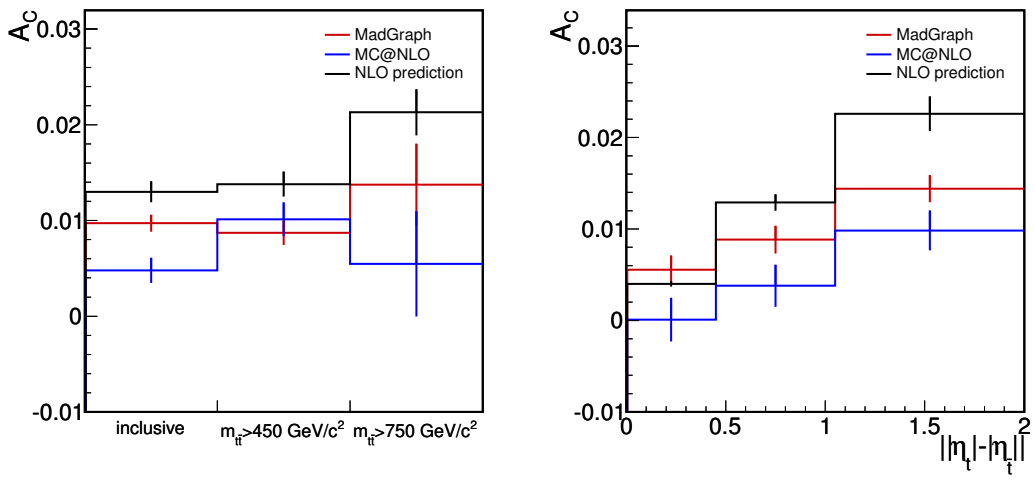

(a) (b)

Figure 3.4: The charge asymmetry in different $m_{\mathrm{t\bar{t}}}$ regions (a) and as function of the absolute value of $|\eta_{\mathrm{t}}| - |\eta_{\bar{\mathrm{t}}}|$ for different generators and the NLO theory prediction [24–26].

MadGraph generator fixes the masses of the simulated top quarks to the value of 172.5 GeV/c^2, top quarks are not allowed to be produced off-shell. Thus, the $m_{\mathrm{t\bar{t}}}$ spectrum shows a sharp cut-off at $2m_{\mathrm{t}}$. MC@NLO varies the mass of the generated top quarks within its natural width which is of the order of 1 GeV/c^2 [35]. Therefore, top quarks can be generated with a mass slightly below 172.5 GeV/c^2. This leads to a smoother turn-on of the invariant mass spectrum. The theoretically predicted peak of a $\mathrm{t\bar{t}}$ bound state just below the $m_{\mathrm{t\bar{t}}}$ threshold (see figure 1.6) is neither simulated by MC@NLO nor by MadGraph. In the tail of the invariant mass spectrum, MC@NLO predicts a slightly larger event fraction of SM $\mathrm{t\bar{t}}$ production with $m_{\mathrm{t\bar{t}}}$ values above 1 TeV/c^2. The effect of an enhanced top quark pair production with high invariant masses induced by the evaluation of NLO diagrams was also found in [74].

The shape of the $|\eta_{\mathrm{t}}| - |\eta_{\bar{\mathrm{t}}}|$ distribution is found to be very similar in the comparison of top quark pair events generated with either MadGraph or MC@NLO. The generated charge asymmetry according to the definition in equation 1.36 is found to be $A_C = 0.0097 \pm 0.0009$ for the MadGraph and $A_C = 0.0048 \pm 0.0013$ in the MC@NLO sample. Here, the quoted uncertainties are statistical uncertainties arising from the limited number of produced Monte Carlo events. Both generators show an asymmetry which differs significantly from zero. Since a charge asymmetry in SM $\mathrm{t\bar{t}}$ production can only occur in beyond LO Feynman diagrams, a non-vanishing asymmetry is expected for the MC@NLO sample which includes NLO Feynman diagrams. In the MadGraph sample, the generated charge asymmetry can solely arise from interference effects of processes with additional initial or final state radiation processes. Although MadGraph does not evaluate loop diagrams, a positive charge asymmetry is simulated from these interference effects of diagrams with additional parton radiations. The charge asymmetry A_C of the $|\eta_{\mathrm{t}}| - |\eta_{\bar{\mathrm{t}}}|$ distribution is shown

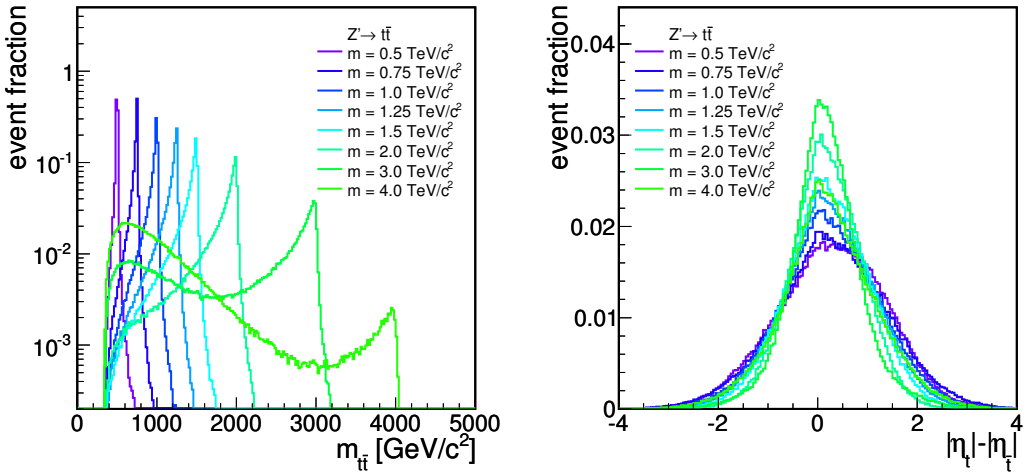

(a) (b)

Figure 3.5: Comparison of the distribution of the invariant mass spectrum of the $t\bar{t}$ system (a) and of $|\eta_t| - |\eta_{\bar{t}}|$ (b) in simulated $Z' \to t\bar{t}$ events for several Z' boson masses.

in figure 3.4 differentially as function of $m_{t\bar{t}}$ and the absolute value $|\eta_t| - |\eta_{\bar{t}}|$ for the different event generators as well as for the theoretical NLO prediction from [24–26]. In figure 3.4(b), the charge asymmetry as function of $||\eta_t| - |\eta_{\bar{t}}||$ is defined as the total charge asymmetry in equation 1.36, but taking into account only $t\bar{t}$ events in a specific $||\eta_t| - |\eta_{\bar{t}}||$ region. The charge asymmetries generated with MadGraph or MC@NLO are both smaller than the full NLO theory prediction also in these differential distributions. Especially for the asymmetry as function of $||\eta_t| - |\eta_{\bar{t}}||$, a clear tendency towards larger asymmetries in the region with higher $||\eta_t| - |\eta_{\bar{t}}||$ is visible for all predictions.

For the search for resonances in the invariant mass spectrum of the top quark pair, alternative Monte Carlo samples are produced. In these samples, the pairs of top and the antitop quarks are produced via the exchange of a heavy boson. For this purpose, also the MadGraph event generator is utilised. A Z' boson is introduced which has identical couplings to SM fermions as the Z boson, but a higher mass. The process $pp \to Z' \to t\bar{t}$ is generated with up to three additional hard parton radiations. The mass of the Z' boson is varied between 500 GeV/c^2 and 4,000 GeV/c^2 and the width of the new boson is set to 1% of its mass. Top quark mass, PDF parametrisation, and tune settings are the same as for the SM $t\bar{t}$ production with MadGraph. Only the scale parameters are set to the mass of the Z' boson. In figure 3.5, the invariant mass spectra as well as the $|\eta_t| - |\eta_{\bar{t}}|$ distributions are presented. In the $m_{t\bar{t}}$ spectrum, peaks are clearly visible at the masses of the respective Z' resonance masses. For increasing Z' masses, a larger fraction of events is produced with $m_{t\bar{t}}$ values below the original mass of the Z' boson. In these events, the Z' is produced off-shell. Although the production of off-shell resonances is expected to be more unlikely compared to on-shell production from just inspecting the amplitudes of the corresponding Feynman diagrams, the off-shell production of a Z' with a mass of

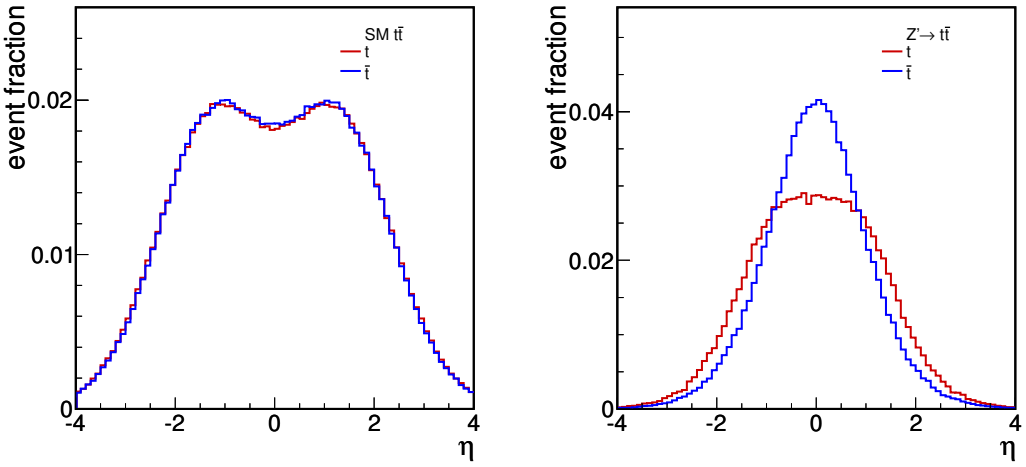

(a) (b)

Figure 3.6: Comparison of the pseudorapidity distributions of top and antitop quarks in SM $t\bar{t}$ production (a) and in the process $Z' \rightarrow t\bar{t}$ with $m_{Z'} = 1.5$ TeV/c^2 (b).

3 or 4 TeV/c^2 is strongly enhanced. This effect can be explained by the proton PDFs. For the production of an on-shell resonance with a mass of several TeV/c^2 in proton-proton collisions with a centre-of-mass energy of 7 TeV, both initial partons in the hard interaction have to carry a large momentum fraction x. The probability for finding two partons with high momentum fractions which can produce a heavy on-shell Z′ resonance is much smaller than having two partons with lower x values which subsequently produce a $t\bar{t}$ pair via the exchange of an off-shell Z′ boson.

In the $|\eta_t| - |\eta_{\bar{t}}|$ distributions of $t\bar{t}$ events produced in the exchange of a Z′ boson, an asymmetry is clearly visible in figure 3.5(b). Although the shape of $|\eta_t| - |\eta_{\bar{t}}|$ becomes more narrow for increasing masses of the Z′ boson, in all generated samples a charge asymmetry of $A_C \approx 0.2$ is observed. This asymmetry is induced by different vectorial and axial couplings of the Z′ boson to fermions. The coupling parameters g_V and g_A of the Z′ boson are set to the coupling values of the SM Z boson in the Monte Carlo generation. Since the values of g_V and g_A differ from the pure vectorial couplings in SM $t\bar{t}$ production via gluon exchange, the pseudorapidity distribution of top quarks in the exchange with a Z′ boson is broader than the pseudorapidity distribution of the antitop quark (see figure 3.6(b)) as it has been discussed in section 1.3.2. This leads to an asymmetric $|\eta_t| - |\eta_{\bar{t}}|$ distribution in $t\bar{t}$ production via the exchange of a Z′ boson. For SM $t\bar{t}$ production, the differences in the pseudorapidity distributions of top and antitop quarks are much smaller (see figure 3.6(a)), since they are induced by higher order effects only, whereas a $t\bar{t}$ charge asymmetry is generated in the Z′ boson samples already at LO.

3.1.3 Background Processes

There are several physical processes which can occur in proton-proton collisions leading to a similar experimental signature as top quark pair production in the lep-

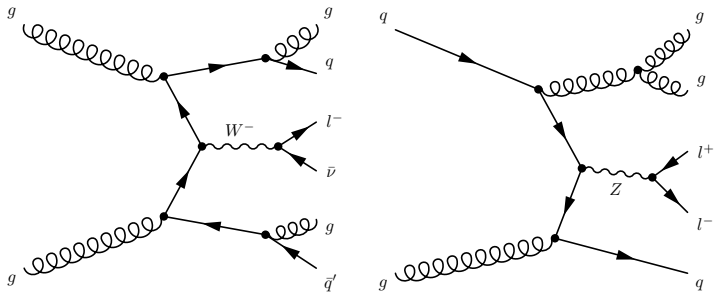

Figure 3.7: Examples for LO Feynman diagrams of W (a) and Z boson (b) production with additional radiations.

ton+jets decay channel. The most prominent background process for $t\bar{t}$ production is electroweak W boson production in association with jets, so-called W+jets events. If the W boson decays into a charged lepton and a neutrino, W+jets events with several hard gluon radiations or additional quark production processes can mimic the final state signature of typical $t\bar{t}$ events in the lepton+jets decay mode. Also Z boson production in association with hard quarks and gluons has a similar event signature. If the Z boson decays into a pair of charged leptons and one of the two leptons is not identified recorded by the detector, the final state of this process is similar to the final state of lepton+jets $t\bar{t}$ events. Exemplary Feynman diagrams of W and Z boson production in association with jets are depicted in figure 3.7. The Z boson production interferes with the same diagrams including a high-energetic photon instead of the Z boson. The combined Z/γ^* production of lepton pairs is referred to as Drell-Yan production. W boson and Drell-Yan processes in addition with up to four hard jets are simulated with MadGraph. For Drell-Yan production a cut on the minimal invariant mass of the lepton pair, $m_{l^+l^-} > 50$ GeV/c^2, is applied to reduce the fraction of low-energetic photon exchanges. Only decays into lepton pairs of the W and Z bosons are simulated in the Monte Carlo generation of these processes. In the simulation of W/Z+jets performed with the MadGraph generator, the CTEQ6L PDF set and the D6T tune have been used and the scale parameters have been set to the respective gauge boson mass adding the transverse momenta of all additional partons.

Another background process having a similar signature as top quark pair production is the electroweak production of single top quarks. There are three LO Feynman diagrams contributing to single top quark production in proton-proton collisions (see figure 3.8), the s-channel, the t-channel, and the associated production with a W boson (tW-channel). Since the cross section of the s-channel process is much smaller than the cross sections of the other two production mechanisms only Monte Carlo simulations of the latter two processes are taken into account in this thesis. Only leptonic decays of the W boson from the top quark decay are considered in the generation of the single top quark t-channel production. For the associated production all decay modes are considered since leptons can also originate from the decay of the associated W boson. The single top quark production processes are generated with

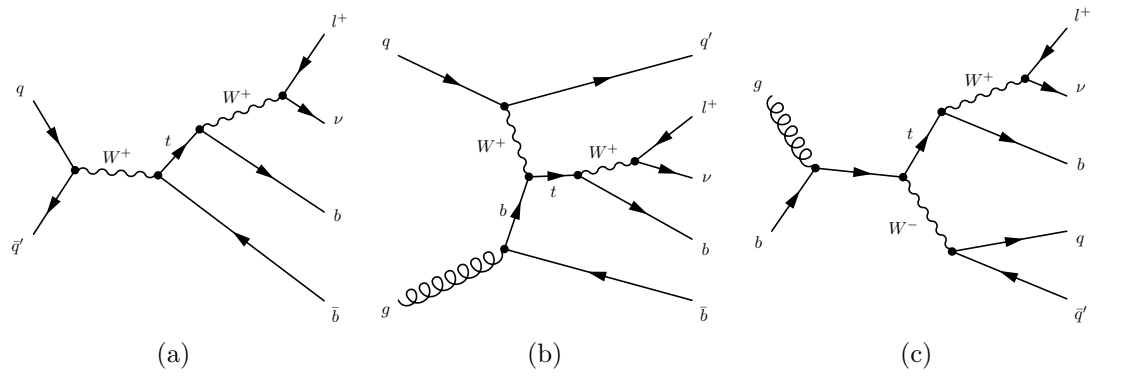

Figure 3.8: Feynman diagrams of electroweak single top quark production in the s-channel (a), the t-channel (b), and in associated production with a W boson (c) with leptonic top quark decays.

the MadGraph generator. For the production of t-channel events, the b-quark in the initial state can be either simulated as a parton originating from the proton according to a b-quark PDF or it can be simulated by a gluon splitting into a $b\bar{b}$ pair in the matrix-element of the hard interaction. Details of a matching of these two descriptions can be found in [147]. Single top quark production is generated using the CTEQ6L PDF parametrisation, the scale parameters are set to the top quark mass of 172.5 GeV/c^2. For the showering, the Pythia tune Z2 [148] has been chosen. The basic Feynman diagrams of single top quark production have only two or three quarks in the final state. Hence, mainly single top quark production with additional radiation processes in the showering imitates the final state of top quark pair production.

A further physical process which can produce a similar final state signature as $t\bar{t}$ production in the lepton+jets decay channel is QCD multi-jet production. Since this process solely depends on the strong interaction, no leptons are expected to occur in the final state of the hard process. However, it is possible that leptons are emitted in such a process. Especially in the hadronisation process, unstable B- or C-hadrons, i. e. hadrons containing b- or c-quarks respectively, can decay leptonically. Such muons can also originate from the in-flight decays of kaons or pions. Also a photon with large momentum can produce electron-positron pairs in conversion processes. Additionally, it is possible that other charged hadrons such as pions or kaons are misidentified as electrons in the detector. Hadrons can also be misidentified as muons, if they are not stopped in the HCAL. These punch-through hadrons can then fake a muon signal in the outer muon chambers.

For QCD events including a muon, only one dedicated sample is produced. In a Monte Carlo event generation with Pythia of QCD di-jet production, a filter on processes including at least one muon stemming mostly from B- or C-hadron or kaon and pion decays is applied. The muon is required to exceed a transverse momentum p_{T} of 15 GeV/c. Since there are different ways to produce electrons than muons in the final state two different approaches to simulate QCD events including electrons are chosen. First of all, a Monte Carlo sample including B- and C-hadrons which have an electron in the decay chain is generated with Pythia. The

electron is required to have $p_{\mathrm{T}} > 10$ GeV/c. This sample is divided into different $\hat{p}_{\mathrm{T}}$ ranges. The variable $\hat{p}_{\mathrm{T}}$ is defined as the transverse momentum transfer of the hard interaction and $\hat{p}_{\mathrm{T}}^2$ is equal to Q^2 for $2 \rightarrow 2$ QCD processes with massless particles in the final state. The electron QCD sample with B- and C-hadron decays is divided into three sub-samples with $\hat{p}_{\mathrm{T}}$ ranges of 20 GeV/$c < \hat{p}_{\mathrm{T}} <$ 30 GeV/c, 30 GeV/$c < \hat{p}_{\mathrm{T}} <$ 80 GeV/c, and 80 GeV/$c < \hat{p}_{\mathrm{T}} <$ 170 GeV/c. The differentiation in $\hat{p}_{\mathrm{T}}$ bins is performed to enrich the number of generated Monte Carlo events in phase space regions with higher momentum transfer. A second QCD sample for the electron+jets channel is used to simulate events which can produce the signal of an isolated electron in the detector. This sample is also generated using Pythia. It contains two types of events. The first component of this sample contains simulated QCD di-jet events where several photons, electrons, charged pions, and charged kaons are clustered together in a small η–ϕ region. The transverse energy of this cluster must have $E_{\mathrm{T}} > 20$ GeV and the cluster is required to be isolated. This means, that no further particles with huge energies are allowed to lie within an isolation cone around the cluster. The energy of all electrically charged particles with a distance $\Delta R := \sqrt{(\Delta\eta)^2 + (\Delta\phi)^2} < 0.2$ must not exceed 5 GeV, the total energy of all particles in this cone must be smaller than 10 GeV. The second class of events in this sample contains events with at least one single electron or charged pion with $E_{\mathrm{T}} > 20$ GeV. This particle is required to be isolated within an isolation cone of radius $R = 0.1$. The energy of additional charged particles in this cone must be smaller than 4 GeV, the total energy of all additional particles in this cone must not be larger than 7 GeV. This QCD sample is also divided into $\hat{p}_{\mathrm{T}}$ ranges of 20 GeV/$c < \hat{p}_{\mathrm{T}} <$ 30 GeV/c, 30 GeV/$c < \hat{p}_{\mathrm{T}} <$ 80 GeV/c, and 80 GeV/$c < \hat{p}_{\mathrm{T}} <$ 170 GeV/c. An overlap of events with the first sample is prevented by rejecting events with an electron originating from B- or C-hadron decays from the second sample.

For the electron+jets channel, another process is simulated which can contribute as background in the analysis of $\mathrm{t\bar{t}}$ events. As already mentioned, the radiation of a photon can produce conversion electrons in the detector material. While the QCD Monte Carlo samples only simulates the showering process, photons can also emerge from the hard interaction directly. The process of photon+jets production is simulated with the MadGraph Monte Carlo event generator. This sample is divided into H_{T} bins of 40 GeV/$c < H_{\mathrm{T}} <$ 100 GeV/c, 100 GeV/$c < H_{\mathrm{T}} <$ 200 GeV/c, and $H_{\mathrm{T}} > 200$ GeV/c where H_{T} is the sum of transverse momenta of all quarks and gluons in the final state. All these QCD background simulations use the CTEQ6L PDF parametrisation and the Z2 Pythia tune, except for the photon+jets sample, which is generated using the D6T tune.

3.2 Detector Simulation

Monte Carlo event generator programs are used to simulate high-energetic proton-proton collisions. Emerging stable particles of each interaction are interacting with the detector and are producing particular signals. For generated proton-proton collisions, the response of the detector has also to be simulated. For this purpose, a

detector simulation based on the software package GEANT4 [149, 150] is employed. GEANT4 is designed to simulate the passage of particles through different kinds of matter. Electromagnetic and hadronic interactions of particles with different energies are included in this simulation. The full CMS detector and all its components are modelled with the GEANT4 toolkit. GEANT4 simulates the flight trajectories in the magnetic field of the detector for all particles generated in the Monte Carlo simulation and models the signals which they produce in the detector. This simulation includes the production of electronic signals in tracker and muon chambers, electromagnetic and hadronic showering processes in the calorimeters as well as the subsequent light emission from these showers, and ionisation processes of charged particles traversing the detector material. The final outcome of the detector simulation is a modelling of all electronic signals produced in the read-out electronics of the CMS detector.

3.3 Reconstruction

From electronic signals produced in the detector by real proton-proton collision events taken with the CMS detector it is not directly possible to conclude which physical process induced these signals. Therefore, several reconstruction algorithms are applied to the raw detector data. These algorithms are, for instance, reconstruction routines for tracks which combine single hits in the tracker modules or muon stations. Other reconstruction techniques are searching for energy depositions in the calorimetry system. The combination of reconstructed objects of all parts of the detector – reconstructed tracks in inner tracker and muon system together with calorimeter information – helps to identify physical objects such as muons, electrons, or jets of hadrons which originate from the emission of quarks or gluons. Especially for the expected event signature of $t\bar{t}$ events in the lepton+jets decay channel the reconstruction of all these objects is required to study the kinematics of top quarks. The same reconstruction algorithms are also applied to the simulation of collision processes with Monte Carlo event generators together with the full CMS detector simulation to have a suitable comparison of theoretical predictions and real data.

3.3.1 Tracks and Primary Vertices

The reconstruction of tracks is an essential ingredient for the identification of charged particles and determination of their momenta and sign of their charge from the curvature of these tracks. The determination of tracks allows to reconstruct a primary vertex which indicates the exact position of a hard proton-proton collision in the interaction region in the centre of the detector. Tracks emerging from secondary vertices are an important indication to identify decay products from B- or C-hadrons. These hadrons are unstable, but their lifetime is long enough to allow these particles to fly over a measurable distance.

A track in the constant magnetic field of the inner CMS detector is defined by five parameters which have to be determined in the track fitting procedure. Since a charged particle describes a helix in a constant magnetic field its trajectory is

defined by the point (x, y, z) the particle is passing, the particle's momentum at this point normalised to its charge p/q which defines the curvature of the track, and the angle between the direction of the magnetic field $\vec{B}$ and the particle's track. The Combinatorial Track Finder (CTF) [151, 152] is used as default reconstruction technique in the CMS experiment to determine the parameters of tracks and consists therefore of four steps: seed generation, pattern recognition, ambiguity resolution, and a final track fit. Hits within the inner pixel detector are used to find a seed for the CTF. A seed is defined as a pair of hits in two layers of the pixel detector with different radii. Adding a third hit from another pixel module to the pair of hits already reduces the rate of fake tracks not produced by particles from the initial parton-parton collision. The pattern recognition utilises a combinatorial Kalman filter [153, 154]. In this method, the filter iteratively extrapolates the tracks from the seeds to the outer layers of the tracker. The tracks from the seeds are extrapolated into the next outermost layer of the tracker accounting for the equation of motion of a charged particle in a constant magnetic field. Also energy losses in the traversed material are taken into account. For each hit in the next layer compatible with the extrapolation, new track candidates are created. The track candidates are successively extrapolated into the next layer of the tracker. In the extrapolation, it is accounted for the possibility that a charged particle does not necessarily produces hits in all layers. If a track passes tracker layers without a hit, the track is assigned to have a so-called invalid hit. To reduce the number of track candidates, quality criteria including the number of hits and invalid hits as well as a χ^2 compatibility with the predicted track of a charged particle are applied during the extrapolation. All tracks are extrapolated simultaneously to the outermost layer of the tracker or until no more compatible hits can be found. Ambiguities in the reconstruction occur if several track candidates are reconstructed starting from the same seed or the track originating from one single particle is reconstructed from different seeds. Therefore, if two tracks share more than 50% of their hits, the track with the smaller number of hits or, if both tracks have the same number of hits, the one with the higher χ^2 is rejected. Finally, all reconstructed trajectories are re-fitted with a combination of a second Kalman filter and a smoothing algorithm to avoid biases which can arise from constraints during the seeding. This second Kalman filter operates in opposite direction to the first tracking filter and extrapolates the tracks from the outermost tracker layer towards the inner pixel detector. To improve the track reconstruction performance, the full CTF algorithm is iteratively applied several times. In each iteration step, tracker hits which were associated to high-purity tracks in the previous run of the CTF algorithm are removed from the collection of hits and the procedure is repeated using remaining hits to reconstruct further track candidates.

From the collection of high-purity tracks, primary vertices can be reconstructed. Finding primary vertices is important to identify the exact position of the initial proton-proton interaction. The number of primary vertices found in one event is also an important quantity to estimate the number of pile-up collisions. In the CMS experiment, there exists several approaches to define the position and the uncertainty of a primary vertex [155]. All techniques are based on the search for a common point of origin in the collision region of several reconstructed tracks. The

most simple algorithms are already running on the HLT using only an extrapolation of the pixel seeds and constraining the search for primary vertices to the centre of the beam pipe, i. e. only the z position of the primary vertex is a free parameter in the vertex determination. In the offline reconstruction, a primary vertex fit is performed based on fully reconstructed tracks which also determines the x and y coordinates of primary vertices. Also the compatibility with the beam spot is taken into account. The beam spot is defined as the actual position of the two colliding proton beams.

An important quantity in the determination of primary vertices is the impact parameter (IP) of a track with respect to a reference point. The reference point can either be a vertex or the beam spot. The IP is defined as the distance between the track and the vertex at the point of closest approach. One distinguishes between the three-dimensional and the two-dimensional IP. The two-dimensional IP is the distance of the track to the vertex in the transverse plane to the beam axis, whereas the three-dimensional IP measures the full distance in all spatial directions. Typically, the significance of the IP is defined to obtain a quality criterion. The IP significance is defined as the IP value divided by the uncertainty on this determination. For the reconstruction of primary vertices, all tracks used to define this primary vertex have to have a significance of the IP with respect to the beam spot below a certain threshold.

The primary vertex determination is divided into two steps. In a first step, track candidates are grouped to define primary vertex candidates. In the second step, the tracks are re-fitted under the assumption that they originate from a common vertex. For this step, different algorithm based on the Kalman filter extrapolating the tracks from the tracker to the primary vertex position exist. The standard procedure to fit primary vertices at the CMS experiment is the Adaptive Vertex Fitter (AVF) [155]. The AVF performs a χ^2 minimisation of the sum of the squared standardised distances of all tracks to the primary vertex candidate. In the AVF method, all tracks are weighted by their compatibility with this vertex candidate. Tracks which are most likely outliers not belonging to the primary vertex are assigned a smaller weight than tracks more compatible with the vertex candidate. The Kalman filter is then applied iteratively several times using the weights in the minimisation. In each iteration step, the weights are updated according to the re-fitted primary vertex candidate. Finally, the quality of the reconstructed primary vertices is defined by their χ^2 values and their compatibility with the beam spot.

3.3.2 Muon Reconstruction

Muons are minimally ionising particles traversing the entire detector depositing only a small fraction of their energy. As charged particles, they produce hits in the tracker and in the muon chambers. At CMS, there exist three approaches to identify muons [119, 156]. The stand-alone muon reconstruction is based on information provided by the muon stations, tracker muons are measured with their tracks in the inner tracker, and global muons combine measurements in both, the tracker and the muon system, to determine the muon's momentum most accurately.

The stand-alone muon reconstruction relies on a track fit to hits in the outer muon chambers. For the track seeding, a linear fit to hits in the layers of a single DT chamber or a single CSC is performed. Only the innermost DT chambers and CSCs are used for the seeding. These seeds serve as starting points for a Kalman filter algorithm which is applied to all hits in the DT chambers, CSCs, and RPCs evolving the muon trajectories from inside out. The traversing of the muon through the material of the muon chambers and the return yoke is simulated incorporating the inhomogeneous magnetic field. The Kalman filter works similarly as the track reconstruction in the inner tracker. When the outermost muon stations are reached, the Kalman filter is applied a second time to fit the muon trajectories from outside in. Finally, the tracks are constrained to have their origin in the beam-spot region.

The second reconstruction method is based on a track fit in the inner track. Calorimetry entries and hits in the muon chambers in the extrapolation of the inner track have to be compatible with a muon hypothesis, but they are not included into the trajectory fit and are therefore not used to measure the muon's momentum.

The global muon reconstruction combines stand-alone muons with information from the tracker. Global muons are reconstructed starting with a stand-alone muon. The stand-alone muon track is then extrapolated inwards towards the inner tracker taking into account the muon's energy loss in the calorimeter and the magnet coil as well as the magnetic field. The extrapolation defines a rectangular η–ϕ region of interest in the tracker layers. All tracks reconstructed in the tracker falling into the region of interest are possible candidates to accomplish the stand-alone track. For a more stringent selection of these tracker track candidates, a matching algorithm aims for the connection of the tracks in the tracker falling into the region of interest with the track of the stand-alone muon by extrapolating both tracks and comparing their parameters. For this purpose, the tracker track as well as the stand-alone muon track are propagated to a common plane which is typically located at the outermost tracker layer or the inner muon station, but in principle each cylindrical layer in the detector can act as such a plane. The plane is chosen such, that the overall uncertainty on the extrapolated track parameters and the number of tracks matched to the stand-alone muon are minimal. For all found tracks in the tracker matched to a stand-alone muon track the complete track is re-fitted using all hits associated to one of both segments of the track, the inner track and the stand-alone muon track. In case of two or more tracker tracks matched to the stand-alone track, the tracker track to stand-alone association with the minimal χ^2 is selected.

3.3.3 Electron Reconstruction

Electrons produce a specific signature in the CMS detector. Since they are charged particles they leave hits in the inner tracker. Electrons are loosing a significant amount of their energy by the emission of bremsstrahlung in the material of the tracker. Finally, they deposit their remaining energy in the ECAL crystals. For the correct determination of the electron's energy, a clustering of ECAL energy depositions which adds up not only the direct electromagnetic shower but also the energy depositions of the emitted bremsstrahlung photons is required. The electron

reconstruction at the CMS experiment [157] combines a clustering of ECAL energy deposits with a specific track reconstruction for electrons performed with a Gaussian Sum Filter (GSF) [158]. For the clustering of energy deposits in ECAL crystal, two different algorithms are utilised for barrel and endcap regions, respectively [159]. The so-called ECAL superclusters are formed starting from a single ECAL crystal signal as seed. The clustering algorithms are searching for additional energy depositions in the adjacent clusters in ϕ direction to add possible energies of bremsstrahlung photons. The hybrid algorithm used for finding superclusters in the barrel region searches for so-called dominoes – groups of ECAL depositions with a width of three or five crystals in η – along the ϕ direction up to an extension from the initial seed of 0.3 rad. In the endcap region, a clustering algorithm is utilised which first searches for energy depositions within 5×5 matrices of crystals. Matrix clusters lying in the ϕ direction from the initial seed are then grouped to the electron supercluster. The maximal radial extension is also 0.3 rad for the superclusters in the endcap.

The corresponding track of the electron candidate is reconstructed in a similar way as the standard tracks described above. The seed of the track consists of two hits in the pixel detector which falls into a restricted region compatible with the supercluster in the ECAL. There exists also the possibility to start the electron reconstruction from a track and search for a compatible ECAL supercluster afterwards. The track fit is again obtained with a Kalman filter, but the extrapolation of the track from inner towards outer layers is modified according to the higher energy losses of electrons due to bremsstrahlung radiation. The track is then re-fitted and smoothed with the GSF algorithm. The GSF is an extension of the Kalman filter. The standard Kalman filter can only handle Gaussian distributed energy losses in the extraploation of the track and uncertainties following Gaussian distributions in the χ^2 fit. Following this approach, the track momentum is shifted by the mean of the expected energy loss distribution and the variance of the energy loss is added to the momentum uncertainty in the propagation. This treatment of energy losses requires that the energy loss function can be described by a Gaussian distribution, but the energy loss due to bremsstrahlung radiation formulated in the Bethe-Heitler model [160] cannot be approximated by a single Gaussian. Therefore, the GSF models the energy loss in each layer of the track with a weighted sum of several Gaussian distributions. For the estimation of the track parameters in each extrapolation step, the Gaussian component with the highest weight or the weighted mean of all Gaussians can be used. Using the component with the highest weight results in a more precise determination of the electron's momentum, whereas the method of choosing the weighted mean of all components gives the smallest biases.

Another caveat the electron reconstruction has to deal with, is the conversion of bremsstrahlung photons into electron-positron pairs. The appearance of electrons in the bremsstrahlung shower close to the initial electron will produce additional tracks. These tracks are often associated to the same ECAL supercluster. To solve the ambiguity of track associations to the same supercluster, the tracks are classified according to their innermost hit position. Only the track with the innermost hit position is kept. If both tracks have their first hit in the same layer, only the candidate with the best energy-to-momentum ratio E/p is considered.

3.3.4 Jets and Missing Transverse Energy

Quarks and gluons emitted from the hard interaction of proton-proton collisions cannot be observed directly since they are colour-charged particles obeying the QCD confinement. Therefore, the radiation of a quark or gluon with high momentum results, after showering and hadronisation processes, in a bunch of colour-neutral particles which can be detected. The task of a jet algorithm is to provide information of a single parton by clustering observable objects originating from showering, hadronisation, and decay processes. Experimentally, the clustering can only be performed on observables in the detector, such as ECAL and HCAL energy depositions or reconstructed tracks. The same clustering algorithms can also be applied to the set of stable particles in the output of a Monte Carlo event generation. In general, the input to a jet clustering algorithm can be any set of objects which are described by a momentum vector. The summation of the clustered momenta then gives an estimate for the momentum of the single particle initiating the jet. At the CMS experiment, several different approaches and algorithms are used for the jet clustering.

Clustering Algorithms

Most commonly used jet clustering algorithms are based on one of two basic approaches, the cone algorithm or the sequential recombination scheme, respectively. In a cone algorithm, the centre of a jet is defined in a specific way and all particles found within a cone of a previously defined radius R in the η–ϕ plane are collected into the jet. At the CMS experiment, the iterative cone [119] and the Seedless Infrared Safe Cone (SISCone) [161] algorithms are used. The iterative cone algorithm starts the clustering with the input object with largest transverse energy E_{T} as seed. The transverse energy of a clustering object is defined as

$$E_{\mathrm{T}} := E \cdot \sin\theta, \tag{3.1}$$

where E is the object's energy and θ is the azimuthal angle of its momentum vector. All objects in a cone around the initial seed are clustered to a proto-jet. The direction of this proto-jet is taken as a new seed for the next iteration of the clustering procedure. The iteration stops, if the energy of all objects clustered to the jet and the direction of the jet do not change significantly any more. Ideally, jet algorithms are required to be collinear and infrared safe [162]. A jet algorithm is called collinear safe, if the result does not change when adding a collinear gluon splitting in the shower. An additional splitting changes the E_{T} ordering of particles and can therefore change the choice of seeds. Infrared safety ensures the stability of the result of the jet algorithm under the influence of soft radiations or additional contributions from pile-up or underlying events. In the iterative cone algorithm, a soft radiation being located between two jets can lead to a merging of these two jets. Unfortunately, the simple cone algorithms are neither collinear nor infrared safe. A cone algorithm which is collinear and infrared safe is the SISCone algorithm. The SISCone algorithm searches for all possible stable cones in an event without introducing seeds. Since these stable cones often overlap, a split-merge procedure is

applied after all stable cones have been identified. Although the SISCone algorithm has the advantage of infrared and collinear safety, the iterative cone algorithm is used for the HLT reconstruction since it is less computing time consuming.

Recombination algorithms are a complementary version of jet clustering algorithms. These algorithms are not based on a fixed geometrical shape as in case of the cone algorithms but on a sequential clustering of input objects. For the sequential clustering, a distance measure $d_{i,j}$ between two input objects i and j is defined. The algorithms creates a list of all distances $d_{i,j}$ between all input objects. This list also includes the distances $d_{i,B}$ of all input objects i to the beam axis. The algorithm then searches for the two objects i and j which exhibits the smallest distance and adds them to a new object k. The individual objects i and j are removed from the list of input objects and the summed object k is added instead. The list of distance measures is updated according to the new list of input objects and again the two closest objects are combined. The recombination of objects stops, if the smallest distance found is the distance $d_{i,B}$ of an object i to the beam axis. Then, the object i is defined as a completed jet and is removed from the list of input objects. The algorithm finishes when all jets are completed and the list of input objects is empty. The main difference between the algorithms based on this recombination scheme is the definition of the distance measure $d_{i,j}$. In the k_{T} algorithm [163], the distances $d_{i,j}$ and $d_{i,B}$ are defined as

$$d_{i,j} := \min\left(p_{\mathrm{T},i}^{2n}, p_{\mathrm{T},j}^{2n}\right) \cdot (\Delta R_{i,j})^2, \tag{3.2}$$

$$d_{i,B} := p_{\mathrm{T},i}^{2n} \cdot D^2, \tag{3.3}$$

where $n = 1$ and $\Delta R_{i,j}$ is the distance of two objects in the η–ϕ plane. The resolution parameter D defines the size of the jets. For larger values of D, on average more clustering steps are required until $d_{i,B}$ is smaller than all other distances $d_{i,j}$ and therefore more objects will be recombined into one jet. The anti-k_{T} algorithm [164] uses the same distance definitions as the k_{T} algorithm, but with the parameter $n = -1$ in equations 3.2 and 3.3. In contrast to the standard k_{T} algorithm, which often leads to fuzzy jet shapes in the η–ϕ plane, the anti-k_{T} algorithm produces jets with a circular shape.Another jet algorithm of this type is the Cambridge-Aachen algorithm [165] which uses $n = 0$, so the distance of two objects is just given by $(\Delta R_{i,j})^2$ in this case. All recombination algorithms are collinear and infrared safe and are less computing time consuming compared to the SISCone algorithm.

All described jet algorithms are based on adding four-momenta of input objects to estimate jet four-momenta. When using calorimeter clusters as input, these input objects have no well-defined four-momentum since the measurement of an energy and a direction only determines a three-vector. The undetermined mass of the four-momentum is therefore set to zero for all input objects used for the jet clustering at the CMS experiment.

Input Objects: The Particle Flow Approach

The Particle Flow (PF) algorithm [166] is designed to identify and to reconstruct all stable particles in the detector individually. For this purpose, the PF algorithm combines measurements of all sub-detectors. Taking these reconstructed particles and

their momenta as input for a jet clustering algorithm provides a more precise determination of jet momenta than clustering only energy deposits from the calorimeters. Main part of the PF algorithm is a linking procedure to connect individual tracks, ECAL clusters, and HCAL energy depositions. Tracks as ingredients for the PF reconstruction are determined by applying the standard track reconstruction algorithm iteratively several times. In each iteration, hits associated to tracks found in the previous iteration are removed from the list of tracker hits and additional tracks are searched for with loosened seeding criteria. This procedure provides a higher tracking efficiency. The energy clustering in the calorimeters is performed separately for all sub-detectors, the ECAL barrel, the ECAL endcap, the HCAL barrel, and the two layers of the PS. In the HF, each single calorimeter cell with a certain energy deposition gives rise to one cluster, in all other sub-detectors specific PF clusters are formed. This PF specific calorimeter clustering starts with single cells with maximal energy depositions as seeds. Topological clusters are formed by aggregating neighboured cells to the seed. These topological clusters are then collected iteratively to form PF clusters.

The linking algorithm connects the reconstructed tracks and the PF clusters in the calorimeter to identify charged particles. Tracks are extrapolated into the calorimeter taking the expected energy losses into account. All PF clusters compatible with this extrapolation are linked to the track. If more than one PF cluster in the same sub-detector is compatible with the track, the track is only linked to the best matching cluster. Also a linking of calorimeter clusters from different sub-detectors is performed by inspecting the geometrical overlap of PF clusters. The PF method also comprises reconstruction procedures for muons and electrons. These reconstruction algorithms are similar to the standard reconstruction methods of charged leptons described above. For muons, a matching between inner tracks and tracks in the muon chambers to global muons is performed. Electron tracks are re-fitted with the GSF algorithm and PF clusters in the ECAL are linked to these tracks, if they are compatible with bremsstrahlung emissions. For the final identification of electrons, several calorimeter and tracking performance variables are combined. All linked particle candidates not consisting of tracks and calorimeter clusters associated to electrons or muons underly further identification and ambiguity resolution steps. ECAL and HCAL clusters are also corrected for the expected energy loss of identified muons. Neutral hadrons and photons can be identified by inspecting calorimeter clusters not matched to any track and by the comparison of track momenta and the energy of linked calorimeter clusters. If ECAL clusters have a much larger energy deposition than expected from the linked track, the excess of the energy is associated to a photon. In the HCAL, such energy deposits not compatible with the track are associated to neutral hadrons. All remaining linked tracks and energy deposits can then be identified as charged hadrons. Only in the forward region of the detector which is not covered by the inner tracker, the PF algorithm can not distinguish between charged and neutral hadrons. The combination of track and calorimeter information then allows for a more precise determination of the energy of charged particles. The PF algorithm finally provides a complete list of all kinds of reconstructed stable particles which can then be clustered with any standard jet

clustering algorithm.

Jet Energy Corrections

The ultimate goal of any jet reconstruction is the estimation of parton momenta from clustered objects. But even the usage of better calibrated objects, such as in the PF algorithm, does not automatically lead to a parton momentum by adding four-momenta of measured objects. Several physics and detector effects are influencing the jet reconstruction. At the CMS experiment, these effects are factorised, i. e. the jet momenta are scaled with an overall factor which is a product of several individually determined factors correcting the jet energy for different effects [167]. In total, there exist seven correction factors called Level 1 to Level 7 corrections.
Level 1: This factor corrects the jet energy for offset effects from pile-up events and electronic noise in the detector.
Level 2 (relative η correction): The jet energy is corrected for different jet responses in various pseudorapidity regions by the Level 2 factor.
Level 3 (absolute p_{T} correction): With the Level 3 correction factor the jet energy is corrected for various jet responses in transverse momentum p_{T} regions.
Level 4: The Level 4 factor corrects for differences in the jet response arising from variations of the fraction of electromagnetic energy of a jet.
Level 5: This factor corrects the jet energy for different expected responses of light quarks, c- and b-quarks, or gluons.
Level 6: The influence of the underlying event is corrected in this step.
Level 7: The previous factors correct the measured jet energy back to the jet energy of a jet which clusters stable particles after the hadronisation with the same jet algorithm. The Level 7 factor further corrects the jet momenta back to the momentum of the final state parton.

The jet correction factors Level 4 to Level 7 are optional corrections which can be applied individually depending on the requirements of the actual analysis. For the analyses in this thesis, only Level 2 and Level 3 jet correction factors are applied, since only these were fully evaluated in collision data [168–170]. The relative correction can be determined from inspecting pure di-jet events. Due to momentum conservation, the two jets are expected to be balanced in p_{T}. This allows the determination of the relative jet energy calibration in such events, if the two jets fall into different η regions of the detector. In a similar way, the absolute energy correction can be estimated in photon+jet events, where the photon balances the jet in its transverse momentum. To account for differences in jet responses found on Monte Carlo simulation and real data, the jets reconstructed in data are further corrected by an additional residual correction to make them compatible with the Monte Carlo samples.

b-Tagging

In top quark pair production, both top quarks are expected to decay into b-quarks with a probability close to 100%. Jets originating from b-quark production – so-called b-jets – can be identified with certain algorithms, called b-taggers. Most of

these b-tagging algorithms make use of the relatively long lifetime of B-hadrons which is of the order of 10^{-12} s. B-hadrons with high momenta can therefore travel for distances which are measurable with the tracking detector. The most prominent signature of B-hadrons are tracks emerging from a secondary vertex apart from the primary vertex. A secondary vertex can be an indication for a B-hadron decay which was originally produced in the hard interaction at the primary vertex. A B-hadron decay can also be identified, if the B-hadron decays semi-leptonically. In this decay mode, an electron or muon which is found inside the jet cone can provide information for the b-jet identification.

Several b-taggers have been developed for the identification of b-jets at the CMS experiment [171]. All these tagging algorithms provide a single discriminator value as output. For the most simple b-tagging algorithm, this number is given by a single observable such as the IP significance of a track. More complex b-taggers combine several observables into a single quantity. Applying a cut on this discriminator value allows to identify b-jets with a certain efficiency and purity. The output can also be transformed into a probability that a jet with a certain discriminator value is a b-jet.

Four types of b-tagging algorithms are currently commissioned by the CMS collaboration [172]. The first class of algorithm are so-called track counting methods. The track counting algorithms are designed to be simple and robust since they do not rely on a full reconstruction of secondary vertices. To identify a b-jet, these algorithms count the numbers of tracks inside a jet which have an IP significance with respect to the primary vertex above a certain value. The Track Counting High Efficiency (TCHE) tagger demands the existence of at least two such tracks. The tracks of the jets are ordered with descending IP significances and the discriminator value of the TCHE tagger is then defined as the IP significance of the second track. The Track Counting High Purity (TCHP) tagger works similarly, but requires the existence of at least three tracks with high IP significance and defines the discriminator value as the IP significance of the third track. The second type of b-tagging algorithms used at CMS are Simple Secondary Vertex (SSV) taggers. These algorithms require a secondary vertex to be reconstructed from at least two or three tracks. The discriminator value of these taggers is a monotonic function of the flight distance between the primary and the secondary vertex. The jet probability taggers are another class of b-tagging algorithms. In these taggers, the probability of each track of a jet to originate from the primary vertex is estimated. A discriminator value can then be defined by combining the probability value of individual tracks. The last class of taggers currently available at the CMS experiment are lepton based b-jet identification methods. These algorithms are searching for reconstructed electrons or muons within a jet and define the discriminator value as the relative transverse momentum of the found lepton with respect to the jet direction.

Missing Transverse Energy

The only stable particles which cannot be detected with the CMS experiment are neutrinos or hypothetically predicted particles in new theoretical approaches which solely interact weakly. All other particles which interact via electromagnetic or

strong interactions with the detector material can be identified and their momenta can be measured. Although weakly interacting particles like neutrinos cannot be detected directly, the presence of neutrinos can be inferred from the summed momenta of all other measurable particles. Due to momentum conservation, the summed momenta of all particles should add up to zero. Deviations from zero in the sum of all momenta can thus be assigned to weakly interacting particles which escaped direct detection. Since the momenta of the initial partons colliding in the hard interaction are not known, only momenta in transverse direction to the beam pipe can be considered for an estimation of neutrino momenta. Practically, since only energies and not momenta can be measured with the calorimeters, not a missing transverse momentum but a missing transverse energy vector is defined as [173]

$$\vec{\not{E}}_{\mathrm{T}} := -\sum_{i=1}^{N} \vec{E}_{\mathrm{T},i}, \tag{3.4}$$

where the sum runs over all N measured calorimeter energy depositions and the magnitude of the two-dimensional vector $\vec{E}_{\mathrm{T},i}$ is given by the measured transverse energy defined as in equation 3.1 of the calorimeter cell i. The direction of $\vec{E}_{\mathrm{T},i}$ points perpendicular to the beam direction towards the ϕ position of the calorimeter cell i. The magnitude of the missing transverse energy vector, $|\vec{\not{E}}_{\mathrm{T}}|$, is usually abbreviated with $\not{E}_{\mathrm{T}}$. The definition of $\vec{\not{E}}_{\mathrm{T}}$ given in equation 3.4 is a purely calorimeter-based. Since muons do not leave significant energy depositions in the calorimeters, this definition of the missing transverse energy has to be corrected when studying collision events containing muons.

An alternative definition of missing transverse energy taking into account not only calorimeter clusters is based on particle flow objects [166]. For the definition of this so-called PF-$\vec{\not{E}}_{\mathrm{T}}$, the sum in equation 3.4 runs over all identified PF candidates found in an event. This definition of $\vec{\not{E}}_{\mathrm{T}}$ therefore contains all types of particles, electrons, muons, and hadrons.

A more precise description of the missing transverse energy accounts also for differences in the calorimeter response. The corrections for calorimeter response which can be applied to the determination of missing transverse energy are called type I and type II corrections [169]. The type I correction makes use of the already determined correction factors of jets. All contributions to $\vec{\not{E}}_{\mathrm{T}}$ originating from calorimeter clusters or PF candidate particles clustered to jets above a p_{T} threshold of 20 GeV/c or 10 GeV/c, respectively, are corrected with the corresponding jet energy correction factors. With the type II corrections, all energy contributions not clustered to any jet above these thresholds but going into the definition of $\vec{\not{E}}_{\mathrm{T}}$ can optionally be corrected for the detector response. These type II correction factors can be obtained from balancing $\mathrm{Z} \to \mathrm{e}^{+}\mathrm{e}^{-}$ events where the expected $\not{E}_{\mathrm{T}}$ is zero. When using PF based $\vec{\not{E}}_{\mathrm{T}}$, the full type I and type II corrections are not applied. Only differences in the jet energy resolution between Monte Carlo simulation and collision data have to be propagated to the calculation of $\vec{\not{E}}_{\mathrm{T}}$.

Chapter 4

Unfolding

The study of top quark properties often requires a measurement of the top quark momentum. Since the top quark is not a stable particle and decays instantaneously, it cannot be measured directly with a particle detector. Only its decay products can be detected and the momentum of the top quark has to be inferred from the four-momenta of its decay products. In the production of top quark pairs, this leads to ambiguities in the assignment of experimentally observed objects either to the top quark or to the anti-top quark. In addition, decay products such as neutrinos cannot be captured in a detector device. Therefore, the reconstructed top quark momenta will not directly correspond to the true particle momenta.

This situation occurs in many experimental measurements, where the quantity of theoretical interest is not directly accessible. The distribution $f(x)$ of a kinematic quantity x is often disturbed by several effects. As in the example of top quark momenta, the variable of interest might not be accessible. Thus, instead of measuring the variable x only a correlated quantity y can be determined. But also directly measurable variables may be smeared due to finite detector resolutions. Other facts causing a distortion are a limited detector acceptance and selection efficiencies. Therefore, in all experiments there exists a transformation of a true quantity x and an accessible quantity y and instead of measuring the distribution $f(x)$ only measurements following a distribution $g(y)$ can be determined. Often, $g(y)$ will additionally be polluted by a background contamination $b(y)$ which contains no real signal but being indistinguishable from signal events.

Mathematically this relation between the distribution $f(x)$ and the measured distribution $g(y)$ can be expressed by an integral equation,

$$g(y) = \int A(y,x) f(x) dx + b(y). \tag{4.1}$$

This kind of equation is called Fredholm integral equation of first kind [174]. The function $A(y,x)$ is a transfer function, which takes into account finite detector resolutions, smearing effects, and efficiency losses. $A(y_0,x_0)$ gives the probability to measure y_0 if the true value was x_0. Although in the mathematical sense equation 4.1 only represents a folding integral if $A(y,x) = A(y-x)$, the process of inverting and solving equation 4.1 to determine $f(x)$ is called unfolding.

Unfolding is particularly useful, when there exists no concrete theoretical model or parametrisation for the distribution $f(x)$. If a specific model predicts a distribution $f_{\text{theory}}(x)$ and also the transfer function $A(y,x)$ is known, it is possible to determine a theoretical distribution $g_{\text{theory}}(y)$ following equation 4.1. $g_{\text{theory}}(y)$ can then be compared with the measured spectrum $g(y)$ directly.

The aim of the unfolding process is to find a good estimate for the distribution $f(x)$ in a model independent way having access to the measured distribution $g(y)$. The advantage of a full unfolding procedure is, that no specific theory prediction on the true distribution is needed. Knowing the measured spectrum $g(y)$ and the transfer function $A(y,x)$ only, the unfolding process allows to find the true distribution $f(x)$ which can than be compared with any theoretical model predicting a distribution $f_{\text{theory}}(x)$. Unfolding also allows a direct comparison of results obtained with different experimental setups. In the following sections several approaches to find appropriate and stable solutions of the unfolding problem including uncertainty estimations are discussed.

4.1 Linear Unfolding Methods

For simplification, and to be able to solve equation 4.1 numerically, the unfolding problem can be written as a discretised matrix equation:

$$\vec{y} = A\vec{x} + \vec{b}. \tag{4.2}$$

In this equation the distributions $f(x)$ and $g(y)$ have been transformed into binned histograms. These histograms are represented by the vectors $\vec{x}$ and $\vec{y}$, where the entries of these vectors correspond to the bin entries of the histograms. If $f(x)$ is represented by a histogram with n elements and $g(y)$ is divided into m bins, $\vec{x}$ and $\vec{y}$ are vectors of dimension n and m respectively. The background distribution $b(y)$ is also described by a vector $\vec{b}$ with m entries. The transfer function $A(y,x)$ is translated into an $m \times n$ matrix A. The element a_{ij} of matrix A can be interpreted as the probability of an event with a true value lying in bin i of the $f(x)$ distribution to be reconstructed with a value y lying in bin j of the measured spectrum $\vec{y}$.

The unfolding problem formulated in equation 4.2 is a linear inverse problem. A naive straight forward approach is to choose equal bin numbers for histograms $\vec{x}$ and $\vec{y}$, i. e. $n = m$. In this case, the solution of equation 4.2 is simply given by

$$\vec{x} = A^{-1}(\vec{y} - \vec{b}) \tag{4.3}$$

assuming $\det A \neq 0$. If the covariance matrix of the measured distribution $\vec{y}$ is given by V_y, the covariance matrix V_x of the true distribution $\vec{x}$ can be calculated by standard error propagation:

$$V_x = A^{-1} V_y (A^{-1})^{\mathrm{T}}. \tag{4.4}$$

These naive solution will show no bias induced by the covariance matrix since $\vec{x}$ does not depend on V_y. However, the solution vector $\vec{x}$ will often show large fluctuations which can arise from strong correlation between neighboured bins.

Several methods exist to solve the unfolding problem trying to avoid these huge fluctuations without introducing biases. A detailed description of unfolding methods can be found e. g. in [175–177].

A standard approach for several unfolding methods is the formulation of equation 4.2 as a least-square problem. The solution vector can be found by minimising a loss function

$$F_{\mathrm{LS}}(\vec{x}) = (A\vec{x} - \vec{y})^{\mathrm{T}}(A\vec{x} - \vec{y}) = \|A\vec{x} - \vec{y}\|^2. \tag{4.5}$$

Without loss of generality, one can assume $\vec{b} = 0$ since the transformation $\vec{y} \to \vec{y} - \vec{b}$ does not effect the structure of the unfolding problem. Aim of the following discussion is to find the vector $\vec{x}_{\mathrm{LS}}$ which minimises the least-square problem. This ansatz allows to solve the unfolding in various numerical ways as well as to choose different dimensions m and n for measured and true distributions. It is recommended to define a finer binning for the measured vector $\vec{y}$, i. e. $m > n$. Otherwise, the corrected spectrum $\vec{x}$ will have a larger number of degrees of freedom than the measured distribution $\vec{y}$.

4.1.1 Generalised Inverse Matrix

A standard method to solve equation 4.5 defines a generalised inverse matrix $A^{\#}$ which is equal to A^{-1} for quadratic transfer matrices but facilitates to solve the inversion problem also in the case of different numbers of bins n and m. The solution will then be given by $\vec{x}_{\mathrm{LS}} = A^{\#}\vec{y}$. In a first step, the covariance matrix V_y is introduced into equation 4.5:

$$F_{\mathrm{LS}}(\vec{x}) = (A\vec{x} - \vec{y})^{\mathrm{T}} V_y^{-1} (A\vec{x} - \vec{y}). \tag{4.6}$$

The solution vector $\vec{x}_{\mathrm{LS}}$ which minimises equation 4.6 is determined in a linear transformation of the measured distribution $\vec{y}$ by introducing the generalised inverse matrix $A^{\#}$. The minimum of equation 4.6 is then given by

$$\vec{x}_{\mathrm{LS}} = A^{\#}\vec{y} \quad \text{with} \quad A^{\#} := \left(A^{\mathrm{T}} V_y^{-1} A\right)^{-1} A^{\mathrm{T}} V_y^{-1}. \tag{4.7}$$

For $n \times n$ matrices A the result is still identical to the naive solution obtained in equation 4.3 since in this case $A^{\#} = A^{-1}$. To study the properties of this solution in more detail, the $n \times n$ matrix $C := A^{\mathrm{T}} V_y^{-1} A$ and the vector $\vec{y}' := \left(A^{\mathrm{T}} V_y^{-1}\right) \vec{y}$ are introduced. The resulting vector $\vec{x}_{\mathrm{LS}}$ and its covariance matrix V_x are then given by:

$$\vec{x}_{\mathrm{LS}} = C^{-1}\vec{y}' \quad , \quad V_x = C^{-1}. \tag{4.8}$$

In a diagonalised form the matrix C can be written as $C = U\Lambda U^{\mathrm{T}}$, where Λ is a diagonal matrix of the eigenvalues λ_i of the matrix C with $\lambda_1 \geq ... \geq \lambda_n \geq 0$. The columns of the orthogonal matrix U (i. e. $U^{\mathrm{T}}U = I$) consist of the normalised corresponding eigenvectors $\vec{u}_i$ of the matrix C. The solution is then calculated via:

$$\vec{x}_{\mathrm{LS}} = C^{-1}\vec{y}' = U\Lambda^{-1}U^{\mathrm{T}}\vec{y}' = U\Lambda^{-1/2}\vec{c}, \tag{4.9}$$

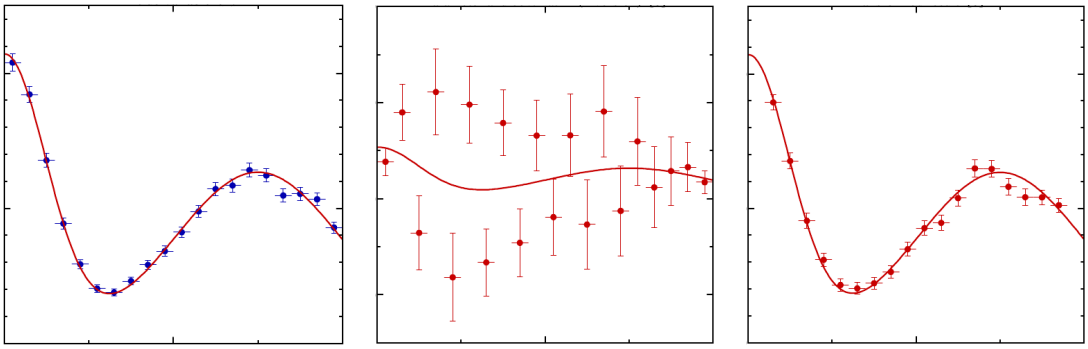

(a) (b) (c)

Figure 4.1: Example of a true distribution shown as curve and simulated data points assuming perfect detector resolution and response (a). The simulated data points are smeared with a detector simulation and the unfolding is applied. In (b), the unfolding result obtained by simple matrix inversion is shown. The unfolded spectrum shows large fluctuations and is practically meaningless. In (c), the unfolding is regularised and the unfolded spectrum follows the true distribution correctly [178].

where in the last step a vector of coefficients $\vec{c} := \Lambda^{-1/2} U^{\mathrm{T}} \vec{y}'$ has been introduced. With this decomposition the solution vector $\vec{x}_{\mathrm{LS}}$ can also be written as

$$\vec{x}_{\mathrm{LS}} = \sum_{i=1}^{n} \frac{1}{\sqrt{\lambda_i}} c_i \vec{u}_i \tag{4.10}$$

with the coefficients $c_i = \frac{1}{\sqrt{\lambda_i}} \vec{y}' \cdot \vec{u}_i$. It can be shown that the statistical uncertainty of all coefficients c_i is equal to 1 [178].

Coefficients c_i belonging to small eigenvectors λ_i might be insignificant, which means that they should follow a normal distribution around 0 with variance 1. From the solution 4.10 it can be seen that a small eigenvalue belonging to an insignificant contribution can dominate the result. Usually, insignificant eigenvalues belong to highly fluctuating eigenmodes, so the result $\vec{x}_{\mathrm{LS}}$ will also be a highly fluctuating distribution.

This analysis of the spectral properties of the matrix C shows that the naive way of matrix inversion as well as the method with a generalised inverse matrix is often not sufficient to solve the unfolding problem. A first approach for a regularised unfolding would be to define a hard cut-off for insignificant eigenvalues, i. e. to define a parameter k with $k < n$ and set all coefficients $c_i = 0$ for $i > k$ in the determination of the solution vector in equation 4.10. A more detailed description of regularisation methods will be discussed in section 4.2. An example distribution unfolded with and without regularisation is shown in figure 4.1.

4.1.2 Singular Value Decomposition

An alternative approach to solve the minimisation of equation 4.5 utilises the singular value decomposition (SVD) of matrix A [179]. The SVD method is similar to

the decomposition of $n \times n$ matrices into eigenvectors, but it can also be applied to decompose non-quadratic matrices. Every real $m \times n$ matrix with $m \geq n$ can be written as a product of three matrices

$$A = U\Sigma V^{\mathrm{T}} = \sum_{i=1}^{n} \vec{u}_i \sigma_i \vec{v}_i^{\mathrm{T}} \tag{4.11}$$

with the $m \times n$ matrix U and the $n \times n$ matrix V which fulfil $U^{\mathrm{T}}U = V^{\mathrm{T}}V = I$. Σ is a diagonal matrix consisting of the so called singular values σ_i which are all greater or equal 0 and conventionally ordered by $\sigma_1 \geq ... \geq \sigma_n \geq 0$. For $m \times n$ matrices, the singular values play the same role as eigenvalues for quadratic matrices. Of course, for the more general SVD two sets of orthonormal vectors (given by the columns of U and V) are defined instead of one set of orthonormal eigenvectors.

With the formalism of the SVD the generalised inverse matrix $A^{\#}$ can be written as

$$A^{\#} = V\Sigma^{-1}U^{\mathrm{T}}. \tag{4.12}$$

For $n \times n$ matrices A, $A^{\#}$ is identical to A^{-1}. It can be shown that also in case of $n \times m$ matrices A the solution of the unfolding problem $A\vec{x} = \vec{y}$ is given by

$$\vec{x}_{\mathrm{LS}} = A^{\#}\vec{y} = \sum_{i=1}^{n} \frac{\vec{u}_i^{\mathrm{T}}\vec{y}}{\sigma_i}\vec{v}_i. \tag{4.13}$$

The solution 4.13 obtained with the SVD is mathematically identical to the solution in equation 4.10. The singular values of matrix A are connected with the eigenvalues of the previously defined matrix C via $\sigma_i^2 = \lambda_i$. Also the covariance matrix of the result can be expressed in terms of singular values:

$$V_x = V\Sigma^{-2}V^{\mathrm{T}} = \sum_{i=1}^{n} \frac{1}{\sigma_i^2}\vec{v}_i\vec{v}_i^{\mathrm{T}}. \tag{4.14}$$

From this equation it is again obvious that also the uncertainties of the solution might be dominated by the smallest singular values. The elements of $\vec{v}_i\vec{v}_i^{\mathrm{T}}$ are usually of the same order of magnitude because of the normalization $\vec{v}_i^{\mathrm{T}}\vec{v}_i = 1$. Therefore, small singular values corresponding to small fluctuations can distend the resulting uncertainties.

4.2 Regularisation

As has been seen all methods to solve the unfolding problem lead to solutions which are affected by large influences of small eigenvalues or singular values. Although the solution $\vec{x}_{\mathrm{LS}}$ is always unbiased it can show large uncertainties and fluctuations. These fluctuations are caused only by the spectral properties of the response matrix A. Therefore, also a distribution measured with high precision and statistics can be rendered useless or even un-physical by a non-regularised unfolding method, if small statistical fluctuations of the measured distribution dominate the unfolding result.

The aim of regularisation is to find a method which stabilises the unfolding results without introducing too large biases. All regularisation methods make some a-priori assumption on the smoothness of the result. Typically, at least one additional parameter τ is introduced which controls the strength of the regularisation. The simplest way to define a regularisation is the cut-off of contributions from small eigenvalues which was already mentioned before. Here, the regularisation parameter τ is given by the cut-off value k. The a-priori assumption in this approach is that the solution will not show fluctuations with higher frequencies than the eigenmode of the k^{th} eigenvector. So the solution will always have a predefined smoothness.

More advanced regularisation methods introduce the smoothing conditions into the loss function 4.5. In the approach of Tikhonov [180] and Phillips [181] the modification of the function $F_{\text{LS}}(\vec{x})$ is:

$$F_\tau(\vec{x}) = \|A\vec{x} - \vec{y}\|^2 + \tau\|L\vec{x}\|^2. \tag{4.15}$$

The matrix L can be an arbitrary $n \times n$ matrix specifying the type of the regularisation, the parameter $\tau > 0$ defines the strength of the regularisation. In the Tikhonov-Phillips approach the minimum $\vec{x}_\tau$ of equation 4.15 respects not only the original unfolding conditions given by the first term of $F_\tau(\vec{x})$ but also the conditions on the smoothness of the solution which have to be incorporated by the matrix L.

The simplest type is $L = I$, in this case the regularisation will prefer a solution where the square norm $\|\vec{x}\|^2$ is minimal. Other types of regularisation correspond to minimising the absolute of the average of first or second derivatives of $f(x)$ to guarantee smooth solutions. Translated into the formalism of discretised histograms, a matrix L accounting for the second derivatives of the unfolded spectrum $f(x)$ would look like

$$L = \begin{pmatrix} -2 & 1 & 0 & 0 & \cdots & 0 & 0 & 0 & 0 \\ 1 & -2 & 1 & 0 & \cdots & 0 & 0 & 0 & 0 \\ 0 & 1 & -2 & 1 & \cdots & 0 & 0 & 0 & 0 \\ \vdots & \vdots & \vdots & \vdots & \ddots & \vdots & \vdots & \vdots & \vdots \\ 0 & 0 & 0 & 0 & \cdots & 1 & -2 & 1 & 0 \\ 0 & 0 & 0 & 0 & \cdots & 0 & 1 & -2 & 1 \\ 0 & 0 & 0 & 0 & \cdots & 0 & 0 & 1 & -2 \end{pmatrix}, \tag{4.16}$$

since in the discretisation formalism the elements x_i'' of the vector $\vec{x}''$ which corresponds to the second derivative of $f(x)$ fulfil

$$x_i'' \propto x_{i-1} - 2x_i + x_{i+1}. \tag{4.17}$$

Given a matrix L for the regularisation minimising the second derivative will provide a solution with minimal average curvature.

To analyse the impact of the regularisation term in the function 4.15 in the following the simplest case $L = I$ is considered. Using the SVD ansatz, a straightforward calculation leads to the modified solution

$$\vec{x}_\tau = \sum_{i=1}^{n} f_i \frac{\vec{u}_i^{\,\text{T}}\vec{y}}{\sigma_i}\vec{v}_i. \tag{4.18}$$

The only difference between equation 4.13 and the solution obtained with a regularisation term is the appearance of the so called Tikhonov filter factors f_i. The filter factors depend on the singular values σ_i and the regularisation parameter τ:

$$f_i := \frac{\sigma_i^2}{\sigma_i^2 + \tau}. \tag{4.19}$$

Contributions from singular values with $\sigma_i^2 \gg \tau$ will lead to filter factors $f_i \approx 1$, whereas for singular values $\sigma_i^2 \ll \tau$ the filter factor f_i will be close to 0. Similar to the hard cut-off of small singular values or eigenvalues the Tikhonov-Phillips regularisation suppresses the contribution originating from small and insignificant singular values. In contrast to the hard cut-off method, the filter factors provide a smoother transition from more relevant to less relevant contributions to the solution. Also in case of using the generalised matrix inversion method presented in section 4.1.1, the standard solution of the unfolding process given in equation 4.10 is modified by the Tikhonov filter factors:

$$\vec{x}_\tau = \sum_{i=1}^{n} f_i \frac{1}{\sqrt{\lambda_i}} c_i \vec{u}_i, \tag{4.20}$$

where the filter factors can be written with the eigenvectors λ_i as

$$f_i := \frac{\lambda_i}{\lambda_i + \tau}. \tag{4.21}$$

4.2.1 Optimal Regularisation Parameter

The regularisation introduces at least one new parameter τ which determines the shape of the unfolded spectrum. If the parameter τ depends on the measured spectrum $\vec{y}$ the regularisation can even abolish the linear properties of the unfolding problem. From equation 4.15 one can estimate the impact of the size of τ to the final result. If τ is chosen too large, the minimisation of $F_\tau(\vec{x})$ will mainly be determined by the regularisation term without accounting for the term $\|A\vec{x} - \vec{y}\|^2$. Using a regularisation matrix L taking into account the second derivatives of the unfolded function will end up in a flat or linear spectrum for large τ without respecting the proper unfolding conditions given by the measured spectrum $\vec{y}$. On the other hand, for too small values of τ the regularisation term will not affect the minimisation of $F_\tau(\vec{x})$. The unfolding result will stay the same as without regularisation.

Besides physically motivated a-priori assumptions on the shape of the unfolded spectrum, there exist several methods to find an appropriate regularisation parameter which does neither introduce large biases nor fluctuations as for the unregularised unfolding.

The L-Curve

The L-curve [182] is a graphical illustration of the trade-off between the original χ^2 term $\|A\vec{x} - \vec{y}\|^2$ and the regularisation term in equation 4.15 of the Tikhonov regularisation. A scan with varying the regularisation parameter τ over many orders

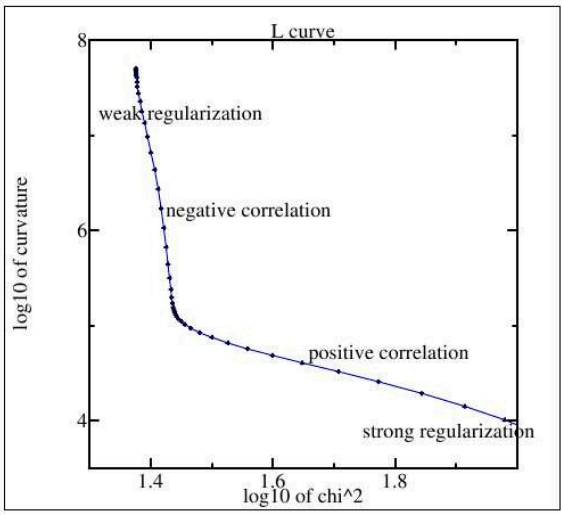

Figure 4.2: Illustration of the L-curve used to derive an optimal regularisation parameter τ. The norm of the χ^2 term $\|A\vec{x}_\tau - \vec{y}\|^2$ is plotted against the norm of the regularisation term $\|L\vec{x}_\tau\|^2$ for different values of τ. The kink position with the highest curvature indicates the transition between too weak and too strong regularisation [178].

of magnitude is performed and $F_\tau(\vec{x})$ is minimised for each value of τ. The resulting values of $\|A\vec{x}_\tau - \vec{y}\|^2$ are plotted versus the values of $\|L\vec{x}_\tau\|^2$ in a double logarithmic histogram.

The resulting curve typically exhibits an L-shape as illustrated in figure 4.2. The two tails of the plot correspond to the two regions where the minimisation is dominated by either the regularisation term or the χ^2 term. The in this sense optimal solution for τ is the kink position of the L-curve, where the unfolding process is driven by both terms in $F_\tau(\vec{x})$. The kink position is determined by the point of largest curvature of the L-curve. The assumption is, that the point of largest curvature corresponds directly to the transition region, where the influence of both terms of the minimised function is of equal size.

The main caveat of this method is that it is not guaranteed that the L-curve will have the explained structure. As explained in [183] the L-curve is always concave at the outer tails and there is no warranty for the existence of a point with positive curvature as it is needed to find a kink position. Therefore, the L-curve might not generally give an appropriate choice for the regularisation parameter.

Global Correlation Coefficients

This alternative method defines the optimal solution of the unfolding as the result with the smallest correlation between the data points of the unfolded distribution. If the regularisation strengths is chosen too small, the unfolded spectrum usually shows large fluctuations which correspond to large anti-correlations between neighboured points in the unfolded spectrum. On the other hand, a too strong regularisation will lead to more or less flat distributions which corresponds to strong positive correlations. Therefore, a single quantity is constructed which accounts for all these correlation effects. In a first step the global correlation coefficient ρ_i is defined for

each data in bin i:

$$\rho_i := \sqrt{1 - ((V_x)_{ii} \cdot (V_x^{-1})_{ii})^{-1}}. \tag{4.22}$$

The global correlation coefficient is a quantity with $0 \leq \rho_i \leq 1$. If all points of the result are completely uncorrelated, the covariance matrix V_x will be diagonal and $(V_x)_{ii} \cdot (V_x^{-1})_{ii} = 1$ for all i. In this case, all coefficients ρ_i will be 0.

A single quantity ρ_{tot} accounting for the total correlation between all data points can be the arithmetic or geometric mean of all correlation coefficients ρ_i. The total correlation coefficient is then defined as

$$\rho_{\text{tot}} := \left(\frac{1}{n} \sum_{i=1}^{n} \rho_i^2 \right)^{\frac{1}{2}}. \tag{4.23}$$

A scan with different regularisation parameters τ is performed and for each value of τ the total correlation ρ_{tot} is calculated for the unfolding result. The minimal total correlation gives the optimal choice for the value of τ. The method of minimising the global correlation has the advantage that the regularisation parameter is always well defined, whereas at the L-curve scan it is not ensured that it will converge in any case.

Effective Number of Degrees of Freedom

This method utilises the statistical properties of the coefficients c_i in the method of the generalised matrix inversion (see section 4.1.1). Coefficients belonging to insignificant eigenmodes should follow a normal distribution $N(0, 1)$, their squares should follow a $\chi^2(1)$ distribution. Coefficients with c_i^2 smaller than a previously defined confidence interval (for instance $c_i^2 < 0.9$ or $c_i^2 < 0.95$) are called insignificant. The number of remaining significant Fourier coefficients defines the effective number of degrees of freedom n_{eff}. The regularization parameter τ is then chosen such, that the sum of filter factors is equal to the effective number of degrees of freedom:

$$\sum_{i=1}^{n} f_i = \sum_{i=1}^{n} \frac{\lambda_i}{\lambda_i + \tau} = n_{\text{eff}}. \tag{4.24}$$

Since there is no unique method to choose an in some sense correct or optimal regularisation parameter the result of the unfolding has always be checked very carefully. Often the a-posteriori determination of τ as it is done by the L-curve scan or the minimisation of global correlations is supplemented by some a-priori information on the unfolded spectrum. If there are for instance assumption on the smoothness or other properties of $f(x)$ given, the regularisation parameter can be adopted accordingly.

4.3 Alternative Unfolding Methods

A completely different approach to solve the unfolding problem has been developed in [184]. Instead of assuming a linear connection between the true distribution $f(x)$

and the measured distribution $g(y)$ used in sections 4.1 and 4.2, an iterative approach based on Bayes theorem [185] is used. Main issue of this method is the more complicated determination of the covariance matrix and the description of correlations which has usually to be exploited in ensemble tests with pseudo experiments and cannot be determined analytically as in a linear inversion approach. Since only methods based on sections 4.1 and 4.2 are utilised in the following analysis the details of the Bayesian unfolding are not discussed here.

4.4 Implementations

Several implementations of unfolding techniques exist. In this analysis the programs RUN [186] and TUnfold [187] are utilised.

RUN

The package RUN (Regularised UNfolding for high-energy physics experiments) is an implementation of a regularised unfolding method based on the approach of generalised inverse matrices. It is originally written in Fortran but has also been translated into C++. The C++ version is called TRUEE (Time-dependent Regularised Unfolding for Economics and Engineerings) [188]. One feature of RUN is the usage of B-splines. B-splines define a set of orthonormal basis functions on a certain domain of definition. Instead of dividing the measured spectrum into a binned distribution it is approximated by a certain number of B-spline functions. Then, the B-spline coefficients are committed to the unfolding process. The result will therefore also be given as a set of B-spline function which can be translated into a binned distribution afterwards. The advantage of the usage of B-splines is that many smooth distributions can be approximated better with a small number of B-splines compared to a simple discretisation with the same number of bins. Only in case of distributions with sharp edges, as for instance the threshold region of the $m_{\mathrm{t\bar{t}}}$ spectrum, the modelling of the distributions with B-splines becomes more difficulty. For the regularisation the effective number of degrees of freedom has to be specified by the user. Besides the regularisation strength the user has also to specify the number of knots used for the B-spline approximation. Additionally, constraints on the unfolded distribution can be defined. The resulting function $f(x)$ can be forced to be positive over the full domain of definition or to go through some user defined points $(x_i, f(x_i))$.

The input to RUN are so called Ntuples, files which consist of a list of events. Three types of inputs are distinguished: the measured data, a Monte Carlo simulation for the signal and optionally a background contribution to the measured spectrum. For the simulation the values of measured and true variable have to be given as input to the program in the Ntuple. The true spectrum $f(x)$ used to define the response matrix A can also be specified analytically by the user. RUN is able to handle up to 32 different measured variables from which the true quantity $f(x)$ is reconstructed. Within the C++ version TRUEE there exists also an interface to ROOT [189] which allows to use ROOT trees as in- and output.

TUnfold

TUnfold is a C++ class which is part of the ROOT framework. It provides an unfolding routine using Tikhonov regularisation. Three different choices for the regularisation matrix L are supported: L can be proportional to the first or second derivatives of the unfolded spectrum or one can choose the simplest case $L = I$. For the determination of the regularisation parameter there exist several methods to perform an L-curve scan or to calculate the global correlation coefficients. The input to TUnfold are ROOT histograms for the measured distribution $\vec{y}$ and the smearing matrix A. Also the unfolded spectrum $\vec{x}$ is provided as ROOT histogram.

TUnfold uses the modified function $F_\tau(\vec{x})$ given in equation 4.15 as ansatz for the minimisation. To solve this equation a standard matrix inversion algorithm implemented in ROOT is used. It is possible to choose a χ^2 function with further modifications which consists of an additional term to constrain the normalisation of the result:

$$F_\tau(\vec{x}, \kappa) := F_\tau(\vec{x}) + \kappa \left(N_{\text{obs}} - \sum_{i=1}^{n} (A\vec{x})_i \right)^2 . \tag{4.25}$$

Herein, N_{obs} is the number of observed data events, $N_{\text{obs}} = \sum_{i=1}^{n} y_i$. The additional term forces the number of estimated events to the number of observed events. The parameter κ is a Lagrangian multiplier. The minimisation is performed with respect to $\vec{x}$ and κ simultaneously. The constraint on the normalisation is important for a reconstructed distribution $\vec{y}$ with non-Gaussian uncertainties. This is for instance the case for small numbers of observed events in some bins of $\vec{y}$ when the statistically uncertainties are Poisson-like and cannot be approximated with Gaussian uncertainties. In the formulation of equation 4.15, the unfolding is a χ^2 minimisation which gives unbiased results only, if the uncertainties are Gaussian. This problem of preserving the area can occur in any χ^2 fit to histograms [190].

Chapter 5

Measurement of the Charge Asymmetry in $t\bar{t}$ Production

For the measurement of the charge asymmetry in top quark pair production, several analysis steps are required to get access to the sensitive variable $|\eta_t| - |\eta_{\bar{t}}|$. First, a data sample enriched in $t\bar{t}$ events is required. For the selected candidate events, a full reconstruction of the four-momenta of top and antitop quarks is performed to have an estimation of the top quark pseudorapidities. Since the top quark four-momenta are not directly accessible in data, the reconstruction makes use of the expected event topology of top quark pair events in the lepton+jets decay channel to combine observable decay products and add their momenta. However, the $|\eta_t| - |\eta_{\bar{t}}|$ distribution reconstructed in this way for selected data events cannot be directly used to measure the charge asymmetry since this distribution is affected by several effects which can change the shape of the measured spectrum. For instance, the distribution is still contaminated with background events which do not include top quarks but imitate the signature of top quark pair production. Furthermore, since the top quark four-momenta are reconstructed from adding the four-momenta of their decay products and the assignment of decay products to either the top or antitop quark contains ambiguities, the reconstructed top quark four-momenta are smeared with respect to the true momenta. Therefore, the reconstructed $|\eta_t| - |\eta_{\bar{t}}|$ distribution does not directly correspond to the true distribution. Also the specific selection of events can change the shape of the reconstructed spectrum since the selection efficiency is not necessarily flat in $|\eta_t| - |\eta_{\bar{t}}|$. For all these effects which disturb the true $|\eta_t| - |\eta_{\bar{t}}|$ distribution, a regularised unfolding method is applied which has been discussed in chapter 4.

5.1 Selection of Events

The selection of top quark pair candidate events exploits the expected event signature of the $t\bar{t}$ process in the lepton+jets decay channel. The LO Feynman diagram of the lepton+jets decay mode as depicted in figure 3.2 contains four quarks, one charged lepton and one neutrino in the final state of the hard process. Therefore, the expected event signature of these events contains four jets originating from the

hadronisation of the four quarks and one charged lepton. In the presented analysis, only electrons and muons are considered as charged leptons in the selection since they produce a cleaner signature in the detector compared to the nearly instantaneously decaying tau. First of all, an accurate description of all objects going to be selected is required according to the expected kinematic behaviour of jets and leptons as decay products of the $t\bar{t}$ process. Quality criteria are added to the definition of primary selected electrons, muons, and jets as they are reconstructed according to the algorithms given in section 3.3. For the final selection, specific multiplicities of the previously defined objects are required to be contained in the selected events. The event selection utilised in the analysis of the $t\bar{t}$ charge asymmetry is adopted from the measurement of the $t\bar{t}$ cross section in the lepton+jets channel with the CMS experiment [23, 132].

Electrons

All selected electrons are based on the reconstructed candidates which are found with the GSF algorithm. The collection of reconstructed electrons contains still a large amount of electron candidates which are not produced in a real W or Z boson decay in the hard interaction but, for instance, in subsequent decays of hadrons in the showering or in conversions of photons into electron-positron pairs. For a further reduction of background events containing electrons not produced in a W boson decay in the hard scattering process as it is the case for $t\bar{t}$ production, cuts on several variables describing the quality of the electron candidate are applied. In a first step, cuts on a set of variables are employed which describe the shower shape of the ECAL supercluster of the electron candidate. The variable $\sigma_{i\eta i\eta}$ measures the average spread of the ECAL supercluster in η direction. Selected electrons have to pass $\sigma_{i\eta i\eta} < 0.01$ in the barrel and $\sigma_{i\eta i\eta} < 0.03$ in the endcap region, respectively. The ratio of energy deposited in the hadron calorimeters to the energy measured in the ECAL, $E_{\mathrm{HCAL}}/E_{\mathrm{ECAL}}$, has to be smaller than 2.5%. Further cuts are applied on the distance between the track and the supercluster (SC) position in η and ϕ. For electrons in the barrel region, cuts of $|\eta_{\mathrm{SC}} - \eta_{\mathrm{track}}| < 0.004$ and $|\phi_{\mathrm{SC}} - \phi_{\mathrm{track}}| < 0.03$ are applied. Selected electron candidates in the endcaps must fulfil $|\eta_{\mathrm{SC}} - \eta_{\mathrm{track}}| < 0.005$ and $|\phi_{\mathrm{SC}} - \phi_{\mathrm{track}}| < 0.02$. The combined cuts on $\sigma_{i\eta i\eta}$, $E_{\mathrm{HCAL}}/E_{\mathrm{ECAL}}$, $|\eta_{\mathrm{SC}} - \eta_{\mathrm{track}}|$ and $|\phi_{\mathrm{SC}} - \phi_{\mathrm{track}}|$ are referred to as simple electron identification requirements.

On average, the charged lepton produced in the decay of a top quark has a larger momentum than leptons in background processes, especially, if these leptons are not originating from a decay of a massive W or Z boson. For electron candidates, a cut of $E_{\mathrm{T}} > 30$ GeV is therefore applied. The electron is also required to have a pseudorapidity of $|\eta| < 2.5$ in order to fall into the acceptance region of the silicon tracker. Electrons falling into the transition region between barrel and endcap with a pseudorapidity of the supercluster of $1.4442 < |\eta_{\mathrm{SC}}| < 1.566$ are excluded from the list of electron candidates. To ensure that selected electrons originate from a proton-proton interaction the absolute value of the impact parameter of the electron track with respect to the beam spot, d_{bs}, must not exceed 0.02 cm. Electrons can also occur in pile-up events in secondary proton-proton interactions. To reduce the number of these electrons the distance in the z direction between the primary

vertex of an event and the electron track in the point of closest approach has to be smaller than 1 cm. A further improvement in the purity of electrons stemming from a hard interaction is obtained from exploiting the isolation of electron candidates. Electrons which are produced in QCD multi-jet events as decay products of unstable hadrons usually appear in the vicinity of a reconstructed jet. For the definition of the isolation of an electron candidate, a cone in the η–ϕ plane is drawn around the vector of the electron's flight direction. The isolation is defined as the sum of all energy deposits not assigned to the electron itself measured in this cone. The individual isolation variables are defined for the tracker (I_{Trk}), the ECAL (I_{ECAL}), and the HCAL (I_{HCAL}). The tracker isolation is defined as the summed transverse momenta of all tracks inside an isolation cone with radius $R = 0.3$. The GSF track of the electron itself and further tracks very close to the electron within a cone radius of $R = 0.015$ are not taken into account for the definition of the tracker isolation. The definition of the isolation in the ECAL and the HCAL also uses cone radii of $R = 0.3$ for summing up energy deposits. Since electrons produce signals in the ECAL, energy contributions in an inner veto cone with a radius of $R = 0.045$ in the barrel and $R = 0.07$ in the endcap, respectively, are not taken into account in the definition of I_{ECAL}. The different radii used to define the inner veto cones respect the granularity of the respective parts of the calorimeter. A combined variable accounting for the isolation in tracker, ECAL, and HCAL is the relative isolation $I^{\mathrm{e}}_{\mathrm{rel}}$. It is defined via

$$I^{\mathrm{e}}_{\mathrm{rel}} := \frac{I_{\mathrm{Trk}} + I_{\mathrm{ECAL}} + I_{\mathrm{HCAL}}}{E_{\mathrm{T}}}, \tag{5.1}$$

where E_{T} is the transverse energy of the electron candidate. For the selection of electrons, a cut on $I^{\mathrm{e}}_{\mathrm{rel}} < 0.01$ is applied.

Muons

Muon candidates which are considered in this analysis have to be reconstructed as global muons from a combined track fit to hits in the inner tracker and the outer muon stations. The selected muon candidates have also to be identified as tracker muons. For a further improvement of the purity of selected muons, several quality cuts are adopted. The number of hits associated to the muon track in the inner tracker has to fulfil $N_{\mathrm{hits}} \geq 11$. In addition, the muon track is required to be reconstructed from hits in at least two muon stations. Muons from the decay of a W boson are expected to carry a high momentum, therefore, a cut on the minimal transverse momentum of the muon candidates of $p_{\mathrm{T}} > 20$ GeV/c is applied. The selected muons have to fall into the central region of the detector with a pseudo-rapidity of $|\eta| < 2.1$. In the same way as it is done for the selection of electrons, the absolute value of the impact parameter of the global muon track with respect to the beam spot has to be smaller than 0.02 cm. Also the distance between primary vertex and the muon track has to be smaller than 1 cm in z direction to reduce the amount of muons from secondary interactions. The main background events containing muons which are not produced in the decay of a W or Z boson in the hard scattering process are muons from leptonic hadron decays. To reduce the amount of such muons in the selection, a cut on the relative isolation of the muon

is used. The definition of the relative isolation slightly differs from the definition for electrons given in equation 5.1. The cone radii for the definition of isolations in tracker, ECAL, and HCAL are also $R = 0.3$, but the definitions of veto cones for the removal of the muon energy itself are different from the definitions used in case of electrons. For the calculation of tracker isolation I_{Trk}, only the momentum of the muon track is excluded. The small energy deposits of the muon in the calorimeters is removed from I_{ECAL} and I_{HCAL} by excluding all energy deposits falling into a veto cone around the muon track with a radius of $R = 0.07$. The relative isolation for muons is then defined as

$$I^{\mu}_{\mathrm{rel}} := \frac{I_{\mathrm{Trk}} + I_{\mathrm{ECAL}} + I_{\mathrm{HCAL}}}{p_{\mathrm{T}}}, \tag{5.2}$$

where the normalisation is performed with respect to the transverse momentum of the muon. All selected muons are required to have $I^{\mu}_{\mathrm{rel}} < 0.05$. In addition, a cut on the minimal distance in the η–ϕ plane between the muon candidate and the closest neighboured jet of $\Delta R(\mu, \mathrm{jet}) > 0.3$ is adopted to remove a possible double-counting of objects, since the jets reconstructed from Particle Flow objects contain by construction also muon candidates. For the definition of this cut, only jets fulfilling the quality criteria given in the next paragraph are used.

Jets

Top quark pair events in the lepton+jets decay channel have at least four quarks in the final state of the hard interaction leading ideally to the production of jets. Two of these final state quarks are b quarks. Therefore, the associated jets can be identified with b-tagging algorithms. The definition of jets used for the selection of $t\bar{t}$ events is based on jets reconstructed with the anti-k_{T} algorithm with Particle Flow objects as input for the clustering. The radius parameter of the anti-k_{T} algorithm is set to 0.5. All selected jets have to fulfil the kinematic requirement of $p_{\mathrm{T}} > 30$ GeV/c where the jet momentum is corrected for Level 2 and Level 3. Only jets with $|\eta| < 2.4$ are considered for the selection since b-tagging is only applicable for jets in the acceptance region of the inner tracker. The clustered PF objects have to fulfil the following criteria:

- At least two PF constituents are required to be clustered to each selected jet.
- The fraction of energy from charged particles in the electromagnetic calorimeter has to be smaller than 99%.
- The fraction of energy from neutral hadrons in the jets has to be smaller than 99%.
- The fraction of energy from charge neutral particles in the ECAL must not exceed 99%.
- The energy fraction originating from charged hadrons clustered to the jet has to differ from zero.

- At least one charged hadron has to be clustered to each jet.

All energy fractions are calculated with respect to the uncorrected jet energy. Since the PF algorithm includes also a reconstruction of electrons and muons these particles are implicitly included into the jet clustering. In the identification of top quark pair events, the previously defined electron and muon candidates have to be separated from the jet collection to allow an assignment of the selected jets to quarks in the $\mathrm{t\bar{t}}$ final state. For this purpose, all jets having a distance of $\Delta R < 0.3$ to one of the previously defined electrons are removed from the list of selected jets. These jets are assumed to be identically to the already reconstructed electron candidates. For the removal of muons from the jet collection, all muons fulfilling the identification criteria listed above – excluding the requirement of $\Delta R(\mu, \mathrm{jet}) > 0.3$ – are taken into account. If a jet has a distance of less than 0.1 in ΔR to one of these muon candidates, it is also removed from the selected jet collection.

Selection Cuts

To trigger data events the used HLT streams have to be chosen such that ideally all produced $\mathrm{t\bar{t}}$ events decaying via one of the focussed decay channels are accepted. For this purpose, single lepton triggers are utilised. The instantaneous luminosity has been continuously increasing during the data taking period. Therefore, the available trigger menus has to be adopted by increasing trigger thresholds according to the instantaneous luminosity in order to keep the final HLT rate constant. This leads to different triggers which were used to select data for this analysis during different run ranges of data taking periods. Events in the electron+jets channel have to be accepted by one of seven different single electron triggers depending on the run range. All of these triggers demand at least one electron to be reconstructed on HLT level. The transverse energy E_T of accepted electron candidates have to be at least 10 GeV, 15 GeV, 17 GeV, or 22 GeV, depending on the actually used trigger. In addition to the E_T thresholds, several electron identification criteria such as isolation requirements are applied in the different electron triggers. Muon+jets events have to be accepted either by a HLT trigger which requires at least one muon which exceeds $p_\mathrm{T} > 9$ GeV/c or by a trigger with a cut of $p_\mathrm{T} > 15$ GeV/c depending on the respective run range. Most trigger selection requirements are not applied to the generated Monte Carlo samples since not all used trigger adjustments were simulated and the trigger selection efficiency is assumed to be flat for all lepton candidates with appropriately high E_T or p_T thresholds. Only for the muon+jets channel, the muon trigger with a threshold of $p_\mathrm{T} > 9$ GeV/c is simulated. All Monte Carlo events in this channel are required to fulfil this trigger requirement. For data taken with the CMS experiment, further cleaning cuts have to be applied to reduce specific detector noise effects which are also not simulated in the Monte Carlo generation. Such noise arises from the instrumental characteristic of the hybrid photodiodes and their read-out boxes in the HCAL barrel and endcap regions.

All following cuts are applied to both, CMS detector data as well as simulated events. Events used for the analysis are required to have at least one well reconstructed primary vertex. All primary vertices are ordered according to the summed

p_T of all tracks associated to the vertex. The number of degrees of freedom in the fit of the first primary vertex has to be larger than 4. This number is effectively given by the weighted sum of the number of tracks used in the fit of the primary vertex. Furthermore, the primary vertex has to be located in the central region of the detector with $|z| < 24$ cm and a radial distance to the centre of the beam pipe of $\rho < 2$ cm.

For the selection of $t\bar{t}$ candidate events in the electron+jets channel, the existence of exactly one electron as defined above is required. To remove a possible overlap with the muon+jets decay channel and also events from $t\bar{t}$ events with two leptonically decaying top quarks, specific cuts on secondary leptons are applied.

In the electron+jets channel, all events containing at least one muon candidate with loosened identification criteria are rejected. The muon definition used for this purpose requires the muon to be identified as a global muon with $p_T > 10$ GeV/c and $|\eta| < 2.5$. Also the isolation requirement is relaxed to $I^e_{rel} < 0.2$. In the electron+jets channel, also events with a secondary electron are rejected to suppress the background stemming from Z boson production. This secondary electron has to fulfil loosened identification cuts. In the barrel region, these electron candidates have to fulfil $\sigma_{i\eta i\eta} < 0.01$, $|\eta_{SC} - \eta_{track}| < 0.007$, $|\phi_{SC} - \phi_{track}| < 0.8$, and $E_{HCAL}/E_{ECAL} < 0.15$; for the endcaps, cuts of $\sigma_{i\eta i\eta} < 0.03$, $|\eta_{SC} - \eta_{track}| < 0.01$, $|\phi_{SC} - \phi_{track}| < 0.7$, and $E_{HCAL}/E_{ECAL} < 0.07$ are used. Futhermore, secondary electrons are required to have $E_T > 20$ GeV, $|\eta| < 2.5$, and $I^e_{rel} < 1.0$. Also the barrel-encap transition region of $1.4442 < |\eta_{SC}| < 1.566$ is excluded for secondary electrons. If one of these secondary electrons forms an invariant mass between 76 GeV/c^2 and 106 GeV/c^2 together with the primary electron, the event is assumed to originate from Z boson production and is rejected.

In the electron+jets channel, further selection cuts are applied to reduce the background contribution from photon conversions into electron-positron pairs. Conversion electrons are usually not produced in the collision region but in the detector material. Therefore, the GSF track of the selected primary electron is required to have its first hit in the innermost layer of the pixel detector, otherwise, the event is not accepted. For a further reduction of conversion processes, a dedicated removal algorithm is applied. Since in photon conversions always an e^+e^- pair is produced, this algorithm searches for a second track in a cone with a radius of $R = 0.3$ around the GSF track of the primary electron with opposite curvature. In conversion events, this track is expected to run in parallel with the track of the primary electron in the r–z plane. Two parameters are introduced to classify secondary tracks. The difference of the inverse tangents of the angles θ of the both tracks, $\Delta \cot \theta$, and the distance d in the x–y plane at the point where the two tracks are running in parallel. Events are rejected, when a secondary track with $\Delta \cot \theta < 0.02$ and $d < 0.02$ is found.

In the muon+jets channel, events with electron candidates exceeding $E_T > 15$ GeV and with $|\eta| < 2.5$ are rejected to remove a potential overlap with the electron+jets selection as well as to reduce the amount of $t\bar{t}$ events decaying in the di-lepton mode. Finally, for both channels the existence of at least four jets is required fulfilling the identification criteria explained above.

Since the $t\bar{t}$ process in the lepton+jets channel includes four quarks in the final state, only events with at least four jets are selected. Although the application of a b-tagging algorithm can improve the purity of the selected $t\bar{t}$ candidate sample by a further reduction of background events, no cut on b-tagging variables is performed. For the modelling of smooth kinematic distributions which is required to perform an unfolding procedure as it is done for the $|\eta_t| - |\eta_{\bar{t}}|$ spectrum, a sufficiently high number of selected $t\bar{t}$ events is required. Since the available number of $t\bar{t}$ events in the early CMS data set collected during the year 2010 is not very large, no b-tagging cut is used in the presented analysis.

5.1.1 Event Yield and Background Estimation

Applying all selection cuts to the data set taken during 2010 which corresponds to an integrated luminosity of 36 pb^{-1}, 428 candidates in the electron+jets channel and 423 events in the muon+jets channel are selected. Although the selection cuts were developed to obtain a $t\bar{t}$ enriched data sample, the final data set is still contaminated with background events. The main backgrounds to top quark pair production in the lepton+jets decay mode were discussed in section 3.1.3. To estimate the $t\bar{t}$ signal contribution and therewith the number of background events, a likelihood fit of signal and background templates to the data has been performed [23, 132]. In this fit, the expected shapes of the various background processes and of the signal in specific kinematic variables are exploited. The main variable for the extraction of the $t\bar{t}$ signal is called $M3$. $M3$ is defined as the invariant mass formed by three jets which have the largest vectorial summed transverse momentum. This variable shows a peak around the top quark mass for $t\bar{t}$ events in the lepton+jets decay channel since the three jets used for the definition of $M3$ can often be associated to the three quarks originating from the hadronically decaying top quark. In most background processes, there is no high-mass particle expected to decay into three jets, so these background processes show a broader distribution in $M3$. Only single top quark production can show a similar peak in the $M3$ distribution, therefore, the single top quark event rate is fixed to its predicted theoretical value in the likelihood fit. Simultaneously to the template fit to $M3$, the distribution of the missing transverse energy, $\not{E}_T$, is fitted in a disjunct data sample to have a better constraint to background processes. Especially Z+jets and QCD events show on average smaller values in $\not{E}_T$ since they do not contain any neutrino in the hard interaction. The fit to $\not{E}_T$ is performed in a data sample which is selected with the same cuts as described before but requiring exactly three jets instead of four or more jets to be found. The results of the combined likelihood fit to $M3$ and $\not{E}_T$ are rate estimations for the individual processes in the data sample selected inclusively with three or more jets. The extrapolation of this fit to the event selection with at least four jets used for the measurement presented here is shown in table 5.1 for the electron and muon channel, respectively. The overall $t\bar{t}$ signal fraction is about 50% in the selected data set. From the Monte Carlo simulation, 88% of all these selected $t\bar{t}$ events are expected to decay in the electron+jets or muon+jets modes. Besides the numbers for signal and background events, also the statistical uncertainties and

process	electron channel	muon channel
$t\bar{t}$	184 ± 16	231 ± 20
single top	9 ± 3	12 ± 4
W+jets	130 ± 8	159 ± 9
Z+jets	20 ± 6	15 ± 5
QCD	64 ± 6	17 ± 5
total extrapolated fit result	407 ± 19	434 ± 22
observed data	428	423

Table 5.1: Measured event yield and observed numbers of events after the final selection requiring at least four jets in the CMS data set corresponding to an integrated luminosity of 36 pb^{-1}. Quoted uncertainties correspond to statistical uncertainties from a fit to the data performed in [23, 132].

their correlations are provided by the fit. The correlation matrix C_b for the individual background processes single top quark production, W+jets, Z+jets, QCD multi-jet production in the muon+jets channel, and QCD/γ+jets events in the electron+jets channel (in this ordering) is given by:

$$C_b = \begin{pmatrix} 1.00 & -0.06 & -0.01 & 0.01 & 0.01 \\ -0.06 & 1.00 & 0.01 & -0.03 & -0.02 \\ -0.01 & 0.01 & 1.00 & -0.19 & -0.24 \\ 0.01 & -0.03 & -0.19 & 1.00 & 0.12 \\ 0.01 & -0.02 & -0.24 & 0.12 & 1.00 \end{pmatrix}. \tag{5.3}$$

The elements of the covariance matrix V_b of the background processes are then derived via

$$(V_b)_{ij} = (C_b)_{ij} \cdot \sqrt{\sigma_i \sigma_j}, \tag{5.4}$$

where σ_i indicates the relative uncertainty on the background process i given in table 5.1.

Most of the templates used for the modelling of the distributions in the likelihood fit are taken from Monte Carlo simulations. Since the selected QCD background corresponds to an outer tail in the phase space of QCD multi-jet production, it is not expected that this phase space is modelled correctly by the Monte Carlo simulation. Although specific QCD Monte Carlo samples with an enriched amount of charged leptons have been generated (see section 3.1.3), the finally selected number of simulated QCD events is also not sufficient for a modelling of smooth kinematic distributions. Thus, the modelling of the QCD multi-jet background is performed with templates from data instead of Monte Carlo simulations. For the electron channel, also the photon+jets process is not taken from the Monte Carlo simulation for the same reason. The data-driven QCD background templates are taken from a sideband region which is expected to be enriched with QCD multi-jet events including leptonic decays. Therefore, data is selected with loosened lepton identification criteria. For the QCD modelling in the muon+jets channel, data events are selected which fulfil all mentioned selection criteria listed above but using muons with a relative isolation of $0.2 < I^{\mu}_{\text{rel}} < 0.5$. The upper cut on I^{μ}_{rel} is imposed to select

muon candidates in a similar phase space region as muons in the signal region. All events with well-isolated muons are rejected for this selection. In the selection of data events for the QCD and γ+jets model in the electron+jets channel, selected electrons are required to fail at least two of three identification criteria. These criteria are the cuts on the relative isolation of $I^{\mathrm{e}}_{\mathrm{rel}} < 0.1$, on the impact parameter with respect to the beam spot $d_{\mathrm{bs}} < 0.02$ cm, and the combined cuts applied for the simple electron identification requirement. All electrons failing two of these three cuts are selected except electron candidates with a relative isolation of $I^{\mathrm{e}}_{\mathrm{rel}} > 0.5$. For the analysis of the $t\bar{t}$ charge asymmetry, the same data-driven QCD background models are used as for the measurement of the $t\bar{t}$ cross section.

A comparison of basic kinematic quantities of background and signal models to the data after the full event selection is presented in figures 5.1, 5.2, and 5.3 for the electron+jets and the muon+jets channels, respectively. The normalisation of the different simulated templates is done according to the event yield given in table 5.1. All distributions show a quite good agreement in the comparison between simulation and data.

5.2 Full Reconstruction of the $t\bar{t}$ Final State

The information of the top quark four-momenta, which are required to measure the $|\eta_{\mathrm{t}}| - |\eta_{\bar{\mathrm{t}}}|$ distribution and therewith the charge asymmetry, is not directly accessible in measured data events and has to be estimated from observed objects. The event topology of a top quark pair event in the lepton+jets decay channel consists in the ideal case of four jets stemming from the two b-quarks and the two light quarks from one W boson decay, one charged lepton, and missing transverse energy from the undetected neutrino. With an assignment of the detected objects to the individual decay products of the $t\bar{t}$ production the momenta of the decay products of the top quarks and consecutively the top quark four-momenta can be approximated. A priori it is obvious, that the reconstruction procedure will not be able to reproduce exactly the true four-momenta. In the MadGraph Monte Carlo simulation of $t\bar{t}$ events in the electron+jets and muon+jets decay channels, only in about 50% of all selected events a matching between generated quarks and leptons to reconstructed jets and measured charged electrons or muons can be found. Events are defined as matched, if the distance in the η–ϕ plane between generated and reconstructed momenta is smaller than $\Delta R = 0.5$ for all final state objects of the $t\bar{t}$ decay. Also ambiguities in assignments of jets to quarks and in the reconstruction of the neutrino momentum will disturb the reconstruction. Therefore, a list of reconstruction hypotheses is created and a selection criterion is constructed to select one reconstruction hypothesis, which will not give the exact top quark four-momenta but a preferably good approximation of these vectors.

In the following discussion, the reconstructed particles are denoted as follows: the semi-leptonically decaying top quark is labelled as $\mathrm{t}_{\mathrm{lep}}$, the hadronically decaying top quark is called $\mathrm{t}_{\mathrm{had}}$. The W boson and b-quark from the semi-leptonic top quark decay are denoted as $\mathrm{W}_{\mathrm{lep}}$ and $\mathrm{b}_{\mathrm{lep}}$, the decay products of the hadronically decaying top quark are abbreviated with $\mathrm{W}_{\mathrm{had}}$ and $\mathrm{b}_{\mathrm{had}}$, respectively. For simplicity reasons,

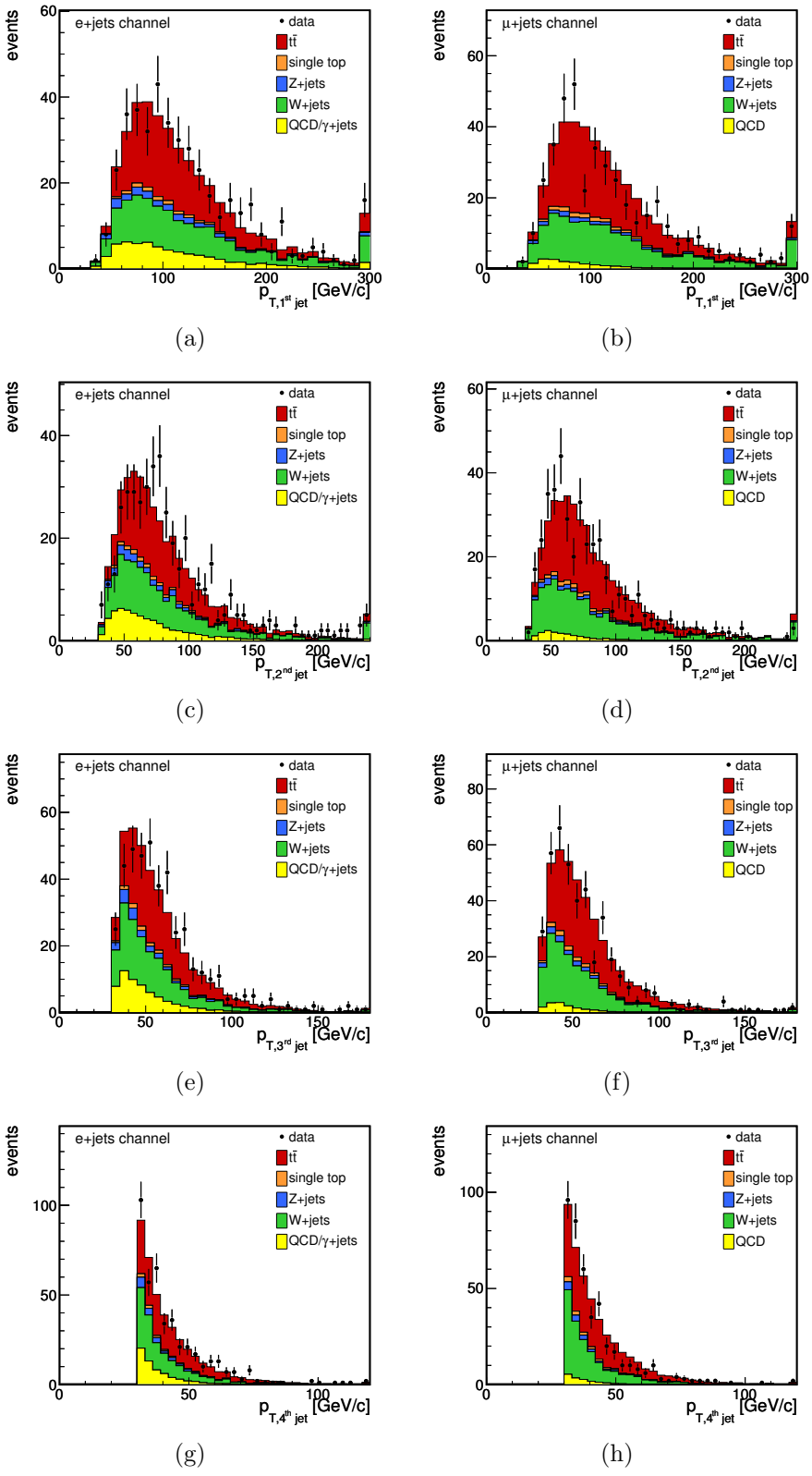

Figure 5.1: Data to Monte Carlo comparison of the transverse momentum p_{T} of the four leading jets in the electron+jets channel (a,c,e,g) and in the muon+jets channel (b,d,f,h). Jets are ordered by their p_{T} from higher to lower values. Only the QCD multi-jet production is modelled from data. All templates are normalised to the fit result of the cross section measurement [23].

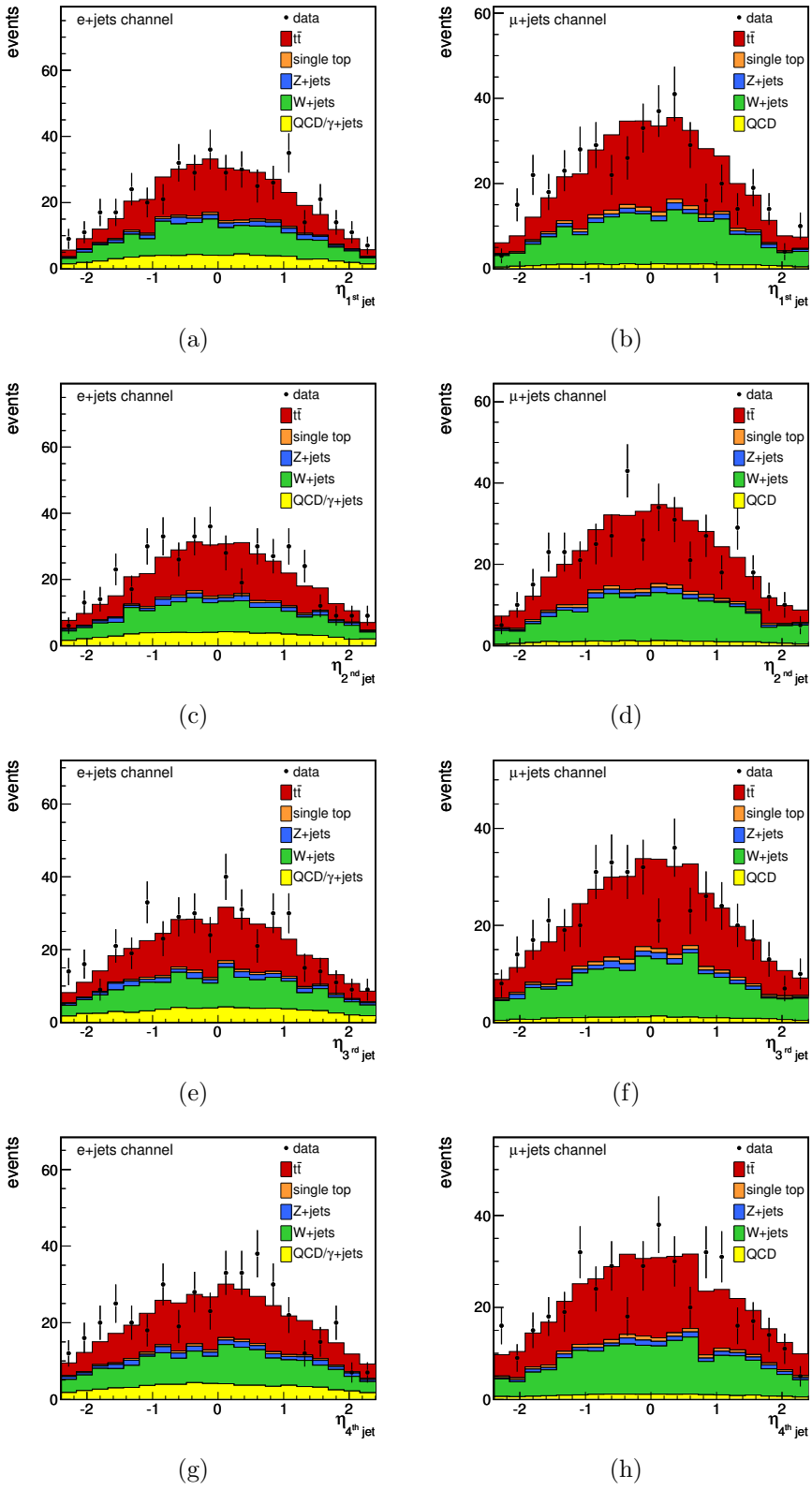

Figure 5.2: Data to Monte Carlo comparison of the pseudorapidity of the four leading jets in the electron+jets channel (a,c,e,g) and in the muon+jets channel (b,d,f,h). Jets are ordered by their p_{T} from higher to lower values. Only the QCD multi-jet production is modelled from data. All templates are normalised to the fit result of the cross section measurement [23].

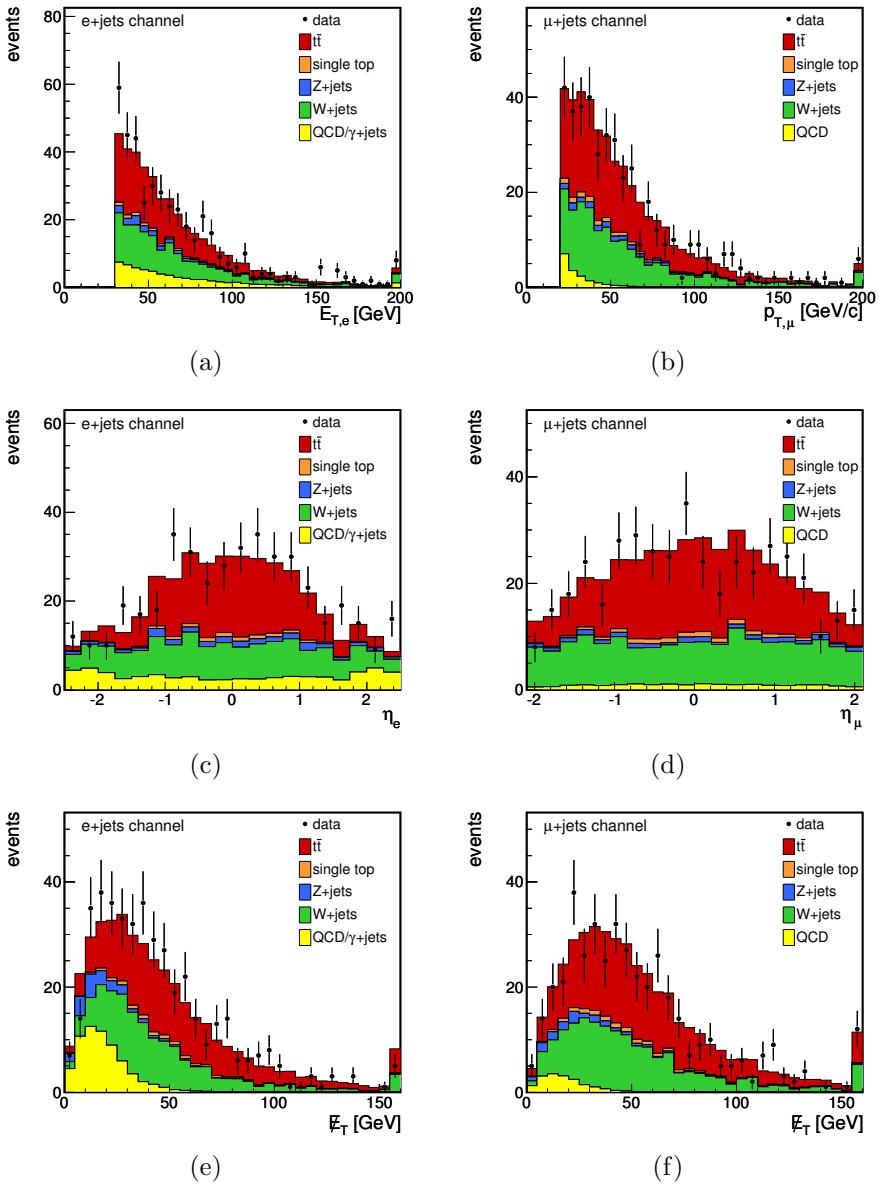

Figure 5.3: Data to Monte Carlo comparison of the transverse momentum and the pseudorapidity of the selected charged lepton, and the missing transverse energy in the electron+jets channel (a,c,e) and in the muon+jets channel (b,d,f). Only the QCD multi-jet production is modelled from data. All templates are normalised to the fit result of the cross section measurement [23].

natural units with $c = 1$ are assumed in the following calculations.

The only particle which can be assigned without any ambiguities is the charged lepton, its four-momentum p_{l} is the measured momentum of the solely well-identified electron or muon. This charged lepton is assumed to originate from the decay of the W boson from the semi-leptonically decaying top quark. The charge of the measured electron or muon also defines whether the $\mathrm{t_{lep}}$ is a top or an antitop quark since a positively charged lepton can only occur in the decay chain of a top quark, whereas a negatively charged lepton can only emerge from an antitop quark decay. The $\mathrm{t_{had}}$ is then assumed to carry the opposite charge of the $\mathrm{t_{lep}}$. The second decay product of the $\mathrm{W_{lep}}$ is a neutrino. For the reconstruction of the neutrino momentum, the missing transverse energy determined with Particle Flow objects is utilised. It is assumed, that the x and y components of the missing transverse energy vector $\vec{\not{E}}_{\mathrm{T}}$ correspond to the transverse momenta $p_{x,\nu}$ and $p_{y,\nu}$ of this neutrino, i. e.:

$$p_{x,\nu} = \vec{\not{E}}_{\mathrm{T},x} \quad \text{and} \quad p_{y,\nu} = \vec{\not{E}}_{\mathrm{T},y}. \tag{5.5}$$

The mass of the neutrino is set to zero in the reconstruction of the neutrino four-momentum. The only missing component of the neutrino four-vector is $p_{z,\nu}$. A solution for the third component of the neutrino momentum vector can be obtained under the assumption that the neutrino and the measured charged lepton originate from the decay of the same W boson. The sum of the two four-momenta should result in the four-momentum of the leptonically decaying W boson:

$$p_{\mathrm{W_{lep}}} = p_{\mathrm{l}} + p_{\nu}. \tag{5.6}$$

The W boson is assumed to be produced on-shell, i. e. the invariant mass of the $p_{\mathrm{W_{lep}}}$ vector is set to $m_{\mathrm{W}} = 80.4\ \mathrm{GeV}/c^2$ for the reconstruction. Under this assumption, a quadratic equation for the solution of $p_{z,\nu}$ can be derived from equation 5.6 [191]. The solution of this equation is given by:

$$p_{z,\nu}^{1,2} = \frac{\mu p_{z,\mathrm{l}}}{p_{\mathrm{T,l}}^2} \pm \sqrt{\frac{\mu^2 p_{z,\mathrm{l}}^2}{p_{\mathrm{T,l}}^4} - \frac{E_{\mathrm{l}}^2 p_{\mathrm{T},\nu}^2 - \mu^2}{p_{\mathrm{T,l}}^2}}, \tag{5.7}$$

where E_{l} is the energy of the charged lepton and $p_{\mathrm{T,l}}$ and $p_{\mathrm{T},\nu}$ denote the transverse momenta of the charged lepton and the neutrino, respectively. In equation 5.7, the parameter μ is defined as:

$$\mu := \frac{m_{\mathrm{W}}^2}{2} + p_{x,\mathrm{l}} \cdot p_{x,\nu} + p_{y,\mathrm{l}} \cdot p_{y,\nu}. \tag{5.8}$$

However, if two real solutions exist in one event, both solutions are taken into account in the list of reconstruction hypotheses. In general, the two solutions $p_{z,\nu}^{1,2}$ for the z component of the neutrino vector from equation 5.7 can be complex. If the solutions have imaginary parts, which is the case for 27% of all selected $t\bar{t}$ Monte Carlo events, only the real part, which is the same for both solutions in this case, is taken as solution for $p_{z,\nu}$. Taking the real part of the complex $p_{z,\nu}$ solution corresponds to the assumption that the $p_{x,\nu}$ and $p_{y,\nu}$ components are still described

by the measured $\vec{\not{E}}_{\mathrm{T}}$ vector, but the W boson is produced slightly off-shell since no real solution for an on-shell W boson can be found.

Having reconstructed the $\mathrm{W_{lep}}$ four-momentum, the list of $t\bar{t}$ reconstruction hypotheses is extended for all possible assignments of jets to the four quarks in the $t\bar{t}$ final state. If N jets are observed in an event, in each hypothesis one of these jets is assigned to the b-quark from the semi-leptonically decaying top quark, $\mathrm{b_{lep}}$. The $\mathrm{t_{lep}}$ is then reconstructed by adding the four-momenta of the $\mathrm{b_{lep}}$ and the previously reconstructed $\mathrm{W_{lep}}$. One of the remaining $N-1$ jets is assigned to the b-quark from the hadronically decaying top quark, $\mathrm{b_{had}}$, and one of the $N-2$ and $N-3$ jets, respectively, are assigned to the two quarks from the hadronically decaying W boson. The latter two jet momenta are added to reconstruct the $\mathrm{W_{had}}$ vector which is then added to the $\mathrm{b_{had}}$ momentum for the reconstruction of the four-momentum of $\mathrm{t_{had}}$. Since in each hypothesis every jet is associated to exactly one quark, the jet assignment gives for each event a list of hypotheses with $N(N-1)(N-2)(N-3)$ possible solutions for the reconstruction. Since the two hypotheses, where only the two jets assigned to the two light quarks from the hadronically decaying W boson are interchanged, are indistinguishable, the number of hypotheses is effectively reduced by a factor of two. For an event with N observed jets, the number of hypotheses is therefore $\frac{N(N-1)(N-2)(N-3)}{2}$ for the jet-to-quark assignment. The overall number of reconstruction hypothesis is multiplied by the number of solutions for the neutrino momentum which is either one or two. In events with exactly four observed jets, this leads to twelve solutions for the assignment of jets to quarks. Together with the solutions for the z momentum of the neutrino, the number of hypotheses can be either 12 or 24 in a four-jet event.

From the list of possible reconstructions, one hypothesis has to be selected which approximates best the top four-momenta in order to reconstruct the $|\eta_{\mathrm{t}}| - |\eta_{\bar{\mathrm{t}}}|$ distribution as close as possible to the true distribution. In $t\bar{t}$ events in the lepton+jets decay mode simulated with the MadGraph Monte Carlo generator, a best possible hypothesis can be defined. On these generated events, the quality of each hypothesis can be tested comparing the reconstructed and true momenta of top quarks and their decay products. For the definition of the best possible hypothesis, the distance in the η–ϕ plane ΔR between reconstructed and true momenta of the two top quarks and the two W bosons is utilised. The hypothesis with minimal

$$\Delta R(p^{\mathrm{rec}}_{\mathrm{W_{lep}}}, p^{\mathrm{true}}_{\mathrm{W_{lep}}}) + \Delta R(p^{\mathrm{rec}}_{\mathrm{W_{had}}}, p^{\mathrm{true}}_{\mathrm{W_{had}}}) + \Delta R(p^{\mathrm{rec}}_{\mathrm{t_{lep}}}, p^{\mathrm{true}}_{\mathrm{t_{lep}}}) + \Delta R(p^{\mathrm{rec}}_{\mathrm{t_{had}}}, p^{\mathrm{true}}_{\mathrm{t_{had}}}) \qquad (5.9)$$

is defined as best possible hypothesis. Here, $p^{\mathrm{rec}}_{\mathrm{W_{lep}}}$, $p^{\mathrm{rec}}_{\mathrm{W_{had}}}$, $p^{\mathrm{rec}}_{\mathrm{t_{lep}}}$, and $p^{\mathrm{rec}}_{\mathrm{t_{had}}}$ are the reconstructed four-momenta, $p^{\mathrm{true}}_{\mathrm{W_{lep}}}$, $p^{\mathrm{true}}_{\mathrm{W_{had}}}$, $p^{\mathrm{true}}_{\mathrm{t_{lep}}}$, and $p^{\mathrm{true}}_{\mathrm{t_{had}}}$ are the corresponding true momenta taken from generator information.

In each selected $t\bar{t}$ candidate event, one reconstruction hypothesis has to be chosen. For the choice of this hypothesis, only measurable quantities can be taken into account. Therefore, a quality criterion has to be introduced to select a reconstruction hypothesis on data. An optimal quality criterion should always select the best possible hypothesis or a hypothesis which provides a similar estimation of the reconstructed four-momenta.The performance of this quality criterion can be tested on Monte Carlo $t\bar{t}$ events where the true momenta of the generated particles

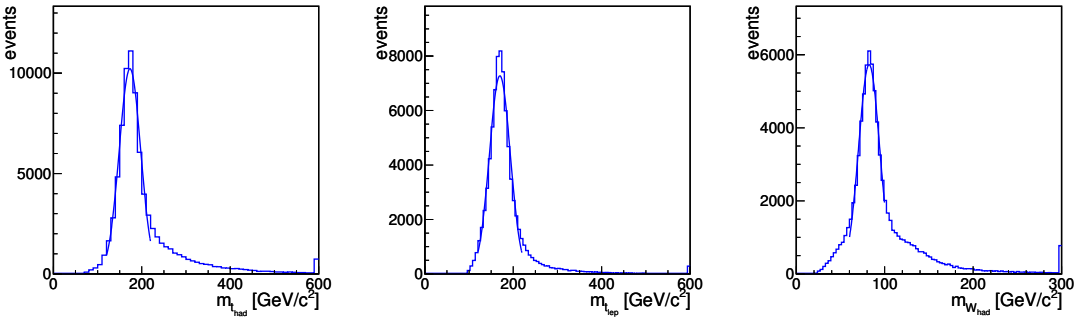

(a) (b) (c)

Figure 5.4: Gaussian fits to the kinematic quantities in the best possible hypothesis used to parameterise the χ^2 variable. The Gaussian distribution approximates position and widths of the central mass peaks quite well.

	mean [GeV/c^2]	σ [GeV/c^2]
$m_{\mathrm{t_{had}}}$	173.2	24.2
$m_{\mathrm{t_{lep}}}$	169.7	23.6
$m_{\mathrm{W_{had}}}$	82.4	11.9

Table 5.2: Mean and width values of the central Gaussian fitted to the mass distributions in the best possible hypothesis.

are known. Possible quality variables are studied on the best possible hypothesis in Monte Carlo events. Several variables, like the reconstructed masses of the top quarks, can be a measure for the quality of a chosen hypothesis. In a correctly reconstructed top quark pair event, the masses of the reconstructed top quarks and of the hadronically decaying W boson should be close to their known values. The mass of the leptonically decaying W boson cannot be used as a constraint to select a hypothesis, since it has been fixed to its theory value in order to reconstruct the neutrino four-momentum. From the behaviour of the reconstructed masses in the best possible hypothesis, a combined quantity is constructed comprising the quality criteria into one single value. For this purpose, a χ^2 variable is build which describes the deviation of any reconstruction hypothesis in data to the average expectation of the reconstructed masses in the best possible hypothesis on the Monte Carlo sample:

$$\chi^2 := \frac{(m^{\mathrm{b.p.}}_{\mathrm{t_{had}}} - m^{\mathrm{rec}}_{\mathrm{t_{had}}})^2}{\sigma^2_{m_{\mathrm{t_{had}}}}} + \frac{(m^{\mathrm{b.p.}}_{\mathrm{t_{lep}}} - m^{\mathrm{rec}}_{\mathrm{t_{lep}}})^2}{\sigma^2_{m_{\mathrm{t_{lep}}}}} + \frac{(m^{\mathrm{b.p.}}_{\mathrm{W_{had}}} - m^{\mathrm{rec}}_{\mathrm{W_{had}}})^2}{\sigma^2_{m_{\mathrm{W_{had}}}}}. \tag{5.10}$$

The parameters $m^{\mathrm{b.p.}}_{\mathrm{t_{had}}}$, $m^{\mathrm{b.p.}}_{\mathrm{t_{lep}}}$, $m^{\mathrm{b.p.}}_{\mathrm{W_{had}}}$, $\sigma_{m_{\mathrm{t_{had}}}}$, $\sigma_{m_{\mathrm{t_{lep}}}}$, and $\sigma_{m_{\mathrm{W_{had}}}}$ are the mean and the width values determined from fits to the respective mass distributions in the best possible hypothesis of all selected $t\bar{t}$ Monte Carlo events in the electron+jets and muon+jets decay channels. For these fits, Gaussian distributions are utilised, the mean and width of the Gaussians fitted to the central peaks are taken as values for the m and σ parameters in equation 5.10. The fitted distributions are shown in

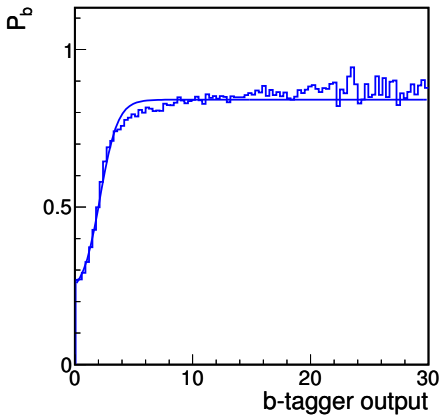

Figure 5.5: The probability P_b that a jet with a certain b-tagger output is assigned to a b-quark in the best possible hypothesis. P_b is parameterised with $P_\mathrm{b}(x) = \frac{p_1}{1+e^{p_2 \cdot x + p_3}} + p_4$.

figure 5.4 and the resulting fit values are summarised in table 5.2.

The purpose of this χ^2 variable is, that the reconstruction hypothesis with smallest χ^2 value comes closest to the best possible hypothesis. This can be tested by comparing the hypothesis with smallest χ^2 with the best possible hypothesis on the $t\bar{t}$ Monte Carlo sample. The selected hypothesis is equal to the best possible hypothesis for 24% of all accepted events in the electron+jets or muon+jets decay channels.

Further improvements on the selection of a hypothesis can be achieved by adding b-tagging information to the χ^2 variable since two of the four jets in each hypothesis are assigned to b-quarks. If there are b-tagged jets in an event, the jets carrying these b-tags belong to the b-quarks more likely than to the light quarks of the final state of the $t\bar{t}$ decay. To quantify this effect, the output of the track counting high efficiency b-tagger is used (see section 3.3.4). The probability, that a jet with a certain b-tagger discriminator value x is assigned to a b-quark and not to one of the two light quarks in the best possible hypothesis, is called $P_\mathrm{b}(x)$. $P_\mathrm{b}(x)$ is parametrised with a function of the form

$$P_\mathrm{b}(x) = \frac{p_1}{1 + e^{p_2 \cdot x + p_3}} + p_4, \tag{5.11}$$

which approximates the shape of $P_\mathrm{b}(x)$ reasonably. The parameters p_i are determined in a fit which is shown in figure 5.5. The fitted parameters are $p_1 = 0.621$, $p_2 = -1.35$, $p_3 = 2.91$, and $p_4 = 0.22$.

The final variable Ψ, which is taken to select a reconstruction hypothesis, is:

$$\Psi := \chi^2 (1 - P_\mathrm{b}(x_{\mathrm{b_{had}}}))(1 - P_\mathrm{b}(x_{\mathrm{b_{lep}}}))P_\mathrm{b}(x_{\mathrm{q_1}})P_\mathrm{b}(x_{\mathrm{q_2}}), \tag{5.12}$$

where $x_{\mathrm{b_{had}}}$ and $x_{\mathrm{b_{lep}}}$ are the b-tagger discriminator values of the jets assigned to the b-quarks from the leptonically and the hadronically decaying top quarks. $x_{\mathrm{q_1}}$ and $x_{\mathrm{q_2}}$ are the b-tagger outputs of the two jets assigned to the two quarks originating from the hadronically decaying W boson. The variable Ψ is calculated for each reconstruction hypothesis. Finally, the hypothesis with smallest Ψ is chosen. In 33%

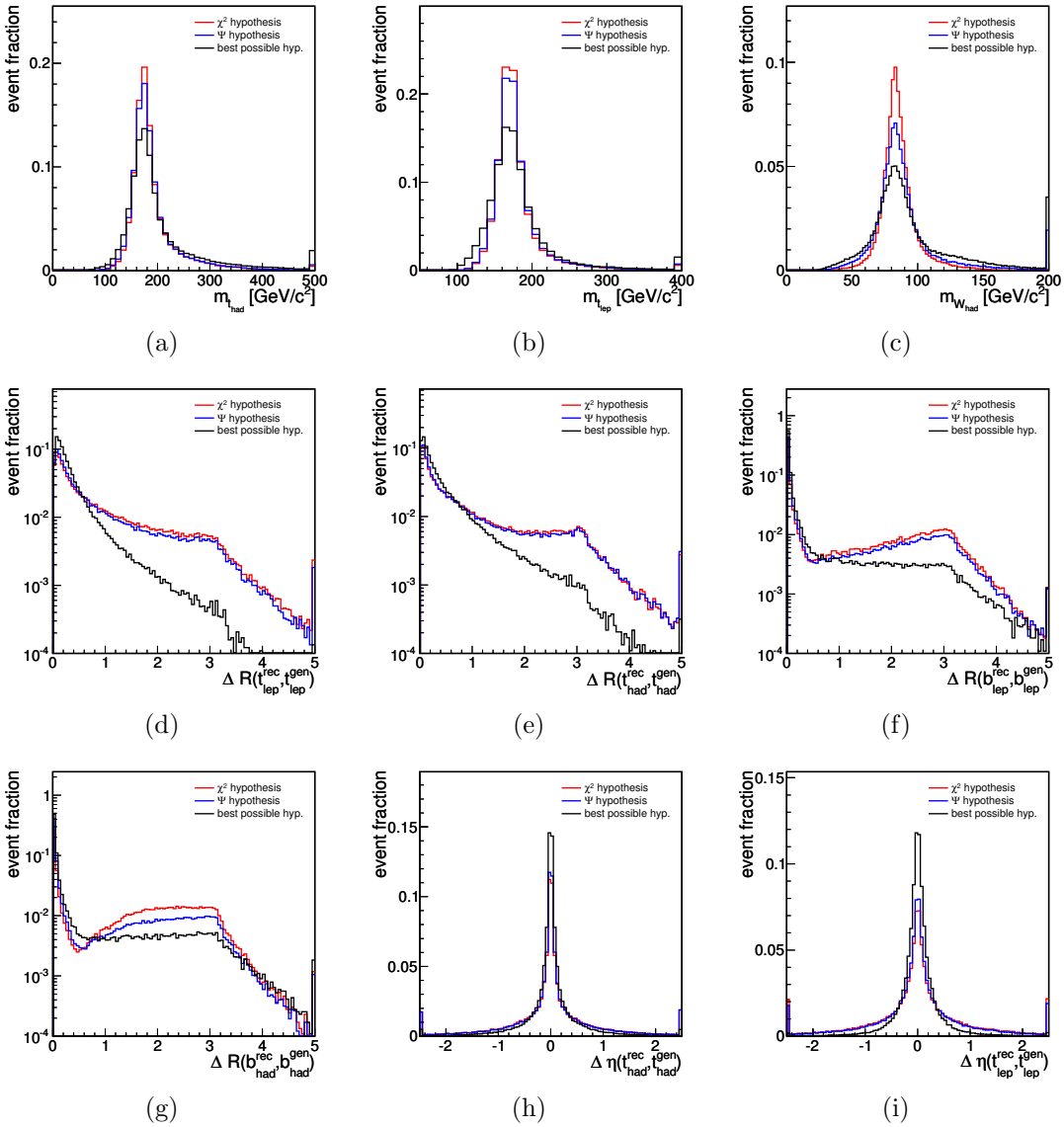

Figure 5.6: Comparison of kinematic quantities in selected $t\bar{t}$ events in the lepton+jets decay channel for the best possible and the selected hypothesis using the MadGraph $t\bar{t}$ Monte Carlo sample. The selected hypothesis chosen with the smallest Ψ is always closer to the best possible hypothesis than the hypothesis with the smallest χ^2.

of all $t\bar{t}$ Monte Carlo events, the selected hypothesis with smallest Ψ is identical to the best possible hypothesis. This indicates a clear improvement with respect to the hypothesis selection using only the χ^2 variable.

The comparison of kinematic variables in the best possible hypothesis with the chosen hypothesis is shown for lepton+jets events from the standard MadGraph top quark pair Monte Carlo sample in figure 5.6. The distributions for the selected hypothesis using the χ^2 variable only and for the hypothesis selected with the variable Ψ including b-tagging information are compared to the best possible hypothesis. The variables used to constrain the selected hypothesis in χ^2 show sharper mass

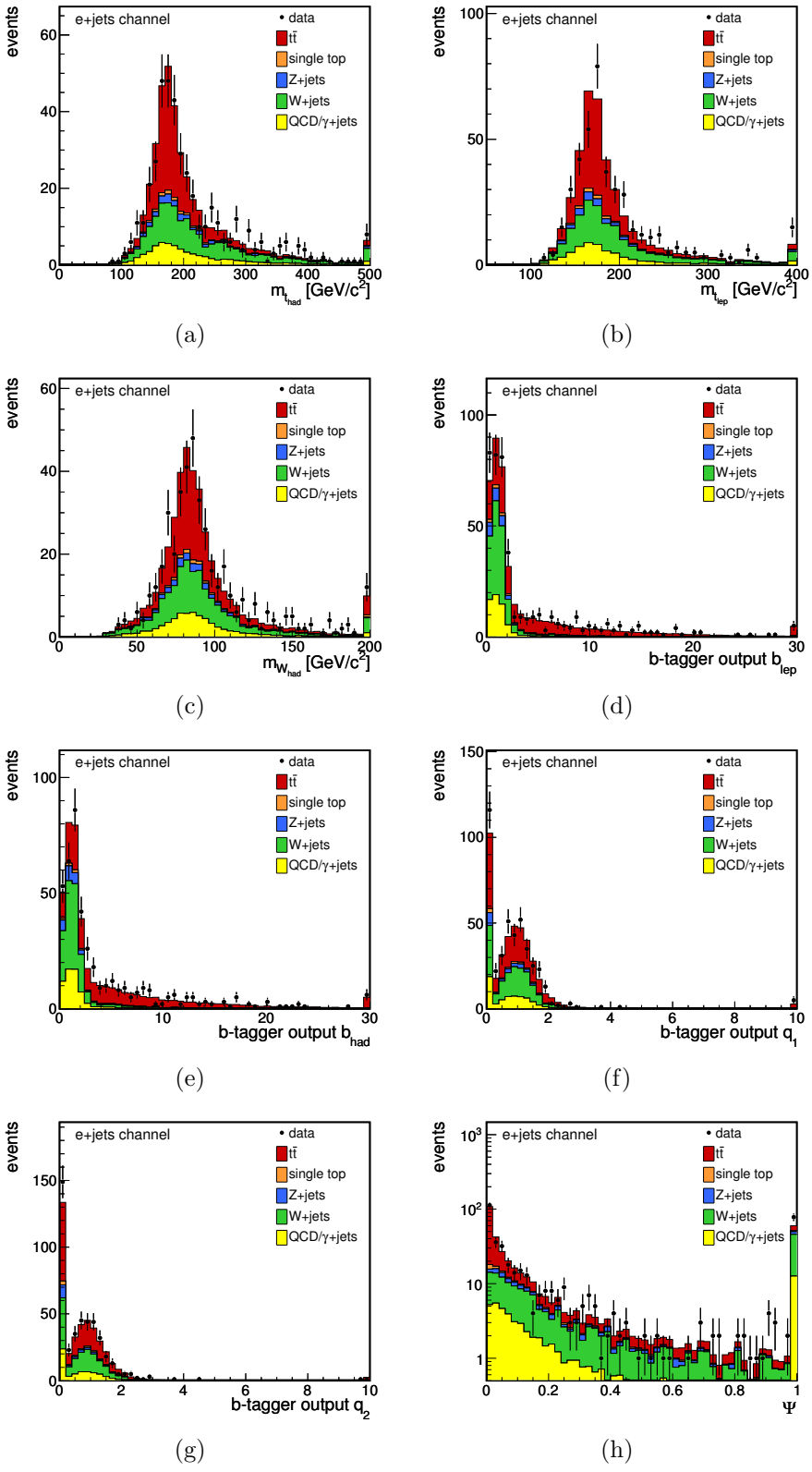

Figure 5.7: Data to Monte Carlo comparison of kinematic quantities (a-c) and the b-tagger outputs (d-g) of jets assigned to b_{had}, b_{lep}, or one of the two light quarks q_1 and q_2 in the selected $t\bar{t}$ reconstruction hypothesis in the electron+jets channel. In histogram (h) the distribution of the Ψ variable in the chosen hypothesis is shown. The Monte Carlo prediction is normalised to the fit result of the $t\bar{t}$ cross section measurement [23].

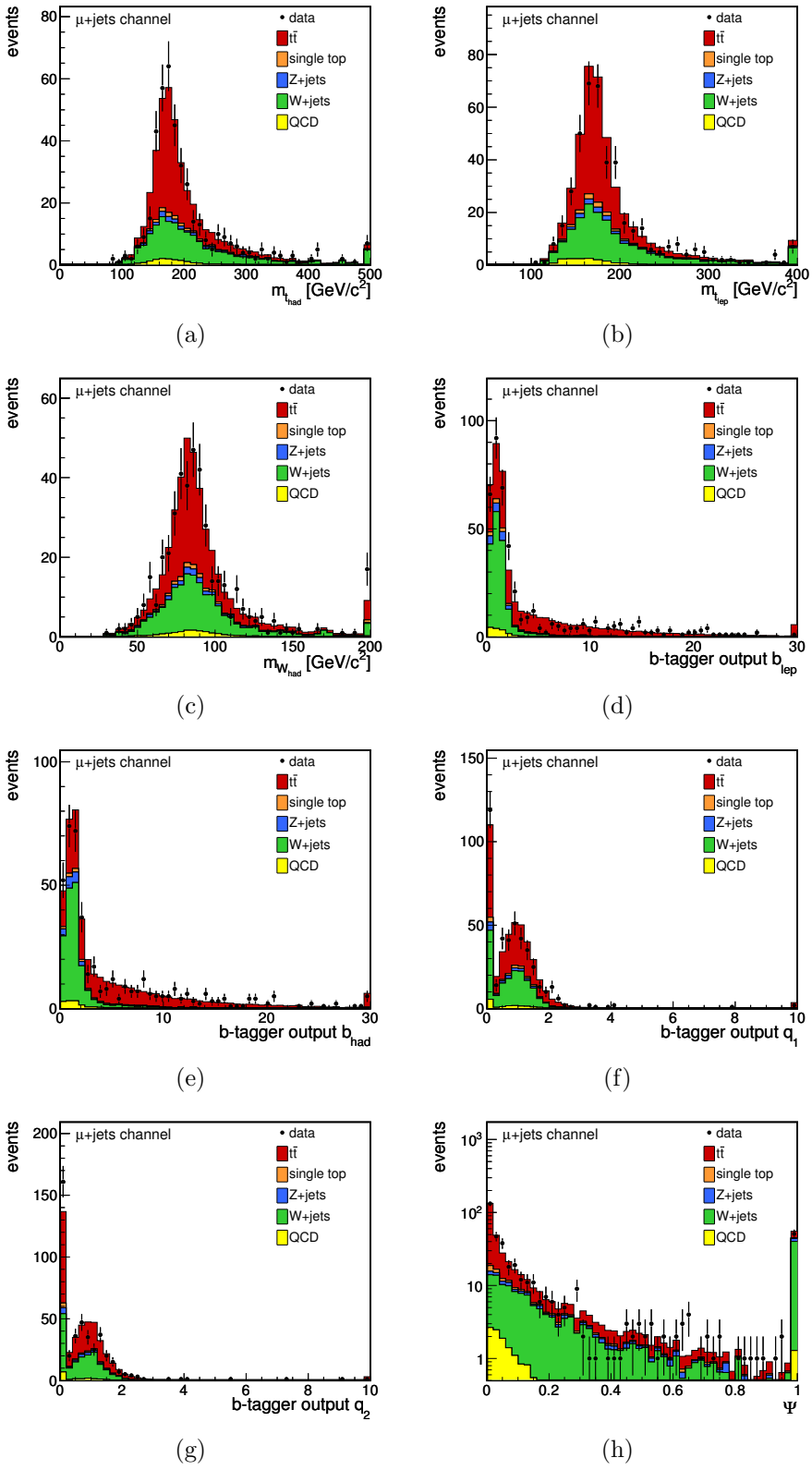

Figure 5.8: Data to Monte Carlo comparison of kinematic quantities (a-c) and the b-tagger outputs (d-g) of jets assigned to b_{had}, b_{lep}, or one of the two light quarks q_1 and q_2 in the selected $t\bar{t}$ reconstruction hypothesis in the muon+jets channel. In histogram (h) the distribution of the Ψ variable in the chosen hypothesis is shown. The Monte Carlo prediction is normalised to the fit result of the $t\bar{t}$ cross section measurement [23].

peaks in the selected hypothesis compared to the best possible one, but the differences between best possible and selected hypothesis is not dramatic. The shapes of variables in the hypothesis chosen with the Ψ variable are always closer to the best possible hypothesis than the hypothesis obtained with the χ^2 method. From the figures 5.6(h) and 5.6(i), also the resolution on the pseudorapidity can be obtained. In most $t\bar{t}$ events, the reconstructed pseudorapidities of both top quarks differ by less then 0.5 from the true pseudorapidities.

The selected hypothesis on data is compared to the prediction for signal and background processes in figures 5.7 and 5.8. The Monte Carlo samples are scaled to the cross section values found in the Standard Model $t\bar{t}$ cross section measurement [23]. The quantities $m_{\mathrm{t_{had}}}$, $m_{\mathrm{t_{lep}}}$, and $m_{\mathrm{W_{had}}}$ which are essential to define the selection of a reconstruction hypothesis show good agreement between data and Monte Carlo simulation. Also the b-tagger output of the four jets assigned to one of the four reconstructed quarks – the b quark originating from the hadronically decaying top quark, the b quark from the leptonically decaying top quark, and the two light quarks – are shown. A reasonable description by the Monte Carlo simulation in all distributions can be seen. The data distribution in the variable Ψ is also described well by the simulation.

5.3 Sideband Study of W+Jets Events

The background in the selected data sample is dominated by W+jets events. The asymmetry between the rate of positively and negatively charged W bosons could have an impact on the reconstructed $t\bar{t}$ charge asymmetry in W+jets, especially if this W^+ to W^- rate asymmetry depends on the reconstructed top quark pseudorapidities. An asymmetry in the total W^+ to W^- rates arises from the different cross sections of processes including either W^+ to W^- bosons in proton-proton collisions and has been measured with the CMS experiment [192]. In figure 5.9, a slight difference in the $|\eta_t| - |\eta_{\bar{t}}|$ distribution is visible in the comparison of W+jets Monte Carlo events with positively and negatively charged leptons. Hence, a variation of the W^+ to W^- ratio can lead to a change of the reconstructed asymmetry in $|\eta_t| - |\eta_{\bar{t}}|$. Therefore, a validation of the reconstruction is performed in a data set obtained with an alternative event selection which is enriched in W+jets events. For this sample, the standard lepton selection cuts are applied but instead of requiring at least four jets, events with one or two jets are selected. To increase the purity of W+jets events and to reduce the amount of background events originating from QCD multi-jet production in this sample, a cut on the transverse mass of the reconstructed W boson of $m_{\mathrm{T,W}} > 50$ GeV/c^2 is applied. The transveres W boson mass is defined as

$$m_{\mathrm{T,W}} = \sqrt{\frac{2 \cdot p_{\mathrm{T,l}} \cdot \not{E}_{\mathrm{T}}}{c^3}(1 - \cos\Delta\phi)}, \tag{5.13}$$

where $p_{\mathrm{T,l}}$ is the transverse momentum of the charged lepton, $\not{E}_{\mathrm{T}}$ is the absolute value of the missing transverse energy and $\Delta\phi$ is the azimuthal angle between the charged lepton and the direction of $\vec{\not{E}}_{\mathrm{T}}$. From Monte Carlo simulations, the expected

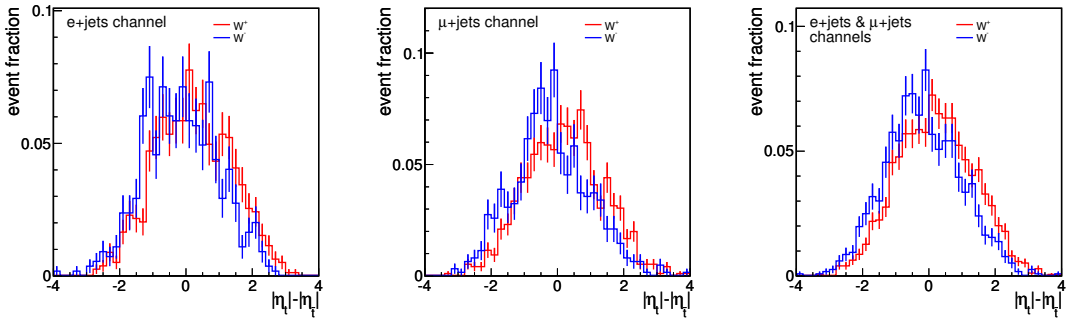

(a) (b) (c)

Figure 5.9: Distribution of $|\eta_{\mathrm{t}}| - |\eta_{\bar{\mathrm{t}}}|$ in W+jets Monte Carlo events with positively and negatively charged leptons after the final selection in the electron+jets channel (a), the muon+jets channel (b), and both channels combined (c).

purity of W+jets events in the selected data sample is 87% in the electron+jets channel and 96% in the muon+jets channel.

In this sample, a full reconstruction of $|\eta_{\mathrm{t}}| - |\eta_{\bar{\mathrm{t}}}|$ is of course not feasible, since it would require the occurrence of at least four jets. However, a reconstruction of a four-momentum which mimics the four-momentum of the leptonically decaying top quark is possible. The leptonically decaying W boson can be reconstructed in the standard way from the charged lepton momentum and the missing transverse energy. This reconstructed four-momentum of the W boson can be paired with one jet to a quantity which is similar to the top quark four-momentum in $\mathrm{t\bar{t}}$ events reconstructed in the sample selected in the inclusive four-jet bin. To select a pairing of jets (in case of events with two jets) and also a neutrino $p_{z,\nu}$ solution, the combination which forms an invariant mass closest to the top quark mass is selected. This selection is similar to the choice of a hypothesis with equation 5.10, taking only into account the constraint on the mass of the leptonically decaying top quark.

Having reconstructed a pseudo-top momentum vector in a W+jets dominated data sample, the shape of $\eta_{\mathrm{t}_{\mathrm{pseudo}}}$ for events with a positively charged lepton can be compared to the shape of $\eta_{\bar{\mathrm{t}}_{\mathrm{pseudo}}}$ in events with negatively charged leptons. In this way, potential differences in the top quark reconstruction between W^+ and W^- events are evaluated. If the $\eta_{\mathrm{t}_{\mathrm{pseudo}}}$ distribution in W^+ events is different to the $\eta_{\bar{\mathrm{t}}_{\mathrm{pseudo}}}$ in W^- events, this could produce an additional asymmetry in $|\eta_{\mathrm{t}}| - |\eta_{\bar{\mathrm{t}}}|$ in the reconstruction of W+jets background events in the finally selected signal region. The $\eta_{\mathrm{t}_{\mathrm{pseudo}}}$ is shown in figures 5.10 and 5.11 for data and Monte Carlo simulation, respectively. Small differences in the shape of $\eta_{\mathrm{t}_{\mathrm{pseudo}}}$ for W^+ compared to W^- events can be seen. The ratio of W^+ to W^- events in $\eta_{\mathrm{t}_{\mathrm{pseudo}}}$ is shown in figure 5.12. The ratio distributions look very similar in the comparison of data and Monte Carlo samples. Two aspects of the top quark reconstruction can be concluded from this illustration: The overall rate of W^+ to W^- events – which can already change the reconstructed charge asymmetry in $|\eta_{\mathrm{t}}| - |\eta_{\bar{\mathrm{t}}}|$ – is modelled correctly by the Monte Carlo simulation and the W^+ to W^- ratio is also well modelled differentially in $\eta_{\mathrm{t}_{\mathrm{pseudo}}}$. The latter supports that their are no potential differences in the reconstruc-

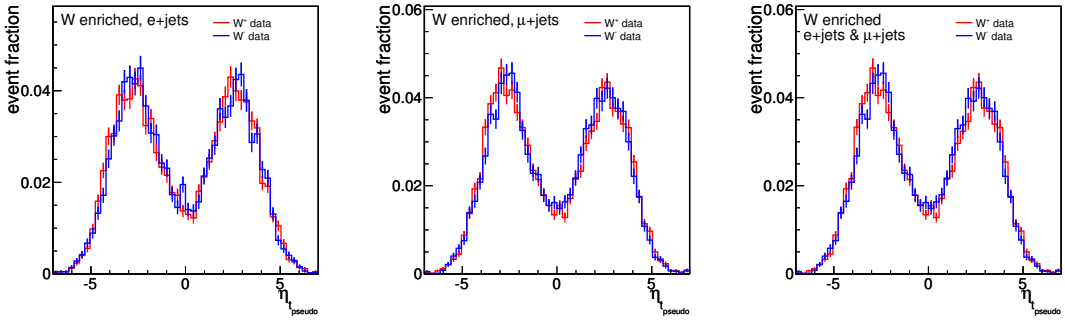

(a) (b) (c)

Figure 5.10: Reconstructed $\eta_{t_{pseudo}}$ in W+jets events in data in the electron+jets channel (a), the muon+jets channel (b), and both channels combined (c).

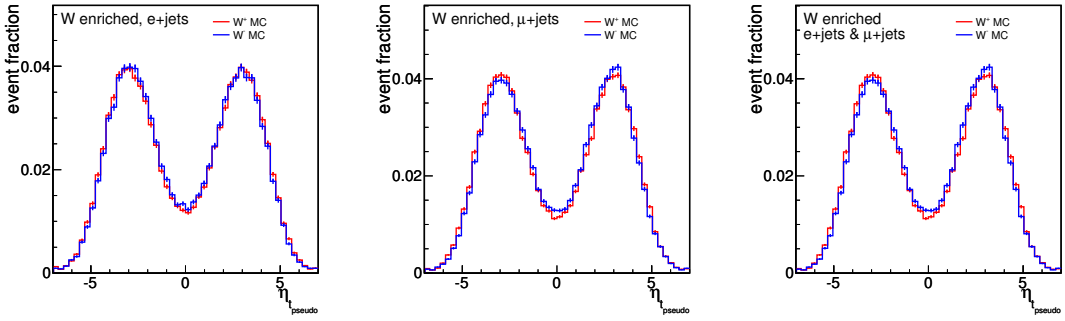

(a) (b) (c)

Figure 5.11: Reconstructed $\eta_{t_{pseudo}}$ in W+jets events from Monte Carlo (MC) simulation in the electron+jets channel (a), the muon+jets channel (b), and both channels combined (c).

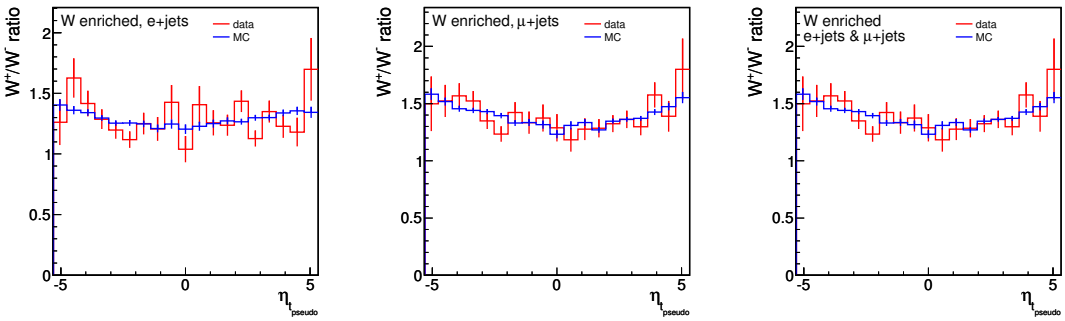

(a) (b) (c)

Figure 5.12: Ratio of W^+ and W^- events in the distributions of $\eta_{t_{pseudo}}$ from figures 5.10 and 5.11 for Monte Carlo (MC) compared to data in the electron+jets channel (a), the muon+jets channel (b), and both channels combined (c).

tion of η_t and $\eta_{\bar{t}}$ in W+jets events which are not described by the Monte Carlo simulation.

5.4 Unfolding of the Charge Asymmetry

The reconstruction of the top quark four-momenta allows the determination of pseudorapidities of top and antitop quarks in each event. The reconstructed pseudorapidities are shown in figures 5.13 and 5.14. From the individual pseudorapidity distributions, the distribution of $|\eta_{\mathrm{t}}| - |\eta_{\bar{\mathrm{t}}}|$ is obtained on an event-by-event basis (see figure 5.15). The uncorrected $\mathrm{t\bar{t}}$ charge asymmetry can be reconstructed from the distributions of $|\eta_{\mathrm{t}}| - |\eta_{\bar{\mathrm{t}}}|$ by counting events with positive (N^+) and negative $|\eta_{\mathrm{t}}| - |\eta_{\bar{\mathrm{t}}}|$ values (N^-), respectively. From these numbers, the charge asymmetry is calculated according to the definition in equation 1.36. In the electron+jets channel, a reconstructed charge asymmetry of $A_C^{\mathrm{rec}} = 0.028 \pm 0.048$ is found; an asymmetry of $A_C^{\mathrm{rec}} = 0.007 \pm 0.049$ is reconstructed in the muon+jets channel. Combining both channels, the reconstructed asymmetry is $A_C^{\mathrm{rec}} = 0.018 \pm 0.034$. All quoted uncertainties a purely statistical.

The value of the reconstructed asymmetry A_C^{rec} is not directly comparable with any theory prediction, since the $|\eta_{\mathrm{t}}| - |\eta_{\bar{\mathrm{t}}}|$ distribution is disturbed by several effects. First, about 50% of all events are expected to be background and thus no real $\mathrm{t\bar{t}}$ events. An even bigger effect arises from the imperfect reconstruction method. In many events, not the best possible hypothesis is selected. Therefore, the reconstructed four-momenta of the top quarks and also the reconstructed value of the charge asymmetry will not directly correspond to the true value of the asymmetry in $|\eta_{\mathrm{t}}| - |\eta_{\bar{\mathrm{t}}}|$. But also in the best possible hypothesis, the reconstructed top quark momenta are smeared with respect to the momenta on generator level due to finite energy and momentum resolutions of the detectors for measurable objects like jets and charged leptons from which the top quark momenta are derived. The event selection efficiency which is not flat in $|\eta_{\mathrm{t}}| - |\eta_{\bar{\mathrm{t}}}|$ does change the shape of $|\eta_{\mathrm{t}}| - |\eta_{\bar{\mathrm{t}}}|$, too. The reconstructed and true values will always be smeared and can only be correlated. The smearing between true and reconstructed $|\eta_{\mathrm{t}}| - |\eta_{\bar{\mathrm{t}}}|$ as well as the differential selection efficiency as function of $|\eta_{\mathrm{t}}| - |\eta_{\bar{\mathrm{t}}}|$ are shown in figure 5.16. For the listed reasons, a regularised unfolding procedure is applied as has been described in chapter 4 using the algorithm provided by TUnfold.

In the first step of the unfolding procedure, the background contributions have to be subtracted from the measured data distribution. For the background subtraction, the result of the Standard Model $\mathrm{t\bar{t}}$ cross section measurement [23] is utilised. In the cross section analysis, the statistical uncertainties including the full covariance matrix V_b are provided for the $N = 5$ individual backgrounds templates $\vec{b}_i$, $i = 1 \ldots N$, for the processes W+jets, Z+jets, single top quark, QCD multi-jet production in the muon+jets channel, and QCD/γ+jets in the electron+jets channel (see equations 5.3 and 5.4). From the diagonalised covariance matrix, orthogonal background templates $\vec{b}'_j$, $j = 1 \ldots N$, are constructed according to the eigenvectors $\vec{v}_j$ of the covariance matrix:

$$\vec{b}'_j := \sum_{i=1}^{N} \vec{b}_i \, (\vec{v}_j)_i^2 \,, \tag{5.14}$$

where the elements of the eigenvectors $\vec{v}_j$ have to be squared to preserve the overall

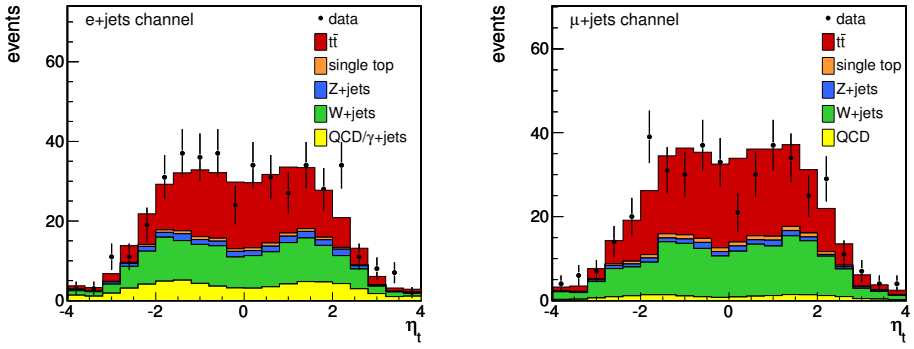

(a) (b)

Figure 5.13: Reconstructed η_t distribution in the electron+jets channel (a) and in the muon+jets channel (b).

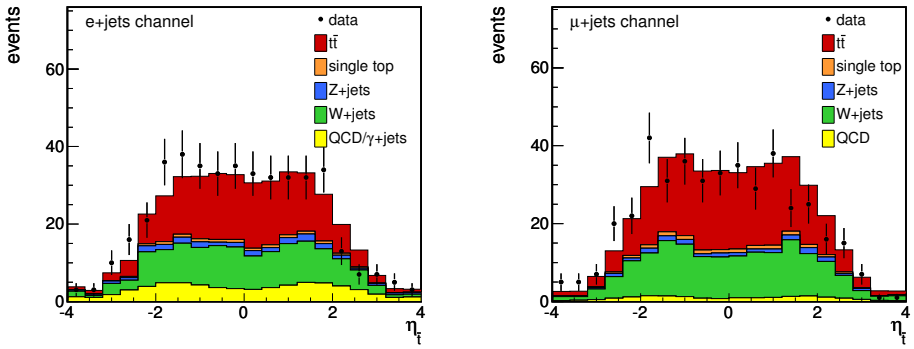

(a) (b)

Figure 5.14: Reconstructed $\eta_{\bar{t}}$ distribution in the electron+jets channel (a) and in the muon+jets channel (b).

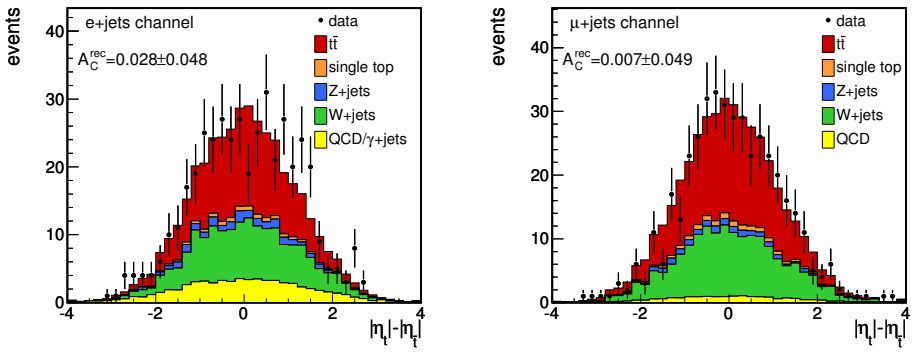

(a) (b)

Figure 5.15: Reconstructed $|\eta_t| - |\eta_{\bar{t}}|$ distribution in the electron+jets channel (a) and in the muon+jets channel (b).

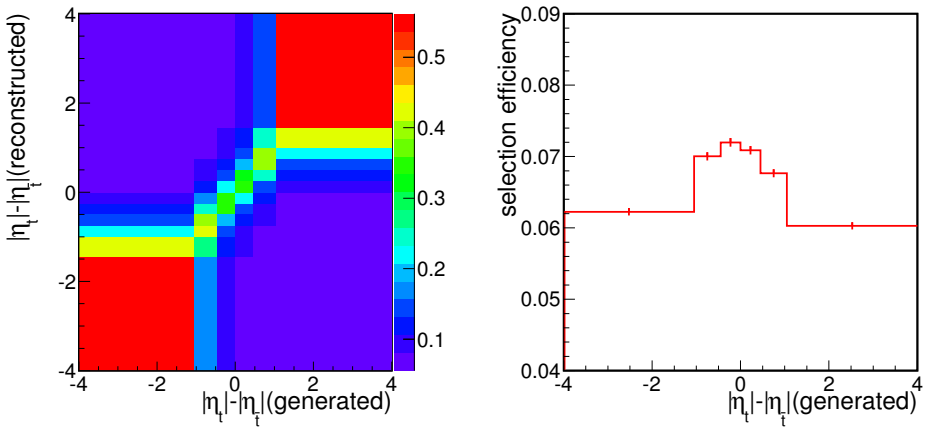

(a) (b)

Figure 5.16: Smearing between true and reconstructed $|\eta_t| - |\eta_{\bar{t}}|$ distribution (a). The entries of the matrix correspond to the probability that a selected $t\bar{t}$ event with a certain generated $|\eta_t| - |\eta_{\bar{t}}|$ value is found with a specific $|\eta_t| - |\eta_{\bar{t}}|$ value after the reconstruction, so each column of the matrix is normalised to unity. In (b), the selection efficiency as function of $|\eta_t| - |\eta_{\bar{t}}|$ is shown.

number of background events. The templates $\vec{b}'_j$ have by construction uncorrelated statistical uncertainties which are given by the squared eigenvalues of the covariance matrix V_b. The contribution from the uncorrelated background templates are then subtracted from the measured spectrum using Gaussian error propagation. In the background subtracted spectrum, a charge asymmetry in the $t\bar{t}$ sample of $A_C^{\text{bkg.subtr.}} = 0.035 \pm 0.070$ is found in the combined electron+jets and muon+jets channels.

The matrix A in the basic unfolding equation 4.2 takes into account the influences on the $|\eta_t| - |\eta_{\bar{t}}|$ spectrum due to smearing and selection efficiency and is illustrated by the two diagrams in figure 5.16. A is basically given by the product of the smearing matrix depicted in figure 5.16(a) and the selection efficiencies from figure 5.16(b) for the individual bins. Smearing and differential selection efficiencies are taken from the simulation of $t\bar{t}$ events with the MadGraph generator. For the unfolding of the $|\eta_t| - |\eta_{\bar{t}}|$ distribution, a 12×6 matrix is utilised, i. e., the measured spectrum is divided into twelve bins and six bins are used to divide the distribution of the true $|\eta_t| - |\eta_{\bar{t}}|$ spectrum. The bin widths are adjusted such, that the expected number of events from the $t\bar{t}$ MadGraph simulation is approximately equal in each bin for the reconstructed as well as for the true distribution. For the binning of the true distribution, bin intervals of $(-\infty,-1.05]$, $[-1.05,-0.45]$, $[-0.45, 0]$, $[0, 0.45]$, $[0.45, 1.05]$, and $[1.05, \infty)$ are chosen. The outcome of the unfolding process is therefore a measurement of the differential $t\bar{t}$ cross section in $|\eta_t| - |\eta_{\bar{t}}|$ divided into these six bins. Although the measurement of the charge asymmetry A_C would require only two bins for positive and negative $|\eta_t| - |\eta_{\bar{t}}|$ values, the usage of more bins provides more information on the differential cross section in $|\eta_t| - |\eta_{\bar{t}}|$ and allows for a more precise determination of migration effects from the left to the right part of the distribution. The overall selection efficiency going into the definition of

matrix A is corrected for the differences found for the selection of $t\bar{t}$ events between Monte Carlo and data in the $t\bar{t}$ cross section measurement [23]. Scale factors found in this measurement for the trigger selection efficiency are 0.982 ± 0.001 for the electron triggers and 0.970 ± 0.002 for the muon triggers. The differences in the lepton identification and isolation requirements result in scale factors between data and Monte Carlo of 0.950 ± 0.033 for the electron selection efficiency and of 0.995 ± 0.030 for the selection efficiency of muons.

The unfolding algorithm used to correct the measured $|\eta_t| - |\eta_{\bar{t}}|$ spectrum is based on solving equation 4.25 including the constraint to preserve the normalisation of the unfolded spectrum. The regularisation scheme used in this analysis takes a regularisation matrix L as defined in equation 4.16 accounting for the second derivatives of the resulting $|\eta_t| - |\eta_{\bar{t}}|$ spectrum.

5.4.1 Sanity Checks with Pseudo Experiments

The performance of the unfolding algorithm is tested in sets of pseudo experiments simulating expected data distributions from the Monte Carlo generation repeatedly many times. In each pseudo experiment, random distributions for $t\bar{t}$ signal and background processes are generated using the corresponding Monte Carlo templates. The number of generated pseudo data events follows a Poisson distributed random number for each process. The mean of this Poisson distribution is the expected number of events. These numbers for background and signal expectations are taken from the $t\bar{t}$ cross section measurement and are summarised in table 5.1. In addition, the number of background events is varied according to the statistical uncertainties from the covariance matrix V_b. According to the drawn event numbers, events are randomly drawn from the templates of $|\eta_t| - |\eta_{\bar{t}}|$ for all processes and are combined into a pseudo data distribution. The process of creating pseudo data is repeated many times and the unfolding method is applied on each pseudo data distribution.

In a first test of the unfolding with pseudo experiments, the determination of the regularisation parameter τ is performed. Two methods were tested to define the

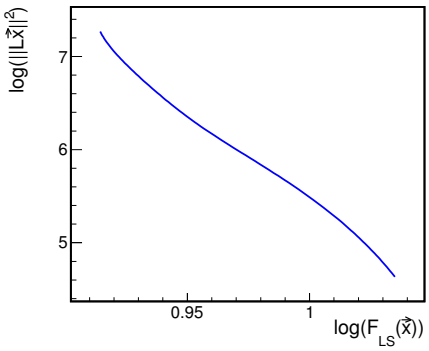

Figure 5.17: The L-curve scan performed on an exemplary pseudo data set. $F_{\mathrm{LS}}(\vec{x})$ is plotted versus $\|L\vec{x}\|^2$ for different values of the regularisation parameter τ. The point with largest positive curvature should identify the optimal regularisation parameter τ, but the kink position is not well established.

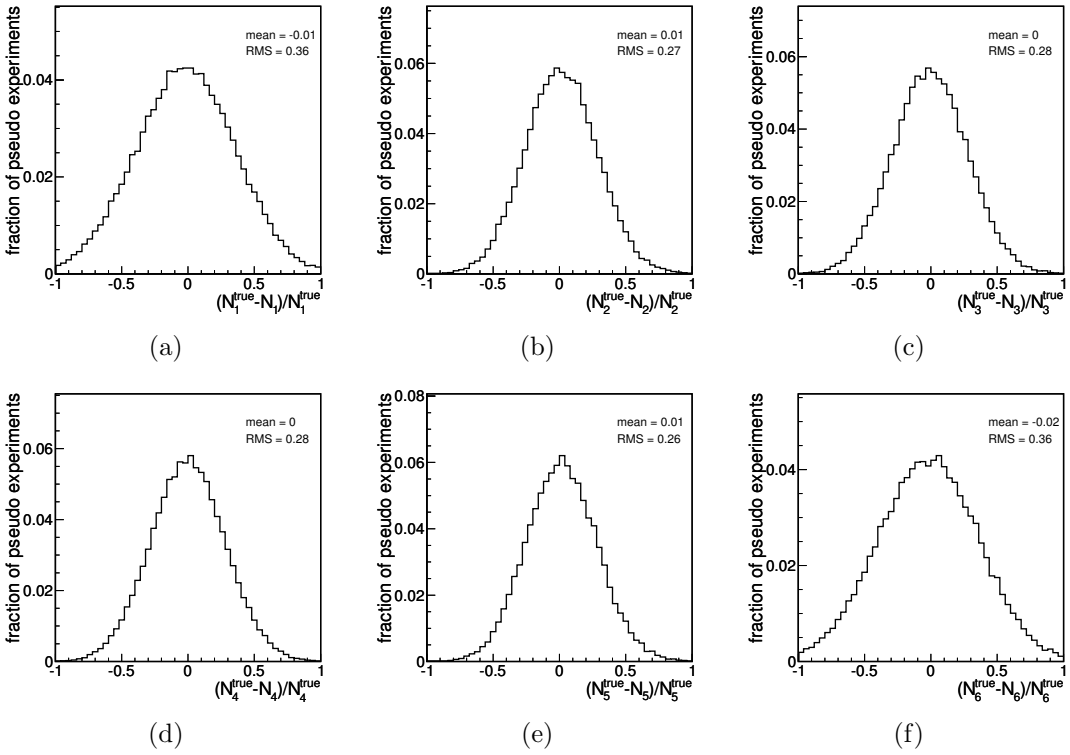

Figure 5.18: Relative difference between the unfolded spectrum in pseudo experiments and the true distribution in each bin of the unfolded spectrum. The root mean square (RMS) of the distributions is a measure for the expected statistical uncertainty in each bin.

optimal regularisation strength, the L-curve scan and the minimisation of global correlation (see section 4.2). The resulting L-curve scan for an exemplary pseudo data set is shown in figure 5.17. The kink with largest positive curvature which should identify the optimal regularisation parameter τ is not well established. Such L-curve shapes without a clear kink position are expected for some specific unfolding problems as discussed in [183]. Hence, the resulting regularisation parameter τ determined with the L-curve scan shows a huge spread between $\tau = 5.0 \cdot 10^{-5}$ and $\tau = 2.5 \cdot 10^{-3}$ in various pseudo experiments. The regularisation parameter τ for the final measurement is therefore determined with the approach of minimising the global correlation coefficient. Again, the τ parameter is determined in the unfolding of pseudo data sets. The average τ value found in this evaluation is $7 \cdot 10^{-4}$ varying only slightly in the set of pseudo experiments. For all further performance tests with pseudo experiments as well as for the unfolding of the measured CMS data, the regularisation parameter is fixed to this value.

Having fixed the regularisation parameter τ the performance of the unfolding procedure is tested by comparing the unfolded spectra from the ensemble of pseudo data to the true distribution of $|\eta_t| - |\eta_{\bar{t}}|$ known from the $t\bar{t}$ Monte Carlo generation. The result of the unfolding is a binned distribution of the true $|\eta_t| - |\eta_{\bar{t}}|$ variable in the binning as it has been defined for the matrix A for the true distribution. The relative difference between true bin content N_i^{true} known from the Monte Carlo simulation

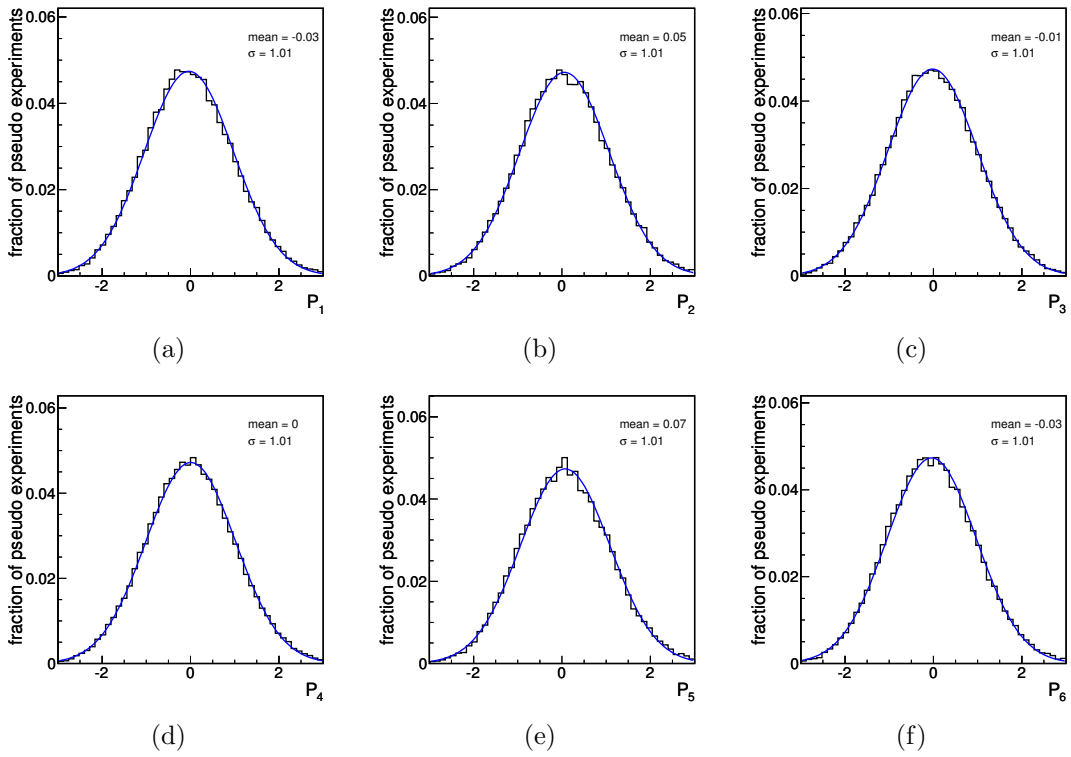

Figure 5.19: Pull distributions in all bins for the unfolding in ensemble tests with pseudo experiments approximated with Gaussian functions. Given are the fitted mean and width (σ) of the respective Gaussian.

and the result from the unfolding process N_i in bin i is shown in figure 5.18 for all six bins of the unfolded $|\eta_t| - |\eta_{\bar{t}}|$ spectrum. This relative difference is defined as the difference between N_i^{true} and N_i divided by N_i^{true}. The mean of these distributions is always close to zero with small shifts of less than 2%. This observation indicates that the true values are reconstructed correctly by the unfolding on average in all pseudo experiments. The widths given by the root mean square (RMS) of the distributions are a measure for the expected statistical uncertainty. This leads to expected statistical uncertainties per bin of 26% to 27% in the inner and 36% in the outer bins of the unfolded spectrum.

The unfolding method itself gives the full covariance matrix V_x on the unfolded spectrum as output. To check, if the diagonal elements of the covariance matrix are providing the correct statistical uncertainty estimation for the individual bins of the unfolded spectrum, pull distributions for all bins are drawn for a set of pseudo experiments (see figure 5.19). The pull P_i in bin i is defined as the difference between the true and the reconstructed values divided by the uncertainty provided by the unfolding method:

$$P_i := \frac{N_i^{\text{true}} - N_i}{\sigma_i}, \tag{5.15}$$

where the uncertainties $\sigma_i = \sqrt{(V_x)_{ii}}$ are related to the diagonal elements of the covariance matrix V_x. If the uncertainty propagation in the unfolding procedure is

done correctly, the uncertainty taken from the covariance matrix should be identical to the expected statistical uncertainty, which can be estimated from the widths of the relative difference distributions in figure 5.18. In this case, the pull distributions can be approximated with a Gaussian function. For a correct uncertainty estimation, the width of the Gaussian function will be close to 1. If the uncertainty provided by the unfolding are overestimating the statistical uncertainties, the pull distributions will have widths smaller than 1, whereas underestimated uncertainties will lead to broader pull distributions. Shifts of the pull distributions correspond to the shifted mean values, which were previously seen in the relative difference plots in figure 5.18. Since the widths of the Gaussian functions fitted to the pull distributions are all close to 1, it can be concluded that the uncertainty propagation is done correctly by the unfolding procedure.

From the unfolded $|\eta_{\mathrm{t}}|-|\eta_{\bar{\mathrm{t}}}|$ spectrum, the corrected charge asymmetry A_C and its uncertainties can be derived. According to the definition of the charge asymmetry in equation 1.36, A_C is calculated via

$$A_C = \frac{N^+ - N^-}{N^+ + N^-} = \frac{\sum_{i=4}^{6} N_i - \sum_{i=1}^{3} N_i}{\sum_{i=1}^{6} N_i}, \tag{5.16}$$

where the N_i are the bin contents of the unfolded spectrum with i being the index of the respective bin. The uncertainty on the charge asymmetry can be derived from the covariance matrix V_x. The statistical uncertainty on A_C can be calculated with standard error propagation:

$$\sigma^2_{A_C} = \left(\frac{\partial A_C}{\partial N_1} \dots \frac{\partial A_C}{\partial N_6} \right) V_x \begin{pmatrix} \frac{\partial A_C}{\partial N_1} \\ \vdots \\ \frac{\partial A_C}{\partial N_6} \end{pmatrix}. \tag{5.17}$$

The partial derivatives of A_C are given by:

$$\begin{aligned} \frac{\partial A_C}{\partial N_i} &= \frac{-2N^+}{(N^+ + N^-)^2} \quad \text{for } i = 1 \dots 3, \\ \frac{\partial A_C}{\partial N_i} &= \frac{2N^-}{(N^+ + N^-)^2} \quad \text{for } i = 4 \dots 6. \end{aligned} \tag{5.18}$$

The correct unfolding of the charge asymmetry A_C is also tested in ensemble tests with pseudo experiments. The distribution of the unfolded asymmetry in pseudo experiments is shown in figure 5.20(a). On average, an asymmetry of $A_C = 0.0080 \pm 0.0008$ is found. This is only slightly biased with respect to the charge asymmetry of $A_C^{\mathrm{true}} = 0.0097 \pm 0.0009$ which is the value of the asymmetry on generator level in the used MadGraph Monte Carlo sample. The corresponding pull distribution of A_C is depicted in figure 5.20(b) and is well described by a Gaussian function with a width of 1. For the statistical uncertainty of the measurement of A_C, on average a statistical uncertainty of 0.138 is expected as can be concluded from the RMS of figure 5.20(a). In addition, the distribution of the individual statistical uncertainties σ_{A_C} is shown in figure 5.20(c). The expected statistical uncertainty ranges from about 0.11 to 0.16.

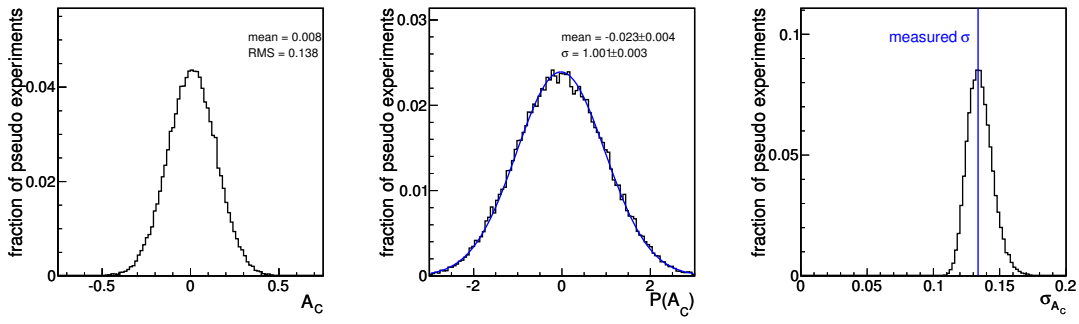

(a) (b) (c)

Figure 5.20: Distribution of the unfolded asymmetries in pseudo experiments (a), pull distribution of the unfolded asymmetry (b), and the distribution of statistical uncertainties σ_{A_C} in pseudo experiments (c). The blue line indicates the measured uncertainty in data.

The outcome of the ensemble test study confirms the correct behaviour of the unfolding procedure, if the signal in the pseudo experiments is drawn from the same sample from which also the matrix A is determined which is the main ingredient of the unfolding algorithm. To check, whether on a data sample showing a sizeable asymmetry, this asymmetry is reconstructed correctly using the standard Monte Carlo sample as input for the unfolding, ensemble tests with pseudo experiments are performed in which an asymmetry is present. To generate samples with different charge asymmetries, the events from the standard $t\bar{t}$ Monte Carlo sample are re-weighted with a factor of $k(|\eta_t| - |\eta_{\bar{t}}|) + 1$. The parameter k is varied between -0.25 and 0.25 to produce different charge asymmetries in the range between approximately -20% and +20%. The re-weighted samples are unfolded using the standard unfolding procedure and the unfolded asymmetry is compared to the generated asymmetry. The outcome of this test is summarised in table 5.3 and illustrated in figure 5.21. The reconstructed asymmetries are determined from the mean of all unfolded asymmetries in sets of pseudo experiments for each value of k. The differences between true and unfolded asymmetry are small and observed biases are mostly of the order of less than 0.003.

5.4.2 Alternative Unfolding Procedure using TRUEE

The unfolding procedure is tested with an alternative implementation of an unfolding algorithm. For this purpose, the package TRUEE is used including the generalised matrix inversion algorithm of RUN (see section 4.4). The unfolding procedure is again tested with pseudo experiments. The free parameters which have to be determined in the unfolding procedure of TRUEE are the effective number of degrees of freedom, n_{eff}, and the number of knots, n_{knots}, used for the approximation of the measured and unfolded spectra with B-splines. It is recommended to choose the number of knots approximately two times larger than n_{eff}, for example $n_{\text{knots}} = 2n_{\text{eff}} + 3$ [186]. The arrangement of bins of the true and measured $|\eta_t| - |\eta_{\bar{t}}|$ spectrum is identical to the binning used in the previous unfolding procedure using TUnfold.

k	generated A_C^{true}	unfolded A_C
0.25	0.2326	0.2330±0.0008
0.2	0.1882	0.1883±0.0008
0.15	0.1437	0.1434±0.0008
0.1	0.0991	0.0984±0.0008
0.05	0.0544	0.0533±0.0008
-0.05	-0.0350	-0.0369±0.0008
-0.1	-0.0798	-0.0821±0.0008
-0.15	-0.1247	-0.1274±0.0008
-0.2	-0.1696	-0.1724±0.0008
-0.25	-0.2144	-0.2165±0.0008

Table 5.3: Generated and unfolded charge asymmetry as performance check of the unfolding method. To generate samples with an asymmetric $|\eta_{\text{t}}| - |\eta_{\bar{\text{t}}}|$ distribution the events of the standard sample are re-weighted with $k(|\eta_{\text{t}}| - |\eta_{\bar{\text{t}}}|) + 1$. Quoted uncertainties on the unfolded asymmetries correspond to the statistical uncertainty arising from the limited number of performed pseudo experiments.

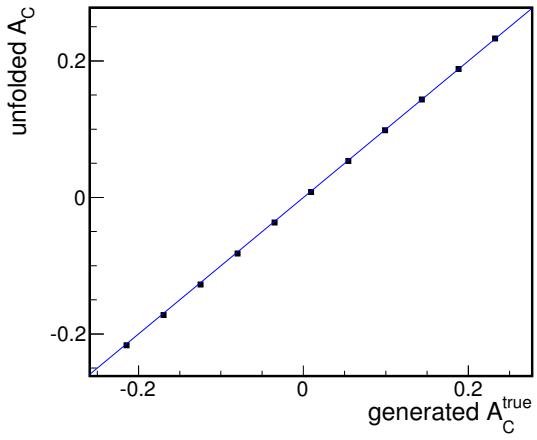

Figure 5.21: Generated and unfolded charge asymmetry as performance check of the unfolding method. The blue line correspond to an optimal response where generated and unfolded asymmetry are equal.

For the background subtraction, TRUEE does only provide a standard routine to handle a background contribution with a statistical uncertainty given by $\sqrt{N_{\text{b}}}$, where N_{b} is the number of expected background events. Hence, for the evaluation of the unfolding algorithm, the background contribution in pseudo experiments is only varied according to the statistical uncertainty of $\sqrt{N_{\text{b}}}$ and does not include the full covariance matrix V_b.

In a first test of the unfolding algorithm provided by TRUEE with pseudo experiments, the unfolding showed an unstable behaviour in the outer bins of the corrected spectrum. In a subset of pseudo experiments, the result of the unfolding procedure in these bins is systematically lower then the expected true value and also the uncertainties in these bins vary significantly from the average values in the majority

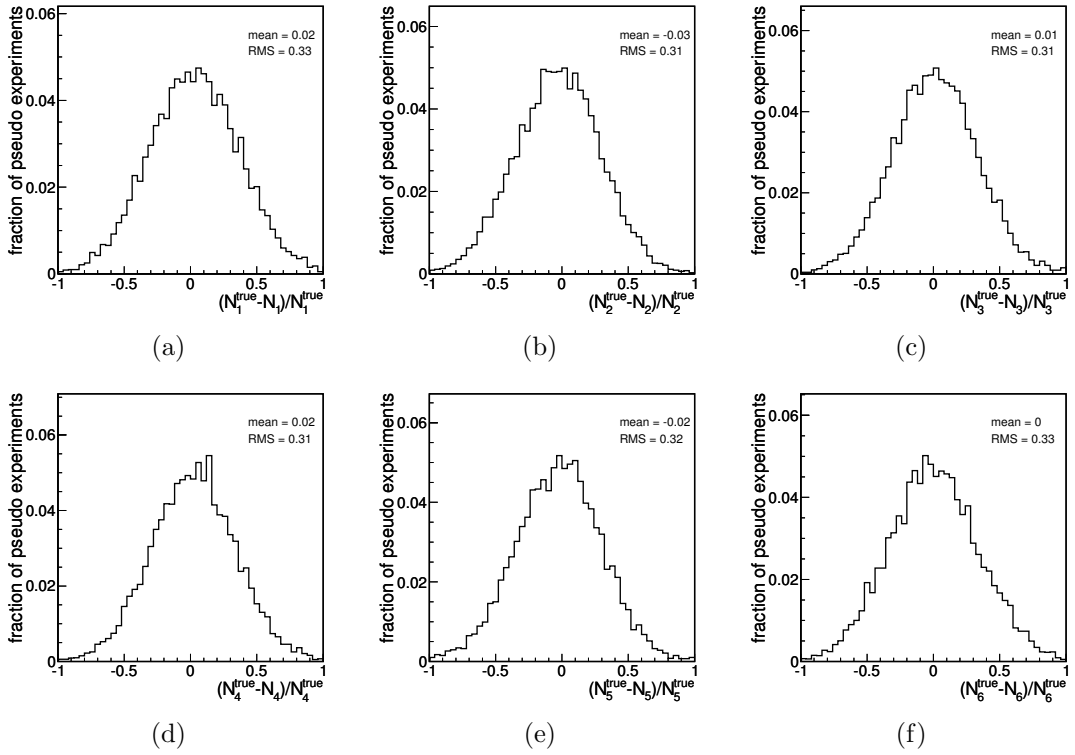

Figure 5.22: Relative difference between the unfolded spectrum in pseudo experiments and the true distribution in each bin of the unfolded spectrum where the unfolding procedure is performed with TRUEE. The root mean square (RMS) of the distributions is a measure for the expected statistical uncertainty in each bin.

of pseudo experiments. Further studies confirmed that this behaviour always occurs when unfolding a distribution which vanishes at its outer tails. To solve this issue the reconstructed as well as the expected true $|\eta_t| - |\eta_{\bar{t}}|$ spectra are transformed with the same bijective mapping. This bijective transformation is adapted such that the expected true spectrum is a flat distribution on the interval $[0, 1]$. Hence, the selected distribution is also defined on the interval $[0, 1]$. Possible asymmetries in the original $|\eta_t| - |\eta_{\bar{t}}|$ spectrum would then lead to a non-flat distribution in the unfolded spectrum on this interval.

The result of the unfolding procedure performed with the TRUEE package are presented in figures 5.22, 5.23, and 5.24. For these results, exemplarily the parameters $n_{\text{eff}} = 5$ and $n_{\text{knots}} = 13$ has been chosen. In figure 5.22, the relative difference between true and unfolded value in the six individual bins of the $|\eta_t| - |\eta_{\bar{t}}|$ spectrum are shown. On average, the bin content of all bins is reconstructed correctly with small biases of up to 3%. The expected statistical uncertainty in all bins is of the order of 31% to 33%. These spreads of the unfolding result in the individual bins are of the same order as for the unfolding performed with TUnfold shown in figure 5.18. However, the bias shifts are found to be slightly larger for the unfolding performed with TRUEE. Similarly to the previous study with TUnfold, also the uncertainty propagation through the unfolding is evaluated with drawing pull

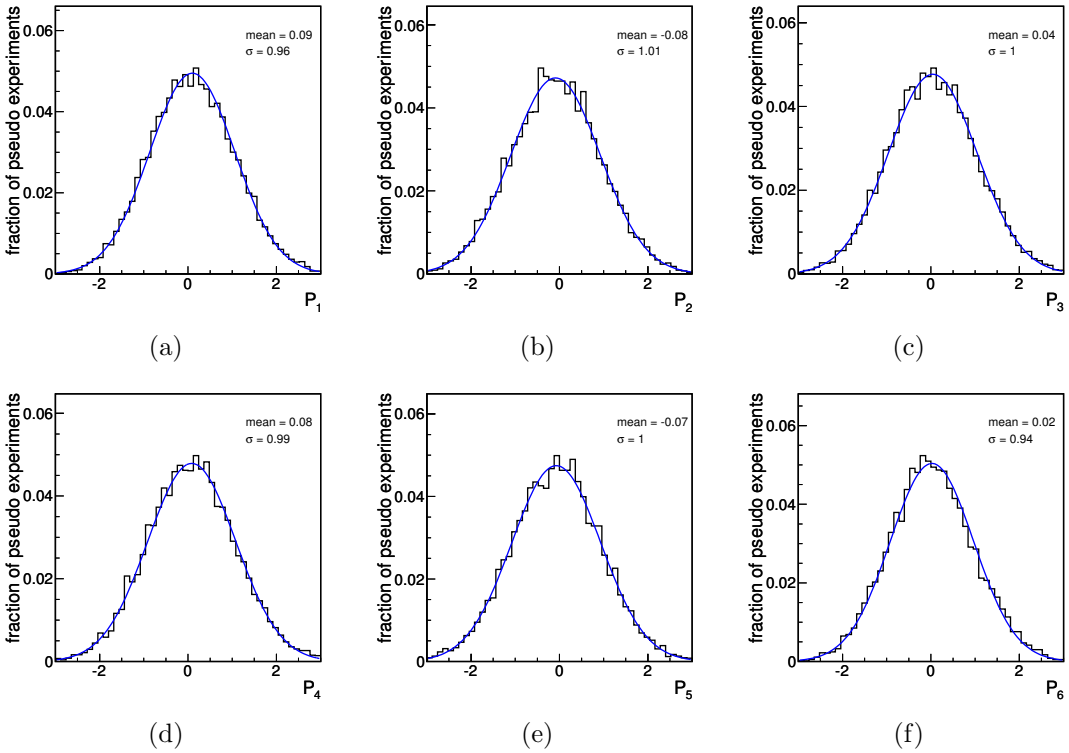

Figure 5.23: Pull distributions in each bins for the unfolding performed with TRUEE in pseudo experiments approximated with Gaussian functions. Given are the fitted mean and width (σ) of the respective Gaussian.

distributions for the six bins of the corrected spectrum (see figure 5.23). The pulls P_i in the respective bin i show a Gaussian shape with a width close to 1 which is an indication for a correct uncertainty treatment of the unfolding method. From the unfolded $|\eta_t| - |\eta_{\bar{t}}|$ spectrum, the charge asymmetry and its uncertainty are calculated according to equation 5.17. The outcome of the unfolding for the charge asymmetry A_C in pseudo experiments is shown in figure 5.24. The expected statistical uncertainty of the measurement lies around 13.5% which is compatible with the expected uncertainty of the asymmetry measurement when using TUnfold. Although the uncertainty on the charge asymmetry σ_{A_C} is estimated correctly (see figure 5.24(b)), the unfolding results for A_C itself shows on average a bias towards smaller asymmetry values. The average unfolded asymmetry found in pseudo experiments is $A_C = 0.001 \pm 0.001$ which is smaller than the expected asymmetry of $A_C^{\text{true}} = 0.0097 \pm 0.0009$.

For the mentioned reasons, the final analysis of the charge asymmetry in top quark pair production has not been performed with TRUEE. Although the issue of an unstable unfolding result in the outer bins of the $|\eta_t| - |\eta_{\bar{t}}|$ spectrum has been solved by transforming all distributions to nearly flat spectra, other critical points remain which make it inefficient to use the TRUEE algorithm for the unfolding procedure. Especially the handling of background contributions does not allow for a treatment of several background processes with partially correlated uncertainties.

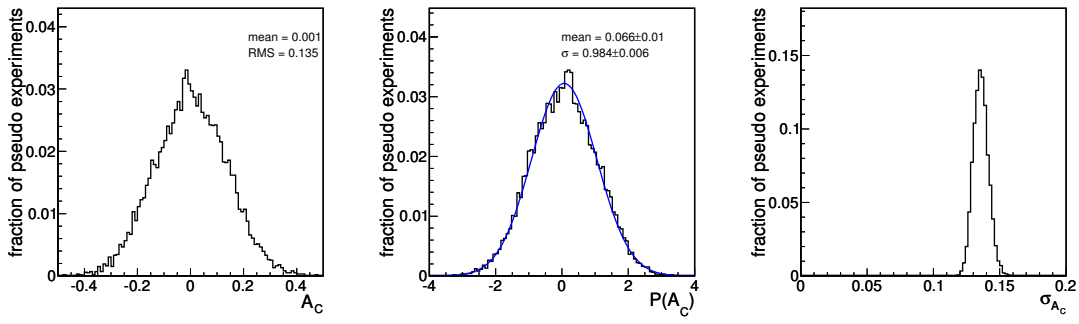

(a) (b) (c)

Figure 5.24: Distribution of the unfolded asymmetry in pseudo experiments (a), pull distribution of the unfolded asymmetry (b), and the distribution of statistical uncertainties σ_A in pseudo experiments (c). The unfolding procedure has been performed with TRUEE.

5.5 Systematic Uncertainties

The measurement of the charge asymmetry A_C might be affected by several sources of systematic uncertainties. In principle, only systematic uncertainties influencing the direction of the reconstructed top quark momenta can change the value of the reconstructed charge asymmetry. The overall selection efficiency and acceptance will not change the measured asymmetry since they equally influence nominator and denominator in the definition of the charge asymmetry in equation 1.36. Therefore, changes in the efficiency cancel out in the calculation of A_C. Only relative uncertainties in the selection efficiency and acceptance could change the shape of the $|\eta_t| - |\eta_{\bar{t}}|$ distribution and therefore the value of the charge asymmetry. The influence of several potential sources of systematic uncertainties is again studied in ensemble tests. For this purpose, pseudo experiments are drawn from systematically shifted templates and the unfolding is performed with the nominal smearing and efficiency matrix A taken from the standard MadGraph $t\bar{t}$ sample. In these pseudo experiments, the overall rate of events is still Poisson distributed around the measured number of data events, but the rate of individual signal and background processes is varied according to the expected changes of the respective systematic uncertainty. Most systematic uncertainties do not only change the expected event rate of the various processes but also the shape of the $|\eta_t| - |\eta_{\bar{t}}|$ spectrum. The expected uncertainty on A_C from each source of systematic is estimated from shifts of the mean value of the distribution of unfolded asymmetries in the performed pseudo experiments. In the following paragraphs, an overview on the considered systematic uncertainties is given.

Jet Energy Scale (JES)

To determine the systematic effect due to the imperfect knowledge on the jet energy scale, simultaneously all jet four-momenta are varied by either $+1\sigma$ or -1σ in their η- and p_T-dependent uncertainties which have been determined in a balancing method of QCD di-jet and photon+jets events [193]. On top of this uncertainty, a

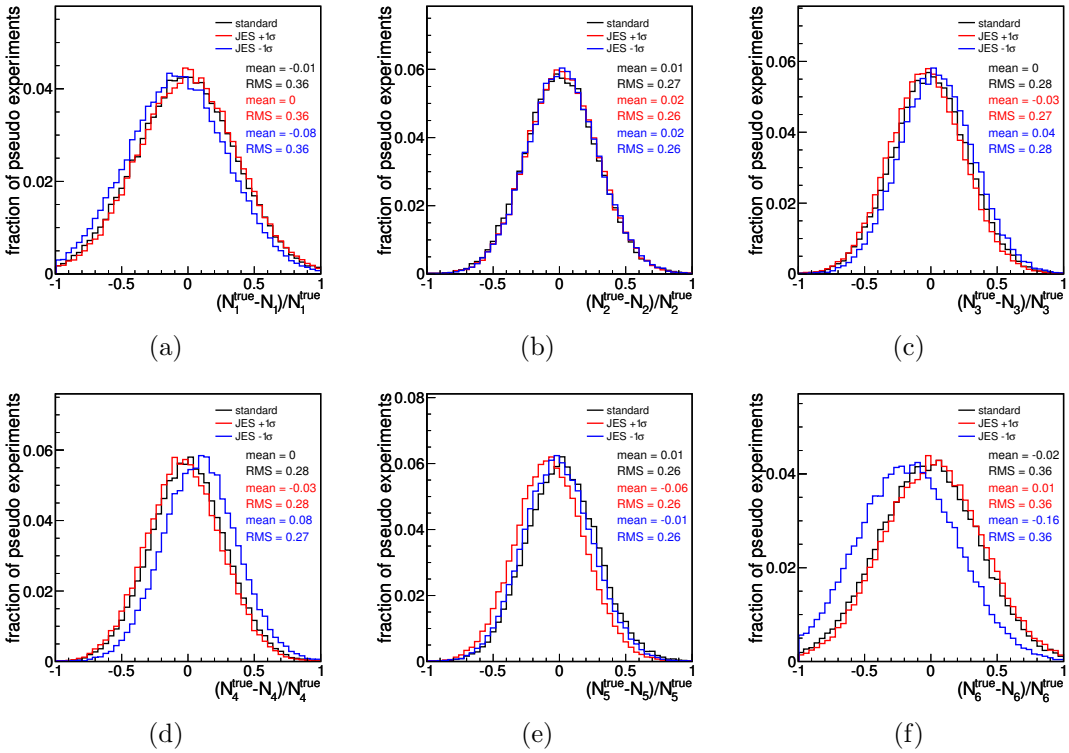

Figure 5.25: Shifts of the averaged unfolding result in the six bins of the $|\eta_t| - |\eta_{\bar{t}}|$ distribution due to jet energy scale (JES) uncertainties.

flat 1.5% shift is added in quadrature to account for calibration changes. To account for uncertainties on the jet energy induced by pile-up processes, an additional uncertainty of $(1.32\ \mathrm{GeV}/c)/p_\mathrm{T}$ is considered. Finally, for jets matched to a b-quark on generator level, an uncertainty of 0.02 for jets with $50\ \mathrm{GeV}/c < p_\mathrm{T} < 200\ \mathrm{GeV}/c$ and $|\eta| < 2.0$ or 0.03 for jets with other p_T or η values is added in quadrature. Since it can be assumed that the energy measurements used to define the missing transverse energy are affected by similar uncertainties, these shifts are propagated to the missing transverse energy by re-determining $\vec{\not{E}}_\mathrm{T}$ taking the systematically shifted jet energies into account. The shifts due to the JES uncertainty are applied for all processes but QCD multi-jet as the QCD multi-jet distributions are obtained directly from data.

The results of the unfolding of the $|\eta_t| - |\eta_{\bar{t}}|$ distribution obtained with pseudo experiments drawn from templates with shifted jet energy scale are shown in figures 5.25 and 5.28(a). Systematic shifts in the individual bins of the $|\eta_t| - |\eta_{\bar{t}}|$ distribution (see figure 5.25) are only shown for the JES uncertainty which has the largest visible effect of all considered systematic uncertainties. Although individual bins of the $|\eta_t| - |\eta_{\bar{t}}|$ distribution are shifted by up to 20%, the asymmetry remains nearly unaffected from the influence of jet energy scale uncertainties since this uncertainty mainly changes the overall rate of the measured spectrum.

Jet Energy Resolution (JER)

The jet p_{T} resolution found in data is worse compared to the Monte Carlo simulations, i. e. the distribution of the reconstructed p_{T} for a jet with a fixed parton jet p_{T} is about 10% broader for data events than for events in the Monte Carlo simulation [194]. This measurement has an uncertainty of about 10%. Therefore, in the standard reconstruction of jets, the momenta of jets in the Monte Carlo samples are scaled in such a way that the p_{T} difference between reconstructed jet and corresponding generator jet is increased by a factor of 0.1. To account for the absolute 10% uncertainty on the JER, two systematically shifted Monte Carlo samples are created by either applying no shift to the jet momenta or by increasing the scale factor to 0.2. As done for the JES uncertainty, the changes in the jet momenta due to the JER shifts are properly propagated to $\vec{\not{E}}_{\mathrm{T}}$.

Factorisation and Renormalisation Scale Uncertainty

The $t\bar{t}$ signal as well as most background processes are produced with the MadGraph generator which relies on the evaluation of LO Feynman diagrams. The calculation of LO amplitudes depends on the choice of the factorisation and renormalisation scale. As a systematic uncertainty on this scale dependence, alternative Monte Carlo samples are generated with varied factorisation and renormalisation scale. The scale factor is changed by factors of 0.5 and 2.0 with respect to the default value. This uncertainty is evaluated for the signal process as well as for the W+jets and Z+jets background processes.

Matching Threshold

An additional uncertainty arises from the choice of the matching threshold in the generation of Monte Carlo samples. The matching threshold is the momentum scale which describes the transition between the hard process generated with MadGraph and the parton showering performed with Pythia in the MLM matching scheme. For a systematic uncertainty, this scale is changed by factors of 0.5 and 2.0, respectively, compared to the default value. Alternative Monte Carlo event samples with varied matching thresholds are produced for $t\bar{t}$, W+jets, and Z+jets production.

Initial and Final State Radiation (ISR/FSR)

For the $t\bar{t}$ signal process, two systematically shifted samples are generated with a varied amount of initial and final state radiation. Technically, several parameters of the Pythia showering algorithm describing the maximum virtuality scale of parton radiation, the maximal transverse momentum of these radiation processes, and the running of the strong coupling constant α_S are adjusted.

PDF Uncertainties

A potential systematic uncertainty arises from the imperfect knowledge on the parton distribution functions. Especially a potential change of the fraction of gluon

fusion processes in the $t\bar{t}$ production can change the measurement of the charge asymmetry because the symmetric gluon-gluon induced $t\bar{t}$ production processes cannot contribute to the asymmetry. To account for PDF uncertainties, all Monte Carlo generated events are re-weighted according to alternative weights obtained from another PDF set. Therefore, the 22 eigenvectors of the CTEQ6.6 [64] parametrisation are utilised. For each eigenvector, a plus and a minus variation exist describing the uncertainty on the PDF parameters in the direction of the respective eigenvector in the parameter space. These variations lead to 44 alternative samples obtained from re-weighting the original Monte Carlo samples. The uncertainties on the charge asymmetry measurement induced by the variations of the 22 individual eigenvectors are assumed to be linearly independent, and are therefore added in quadrature.

b-Tagging Uncertainty

The output of the track counting high efficiency b-tagger is utilised to select a $t\bar{t}$ reconstruction hypothesis. To account for uncertainties on the b-tagger discriminator value, the b-tagger output for each jet in the Monte Carlo simulation of signal and background events is shifted. Shifts in different directions are applied for jets matched to b-quarks and jets which are not matched to b-quarks. This matching is based on a comparison of jets based on generated particles and reconstructed jets in the Monte Carlo simulation. If the ΔR distance between the reconstructed jet and a generated jet containing a b-quark is less than 0.4 and $\frac{\Delta p_{\mathrm{T}}(\text{reco-jet, gen-jet})}{p_{\mathrm{T,\ gen\text{-}jet}}} < 3.0$, the reconstructed jet is matched to the generated b-jet. The discriminator value of the b-tagger of jets matched to b-quarks is shifted by ± 0.8, the b-tagger output of all other jets is shifted by ± 0.2. These shifts are chosen in such a way, that they lead to shifts in the b-tagging and mis-tagging efficiencies of the loose and medium working points of the track counting high efficiency b-tagger which are of similar size as the b-tagging uncertainties measured in [195] and [196]. The b-tagger outputs with applied variations are shown in figure 5.26 for the various shifted simulation samples compared to data. The chosen hypothesis is then determined by plugging the shifted b-tagger outputs into the unchanged parameterisation of $P_{\mathrm{b}}(x)$ subject to the variable Ψ (see equation 5.12).

Lepton Efficiency

An artificially reconstructed charge asymmetry could occur from lepton efficiencies which are different for positively and negatively charged leptons since top quark momenta in the used reconstruction scheme for the lepton+jets decay channel are reconstructed including the momenta of positively charged leptons whereas anti-top quarks are reconstructed from negatively charged leptons. As mentioned above, the used trigger and selection efficiency scale factors include uncertainties. Since only overall and no differential lepton selection efficiencies in lepton charge and pseudorapidity have been measured, a re-weighting of all Monte Carlo events within the uncertainties on the overall scale factors is performed.

The re-weighting is applied such, that the changes of the scale factors are maximally different for negatively and positively charged leptons within the overall uncer-

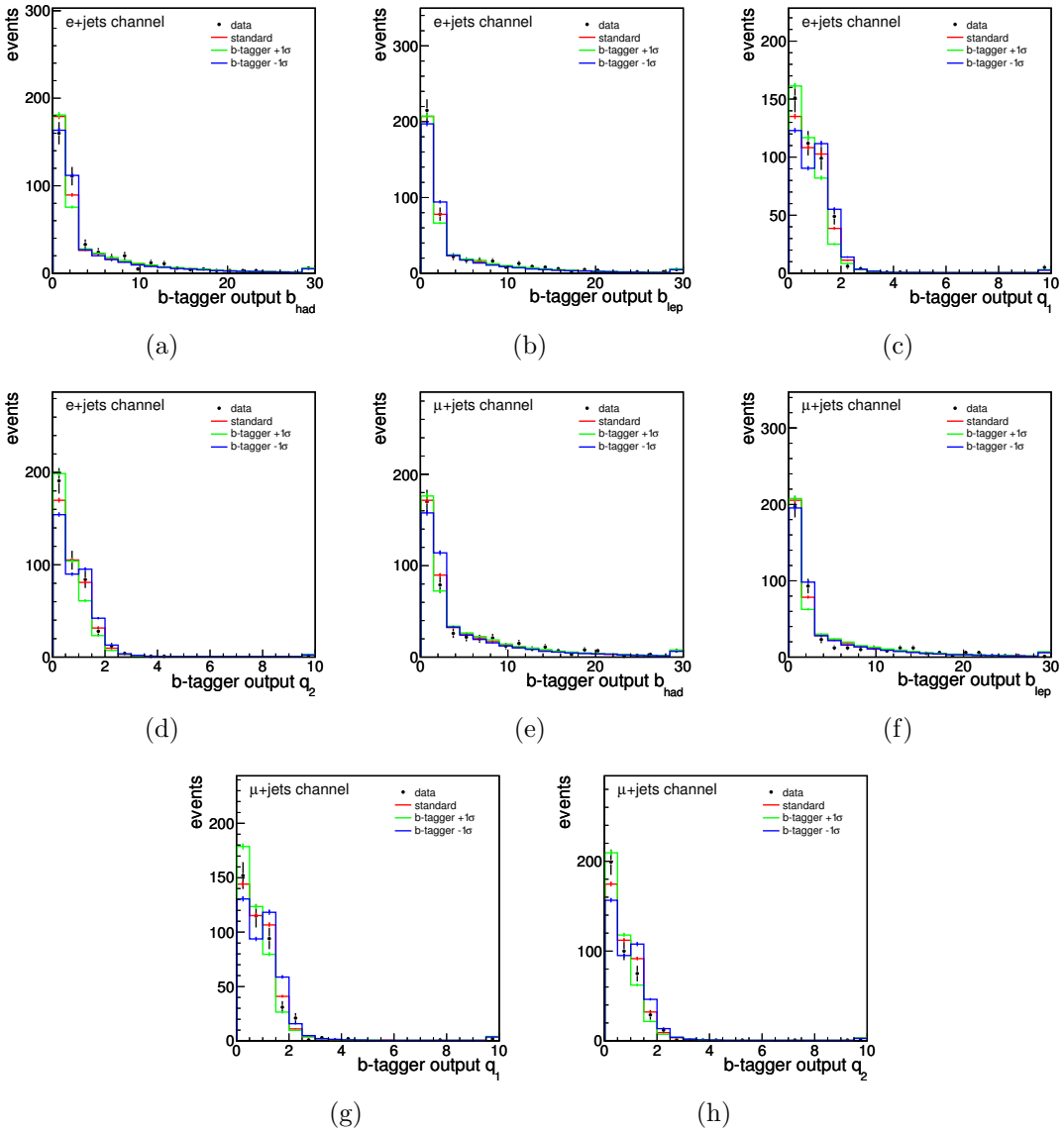

Figure 5.26: Comparison of data to the combined Monte Carlo simulation of all processes $t\bar{t}$, W+jets, Z+jets, and single top quark production with systematically shifted b-tagger outputs in the electron+jets channel in (a) to (d) and in the muon+jets channel in (e) to (h). The sample for QCD multi-jet production is added to the combined simulation but its b-tagger outputs are not shifted since this sample is obtained from data.

tainties. For one direction of an uncertainty, all events in the Monte Carlo generator samples with positively charged leptons are scaled with a factor of $1 + \sigma - \frac{2\sigma}{\eta_{\max}}|\eta_{\text{lep}}|$ and negatively charged leptons with a factor of $1 - \sigma + \frac{2\sigma}{\eta_{\max}}|\eta_{\text{lep}}|$. Here, σ is the lepton scale factor uncertainty as shown on page 105 and $\eta_{\max} = 2.5$ and $\eta_{\max} = 2.1$ for electron+jets and muon+jets events, respectively. For the other direction of this uncertainty the shifts for positively and negatively charged leptons are exchanged.

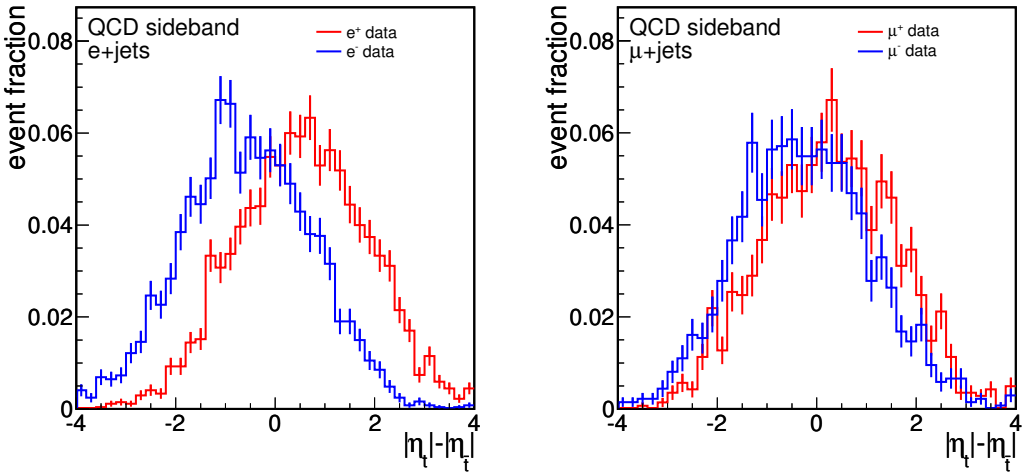

Figure 5.27: Comparison of the $|\eta_t| - |\eta_{\bar{t}}|$ shape in the sideband QCD models with positively and negatively charged electrons (a) and muons (b).

QCD Background Modelling

The QCD multi-jet background can show asymmetries, if the rates of positively and negatively charged leptons in this sample differ. Events from the data sideband used to model QCD multi-jet background events have on average different reconstructed asymmetries in the $|\eta_t| - |\eta_{\bar{t}}|$ distribution depending on the lepton charge, especially in case of the electron+jets channel (see figure 5.27). The differences arise from the lepton pseudorapidity in the QCD sample which is on average higher than in the $t\bar{t}$ signal and the other background processes. Especially in case of the electron+jets selection, the larger amount of material in the forward region of the detector leads to more photon conversions resulting in more background electrons with high pseudorapidities. Since the lepton pseudorapidity is on average larger than the jet pseudorapidities in QCD events, the four-momentum of the reconstructed leptonically decaying top quark will on average have a larger pseudorapidity than the reconstructed hadronically decaying top quark, i. e. $\langle|\eta_{t_{lep}}|\rangle > \langle|\eta_{t_{had}}|\rangle$. For positively charged leptons that means, $\langle|\eta_t|\rangle > \langle|\eta_{\bar{t}}|\rangle$, whereas for negatively charged leptons this leads to $\langle|\eta_{\bar{t}}|\rangle > \langle|\eta_t|\rangle$. The numbers of positively and negatively charged leptons in the QCD background in the finally selected data sample are not a priori known, these numbers are extrapolated from the observation in the QCD sidebands. A validation of several QCD Monte Carlo samples in the sideband as well as in the signal region yields variations of the ratio of positively to negatively charged leptons by up to 5%. For the QCD background modelling, the following modifications of the QCD templates are therefore considered as systematically shifted templates: by re-weighting the events in the QCD sideband sample, the rate of positively charged leptons in the QCD templates is increased by 5%, the rate of negatively charged leptons is decreased by 5% and vice versa.

Monte Carlo Generator

The standard $t\bar{t}$ signal template and also the unfolding matrix is obtained from the MadGraph generator. To investigate a possible systematic uncertainty, an alternative Monte Carlo generator is utilised to produce the $t\bar{t}$ signal in pseudo data sets which are then unfolded with the standard sample. For this purpose, the $t\bar{t}$ process is modelled with the MC@NLO generator as described in section 3.1.2.

Pile-Up Simulation

The standard Monte Carlo simulation used for this analysis does not include any pile-up contributions. Although the amount of pile-up events is expected to be small in the analysed CMS data set, a systematic uncertainty is considered to account for possible influences from pile-up events to the measurement of the charge asymmetry. Therefore, a dedicated Monte Carlo sample for the $t\bar{t}$ signal process including the simulation of pile-up events is used. The number of pile-up events can be estimated from the observed number of primary vertices in collision data. According to the observed number of primary vertices in the most recent data taken in 2010, the number of pile-up events for the simulation has been adopted.

source of systematic	positive shift in A_C	negative shift in A_C
jet energy scale	0.017	-
jet energy resolution	0.007	-0.006
factorisation/renormalisation scale	0.003	-0.007
matching threshold	0.004	-0.006
ISR/FSR	0.005	-0.001
PDF	0.004	-0.011
b-tagging	0.007	-
lepton efficiency	0.017	-0.018
QCD model	0.005	-0.005
MC generator	0.0004	-
pile-up	0.002	-
overall	$\pm$0.026	

Table 5.4: List of the impact of systematic uncertainties taken into account in the measurement of the charge asymmetry A_C. Listed are the positive and negative shifts induced by systematics in ensemble tests. For systematic uncertainties which shift A_C in only one direction only the maximal shift in this direction is quoted. The overall systematic uncertainty is obtained from adding the individual contributions in quadrature and symmetrising the result.

The resulting unfolded charge asymmetry when including the systematic uncertainties listed above are summarised in table 5.4 and visualised in figure 5.28. For systematic uncertainties which shift the asymmetry in the same direction for both up- and downwards fluctuations, only the maximal deviation is quoted. For the Monte Carlo generator uncertainty and the pile-up variation, only one alternative template exists and the reconstructed asymmetry is shifted into one direction only.

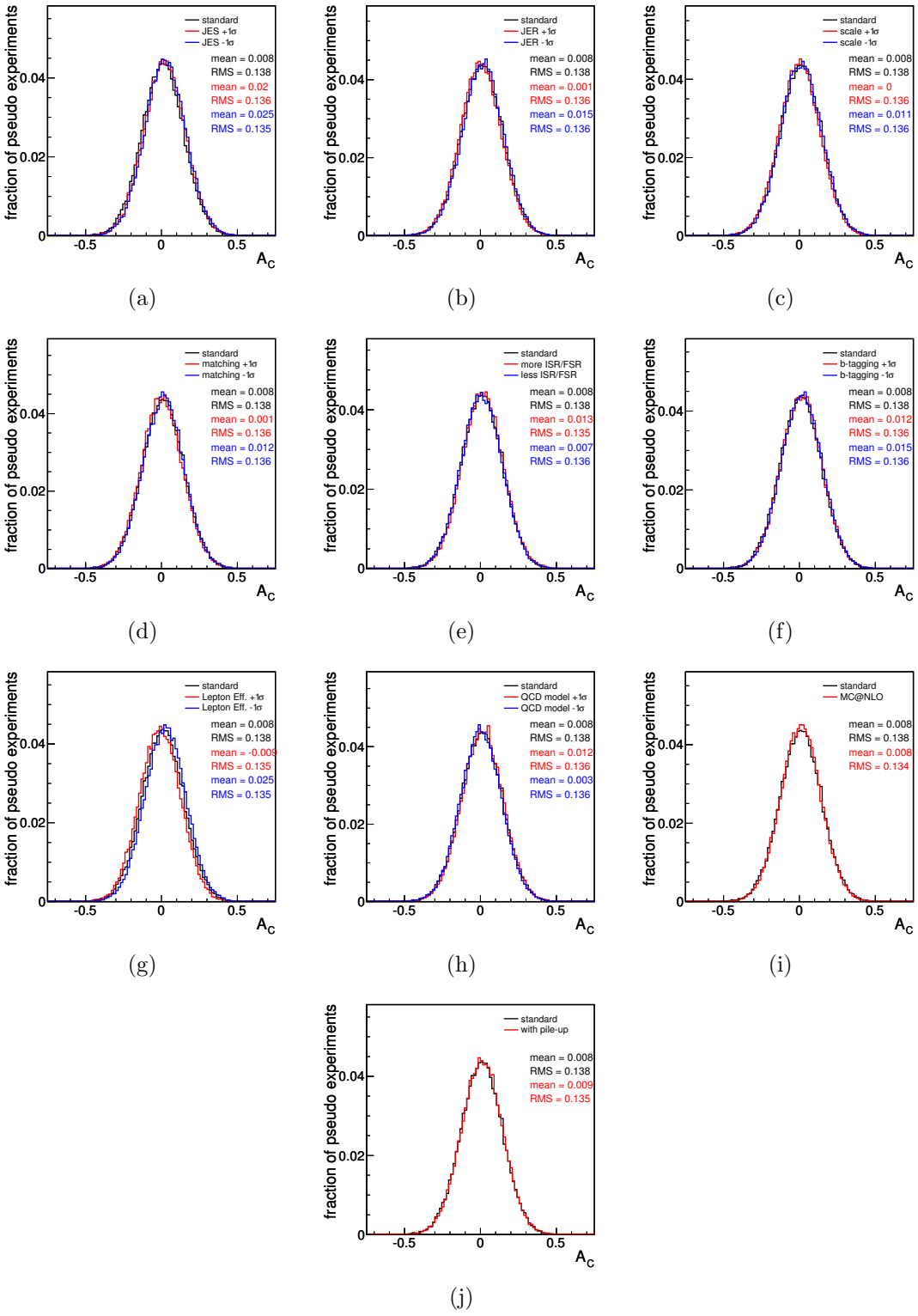

Figure 5.28: Unfolded charge asymmetry in pseudo experiments varying the jet energy scale (a), jet energy resolution (b), factorisation and renormalisation scale (c), matching threshold (d), initial and final state radiation (e), b-tagging discriminator value (f), lepton efficiency (g), the QCD model (h), the signal Monte Carlo generator (i), and the amount of simulated pile-up events (j).

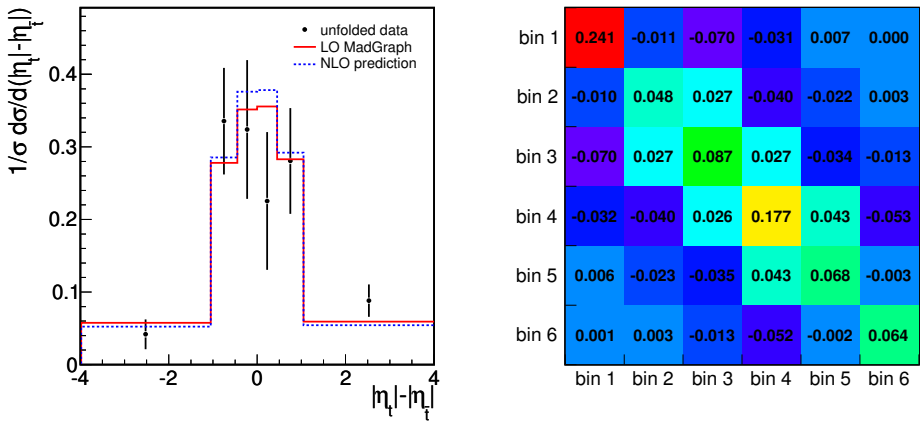

(a) (b)

Figure 5.29: Distribution of the unfolded $|\eta_t| - |\eta_{\bar{t}}|$ spectrum (a). The shown theory curves are the prediction from the MadGraph generator and the NLO prediction from [24–26]. In (b), the full covariance matrix for the measured spectrum is shown.

The overall systematic uncertainty on the measurement of the charge asymmetry in $t\bar{t}$ production is obtained by adding the shifts found for the individual sources of systematic uncertainties in quadrature. To obtain one single number for the overall systematic uncertainty, the total shifts on A_C in positive and negative directions are averaged. After this symmetrisation, an systematic uncertainty of ± 0.026 on the measurement of A_C is expected.

5.6 Result

Having evaluated the correct behaviour of the unfolding mechanism and the impact of several systematic uncertainties in ensemble tests, the unfolding is applied to the measured data. The unfolded $|\eta_t| - |\eta_{\bar{t}}|$ spectrum is depicted in figure 5.29 together with the full covariance matrix containing the correlations between the individual bins. From the unfolded spectrum, the charge asymmetry and its statistical uncertainty can be derived according to equations 5.16 and 5.17. Including also the systematic uncertainty, the final measurement of the charge asymmetry in top quark pair production in proton-proton collisions at a centre-of-mass energy of 7 TeV with the first CMS data corresponding to an integrated luminosity of 36 pb^{-1} results in:

$$A_C = 0.060 \pm 0.134(\text{stat.}) \pm 0.026(\text{syst.}). \tag{5.19}$$

This is the first measurement of the charge asymmetry in top quark pair production performed in proton-proton collisions. The result is dominated by a large statistical uncertainty and shows no deviation from the Standard Model expectation of $A_C^{\text{theo}} = 0.0130 \pm 0.0011$ [24–26] so far, but the developed analysis shows that effects induced by asymmetric couplings of top and antitop quarks can in principle be measured at the LHC.

Chapter 6

Study of High-Mass Resonances Decaying to Top Quark Pairs

Besides the measurement of the $t\bar{t}$ charge asymmetry, the search for resonances in the invariant mass spectrum of the top quark pair is a more direct method to study the potential influence of unknown gauge bosons to $t\bar{t}$ production. Within this chapter, an analysis is presented which focusses on the search for such exchange particles with masses of more than 1 TeV/c^2. This search necessitates different selection and reconstruction techniques due to the special kinematic properties of top quarks originating from the decay of a heavy resonance compared to top quarks produced in Standard Model processes. Aim of the presented analysis is to reconstruct the $m_{t\bar{t}}$ distribution and either observe possible narrow resonances or to set upper limits on such resonances decaying into top quark pairs from a statistical inference of this mass spectrum. The reference signal templates used for the extraction of cross section limits include the process $pp \to Z' \to t\bar{t}$ with a narrow resonance width generated with MadGraph as described in chapter 3.1.2. For the estimation and modelling of expected background processes, data selected in appropriate disjunct phase space regions is used. The presented study used the full data set collected during 2010 in proton-proton collisions corresponding to an integrated luminosity of 36 pb^{-1}.

6.1 Event Topology and Selection

Collision events with top quarks originating from the decay of a heavy resonance possess a unique kinematic topology. Due to the high mass of this potential new particle, top quarks are predicted to be produced with large boost factors in such decays. Therefore, the decay products of the top quarks – the W boson and the b-quark – are often produced with a small angular separation. Also the subsequent decay products of the W bosons are emitted with small phase space distances. The angular distances ΔR in the η–ϕ plane between the top quarks and the decay products of the top quarks are shown in figure 6.1. Presented are the ΔR distributions for Standard Model $t\bar{t}$ production and the process $pp \to Z' \to t\bar{t}$ from the simulation described in section 3.1.2. In such boosted $t\bar{t}$ events, the momenta of quarks in the final state of the hard process are often pointing into nearly the same direction,

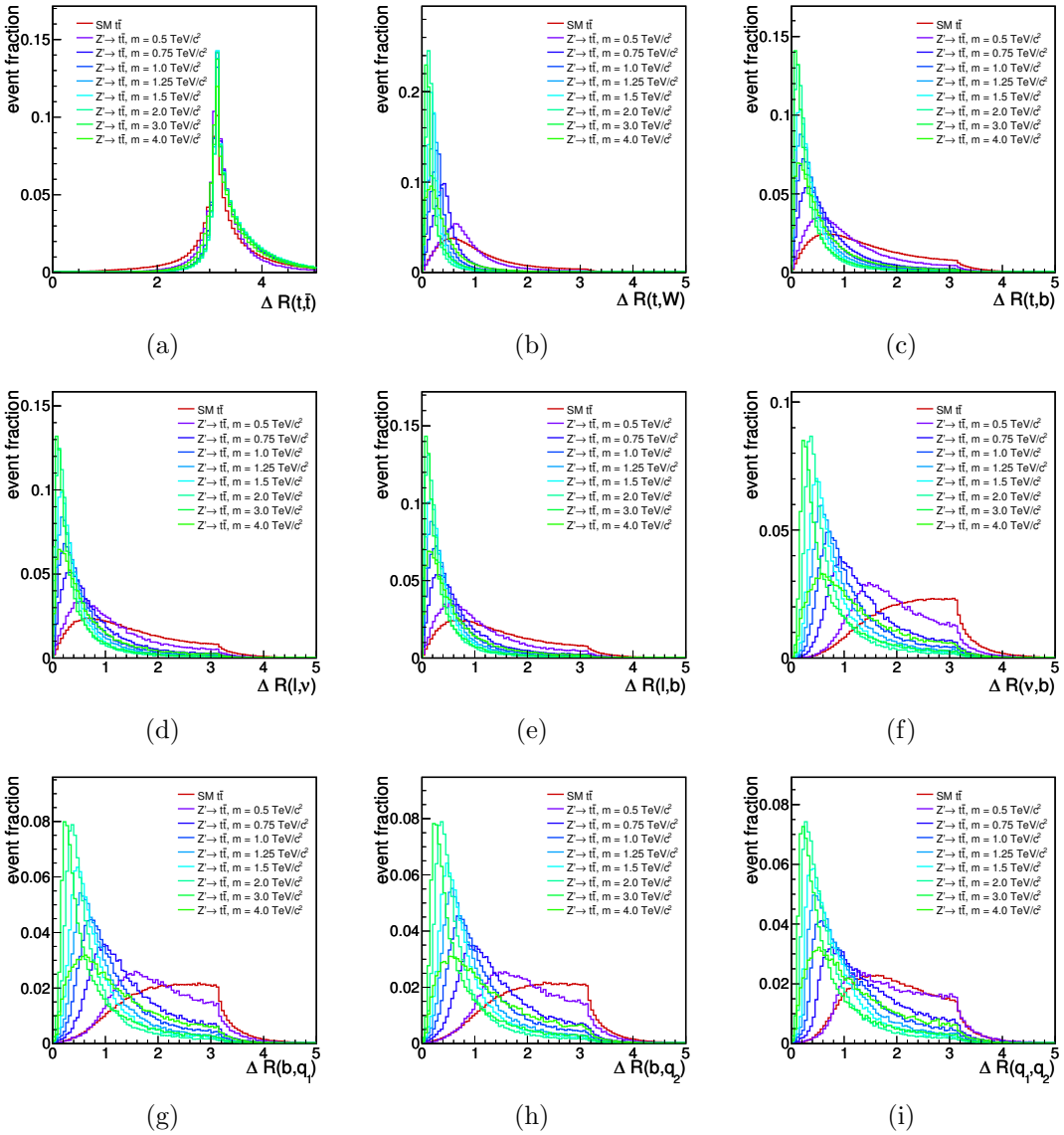

Figure 6.1: Angular distances ΔR in the η–ϕ plane between the two top quarks (a) and the top quarks and their direct decay products, the W boson (b) and the b-quark (c) for Standard Model $t\bar{t}$ production compared to the simulation of $Z' \to t\bar{t}$ events for various Z' boson masses. The width of the Z' resonance is set to 1% of its mass in these samples. Plots (d) to (i) show ΔR distances between the final state particles of the hard $t\bar{t}$ process in the lepton+jets decay channel for SM top quark pair production as well as for the production of $t\bar{t}$ via a Z' boson.

hence, the showering and hadronisation processes of these quarks will not lead to several distinguishable jets in the detector. The stable hadrons emerging from these quarks are more likely to be reconstructed in a single jet in case of the decay of a heavy particle into $t\bar{t}$. In the lepton+jets decay channel, the small angular distance between the charged lepton and the b-quark originating from the same top quark decay can lead to a less well isolated charged lepton in the detector, if the lepton is falling into the reconstructed jet originating from the corresponding b-quark.

Due to this specific event topology of boosted top quarks, the event selection as it is used for the study of Standard Model $t\bar{t}$ events as presented in section 5.1 is not adequate to select events for the study of massive resonances. Therefore, modifications of object definitions and an alternative event selection are developed. The selection cuts are adapted to select highly boosted $t\bar{t}$ events in the muon+jets decay channel.

Muons

Most cuts applied for the definition of a well reconstructed muon follow the description given in section 5.1. Only the cut on the relative isolation, $I^{\mu}_{\text{rel}} < 0.05$, and the cut on the minimal distance between the muon and the closest jet, $\Delta R(\mu, \text{jet}) > 0.3$, are not imposed since the muon in semi-leptonic top quark decays is expected to be less well separated from the b-jet originating from the b-quark in the decay of the same boosted top quark. The kinematic requirements of the muon to fulfil $p_{\text{T}} > 20$ GeV/c and $|\eta| < 2.1$ are the same as in the previous definition of muons.

Electrons

Objects fulfilling the requirements given in section 5.1 for the definition of electron candidates are also used in the analysis of boosted top quarks. As for the muon definition, only the cut on $I^{\text{e}}_{\text{rel}}$ is not applied here. All electrons exceeding $E_{\text{T}} > 30$ GeV and being detected with a pseudorapidity of $|\eta| < 2.5$ are taken into account.

Jets

Jets are reconstructed from Particle Flow objects with the anti-k_{T} algorithm with a radius parameter of 0.5. All selected jets are required to fulfil the identification criteria given in section 5.1 for the definition of jets in the standard $t\bar{t}$ event selection. Only the handling to remove possible overlaps with objects defined as muons or electrons is modified. In the standard selection, all jets with a small ΔR distance to an electron or muon candidate are simply removed from the list of jets. This procedure is not adequate for the selection of jets originating from boosted top quark decays where charged leptons are expected to be emitted close to or even inside a jet. Therefore, particle flow candidate objects, which are identified as an electron or muon with the criteria explained above, have to be removed from a jet, if they have also been used for the clustering of this jet. Therefore, the four-momentum of such an electron or muon is subtracted from the uncorrected momentum vector of the jet. Another modification of jets concerns the minimal transverse momentum defined for their selection. Jets originating from the decay of boosted top quarks carry on average larger momenta. Hence, a cut of $p_{\text{T}} > 50$ GeV/c instead of $p_{\text{T}} > 30$ GeV/c is applied for the selection of jets.

Final Selection Cuts

The final selection cuts being applied to select $t\bar{t}$ candidate events in the muon+jets decay mode are adopted to the expected kinematic topology of top quarks originating

from the decay of a massive resonance particle. The requirements on triggers and on the primary vertex are the same as for the selection used to select events in the muon+jets channel for the measurement of the charge asymmetry described in section 5.1. In addition to trigger and primary vertex conditions, at least one muon with the modified identification criteria as described above has to be found in selected events. Furthermore, all selected candidate events are required to have at least two jets. The minimal number of jets required to select events is relaxed to two since the individual quarks in the final state of a boosted $\mathrm{t\bar{t}}$ event are no longer expected to produce four individual jets. For jets reconstructed with the anti-k_T algorithm with radius $R = 0.5$, the minimal distance between two jet axes is also 0.5 in the η–ϕ plane. If quarks are produced in the hard process with a smaller angular separation, the showering and hadronisation of these quarks will often lead to only one jet in the reconstruction step.

The selected data sample is still dominated by events from QCD multi-jet production since no lepton isolation requirements are applied so far. Therefore, most selected events contain muons originating from the decay of B- or C-hadrons. Since a tight isolation cut is not suitable for the selection of muons from boosted top quark decays, a combination of cuts is developed to reduce the amount of QCD background events. The two variables used to define a cut for the reduction of QCD multi-jet events are the minimal distance in the η–ϕ plane between the charged lepton and the neighboured jet, $\Delta R(\mathrm{l}, \mathrm{jet})$, and the relative transverse momentum of the charged lepton with respect to the direction of the closest jet, $p_\mathrm{T}^\mathrm{rel}$. For the definition of $\Delta R(\mathrm{l}, \mathrm{jet})$ and $p_\mathrm{T}^\mathrm{rel}$, all jets are taken into account with the quality criteria given above but with a relaxed cut on the transverse momentum of $p_\mathrm{T} > 25$ GeV/c. Charged leptons produced from real W or Z boson decays in the hard interaction and not in secondary hadron decays are expected to exhibit larger values in at least one of these two quantities. Muon and electron candidates used for the final selection are therefore required to have either $\Delta R(\mathrm{l}, \mathrm{jet}) > 0.5$ or $p_\mathrm{T}^\mathrm{rel} > 25$ GeV/c. The combined cut on $\Delta R(\mathrm{l}, \mathrm{jet})$ and $p_\mathrm{T}^\mathrm{rel}$ is referred to as 2D cut. This 2D cut has been found to be more efficient for the selection of $\mathrm{t\bar{t}}$ events with high invariant masses than a cut on the isolation of the muon and provides a selection efficiency which is nearly constant as a function of $m_{\mathrm{t\bar{t}}}$ [197]. For the selection of candidate events for boosted top quarks in the muon+jets decay channel, the selected muon is required to fulfil the 2D cut. In addition, events are rejected, if an electron fulfilling all selection criteria including the 2D cut is found with a transverse energy larger than the transverse momentum of any selected muon in the event.

To achieve a further suppression of background events from nearly all processes – W+jets, Z+jets, single top, QCD multi-jet, and Standard Model $\mathrm{t\bar{t}}$ production – an additional cut exploiting the expected high transverse momenta of leptons in the production of boosted top quarks is applied. Therefore, the leptonic transverse momentum, $H_\mathrm{T}^\mathrm{lep}$, is defined as the sum of the transverse momentum of the charged lepton and the missing transverse energy usually associated to the neutrino momentum:

$$H_\mathrm{T}^\mathrm{lep} := p_{\mathrm{T,l}} \cdot c + \not{E}_\mathrm{T}. \tag{6.1}$$

Selected events are required to exceed $H_\mathrm{T}^\mathrm{lep} > 150$ GeV. The expected number of

process	σ [pb]	without $H_{\mathrm{T}}^{\mathrm{lep}}$ cut	$H_{\mathrm{T}}^{\mathrm{lep}} > 150$ GeV
$\mathrm{t\bar{t}}$	165 ± 10	599 ± 44	117 ± 9
W+jets	$31,314 \pm 1,558$	$1,346 \pm 87$	171 ± 11
Z+jets	$3,048 \pm 132$	277 ± 17	22 ± 1
single top, t-channel	64.6 ± 3.3	148 ± 10	11 ± 1
single top, tW-channel	10.6 ± 0.8	25 ± 2	5.4 ± 0.5
QCD	(79,688)	$4,226 \pm 170$	5.3 ± 0.2
sum		$6,622 \pm 277$	331 ± 17
observed data		7,228	389

Table 6.1: Expected number of events after the full event selection before and after the cut on $H_{\mathrm{T}}^{\mathrm{lep}}$. The expectations obtained from Monte Carlo simulations are normalised to the cross section σ of the respective processes and the integrated luminosity of 36 pb^{-1}. Quoted are the combined uncertainties on cross section, number of generated Monte Carlo events, and the uncertainty on the luminosity of 4%. The $\mathrm{t\bar{t}}$ cross section is taken from [65], W+jets, Z+jets, and single top cross sections are computations obtained with the FEWZ [198] and MCFM [199] packages. For the QCD multi-jet background, only the LO cross section provided by Pythia for the muon enriched QCD sample is quoted.

events for the different background processes as described in section 3.1.3 before and after this final cut are summarised in table 6.1. The event numbers are normalised to the theoretical cross sections and an integrated luminosity of 36 pb^{-1}. The $H_{\mathrm{T}}^{\mathrm{lep}}$ cut reduces the main background processes by approximately one order of magnitude. Especially the QCD multi-jet background is suppressed from several thousands to less than ten events. Most important background processes after the final $H_{\mathrm{T}}^{\mathrm{lep}}$ cut are W+jets production and SM $\mathrm{t\bar{t}}$ processes. The number of observed events in data lies slightly above the expectations from Monte Carlo simulations, but the quoted uncertainties do not include any uncertainty on the cross section of the QCD multi-jet background and no systematic uncertainties on the Monte Carlo modelling.

A comparison of the observed data to the Monte Carlo simulation is shown in figure 6.2. Besides the excess of data over the Monte Carlo prediction, also the shape of the shown variables is not perfectly described by the simulation. Especially in the tail of the $H_{\mathrm{T}}^{\mathrm{lep}}$ spectrum a larger amount of data is observed compared to the expectation. A selection of kinematic distributions showing the comparison between data and Monte Carlo simulation after the final selection including the $H_{\mathrm{T}}^{\mathrm{lep}}$ cut are presented in figure 6.3. In all variables, a slight discrepancy in the normalisation of the Monte Carlo simulation samples with the observed data can be seen. Within the statistical uncertainties, the shapes of these kinematic variables are described well.

In table 6.2, the numbers of generated and selected events in the MadGraph simulation of an exotic Z′ boson for various resonance masses are listed. The final selection efficiency for these samples is of the order of 10% for all mass points above 1 TeV/c^2. As can bee seen, the final $H_{\mathrm{T}}^{\mathrm{lep}}$ cut does reduce the amount of selected signal events with high resonance masses only by a small fraction of about 20%. The overall cut efficiency in the muon+jets decay channel, which is considered as the signal process in this analysis, is between 40% and 50% for resonance processes with

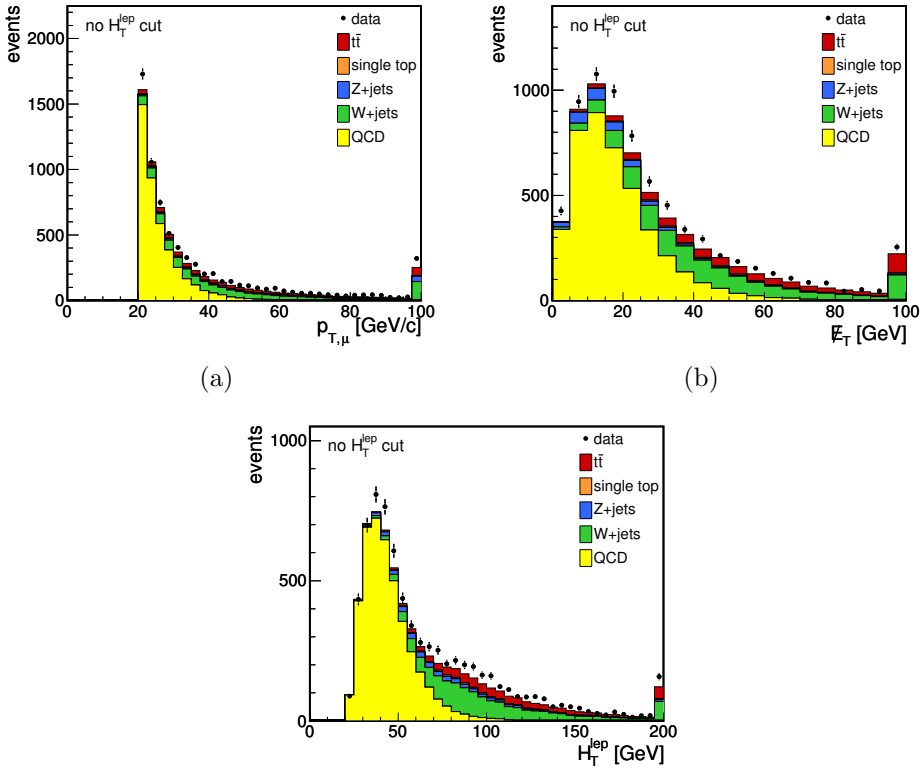

Figure 6.2: Comparison of the Monte Carlo simulation of various background processes to the measured data for the transverse momentum of the muon (a), missing transverse energy (b), and their sum $H_{\mathrm{T}}^{\mathrm{lep}}$ (c) before applying the final cut of $H_{\mathrm{T}}^{\mathrm{lep}} > 150$ GeV. The simulation is normalised to the prediction given in table 6.1.

process	no cut	without $H_{\mathrm{T}}^{\mathrm{lep}}$ cut	$H_{\mathrm{T}}^{\mathrm{lep}} > 150$ GeV	ϵ [%]
Z′ ($m = 0.5$ TeV/c^2)	227,068	23,644	4,563	2.0
Z′ ($m = 0.75$ TeV/c^2)	204,819	25,772	12,970	6.3
Z′ ($m = 1.0$ TeV/c^2)	213,384	29,470	19,992	9.4
Z′ ($m = 1.25$ TeV/c^2)	233,361	33,764	26,197	11.2
Z′ ($m = 1.5$ TeV/c^2)	193,779	28,688	23,807	12.3
Z′ ($m = 2.0$ TeV/c^2)	238,752	36,191	32,148	13.5
Z′ ($m = 3.0$ TeV/c^2)	205,270	30,577	25,927	12.6
Z′ ($m = 4.0$ TeV/c^2)	183,920	24,911	16,448	8.9

Table 6.2: Number of generated Monte Carlo events for the process $\mathrm{pp} \to \mathrm{Z}' \to \mathrm{t\bar{t}}$ for various masses of the Z′ boson. The width of the Z′ resonance is set to 1% of its mass in these samples. The simulation contains all possible decay channels of the top quark pair. Quoted are the total number of generated events and the number of selected events before and after the final cut on $H_{\mathrm{T}}^{\mathrm{lep}}$ as well as the total selection efficiency ϵ.

Z′ boson masses larger than 1 TeV/c^2. Other decay channels are also contributing to the finally selected signal samples. The individual decay channel contributions

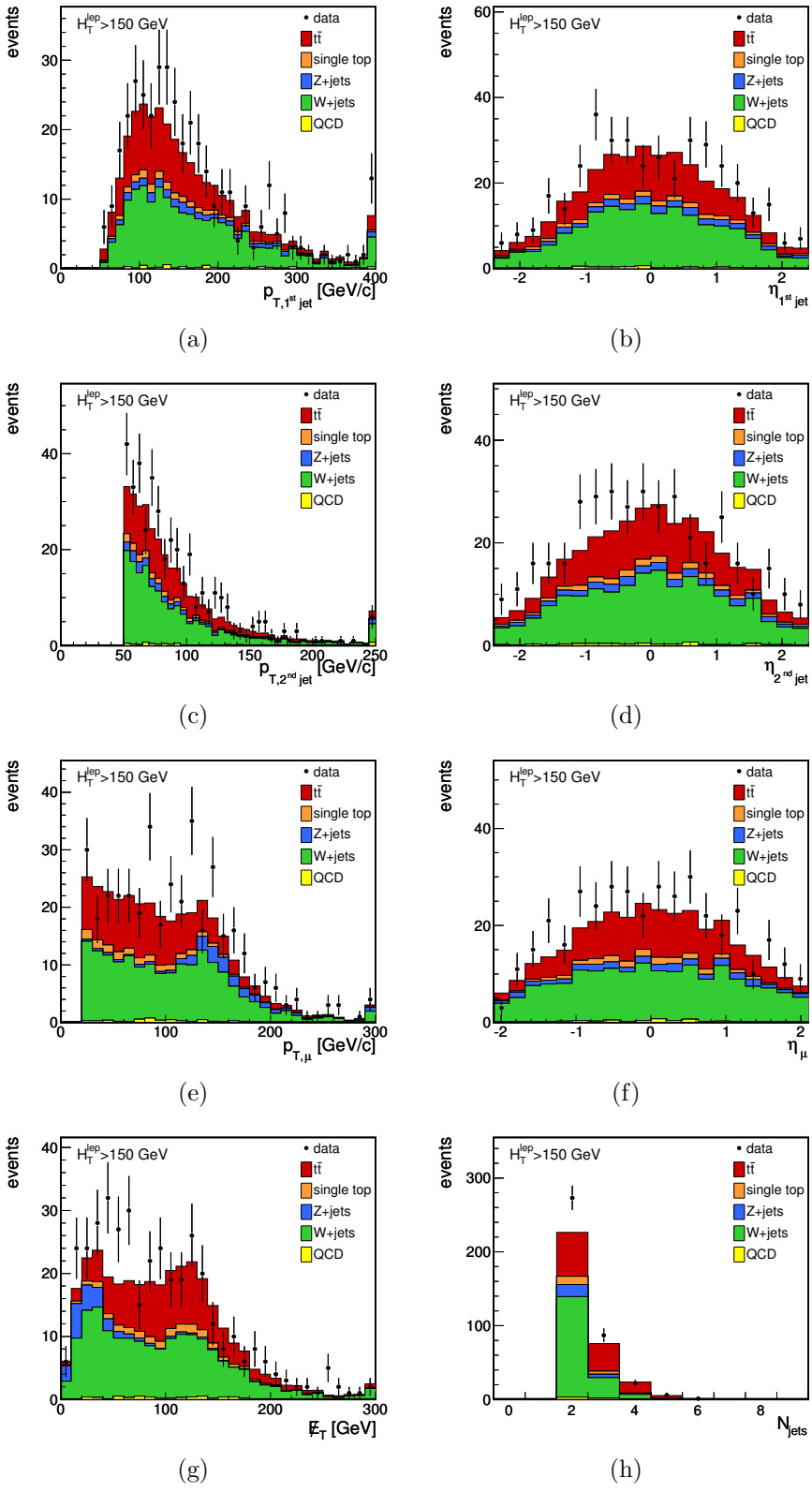

Figure 6.3: Comparison of the Monte Carlo simulation of various background processes to the measured data after applying the final cut of $H_{\mathrm{T}}^{\mathrm{lep}} > 150$ GeV for the transverse momenta and pseudorapidities of the two jets with highest and second highest p_{T} in (a) to (d), transverse momentum and pseudorapidity of the muon in (e) and (f), the missing transverse energy (g), and the number of jets (h).

process	μ+jets	e+jets, τ+jets	di-lepton	all-hadronic
Z′ ($m = 0.5$ TeV/c^2)	66.1%	4.6%	29.4%	0.0%
Z′ ($m = 0.75$ TeV/c^2)	70.2%	6.3%	23.4%	0.1%
Z′ ($m = 1.0$ TeV/c^2)	67.9%	6.6%	25.2%	0.4%
Z′ ($m = 1.25$ TeV/c^2)	67.2%	6.6%	25.2%	1.0%
Z′ ($m = 1.5$ TeV/c^2)	65.9%	6.6%	25.6%	1.9%
Z′ ($m = 2.0$ TeV/c^2)	64.4%	6.7%	26.0%	3.0%
Z′ ($m = 3.0$ TeV/c^2)	64.1%	6.4%	26.5%	3.0%
Z′ ($m = 4.0$ TeV/c^2)	65.2%	6.5%	26.7%	1.6%

Table 6.3: Contributions from the $t\bar{t}$ decay channels to the finally selected signal samples.

for the considered Monte Carlo samples are summarised in table 6.3. Events in the muon+jets channel contribute to about two third of the selected samples. The second largest contribution to the signal originates from $t\bar{t}$ events in the di-lepton decay mode where mostly the $\mu + \tau$ decay channel has a similar signature as the muon+jets decay process. Also events from the lepton+jets channel with τ leptons are accounting for approximately 6% of the selected signal samples. For Z′ boson masses of several TeV/c^2, also a few events from the all-hadronic decay channel are selected. The Monte Carlo sample for a Z′ boson with a mass of 4 TeV/c^2 shows a smaller selection efficiency than the samples with Z′ boson masses of 2 TeV/c^2 and 3 TeV/c^2. Also the contributions of the individual decay channels for this sample shown in table 6.3 are more similar to the samples with lower Z′ boson masses of 1.25 TeV/c^2 or 1.5 TeV/c^2. This effects can be explained by the fact that in most events of this sample the Z′ boson is produced off-shell with lower invariant masses as has been shown in figure 3.5.

6.2 Reconstruction of the Invariant Mass of the Top Quark Pair

For a further discrimination of heavy resonances in $t\bar{t}$ production from SM background processes, the invariant mass $m_{t\bar{t}}$ of the top quark pair system can be exploited. As has been shown in figures 3.3 and 3.5, the invariant mass spectrum shows clear peaks around the mass of the new gauge boson in case of $t\bar{t}$ production via the exchange of such heavy resonances. As the variable $|\eta_t| - |\eta_{\bar{t}}|$ used in chapter 5 to measure the charge asymmetry in top quark pair production, also the invariant mass cannot be measured directly and has to be estimated from measurable detector objects. The full reconstruction of all final state particles in the hard process of the $t\bar{t}$ production as it has been used in section 5.2 is no longer feasible for the study of boosted top quarks. The previously used reconstruction technique is based on the assumption that always one measured jet can be assigned to each final state quark. Due to the specific topology of boosted top quark events often leading to merged jets, this jet-to-quark assignment cannot be utilised for the reconstruction of top

quark momenta in this case.

Therefore, the reconstruction of the top quark four-momenta in the analysis of boosted top quarks does not rely on the full reconstruction of all final state particles but exploits the specific signature and kinematic behaviour of top quarks originating from the decay of a heavy resonance particle to allow an event-by-event estimation of the invariant mass $m_{\mathrm{t\bar{t}}}$. For this purpose, a similar approach of creating a list of reconstruction hypotheses for different object assignments as it has been done in section 5.2 is performed. In a second step, a quality criterion is constructed to select a reconstruction hypothesis which results in a good estimation of $m_{\mathrm{t\bar{t}}}$.

The only particles in the final state of the $\mathrm{t\bar{t}}$ process in the muon+jets decay channel which can still be reconstructed individually are the charged lepton and the corresponding neutrino. The reconstruction of the leptons is performed in the same way as described in section 5.2. For the muon momentum, the momentum of the reconstructed muon fulfilling all identification criteria with the largest p_{T} is taken. The x and y components of the neutrino momentum p_ν are reconstructed from the observed missing transverse energy according to equation 5.5 as it is done for the reconstruction of the neutrino in the previous analysis. For the reconstruction of the z coordinate of the neutrino's momentum vector, the solutions of equation 5.7 are considered. In case of non-real solutions for $p_{z,\nu}$, only the real part is taken into account. Hence, the determination of the neutrino momentum leads to one or two different reconstruction hypotheses. From the reconstructed lepton momenta, the four-momentum of the leptonically decaying W boson, $\mathrm{W_{lep}}$, is determined for each neutrino hypothesis.

The list of reconstruction hypotheses is accomplished by the assignment of jets. Since also events with less than four jets are selected, jets cannot be assigned to the quarks in the decay chain of the two top quarks. Therefore, jets are directly assigned to originate from the top or the antitop quark. Each jet can either be assigned to the leptonically decaying top quark $\mathrm{t_{lep}}$, to the hadronically decaying top quark $\mathrm{t_{had}}$, or to none of them. The latter case takes into account the possibility that an observed jet originates from an initial state radiation and has no direct connection to the top quark pair. If N jets are observed in an event, the assignment of jets leads in principle to 3^N reconstruction hypotheses. The number of hypotheses is reduced since only hypotheses are taken into account where at least one jet is assigned to $\mathrm{t_{lep}}$ and $\mathrm{t_{had}}$, respectively. For instance, in a two-jet event, only two possibilities for the jet assignment are considered. The first jet can be assigned to $\mathrm{t_{lep}}$ and the second jet to $\mathrm{t_{had}}$ or vice-versa. Together with the one or two interpretations of the neutrino momentum, this leads to two or four different reconstruction hypotheses for events with exactly two jets. For a further simplification and reduction of the number of reconstruction hypotheses in events with more than two jets, only jets are taken into account in the assignment to the top quarks which exceed $p_{\mathrm{T}} > 0.1 \cdot H_{\mathrm{T}}$ where H_{T} is defined as the scalar sum of the transverse momenta of all jets, the transverse momentum of the leading charged lepton, and the missing transverse energy $\not{E}_{\mathrm{T}}$.

In each considered reconstruction hypothesis, the four-momentum of the hadronically decaying top quark $\mathrm{t_{had}}$ is reconstructed by adding the four-momenta of all jets assigned to this quark. All jets assigned to the semi-leptonically decaying top quark

t_{lep} are also added. These jets are assumed to originate from the b_{lep}. Together with the previously reconstructed W_{lep}, the four-momenta of this W boson and the reconstructed b-quark are added to give the t_{lep} vector. From the reconstructed top quark four-momenta, also the invariant mass $m_{t\bar{t}}$ can be determined in each event.

For the selection of a single reconstruction hypothesis in each event, the expected event topology of a high-mass resonance decaying to $t\bar{t}$ is exploited. Since only the decay products of t_{lep} – the b_{lep}, the neutrino ν, and the charged lepton l – can be determined individually, in a first step only the reconstruction of these objects is considered to select possible reconstruction hypotheses. In the decay of a heavy resonance, the decay products of the top quarks are expected to be produced with small angular separation. Therefore, all selected hypotheses are required to have a minimal ΔR_{sum}, where ΔR_{sum} is defined as the sum of distances in the η–ϕ plane between the reconstructed top quark t_{lep} and its decay products:

$$\Delta R_{\text{sum}} := \Delta R(p_{b_{lep}}, p_{t_{lep}}) + \Delta R(p_\nu, p_{t_{lep}}) + \Delta R(p_l, p_{t_{lep}}). \tag{6.2}$$

Up to now, only the semi-leptonically decaying top quark has been taken into account to find a final reconstruction hypothesis. Therefore, several hypotheses might exist which have the same minimal ΔR_{sum} value but differ in the reconstruction of the hadronically decaying top quark. If this is the case, the hypothesis with largest angular separation between the two top quark momenta $\Delta R(p_{t_{had}}, p_{t_{lep}})$ is finally selected as reconstruction hypothesis because the two top quarks are expected to be produced most likely in a back-to-back topology.

For a validation of the reconstruction performance, a best possible hypothesis can be defined in generated Monte Carlo events. In the analysis of the charge asymmetry in $t\bar{t}$ production, the best possible solution has been defined as the hypothesis which minimises the term 5.9. Since the hadronically decaying W boson is not reconstructed in case of boosted top quarks, the best possible solution on Monte Carlo events is defined as the hypothesis with minimal distances between true and reconstructed top quark momenta only, i. e. the hypothesis for which

$$\Delta R(p^{\text{rec}}_{t_{lep}}, p^{\text{true}}_{t_{lep}}) + \Delta R(p^{\text{rec}}_{t_{had}}, p^{\text{true}}_{t_{had}}) \tag{6.3}$$

is minimal. A comparison of the best possible hypothesis to the selected hypothesis in Monte Carlo simulations of a Z' boson decaying to $t\bar{t}$ in the muon+jets decay channel is presented in figure 6.4. Shown are the relative resolutions of the reconstructed $m_{t\bar{t}}$ for various Z' boson masses in both reconstruction hypotheses. In the chosen reconstruction hypothesis, biases of the reconstructed $m_{t\bar{t}}$ towards lower values can be seen especially for the samples with smaller Z' boson masses, but slightly smaller biases are already visible in the best possible hypothesis. To have a better estimation of the quality of the reconstruction, a Gaussian function is fitted to the central peaks of the resolution distributions. The resulting values for means and widths of the Gaussian fits are summarised in table 6.4. The selected hypothesis is mostly close to the best possible hypothesis concerning the results of this fits. For high-mass resonances with masses above 1 TeV/c^2, a mass resolution of approximately 10% or lower is reached and the biases on the central value of the reconstructed $m_{t\bar{t}}$ distributions are of the order of a few percent.

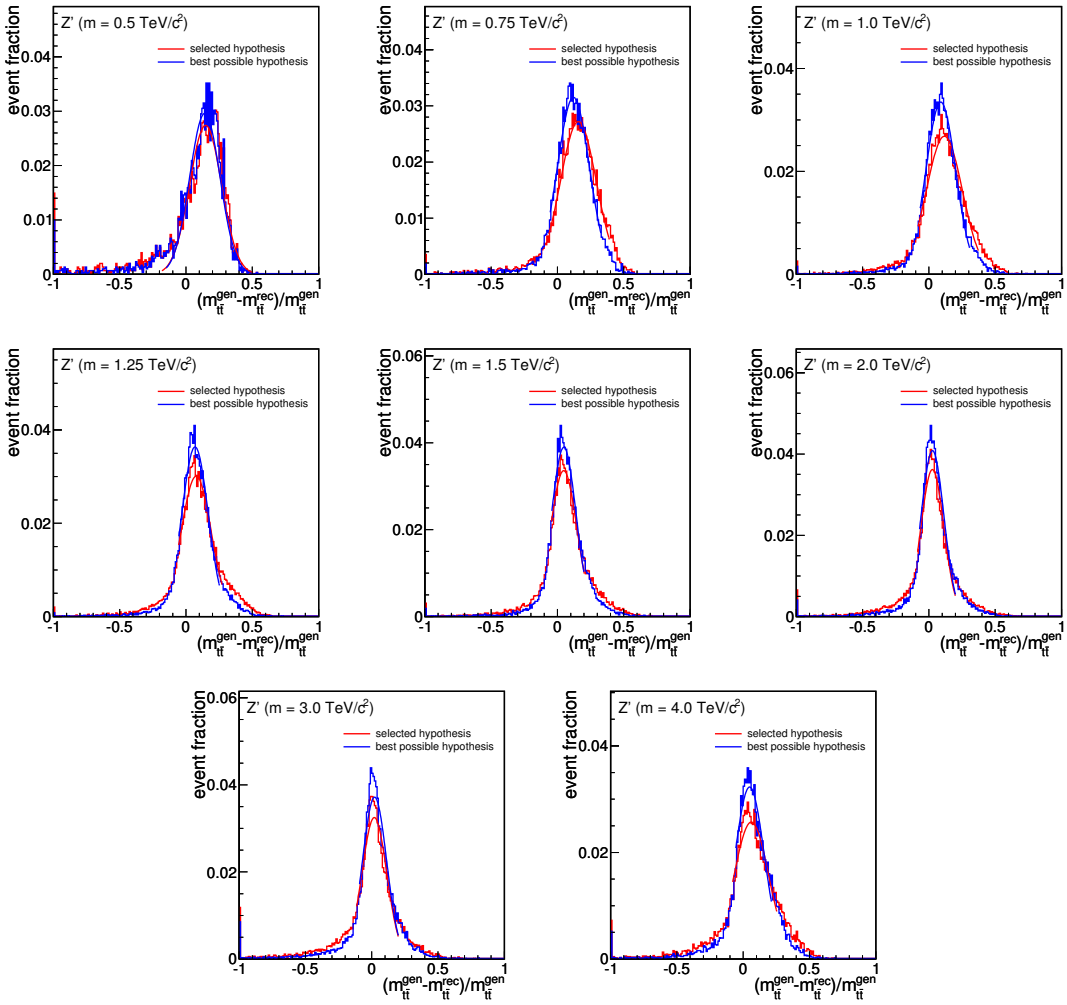

Figure 6.4: Relative resolution of the top quark pair invariant mass for the best possible hypothesis and the hypothesis using ΔR_{sum} for Z′ samples with various resonance masses between 0.5 TeV/c^2 and 4.0 TeV/c^2.

	best possible hypothesis		selected hypothesis	
process	mean	width	mean	width
Z' $(m = 0.5$ TeV$/c^2)$	0.142	0.114	0.148	0.120
Z' $(m = 0.75$ TeV$/c^2)$	0.120	0.121	0.158	0.136
Z' $(m = 1.0$ TeV$/c^2)$	0.090	0.112	0.117	0.136
Z' $(m = 1.25$ TeV$/c^2)$	0.068	0.100	0.077	0.114
Z' $(m = 1.5$ TeV$/c^2)$	0.048	0.093	0.047	0.100
Z' $(m = 2.0$ TeV$/c^2)$	0.027	0.086	0.026	0.087
Z' $(m = 3.0$ TeV$/c^2)$	0.021	0.091	0.019	0.094
Z' $(m = 4.0$ TeV$/c^2)$	0.048	0.111	0.061	0.131

Table 6.4: Mean and width values of Gaussian functions fitted to the central peaks of the resolution of $m_{\mathrm{t\bar{t}}}$ for the various signal Monte Carlo samples shown in figure 6.4.

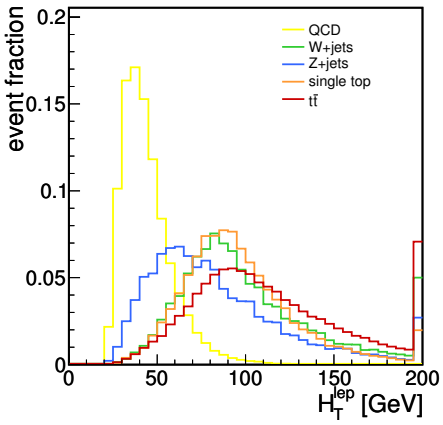

Figure 6.5: Distribution of $H_{\mathrm{T}}^{\mathrm{lep}}$ in the Monte Carlo simulation of various background processes.

6.3 QCD Background Modelling

The exploration of the invariant mass spectrum of the top quark pair requires a good understanding of the SM background processes. To estimate the rate of the individual contributions of the backgrounds to the selected data sample, the specific features of the $H_{\mathrm{T}}^{\mathrm{lep}}$ variable are utilised. $H_{\mathrm{T}}^{\mathrm{lep}}$ shows different characteristic shapes for various background processes (see figure 6.5). QCD mulit-jet production is expected to contain neither charged leptons nor neutrinos with large transverse momenta, thus, QCD events show on average small $H_{\mathrm{T}}^{\mathrm{lep}}$ values. W+jets, SM $\mathrm{t\bar{t}}$, and single top quark production leads to a charged lepton and a neutrino from the decay of a real W boson. This leads to relatively large momenta for the observed muon and also to larger values of $\not\!\!E_{\mathrm{T}}$. Hence, also the sum of lepton momentum and $\not\!\!E_{\mathrm{T}}$ shows on average higher values compared to QCD multi-jet events for background processes containing W boson production. Selected Z+jets events contain charged leptons from the decay of a Z boson with relatively large momenta, but in those events no neutrinos are expected to occur in the hard scattering process. Therefore, the maximum in the $H_{\mathrm{T}}^{\mathrm{lep}}$ shape of Z+jets events is larger than the average $H_{\mathrm{T}}^{\mathrm{lep}}$ values in QCD multi-jet production but smaller than the average $H_{\mathrm{T}}^{\mathrm{lep}}$ in typical W boson events.

The specific shape of the $H_{\mathrm{T}}^{\mathrm{lep}}$ variable allows to constrain the individual background event rates. In the presented analysis, the selected data in the distribution of $H_{\mathrm{T}}^{\mathrm{lep}}$ is examined in the region with $H_{\mathrm{T}}^{\mathrm{lep}} < 150$ GeV. A statistical inference of the $H_{\mathrm{T}}^{\mathrm{lep}}$ distribution is performed simultaneously with the reconstructed $m_{\mathrm{t\bar{t}}}$ distribution in the signal region with $H_{\mathrm{T}}^{\mathrm{lep}} > 150$ GeV to estimate upper limits on the cross section of possible resonances in top quark pair production. This combined statistical examination of both distributions allows to constrain the background contributions in the $m_{\mathrm{t\bar{t}}}$ signal region from the extrapolation of the result in the low-$H_{\mathrm{T}}^{\mathrm{lep}}$ region.

To perform the explained statistical procedure, an adequate modelling of the used variables is required. As can be seen in figure 6.2 (c), the $H_{\mathrm{T}}^{\mathrm{lep}}$ distribution measured

in data is not correctly modelled by the Monte Carlo simulation. The main background process in the region with low $H_{\mathrm{T}}^{\mathrm{lep}}$ values is QCD multi-jet production. For a more suitable description of $H_{\mathrm{T}}^{\mathrm{lep}}$, a QCD model based on measured collision data and not on the generation of Monte Carlo events is developed. The data used to model the QCD background processes has to be taken from a statistically independent sideband region which is dominated by QCD multi-jet production. However, this sideband has to be as close as possible in phase space to the one for QCD multi-jet production in the signal region to allow a reliable extrapolation. The most natural way to choose a sideband region in data for the QCD modelling is to apply the full event selection but with relaxed cuts on the muon identification criteria. The 2D cut has been introduced to separate muons having their origin in QCD multi-jet production from muons produced in signal-like processes. Hence, an inversion of this cut when selecting data for the QCD sideband model ensures to select data events dominated by muons not produced in hard scattering processes including W or Z boson exchanges. Selected events for the QCD sideband have therefore to fulfil all selection requirements including the existence of two jets and one muon. However, the muon candidate has to fail the 2D cut on $\Delta R(\mathrm{l},\mathrm{jet}) > 0.5$ and $p_{\mathrm{T}}^{\mathrm{rel}} > 25$ GeV/c, events with a second muon fulfilling the 2D cut are also rejected for this selection. Obviously, the cut on $H_{\mathrm{T}}^{\mathrm{lep}} > 150$ GeV is not applied, too.

For a validation of the QCD model obtained from inverting the 2D cut, the sideband region is divided into different sub-samples. The sideband regions S_0 to S_3 are defined by the various $\Delta R(\mathrm{l},\mathrm{jet})$ values of the selected muon candidates. Muon candidates of selected events in the sideband regions S_0, S_1, S_2, and S_3 are required to fulfil $\Delta R(\mathrm{l},\mathrm{jet}) \in [0.0, 0.1]$, $\Delta R(\mathrm{l},\mathrm{jet}) \in [0.1, 0.2]$, $\Delta R(\mathrm{l},\mathrm{jet}) \in [0.2, 0.3]$, and $\Delta R(\mathrm{l},\mathrm{jet}) \in [0.3, 0.5]$, respectively. The shapes of the $H_{\mathrm{T}}^{\mathrm{lep}}$ distribution in the individual sideband regions for data and for the Pythia Monte Carlo simulation of muon enriched QCD multi-jet production are shown in figure 6.6. In the Monte Carlo simulation presented in figure 6.6(a), the shape of $H_{\mathrm{T}}^{\mathrm{lep}}$ of the QCD multi-jet production in the signal region is well reproduced by the simulation of the three sideband regions S_1, S_2, and S_3. Only the sideband region S_0 shows a systematically shifted $H_{\mathrm{T}}^{\mathrm{lep}}$ distribution with respect to the QCD multi-jet production in the signal region. The observation in the simulation supports the assumption that the distribution of $H_{\mathrm{T}}^{\mathrm{lep}}$ in the region with all muon identification criteria being applied is well modelled by QCD multi-jet events from the sideband region. Only the sideband region S_0 with smallest $\Delta R(\mathrm{l},\mathrm{jet})$ values has to be excluded when modelling the QCD sample from a sideband with inverted 2D cut. In the $H_{\mathrm{T}}^{\mathrm{lep}}$ distribution of sideband events taken from data shown in figure 6.6(b), it can also be seen that the respective shapes of this distribution are similar for the sideband regions S_1, S_2, and S_3. From the Monte Carlo simulation, the expected purity of QCD multi-jet events in the combined sidebands S_1, S_2, and S_3 excluding the sideband region S_0 is still larger than 99%.

The main contribution of QCD multi-jet background consists of events with $H_{\mathrm{T}}^{\mathrm{lep}}$ values smaller than 150 GeV. The sideband model can also be used to estimate the fraction of QCD events in the finally selected data sample with $H_{\mathrm{T}}^{\mathrm{lep}} > 150$ GeV and to model the template of the $m_{\mathrm{t\bar{t}}}$ distribution for this process. This modelling

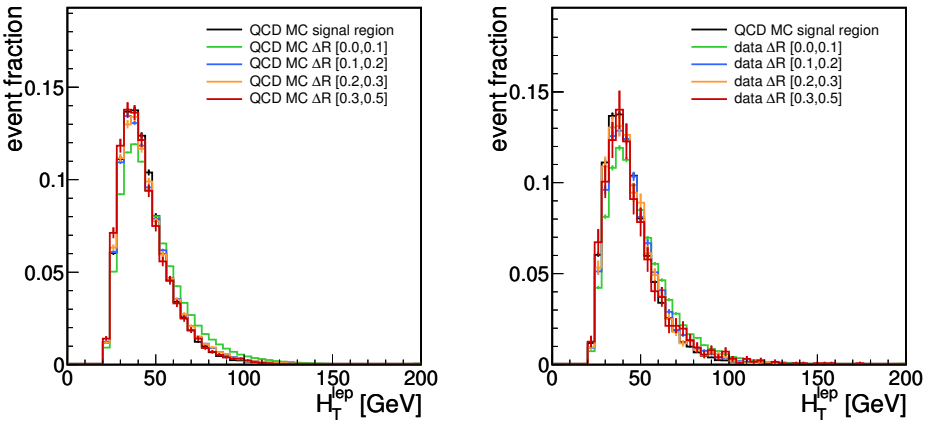

(a) (b)

Figure 6.6: Comparison of H_T^{lep} for the sideband regions S_i and the signal region. In (a), the sideband distributions are taken from QCD Monte Carlo, in (b) the sideband distributions are obtained from data.

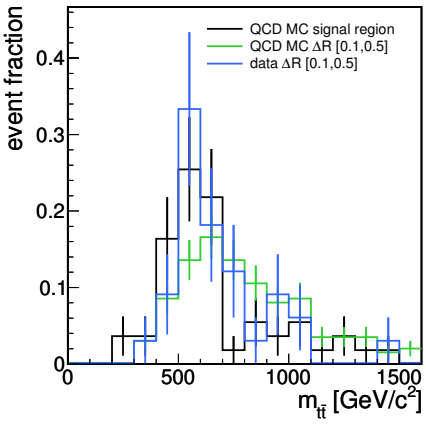

Figure 6.7: Distribution of $m_{t\bar{t}}$ for events with $H_T^{lep} > 150$ GeV in the QCD Monte Carlo sample for the standard selection and the sideband selection compared to the QCD sample obtained from sideband data.

mainly relies on the correct extrapolation of the fraction of QCD events in the signal region with high H_T^{lep} values from the examination of the H_T^{lep} distribution in the region with $H_T^{lep} < 150$ GeV. In the QCD Monte Carlo sample, the ratio of QCD multi-jet events with $H_T^{lep} > 150$ GeV to the fraction of QCD multi-jet events in the low-H_T^{lep} region is 0.0013 ± 0.0002. Taking QCD events from the Monte Carlo simulation in the combined sideband regions S_1, S_2, and S_3, this fraction is found to be 0.00129 ± 0.00009. Both ratios agree very well, i. e. using the data sideband gives the correct estimate of QCD multi-jet events in the signal region for the Monte Carlo simulation. In the data of the sideband region, a ratio of 0.0016 ± 0.0003 is found which is also consistent with the expectation from the simulation. The slightly larger value for this ratio can also be explained by a contamination of the QCD sideband

region with W+jets and $t\bar{t}$ events in the region with $H_T^{lep} > 150$ GeV which is of the order of 20% to 30% according to the Monte Carlo simulation. A comparison of the $m_{t\bar{t}}$ distribution for the three templates – the QCD Monte Carlo in signal and sideband regions and the sideband model from data – is shown in figure 6.7. Within the statistical fluctuations, the three templates agree well, although the QCD Monte Carlo sample in the sideband shows a slight tendency towards higher $m_{t\bar{t}}$ values. For the modelling of the few expected QCD multi-jet events in the signal region with $H_T^{lep} > 150$ GeV the usage of the QCD model taken from the data sideband is sufficient according to the outcome of the presented sideband study.

6.4 Determination of Upper Limits on Resonance Cross Sections

Aim of the presented analysis is the extraction of upper limits on the cross section of narrow resonances in top quark pair production. For the determination of these limits with 95% confidence level, a statistical inference of the distribution of the invariant mass of the top quark pair system $m_{t\bar{t}}$ is performed constructing a likelihood function taking into account the rates of background and possible signal processes. To constrain the background event rate in the $m_{t\bar{t}}$ distribution for all selected events with $H_T^{lep} > 150$ GeV, also the distribution of H_T^{lep} for all events with $H_T^{lep} < 150$ GeV is going to be examined in the likelihood function as has been mentioned before. A combined likelihood function for the $m_{t\bar{t}}$ and H_T^{lep} distributions is constructed since there might exist a possible contamination of a heavy resonance signal process in the low-H_T^{lep} region. In a fit of the two distributions, the rates of the individual background processes and possible resonance processes are determined. The fit templates for resonant $t\bar{t}$ production are obtained from the MadGraph simulation of a Z′ boson decaying to a top quark pair. In the likelihood function, also the influence of systematic uncertainties is considered. Using the number of signal events as test statistic, upper limits on resonance cross sections are obtained in a fully Bayesian statistical treatment. The statistical evaluation of this analysis is performed using the software package theta [200].

6.4.1 The Likelihood Function

The fraction of background and signal events is obtained in a binned likelihood fit of the $m_{t\bar{t}}$ and H_T^{lep} distributions. The fit parameters β_k in the likelihood function are defined as

$$\beta_k := \frac{\nu_k}{\nu_k^{exp}}, \tag{6.4}$$

where ν_k is the fitted number and ν_k^{exp} is the expected number of events in both examined distributions for the certain process k. In the statistical inference of the likelihood function, the templates of SM $t\bar{t}$, W+jets, Z+jets, single top quark, QCD multi-jet production and of the $Z' \to t\bar{t}$ signal process are taken into account. This leads to $N = 6$ individual templates. The templates for background and signal

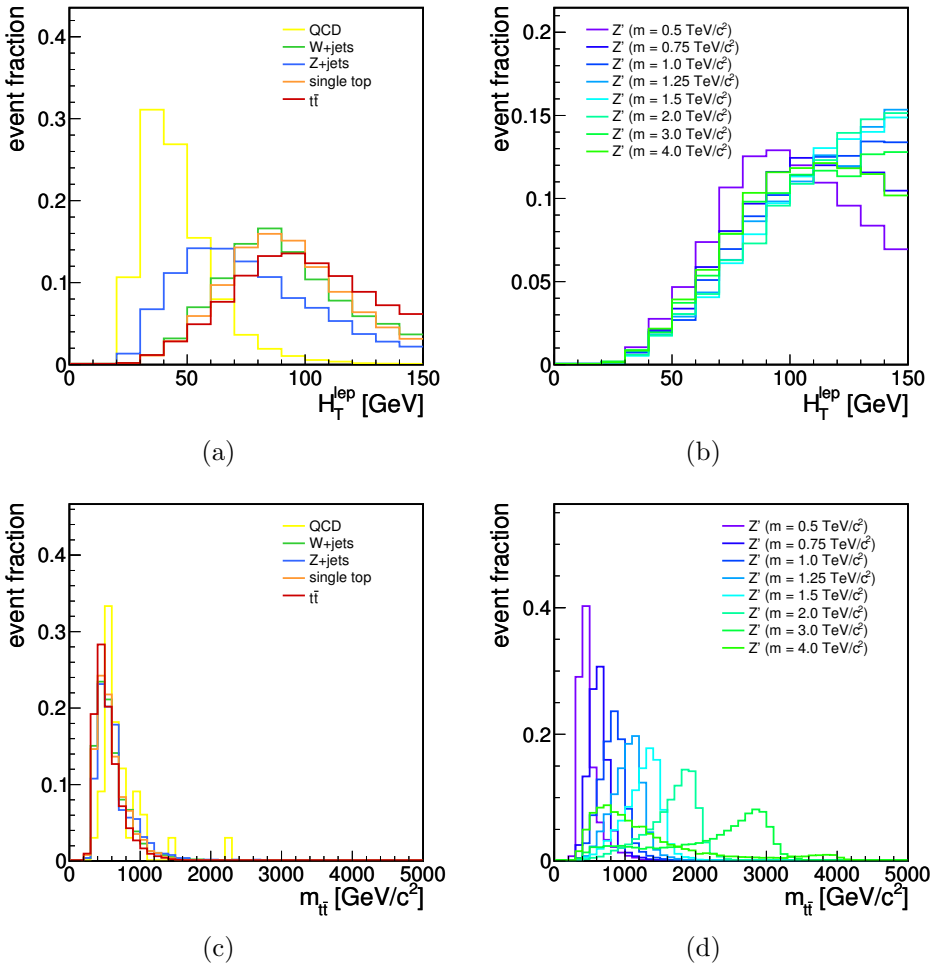

Figure 6.8: Templates for background processes and the reference $Z' \to t\bar{t}$ signal samples used for the likelihood function: H_T^{lep} (a, b) in the sideband region with H_T^{lep} <150 GeV and $m_{t\bar{t}}$ (c, d) for H_T^{lep} >150 GeV are examined simultaneously in the statistical method to obtain upper limits on signal cross sections. The shown QCD model is taken from sideband data, all other processes are modelled with Monte Carlo generators.

processes are shown in figure 6.8. Predicted event numbers ν_k^{exp} for the background processes are obtained from the Monte Carlo simulation of these processes and are given in table 6.1. Hence, a rate parameter of $\beta_k = 1$ corresponds to the exact reproduction of the prediction in the fit. The signal process with $k = 1$ is normalised to an arbitrary cross section of 1 pb which allows the interpretation of the determined value β_1 for the rate of signal events directly as cross section given in units of pb. The number of expected events μ_i^λ in bin i of the distribution of the respective variable λ ($\lambda = m_{t\bar{t}}$ or H_T^{lep}) is then given by

$$\mu_i^\lambda(\beta_1, \ldots, \beta_N) = \sum_{k=1}^{N} \beta_k \nu_k^{exp} \cdot \left(\alpha_k^\lambda\right)_i \ , \tag{6.5}$$

where $\left(\alpha_k^\lambda\right)_i$ is the fraction of selected events of process k predicted to be found in bin i of the histogram λ. These templates α_k^λ are normalised to unity, i. e.

$$\sum_\lambda \sum_{i=1}^{N_{\text{bins}}^\lambda} \left(\alpha_k^\lambda\right)_i = 1, \tag{6.6}$$

where N_{bins}^λ is the number of bins of the respective distribution λ. The likelihood function for the examination of the single histogram λ is a product of Poisson terms for all bins of the examined distribution comparing the measured number n_i^λ with the predicted number μ_i^λ in bin i:

$$L_\lambda(\beta_1, \ldots, \beta_N) := \prod_{i=1}^{N_{\text{bins}}^\lambda} \frac{\left(\mu_i^\lambda(\beta_1, \ldots, \beta_N)\right)^{n_i^\lambda} e^{-\mu_i^\lambda(\beta_1,\ldots,\beta_N)}}{n_i^\lambda!}. \tag{6.7}$$

The likelihood function L for the simultaneous treatment of the two histograms of $m_{\mathrm{t\bar{t}}}$ and $H_{\mathrm{T}}^{\text{lep}}$ is then given by the product of the individual likelihood functions L_λ:

$$L(\beta_1, \ldots, \beta_N) = L_{m_{\mathrm{t\bar{t}}}}(\beta_1, \ldots, \beta_N) \cdot L_{H_{\mathrm{T}}^{\text{lep}}}(\beta_1, \ldots, \beta_N)\ . \tag{6.8}$$

Since the templates of the SM $\mathrm{t\bar{t}}$ and single top quark production have very similar shapes in $m_{\mathrm{t\bar{t}}}$ and $H_{\mathrm{T}}^{\text{lep}}$ the likelihood function is not sensitive to distinguish these two processes. Therefore, the ratio of the considered numbers of SM $\mathrm{t\bar{t}}$ and single top quark production is fixed to its predicted value. Also the background processes of W+jets and Z+jets production are very similar, thus, the ratio of their rate parameters is fixed to the theory prediction, too. This simplification reduced the number of effective β_k parameters N from six to four. Furthermore, all parameters β_k are constrained to values equal or larger than zero because a negative β_k value would correspond to a negative cross section which does not allow for a meaningful physical interpretation.

6.4.2 Systematic Uncertainties

The shape of the templates might be distorted by several sources of systematic uncertainties. Also the overall signal and background selection efficiency and acceptance might be affected. Systematic uncertainties on the shape and rate of the examined distributions of $m_{\mathrm{t\bar{t}}}$ and $H_{\mathrm{T}}^{\text{lep}}$ are incorporated into the statistical method by adding additional parameters to the likelihood function. For each source of a systematic uncertainty u, a new parameter δ_u is introduced parametrising the strength of the template variation induced by the respective uncertainty. Thus, the number of expected events μ_i^λ given in equation 6.5 as well as the likelihood function in equation 6.8 become functions of the parameters β_k and δ_u, i. e. $\mu_i^\lambda = \mu_i^\lambda(\beta_1, \ldots, \beta_N, \delta_1, \ldots, \delta_{N_{\text{syst}}})$ and $L = L(\beta_1, \ldots, \beta_N, \delta_1, \ldots, \delta_{N_{\text{syst}}})$. For each template α_k^λ, alternative templates for all systematic uncertainties u are utilised. Usually, two alternative templates $\alpha_{k,u,\pm}^\lambda$ corresponding to $\pm 1\sigma$ deviations exist. The normalisation of the templates $\alpha_{k,u,\pm}^\lambda$ includes changes in the acceptance induced by the systematic uncertainties. Thus,

the systematically shifted templates are not normalised to unity as the standard templates in equation 6.6. With the new parameter δ_u, an interpolation between the standard templates α_k^λ and the distorted templates $\alpha_{k,u,\pm}^\lambda$ is performed. This interpolation is done in such a way, that, if $\delta_u = 0$ for all systematic uncertainties u, the standard template is reproduced and used in the likelihood function in the definition of μ_i^λ. If $\delta_u = 1$ for one uncertainty u, the template $\alpha_{k,u,+}^\lambda$ is used as template in the likelihood function, for $\delta_u = -1$, the statistical method is performed using the template $\alpha_{k,u,-}^\lambda$. In case of $\delta_u \in (-1, 0)$, a cubic interpolation between the bin entries i of the nominal template and the distorted template $\alpha_{k,u,-}^\lambda$ is done. For $\delta_u \in (0, 1)$, the actual template is a cubic interpolation between α_k^λ and $\alpha_{k,u,+}^\lambda$. If $|\delta_u| > 1$, a linear extrapolation of the form $|\delta_u| \cdot \left(\left(\alpha_k^\lambda\right)_i - \left(\alpha_{k,u,\pm}^\lambda\right)_i \right)$ is added to the expected number of events μ_i given in equation 6.5. The extra- and interpolation between the different templates is performed such that μ_i is a continuous and differentiable function of the additional parameter δ_u. If $\delta_u \neq 0$ for more than on systematic uncertainty u, the combined inter- or extrapolations of the respective templates are added in the definition of μ_i. The parameters δ_u are constrained with Gaussian functions centered around zero and a width of one. Therefore, the likelihood function in equation 6.8 is modified as follows:

$$L(\beta_1, \ldots, \beta_N) \rightarrow$$

$$\tilde{L}(\beta_1, \ldots, \beta_N, \delta_1, \ldots, \delta_{N_{\text{syst}}}) := L(\beta_1, \ldots, \beta_N, \delta_1, \ldots, \delta_{N_{\text{syst}}}) \cdot \prod_{u=1}^{N_{\text{syst}}} \frac{1}{\sqrt{2\pi}} e^{-\frac{\delta_u^2}{2}}. \quad (6.9)$$

Most systematic uncertainties taken into account for this measurement have been explained in section 5.5. Alternative templates with changed jet energy scale and jet energy resolution are considered as systematic distortion of the original templates for all processes except the QCD multi-jet model which is taken from data. Further systematic uncertainties are considered for the variation of the factorisation and renormalisation scale and the matching threshold in the generation of Monte Carlo events. Alternative Monte Carlo simulations with varied scale and matching parametrisations are generated for the SM $\mathrm{t\bar{t}}$, W/Z+jets, and single top quark background processes. For the $\mathrm{t\bar{t}}$ process, also templates with changed amount of initial and final state radiation are generated and included as systematic uncertainty. The analysis specific uncertainties arising from b-tagging, variation of the lepton selection efficiency in pseudorapidity, and the QCD modelling as described in section 5.5 for the measurement of the charge asymmetry are obviously not affecting the evaluation of the invariant mass spectrum.

Another systematic uncertainty considered in the analysis of high-mass resonances in the $m_{\mathrm{t\bar{t}}}$ spectrum which has not been taken into account in the measurement of the charge asymmetry accounts for the uncertainty on the measurement of energy deposits clustered to the missing transverse energy but not to any jet. Uncertainties on the jet energy scale and resolution are propagated to $\not\!\!E_{\mathrm{T}}$, whereas further energy contributions to $\not\!\!E_{\mathrm{T}}$ are not changed in the treatment of those systematic uncertainties. Therefore, an additional systematic uncertainty on this $\not\!\!E_{\mathrm{T}}$ contribution is considered by scaling those un-clustered energy deposits by $\pm 10\%$. Since $\not\!\!E_{\mathrm{T}}$ is part

	uncertainty on acceptance [%]									
	JES		JER		scale		matching		ISR/FSR	
process	+	−	+	−	+	−	+	−	+	−
$t\bar{t}$	4.9	−6.4	−1.0	1.1	−0.2	2.3	0.2	0.3	−1.4	−0.5
W+jets	15	−15	−0.05	0.05	−30	84	11	−5.2	–	–
Z+jets	17	−15	0.8	−0.5	−28	73	7.5	−8.6	–	–
single top	9.8	−11	−1.0	1.0	–	–	–	–	–	–
Z' ($m = 0.5$ TeV/c^2)	2.7	−3.7	−0.9	1.2	–	–	–	–	–	–
Z' ($m = 0.75$ TeV/c^2)	0.2	−0.8	−0.7	0.8	–	–	–	–	–	–
Z' ($m = 1.0$ TeV/c^2)	−1.5	0.7	−0.5	1.0	–	–	–	–	–	–
Z' ($m = 1.25$ TeV/c^2)	−2.8	1.0	−0.6	1.0	–	–	–	–	–	–
Z' ($m = 1.5$ TeV/c^2)	−3.0	1.2	−0.5	0.8	–	–	–	–	–	–
Z' ($m = 2.0$ TeV/c^2)	−2.5	1.2	−0.5	0.7	–	–	–	–	–	–
Z' ($m = 3.0$ TeV/c^2)	−1.7	0.7	−0.4	0.6	–	–	–	–	–	–
Z' ($m = 4.0$ TeV/c^2)	−1.2	0.1	−0.5	0.8	–	–	–	–	–	–

Table 6.5: Variations on the acceptance due to different sources of systematic uncertainties for signal and background processes. The quoted variations account for the overall change of event rates in both examined variables $m_{t\bar{t}}$ and H_T^{lep}. Considered rate uncertainties arise from changes in the jet energy scale (JES), the jet energy resolution (JER), factorisation and renormalisation scale, the matching threshold and the simulated amount of initial and final state radiation (ISR/FSR).

of the examined H_T^{lep} variable in this analysis, the uncertainty on un-clustered energy contributions has a larger impact compared to the measurement of the charge asymmetry. The uncertainty on un-clustered energy does not influence the overall acceptance of the event selection before the H_T^{lep} cut. Since the simultaneous statistical inference of $m_{t\bar{t}}$ and H_T^{lep} takes into account all events selected without the H_T^{lep} cut, the total number of selected events is not changed by a variation of $\not{E}_T$. Only the ratio of event numbers in the low- compared to the high-H_T^{lep} region is affected by this uncertainty.

For the modelling of the QCD multi-jet background, a systematic uncertainty is considered to account for changes in the shape of the QCD multi-jet background template obtained from the sideband region. Therefore, variations of the templates from the three sub-sidebands S_1, S_2, and S_3 are examined. To construct two systematically distorted templates for the $\pm 1\sigma$ uncertainties of the QCD background template, the bin-wise maximum or minimum, respectively, of the three sideband templates is taken.

As an example, the shifted templates for the $\pm 1\sigma$ variations of the JES are shown in figures 6.9 and 6.10 for the signal as well as for the background processes. The JES uncertainty has the largest impact of all considered systematic uncertainties on the shape of the signal samples. A variation of the JES leads to a shift of the peak position of the $Z' \to t\bar{t}$ processes in the reconstructed $m_{t\bar{t}}$ distribution. The alternative templates for all other considered systematic uncertainties can be found in appendix A.

The impact of the individual sources of systematic uncertainties on the acceptance of signal and background processes is summarised in table 6.5. The quoted variations account for the overall change of event rates in both examined variables $m_{t\bar{t}}$ and H_T^{lep}.

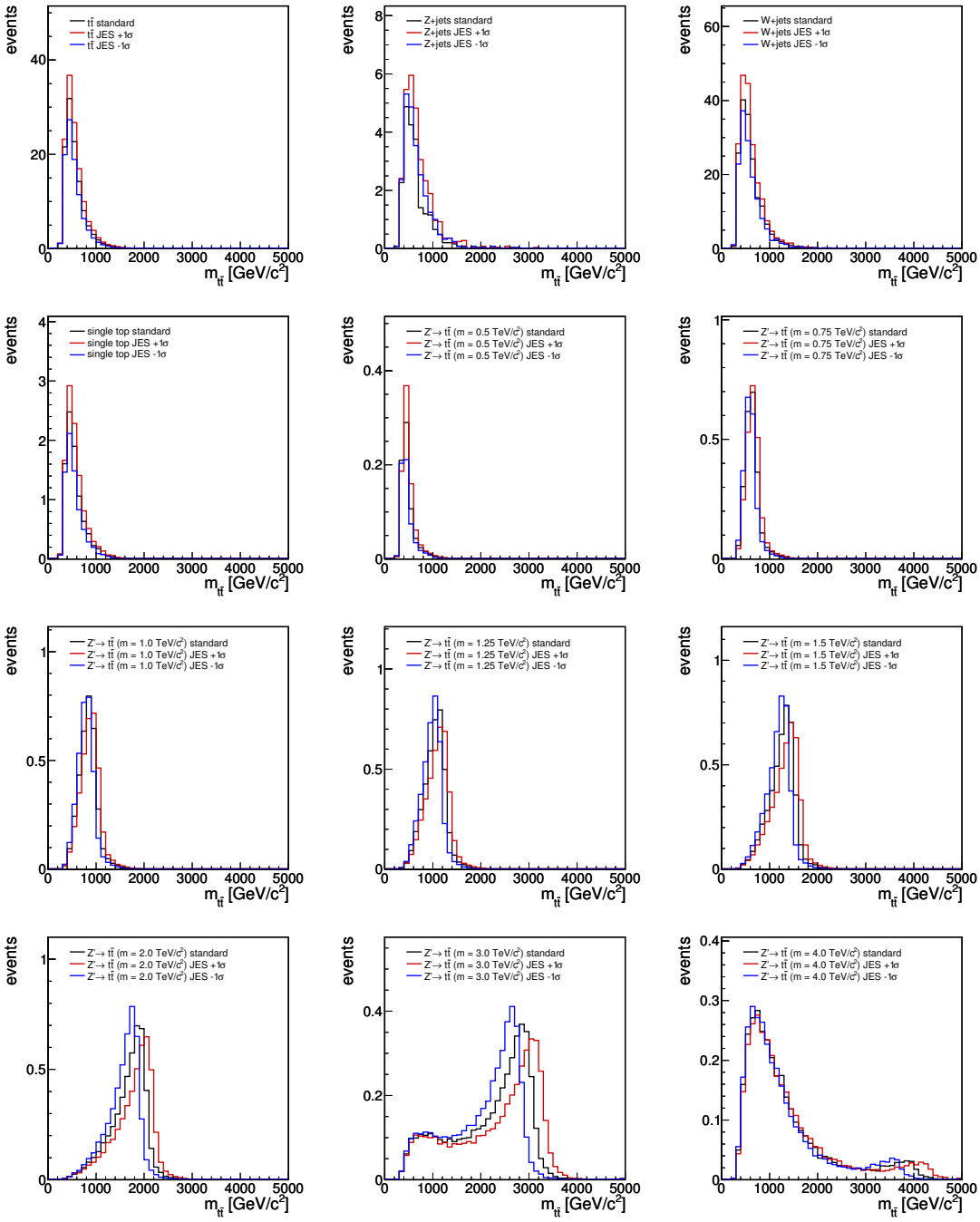

Figure 6.9: Impact of varying the jet energy scale on the shape and rate of $m_{t\bar{t}}$ after the final selection with H_T^{lep} >150 GeV. The Z′ → $t\bar{t}$ signal samples are normalised to an arbitrary cross section of 1 pb.

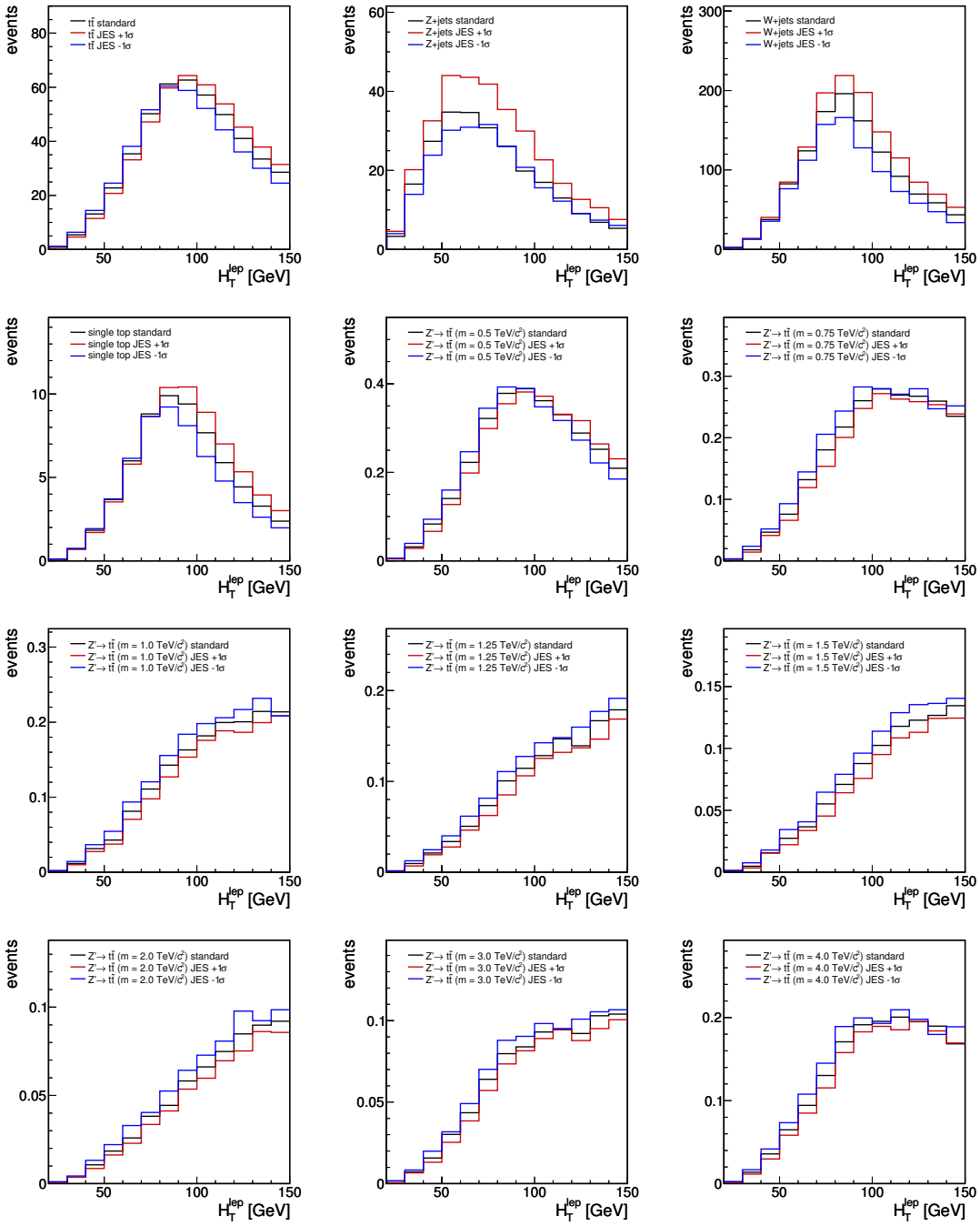

Figure 6.10: Impact of varying the jet energy scale on the shape and rate of $H_{\mathrm{T}}^{\mathrm{lep}}$ after the final selection with $H_{\mathrm{T}}^{\mathrm{lep}}$ <150 GeV. The Z′ → $t\bar{t}$ signal samples are normalised to an arbitrary cross section of 1 pb.

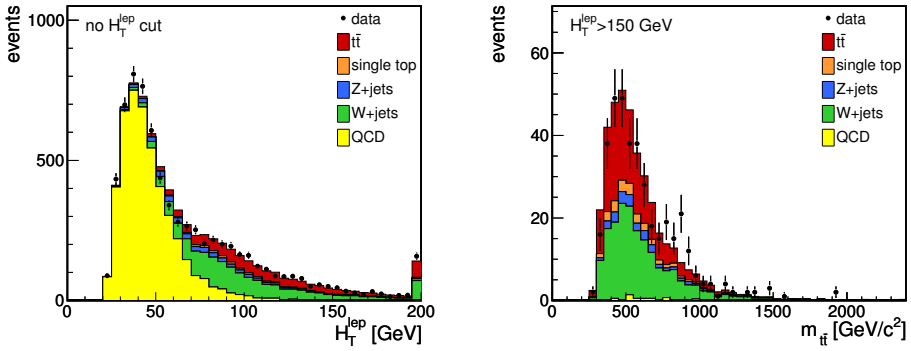

(a) (b)

Figure 6.11: Data distributions of the two fit variables $H_{\mathrm{T}}^{\mathrm{lep}}$(a) and $m_{\mathrm{t\bar{t}}}$(b) compared to the background simulation. Shown are the nominal templates for the background processes scaled to the result of a likelihood fit of the data neither including signal processes nor systematic uncertainties.

Largest variations of up to 84% are observed for the W+jets and Z+jets background processes when changing the factorisation and renormalisation parameters in the Monte Carlo simulation.

6.4.3 Results

In a first step to compare the used background templates in the likelihood function with the measured data and in order to illustrate the performance of the statistical method, a template fit to the data is performed neither including possible signal templates nor templates for systematic uncertainties. For this purpose, the likelihood function given in equation 6.8 is maximised with respect to the β_k parameters of the background processes fixing the signal rate to zero. This likelihood fit yields an estimation for the background event rates under the assumption that no signal is included and that the $m_{\mathrm{t\bar{t}}}$ and $H_{\mathrm{T}}^{\mathrm{lep}}$ distributions are well modelled by the nominal templates. The outcome of this fit predicts increased background event rates for all background processes. The fitted β_k parameters are 1.09 for the QCD multi-jet production, 1.05 for the W+jets and Z+jets processes, and 1.38 for the combined $\mathrm{t\bar{t}}$ and single top quark production processes. In figure 6.11, the fit templates of the background processes are scaled to the fit result and are compared to the observed data. Compared to figure 6.2(c) where the background templates have been scaled to the Monte Carlo prediction, a much better agreement between data and background description is achieved. In the distribution of $m_{\mathrm{t\bar{t}}}$, only a small upwards fluctuation in data can be seen at an invariant mass around 900 GeV/c^2. Also the distributions of other kinematic variables which are not used as fit variables directly are described better when scaling the background templates according to the fit result (see figure 6.12) compared to figure 6.3 where the templates are scaled according to their cross section predictions.

To obtain upper limits on the cross section of high-mass resonances decaying to top quark pairs, a Bayesian examination of the likelihood function is utilised. The

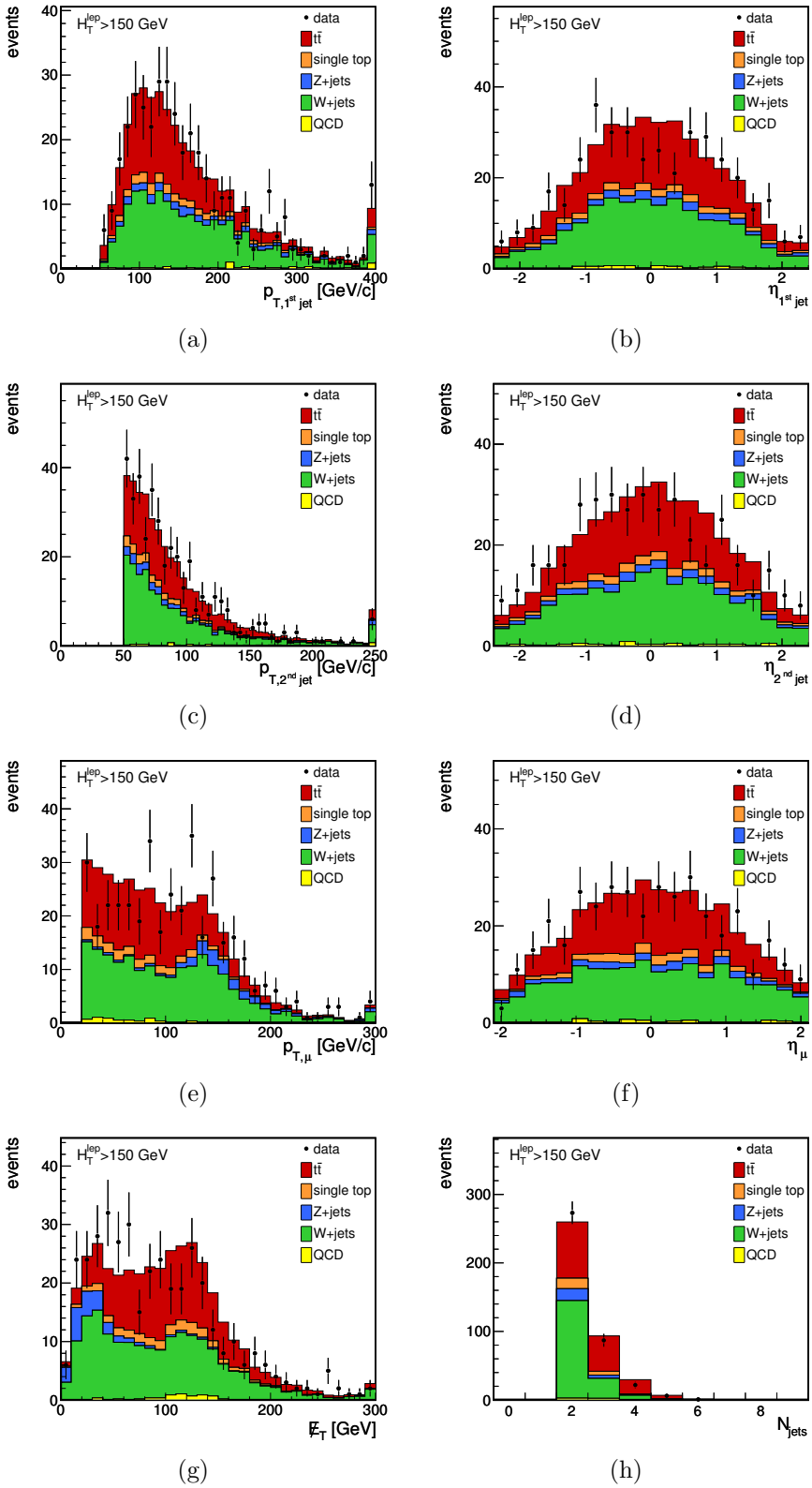

(a) (b) (c) (d) (e) (f) (g) (h)

Figure 6.12: Comparison of the Monte Carlo simulation of various background processes to the measured data for the transverse momenta and pseudorapidities of the two jets with highest and second highest p_T in (a) to (d), transverse momentum and pseudorapidity of the muon in (e) and (f), the missing transverse energy (g), and the number of jets (h). Compared to figure 6.3, the QCD model from sideband data and not from Monte Carlo simulation is included and all templates are scaled according to the result of the likelihood fit.

likelihood function given in equation 6.9 is used as a-priori probability to observe a certain data distribution for a given parameter set $(\beta_1, \ldots, \beta_N, \delta_1, \ldots, \delta_{N_{\text{syst}}})$. In the likelihood function, the Gaussian priors for the systematic uncertainty parameters δ_u are included as described above. The signal and background rate parameters β_k, especially the one for the signal, are not constraint, i. e. flat priors are assumed for their distributions (except the constraint $\beta_k \geq 0$). To obtain a 95% confidence level limit on the signal cross section parameter for the observed data set, the likelihood function is marginalised. If the signal cross section is given by the parameter β_1 and the background event rates are described by the parameters $\beta_2, \ldots, \beta_N$, the 95% confidence level upper limit $\hat{\beta}_1$ on the signal cross section is obtained from solving the following equation for $\hat{\beta}_1$:

$$\frac{1}{M}\int_0^{\hat{\beta}_1} d\beta_1 \int d\beta_2 \ldots d\beta_N d\delta_1 \ldots d\delta_{N_{\text{syst}}} \tilde{L}(\beta_1, \ldots, \beta_N, \delta_1, \ldots\ \delta_{N_{\text{syst}}}) = 0.95. \quad (6.10)$$

Here, the integration of the background parameters $\beta_2, \ldots, \beta_N$ is performed over the entire allowed range from 0 to ∞. The parameters δ_u describing the systematic uncertainties have an integration range from $-\infty$ to $+\infty$. M is a normalisation constant which ensures that the left hand side of equation 6.10 is normalised to unity for $\hat{\beta}_1 \to \infty$. To perform the marginalisation of the likelihood function a Markov Chain Monte Carlo integration method [201] is used.

Expected upper limits on the signal cross section are determined in ensemble tests. In these tests, pseudo experiments are randomly drawn from the various background templates according to their prediction as explained in section 5.4.1. The numbers of pseudo experiments for all processes are varied according to the uncertainties quoted in table 6.1. In the generation of pseudo experiments, also the influence of systematic uncertainties is considered. Therefore, pseudo data is not necessarily produced according to the nominal templates, but to systematically distorted distributions for the templates of $m_{\text{t}\bar{\text{t}}}$ and $H_{\text{T}}^{\text{lep}}$. In each pseudo experiment, the parameters δ_u are drawn randomly from a Gaussian distribution with a mean of zero and a width of one. Pseudo data is then created from the interpolated templates between nominal histograms α_k^{λ} and shifted templates $\alpha_{k,u,\pm}^{\lambda}$ where the interpolation is performed as described before. Signal processes are not included into these pseudo experiments. Applying the marginalisation on those pseudo data gives an estimation of the expected cross section limits $\hat{\beta}_1$ in the absence of any signal process. This is done by scanning the signal parameter β_1 in equation 6.10 for the various signal templates corresponding to different Z′ boson masses.

The central belts of the expected limits found in pseudo experiments corresponding to 68% and 95% confidence intervals, are presented in figure 6.13. The expected upper limits on the cross section of a heavy resonance decaying to $\text{t}\bar{\text{t}}$ are compared to observed limits when applying the marginalisation method on data. With the data set corresponding to an integrated luminosity of 36 pb^{-1}, no significant deviation from the expectation in ensemble tests is found. The most prominent difference between expected and observed limit is found for a resonance mass of 1 TeV/c^2. The observed limit is slightly larger than the expected one, but is still consistent with the expectation within a statistical 2σ fluctuation. This deviation is mainly caused

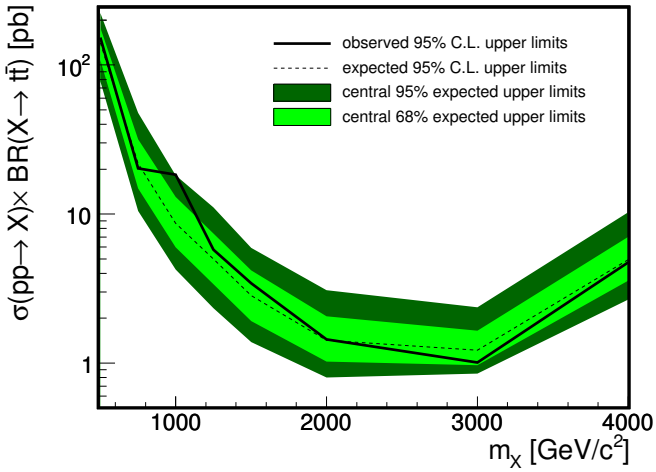

Figure 6.13: Expected and observed 95% confidence level upper limits on the cross section of the process $pp \to X \to t\bar{t}$ with a new exchange particle X as function of the mass of the resonance particle.

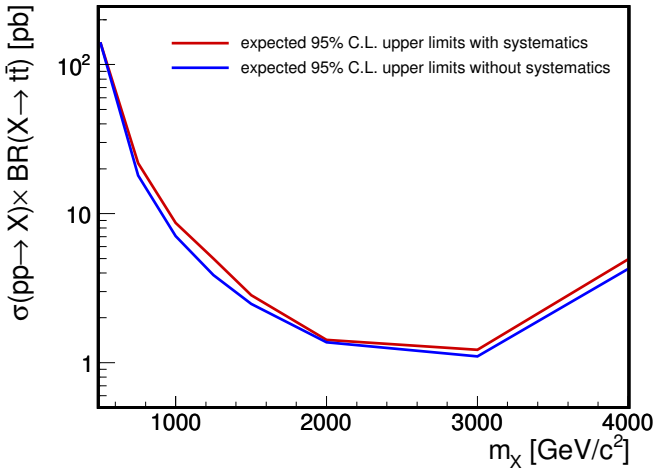

Figure 6.14: Median expected 95% confidence level upper limits on the cross section of the process $pp \to X \to t\bar{t}$ with a new exchange particle X as function of the mass of the resonance particle with and without systematic uncertainties included in the marginalisation of the likelihood.

by the slight data excess in the $m_{t\bar{t}}$ distribution shown in figure 6.11(b). Taking also the look-elsewhere effect into account, i. e. accounting for the probability to observe a deviation from the expectation when looking at several test points, the significance of this excess is further reduced. Since in this analysis eight resonance masses are examined, the probability is more than 30% to observe one 2σ excess at one of these mass points. Hence, the observed limits are assumed to be in full agreement with the expectation within statistical fluctuations.

To all cross section limits shown in figure 6.13, an uncertainty of 4% accounting for the uncertainty on the luminosity determination [115,116] has to be added since

a variation of the luminosity affects the rate of all signal and background processes similarly. The limits on the signal cross section are of the order of several picobarn for all mass points above 1 TeV/c^2. For lower resonance masses, the found limits are much larger. In this mass domain, the signal templates have a very similar shape compared to the expected background distribution. The likelihood function can therefore not well distinguish between signal and background contributions. Best limits are obtained for masses of 2 TeV/c^2 and 3 TeV/c^2 which are approximately 1 pb for the process $pp \to X \to t\bar{t}$ with a new exchange particle X. The cross section limit for a particle with a mass of 4 TeV/c^2 is again slightly larger since such a particle is more likely to be produced off-shell and shows no clear resonance peak in the $m_{t\bar{t}}$ distribution when assuming a resonance width of 1% of the mass as has been discussed in section 3.1.2.

In figure 6.14, the expected upper limits obtained in ensemble tests for an integrated luminosity of 36 pb^{-1} are shown for the nominal analysis compared to the results obtained from performing the marginalisation of the likelihood function in equation 6.10 without including systematic uncertainties. Including systematic uncertainties to the limit calculation leads to only slightly larger expected limits, although the rate uncertainties on the backgrounds given in table 6.5 are quite large. Especially in the nearly background-free region of high-resonance masses of several TeV/c^2, the analysis is dominated by the statistical uncertainty. As can be seen in figure 6.11(b), no candidate event with a reconstructed invariant mass above 2 TeV/c^2 has been observed so far.

The measurement developed in this thesis can be compared to a search for resonances in $t\bar{t}$ production performed with the CMS experiment described in [202]. This analysis focusses on the search for new particles with relatively low masses. In the decay of such particles, the expected kinematic topology of the top quarks is still similar to SM $t\bar{t}$ production. Therefore, a reconstruction using the full event kinematic of the decay products in the lepton+jets decay mode of the top quark pair can be exploited in this analysis. The obtained limits on signal cross sections with masses below 1.25 TeV/c^2 determined in [202] are better than the results obtained in the analysis presented here. For larger masses, the used reconstruction and selection techniques in [202] become less efficient. Hence, the cross section limits derived for high-mass resonances are of the order of 4 pb, whereas in the analysis developed in this thesis, limits of approximately 1 pb on resonance processes with masses of 2 TeV/c^2 or 3 TeV/c^2 are found. Both analyses can be treated as complementary aspects of the direct search for new particles in top quark pair production exploiting the different kinematic topologies of low- and high-mass $t\bar{t}$ resonances. Compared to the measurements performed at the Tevatron collider [77, 78], the sensitivity of the presented analysis is not yet high enough to extend the limits on the topcolour Z′ [67] model used as reference model by the Tevatron analyses. Nevertheless, in the presented study, a first search for $t\bar{t}$ resonances with masses of several TeV/c^2 has been performed, a mass domain which has not even been accessible at the Tevatron.

Chapter 7

Conclusion and Outlook

The study of top quarks in proton-proton collisions at the Large Hadron Collider offers the opportunity for testing the properties of the Standard Model and to search for influences of possible but unknown physical effects. Within the presented analyses, two aspects of top quark pair production have been investigated. Both studies are sensitive to the presence of undiscovered heavy exchange particles in the $t\bar{t}$ production. Beside the direct search for resonances in the spectrum of the invariant mass of the top quark pair, for the first time a measurement of the charge asymmetry in $t\bar{t}$ production at a proton-proton collider has been performed.

The measurement of the charge asymmetry is mainly motivated by recent measurements performed with proton-antiproton collisions at the Tevatron accelerator. These measurements see a deviation from the SM prediction.Top quarks are more likely produced with a flight direction close to the direction of the incoming proton, whereas antitop quarks are preferably produced in the opposite direction. This effect results in an observable asymmetry in the difference of the rapidities of top and antitop quarks. Several theoretical explanations for this observation exist. Most of them introduce a new gauge boson with different vector and axial-vector couplings to quarks.

For a final test of the reliability of these measurements, a complementary measurement of this asymmetry in proton-proton collisions at the LHC has been developed. This measurement uses the data sample recorded with the Compact Muon Solenoid during 2010. Since a forward-backward asymmetry as it is used to define a charge asymmetry at the Tevatron cannot be measured in the completely symmetric proton-proton collisions at the LHC, a variable had to be found which is sensitive to the same physical effects which could cause the observed forward-backward asymmetry in top quark pair production. The rapidity distributions of top and antitop quark momenta will always be symmetrically distributed around zero at the LHC, only the widths of these distribution can differ in case of a production mechanism with asymmetric couplings. For a practicable measurement of this asymmetry in the widths of these angular distributions, the difference of the absolute values of the pseudorapidities of top and antitop quarks, $|\eta_t| - |\eta_{\bar{t}}|$, is introduced as sensitive variable. The charge asymmetry A_C in top quark pair production in symmetric proton-proton collisions can then be defined as the asymmetry in $|\eta_t| - |\eta_{\bar{t}}|$.

The measurement of the charge asymmetry as it has been performed here is based on the selection of $t\bar{t}$ candidate events in the electron+jets and muon+jets decay channels where one top quark decays hadronically into three quarks and the second top quark decays into one quark and a lepton pair. The expected kinematic of the $t\bar{t}$ system is exploited to reconstruct the $|\eta_t| - |\eta_{\bar{t}}|$ distribution on an event-by-event basis. Although the reconstruction method gives already a good approximation of the true top quark momenta and therewith the charge asymmetry, the reconstructed $|\eta_t| - |\eta_{\bar{t}}|$ is still affected by background contributions and smearing effects induced by the reconstruction method and the imperfect detector resolution. To correct the reconstructed spectrum for these effects, several regularised unfolding procedures have been tested in order to provide a measurement of A_C which is cleaned for these effects and can directly be compared with theory predictions. Applying the reconstruction and unfolding methods to the collected data, a charge asymmetry of

$$A_C = 0.060 \pm 0.134(\text{stat.}) \pm 0.026(\text{syst.})$$

has been measured. This result is dominated by the statistical uncertainty and is therefore still consistent with the SM prediction of $A_C = 0.0130 \pm 0.0011$ [24–26]. To reach a similar sensitivity as the Tevatron measurements the uncertainty of the measurement of A_C has to be reduced to less than 2%, since the measured asymmetry at the Tevatron would correspond to A_C values of about 4% at the LHC. The fraction of $t\bar{t}$ production in symmetric gluon-gluon fusion processes is much larger at the LHC, but a charge asymmetry can only arise from $t\bar{t}$ events produced with asymmetric initial states such as quark-antiquark or quark-gluon processes. Therefore, influences of undiscovered effects which could explain the forward-backward asymmetry observed at the Tevatron would lead to smaller deviations from the SM in the charge asymmetry A_C at the LHC. To evaluate the evolution of the expected statistical uncertainty on the measurement on A_C, pseudo data sets are created corresponding to larger data sets with increased integrated luminosity. The measurement of A_C is performed without any changes in the unfolding procedure on top of these pseudo data samples. The average statistical uncertainty found in pseudo experiments as function of the integrated luminosity L_{int} is shown in figure 7.1. From this study, the statistical uncertainty is expected to decrease roughly with $\sqrt{L_{\text{int}}}$. This will allow to reach the same sensitivity as the Tevatron measurements with more than an 1 fb^{-1} of integrated luminosity. The sensitivity of this analysis can also be increased by restricting the measurement to a data sample with an enhanced $t\bar{t}$ fraction and thus reducing the uncertainties arising from the background subtraction. This requires to apply a tighter event selection including for instance cuts based on b-tagging discriminator values. In the presented study, the selected data sample contains still a large background fraction. However, harder cuts would further reduce the available number of $t\bar{t}$ events and would it make more difficult to perform the unfolding technique which requires a more or less smooth modelling of the measured distribution. Also the systematic uncertainty on A_C is expected to become smaller with a larger available data set. Especially the main systematic deviations arising from the uncertainties on the jet energy scale and on the lepton selection efficiency will be reduced in more precise and dedicated studies with more data.

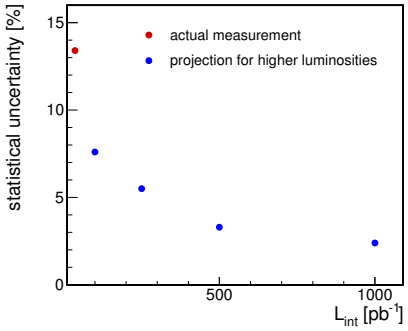

Figure 7.1: Expected statistical uncertainty on the measurement of the charge asymmetry A_C as projection for data sets corresponding to higher integrated luminosities.

Further improvements on the analysis of the charge asymmetry can be achieved by a measurement of A_C differentially in specific quantities. If the charge asymmetry observed at the Tevatron is induced by the exchange of a heavy gauge boson in $t\bar{t}$ production, deviations from the SM prediction will become more prominent in specific phase space regions with high invariant top quark pair masses $m_{t\bar{t}}$. A measurement of A_C as function of $m_{t\bar{t}}$ will therefore increase the sensitivity to possible effects of unknown physical processes. The z component of the momentum of the top quark pair, $p_z^{t\bar{t}}$, is another quantity which can be used in the measurement of A_C. Since a non-vanishing A_C is only expected to occur in $t\bar{t}$ production in the quark-antiquark annihilation processes and since the top quark pair system is more likely being produced with large absolute values of $p_z^{t\bar{t}}$ in this production channel, the measurement of the charge asymmetry as function of this quantity could also lead to a higher sensitivity. Also the determination of A_C as function of $|\eta_t| - |\eta_{\bar{t}}|$ itself could provide additional information on the coupling structure of $t\bar{t}$ production.

A more direct search for influences of unknown production mechanisms is performed in the second analysis presented in this thesis. The inspection of the invariant mass distribution of the top quark pair offers the opportunity to find or exclude hypothetical narrow resonances decaying to $t\bar{t}$. Such resonances could appear as peak structure in the measured $m_{t\bar{t}}$ distribution. Many theoretical models predict $t\bar{t}$ resonances with masses above 1 TeV/c^2, a kinematic region which is accessible at the LHC for the first time in experiments. In the decay of such a heavy resonance, the top quarks are produced with relatively high boost factors. Therefore, their decay products are no longer measurable as separated objects within the detector. Jets emerging from hadronically decaying top quarks can often merge into single jets and charged leptons from semileptonic top decays are typically less well isolated from hadronic interactions in the detector.

In this thesis, a method has been developed to select candidate events with such a specific event topology in the muon+jets decay channel of the $t\bar{t}$ pair. Furthermore, a new reconstruction technique has been invented to estimate the top quark four momenta and therewith $m_{t\bar{t}}$. A $m_{t\bar{t}}$ resolution of about 10% can be achieved with this reconstruction method. Besides the reconstruction, a method to estimate the individual background event rates contributing to the selected data sample has

been performed mainly relying on the characteristic of the total transverse leptonic energy, $H_{\mathrm{T}}^{\mathrm{lep}}$. Especially the background of QCD multi-jet production is difficult to model in the selected phase space region with Monte Carlo simulations. Therefore, a modelling of this background based on collision data has been developed. A combined statistical inference of the distributions of the invariant mass $m_{\mathrm{t\bar{t}}}$ and of $H_{\mathrm{T}}^{\mathrm{lep}}$ allows to estimate the contributions of the background processes and to search for high-mass resonances in the $m_{\mathrm{t\bar{t}}}$ spectrum. As reference model for signal resonances in the statistical analysis, the Monte Carlo simulation of a Z′ boson decaying to $\mathrm{t\bar{t}}$ is considered. The width of the resonance peak in the generation is set to 1% of the respective resonance mass. Limits on the cross section of such resonances decaying to top quark pairs found in the statistical analysis performed on the data set corresponding to an integrated luminosity of 36 pb^{-1} are of the order of a few picobarn for resonance masses of more than 1 TeV/c^2. The observed cross section limits are consistent with the expectation found in pseudo data samples generated according to the SM prediction for the background processes and not including any signal events. So far, no significant excess in the invariant mass distribution has been found. The reached cross section limits are still above the theory predictions on the cross section of most models predicting new exchange particles in $\mathrm{t\bar{t}}$ production shown in figure 1.7. Compared to the study of $\mathrm{t\bar{t}}$ resonances using selection and reconstruction techniques according to the SM-like $\mathrm{t\bar{t}}$ event kinematic [202], an improvement in the reached cross section limits for resonance masses of several TeV/c^2 of a factor of up to four can be reached with the presented analysis technique.

A larger amount of collision data will help to improve the sensitivity of the search for resonances in the $m_{\mathrm{t\bar{t}}}$ spectrum in the future. Also the electron+jets decay channel might be included to this analysis to increase the overall signal acceptance, but less well-isolated electrons as they will typically occur in the decay of boosted top quarks cannot be separated as easily as muons from jets. Another analysis technique suitable for the identification of top quarks originating from the decay of a heavy particle is the so-called top-tagging [203]. Top-tagging algorithms are used to search for merged jets from the hadronic decay of a boosted top quark. These algorithms try to identify substructures in the merged jet arising from the individual decay products of the top quark contributing to a single jet. Some studies of jet substructure algorithms have already been performed with the data collected by CMS in 2010 [204]. Top-tagging algorithms have originally been developed to study top quark pair production in the full-hadronic decay mode, but they might also be useful in the identification and reconstruction of the lepton+jets decay channel [205].

Both measurements presented in this thesis have not yet reached the sensitivity required to test most theoretical models predicting new production mechanisms of top quark pairs in proton-proton collisions. In the first collision data taken with the CMS detector during 2010, an evaluation of these measurements has been performed. With the upcoming data collected at the LHC in the next few years, the established analyses of top quark pair production mechanisms will become much more sensitive to influences of yet undiscovered processes. The presented analysis techniques will allow for a precise validation of Standard Model predictions and for a search for such unknown effects in top quark pair production in the future.

Appendix A

Templates for Systematic Uncertainties

In this appendix, all additional templates accounting for systematic uncertainties considered in the likelihood function described in section 6.4.2 are illustrated. These templates correspond to the systematically shifted templates $\alpha^{\lambda}_{k,u,\pm}$ used for the statistical inference of $H_{\mathrm{T}}^{\mathrm{lep}}$ and $m_{\mathrm{t\bar{t}}}$. All shown templates are normalised to the predictions obtained from Monte Carlo simulations.

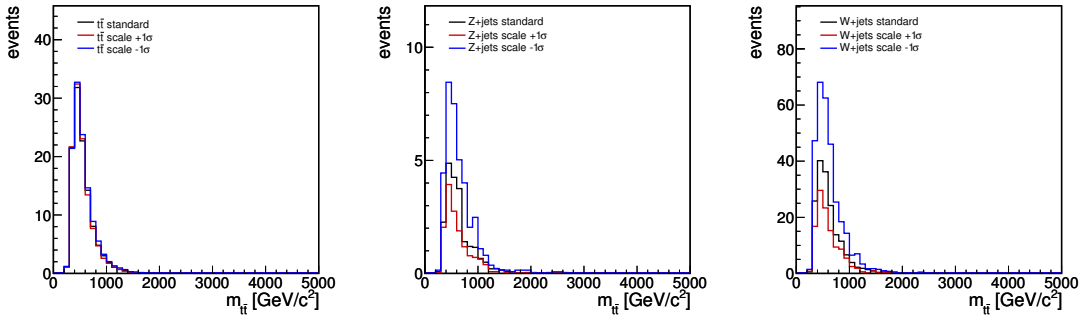

Figure A.1: Impact of varying the factorisation and renormalisation scale parametrisations in the Monte Carlo simulation on the shape and rate of $m_{\mathrm{t\bar{t}}}$ after the final selection with $H_{\mathrm{T}}^{\mathrm{lep}}$ >150 GeV.

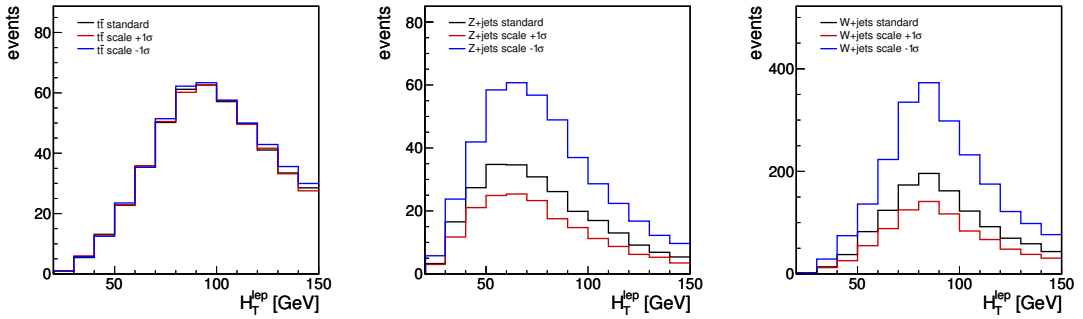

Figure A.2: Impact of varying the factorisation and renormalisation scale parametrisations in the Monte Carlo simulation on the shape and rate of $H_{\mathrm{T}}^{\mathrm{lep}}$ after the final selection with $H_{\mathrm{T}}^{\mathrm{lep}}$ <150 GeV.

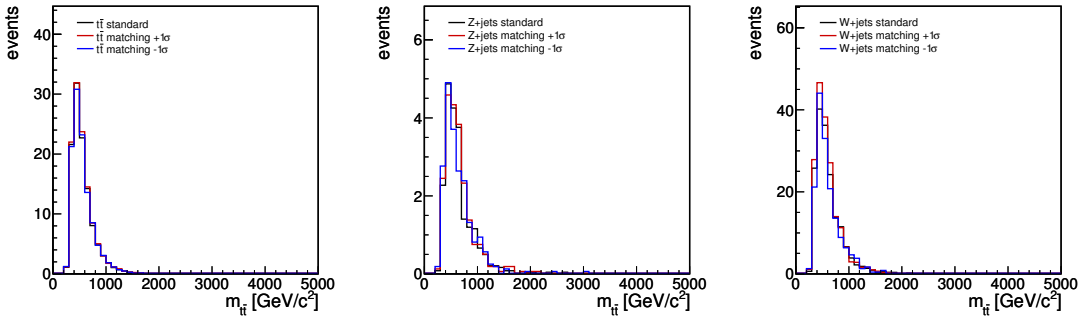

Figure A.3: Impact of varying the matching threshold in the Monte Carlo simulation on the shape and rate of $m_{\mathrm{t\bar{t}}}$ after the final selection with $H_{\mathrm{T}}^{\mathrm{lep}}$ >150 GeV.

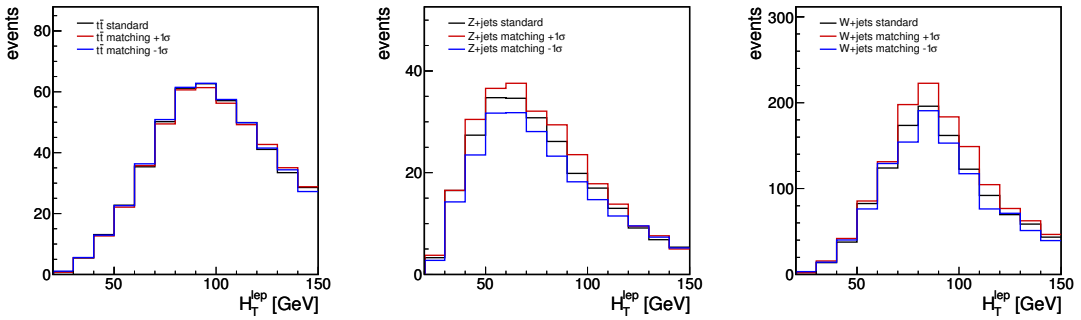

Figure A.4: Impact of varying the matching threshold in the Monte Carlo simulation on the shape and rate of $H_{\mathrm{T}}^{\mathrm{lep}}$ after the final selection with $H_{\mathrm{T}}^{\mathrm{lep}}$ <150 GeV.

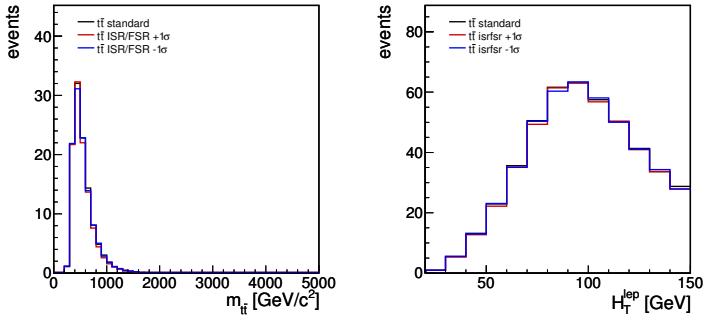

Figure A.5: Impact of varying the amount of initial and final state radiation in the Monte Carlo simulation on the shape and rate of $m_{\mathrm{t\bar{t}}}$ and $H_{\mathrm{T}}^{\mathrm{lep}}$.

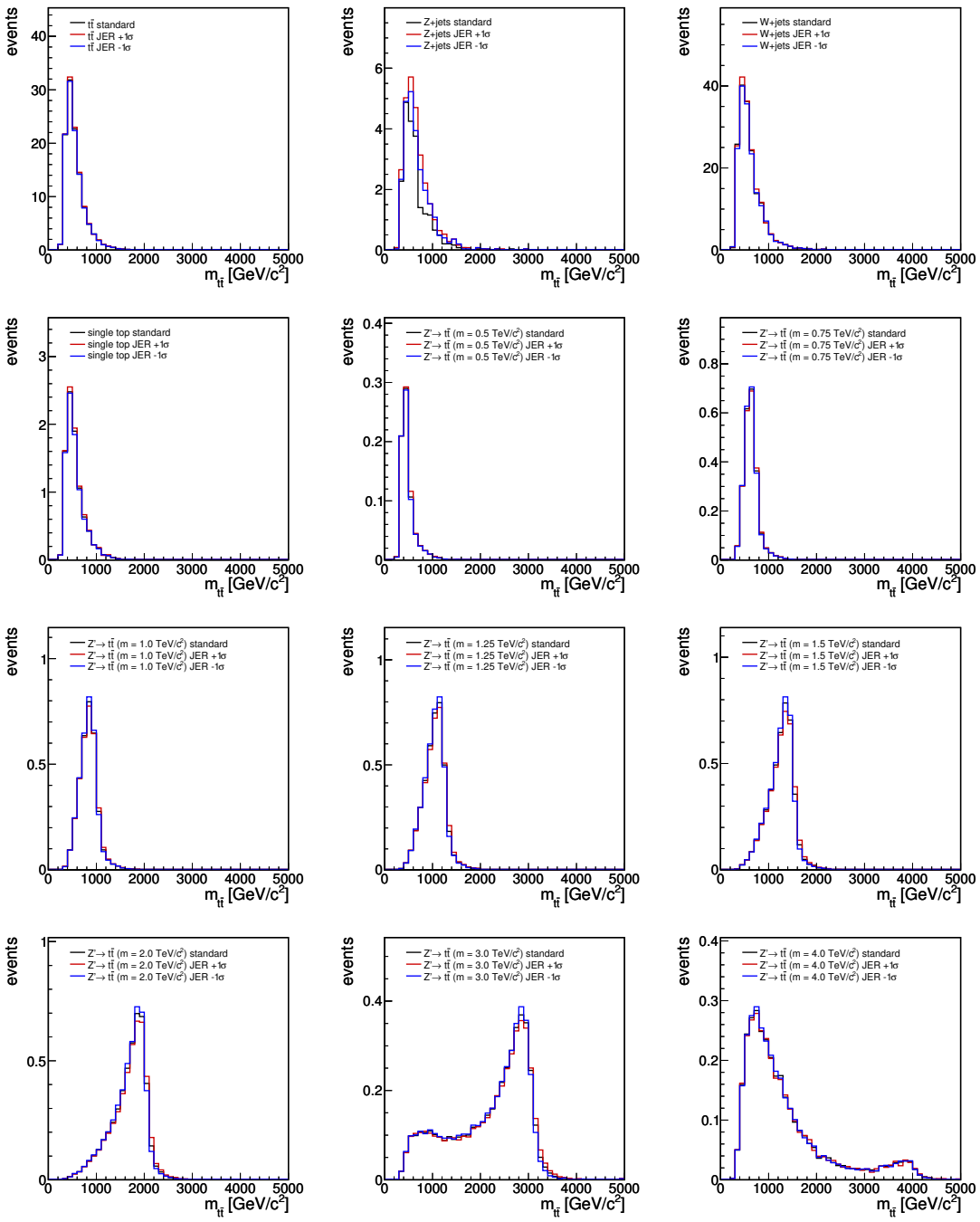

Figure A.6: Impact of varying the jet energy resolution on the shape and rate of $m_{t\bar{t}}$ after the final selection with H_T^{lep} >150 GeV. The $Z' \rightarrow t\bar{t}$ signal samples are normalised to an arbitrary cross section of 1 pb.

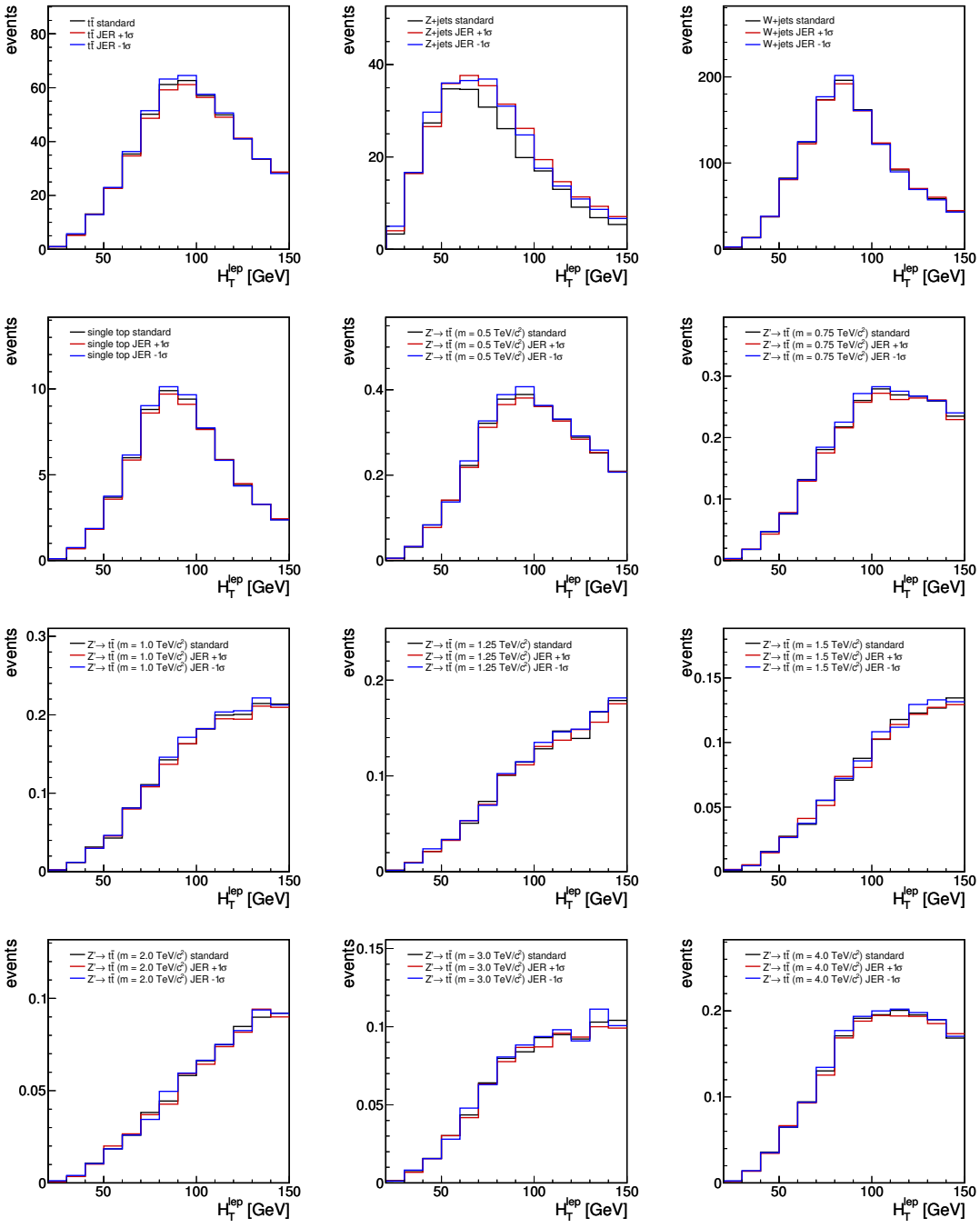

Figure A.7: Impact of varying the jet energy resolution on the shape and rate of $H_{\mathrm{T}}^{\mathrm{lep}}$ after the final selection with $H_{\mathrm{T}}^{\mathrm{lep}}$ <150 GeV. The $\mathrm{Z}' \to \mathrm{t\bar{t}}$ signal samples are normalised to an arbitrary cross section of 1 pb.

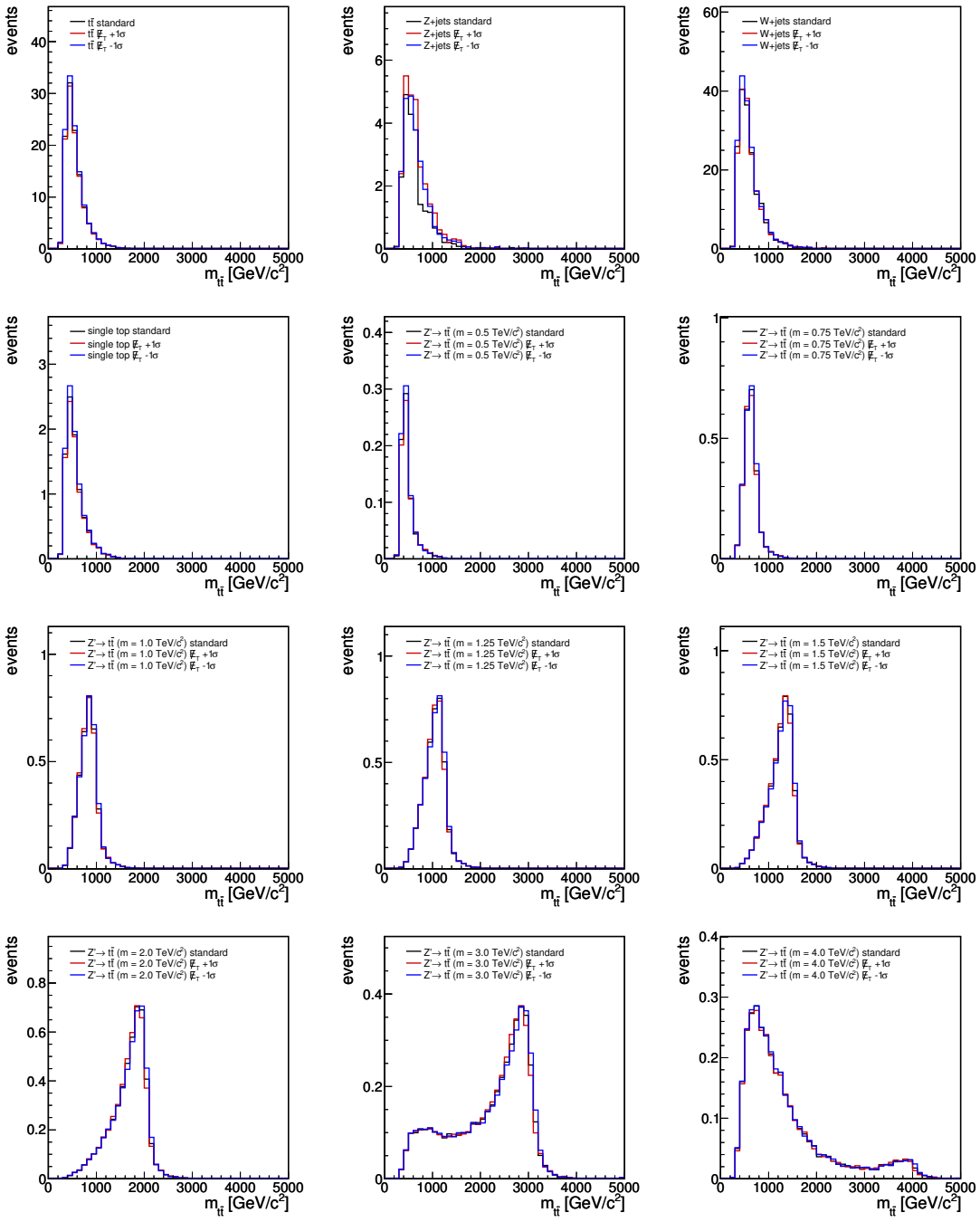

Figure A.8: Impact of varying the unclustered energy contributions to $\not\!\!E_{\mathrm{T}}$ on the shape and rate of $m_{\mathrm{t\bar{t}}}$ after the final selection with $H_{\mathrm{T}}^{\mathrm{lep}}$ >150 GeV. The $\mathrm{Z}' \to \mathrm{t\bar{t}}$ signal samples are normalised to an arbitrary cross section of 1 pb.

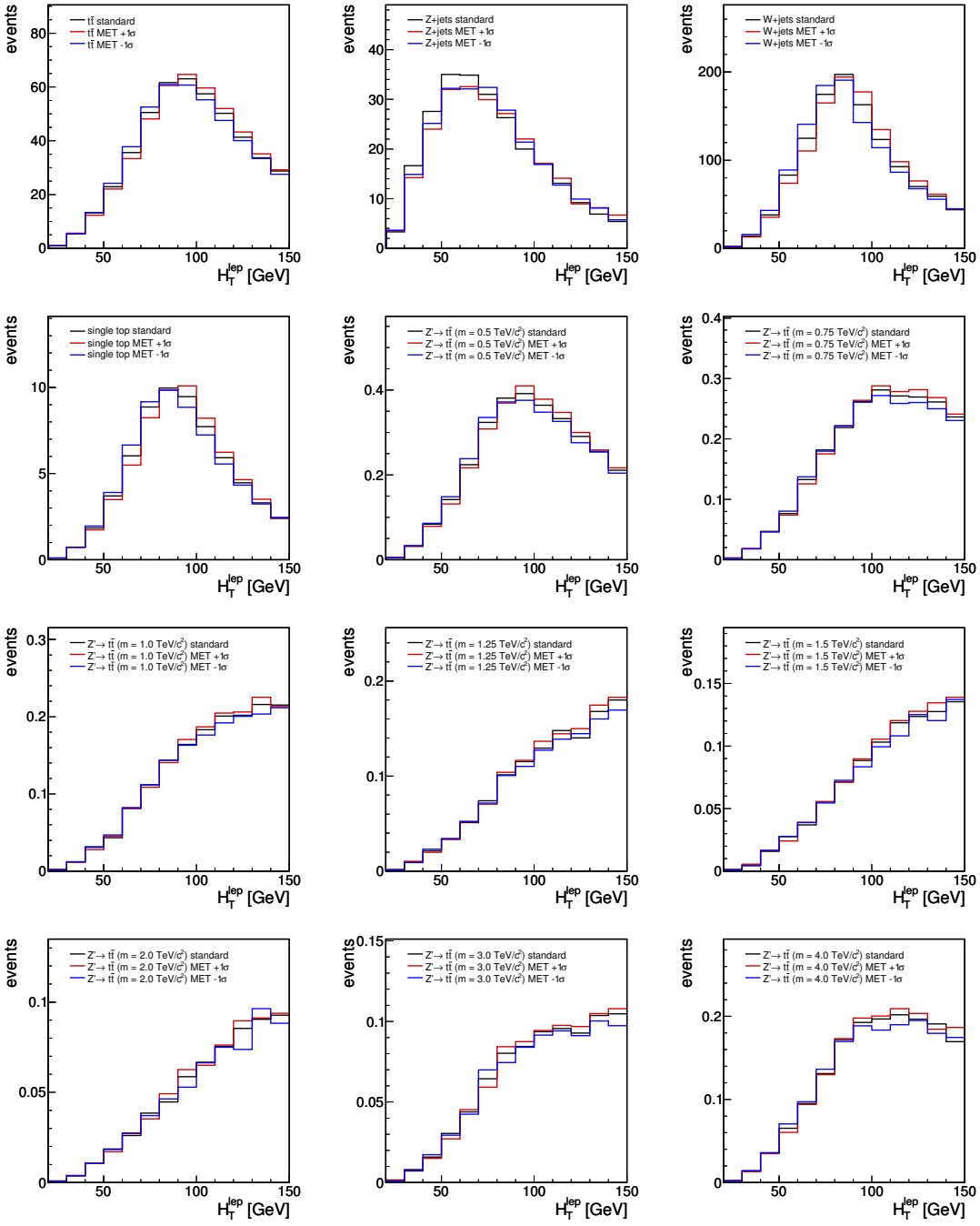

Figure A.9: Impact of varying the unclustered energy contributions to $\not\!\!E_{\mathrm{T}}$ on the shape and rate of $H_{\mathrm{T}}^{\mathrm{lep}}$ after the final selection with $H_{\mathrm{T}}^{\mathrm{lep}}$ <150 GeV. The $\mathrm{Z}' \to \mathrm{t\bar{t}}$ signal samples are normalised to an arbitrary cross section of 1 pb.

Bibliography

[1] M. Gell-Mann, "A Schematic Model of Baryons and Mesons", Phys. Lett. 8, 214–215 (1964).

[2] S. Weinberg, "A Model of Leptons", Phys. Rev. Lett. 19, 1264–1266 (1967).

[3] A. Salam and J. C. Ward, "Electromagnetic and Weak Interactions", Phys. Lett. 13, 168–171 (1964).

[4] S. L. Glashow, "Partial Symmetries of Weak Interactions", Nucl. Phys. 22, 579–588 (1961).

[5] S. L. Glashow, J. Iliopoulos, and L. Maiani, "Weak Interactions with Lepton-Hadron Symmetry", Phys. Rev. D2, 1285–1292 (1970).

[6] G. 't Hooft, "Renormalizable Lagrangians for Massive Yang-Mills Fields", Nucl. Phys. B35, 167–188 (1971).

[7] G. 't Hooft and M. J. G. Veltman, "Regularization and Renormalization of Gauge Fields", Nucl. Phys. B44, 189–213 (1972).

[8] D. J. Gross and F. Wilczek, "Asymptotically Free Gauge Theories. 1", Phys. Rev. D8, 3633–3652 (1973).

[9] D. J. Gross and F. Wilczek, "Ultraviolet Behavior of Non-Abelian Gauge Theories", Phys. Rev. Lett. 30, 1343–1346 (1973).

[10] H. D. Politzer, "Reliable Perturbative Results for Strong Interactions?", Phys. Rev. Lett. 30 no. 26, 1346–1349 (Jun, 1973).

[11] H. Fritzsch, M. Gell-Mann, and H. Leutwyler, "Advantages of the Color Octet Gluon Picture", Phys. Lett. B47, 365–368 (1973).

[12] A. Einstein, "Grundlage der Allgemeinen Relativitätstheorie", Annalen Phys. 49, 769–822 (1916).

[13] F. Englert and R. Brout, "Broken Symmetry and the Mass of Gauge Vector Mesons", Phys. Rev. Lett. 13, 321–322 (1964).

[14] P. W. Higgs, "Broken Symmetries and the Masses of Gauge Bosons", Phys. Rev. Lett. 13, 508–509 (1964).

[15] G. S. Guralnik, C. R. Hagen, and T. W. B. Kibble, "Global Conservation Laws and Massless Particles", Phys. Rev. Lett. 13, 585–587 (1964).

[16] L. Evans and P. Bryant, "LHC Machine", JINST 3, S08001 (2008).

[17] T. Aaltonen et al., "Forward-Backward Asymmetry in Top Quark Production in $p\bar{p}$ Collisions at $\sqrt{s} = 1.96$ TeV", Phys. Rev. Lett. 101, 202001 (2008).

[18] T. Aaltonen et al., "Evidence for a Mass Dependent Forward-Backward Asymmetry in Top Quark Pair Production", `arXiv:hep-ex/1101.0034` (2011).

[19] CDF Collaboration, "Measurement of the Forward Backward Asymmetry in Top Pair Production in the Dilepton Decay Channel using 5.1 fb^1", CDF Note 10436 (2011).

[20] V. M. Abazov et al., "Measurement of the Forward-Backward Charge Asymmetry in Top-Quark Pair Production", Phys. Rev. Lett. 100 no. 14, 142002 (2008).

[21] D0 Collaboration, "Measurement of the Forward-Backward Production Asymmetry of t and $\bar{t}$ Quarks in $p\bar{p} \to t\bar{t}$ Events", D0 Note 6062-CONF (2011).

[22] R. Adolphi et al., "The CMS Experiment at the CERN LHC", JINST 3, S08004 (2008).

[23] CMS Collaboration, "Measurement of the $t\bar{t}$ Production Cross Section in pp Collisions at $\sqrt{s} = 7$ TeV using the Kinematic Properties of Events with Leptons and Jets", to be published in Eur. Phys. J. (2011).

[24] P. Ferrario and G. Rodrigo, "Massive Color-Octet Bosons and the Charge Asymmetries of Top Quarks at Hadron Colliders", Phys. Rev. D78, 094018 (2008).

[25] P. Ferrario and G. Rodrigo, "Heavy Colored Resonances in Top-Antitop + jet at the LHC", JHEP 02, 051 (2010).

[26] G. Rodrigo, Private Communication (2011).

[27] E. Noether, "Invariante Variationsprobleme", Nachr. d. König. Ges. d. Wiss. zu Göttingen, Math-Phys. Klasse 235–257 (1918).

[28] R. P. Feynman, "Mathematical Formulation of the Quantum Theory of Electromagnetic Interaction", Phys. Rev. 80, 440–457 (1950).

[29] R. P. Feynman, "Space-Time Approach to Quantum Electrodynamics", Phys. Rev. 76, 769–789 (1949).

[30] R. P. Feynman, "The Theory of Positrons", Phys. Rev. 76, 749–759 (1949).

[31] J. S. Schwinger, "Quantum Electrodynamics. I: A Covariant Formulation", Phys. Rev. 74, 1439 (1948).

[32] J. S. Schwinger, "Quantum Electrodynamics. II: Vacuum Polarization and Selfenergy", Phys. Rev. 75, 651 (1948).

[33] J. S. Schwinger, "Quantum Electrodynamics. III: The Electromagnetic Properties of the Electron: Radiative Corrections to Scattering", Phys. Rev. 76, 790–817 (1949).

[34] S. Tomonaga, "On a Relativistically Invariant Formulation of the Quantum Theory of Wave Fields", Prog. Theor. Phys. 1, 27–42 (1946).

[35] K. Nakamura et al., "Review of Particle Physics", J. Phys. G37, 075021 (2010).

[36] F. J. Hasert et al., "Observation of Neutrino-like Interactions Without Muon or Electron in the Gargamelle Neutrino Experiment", Phys. Lett. B46, 138–140 (1973).

[37] G. Arnison et al., "Experimental Observation of Isolated Large Transverse Energy Electrons with Associated Missing Energy at $s^{1/2} = 540$ GeV", Phys. Lett. B122, 103–116 (1983).

[38] M. Banner et al., "Observation of Single Isolated Electrons of High Transverse Momentum in Events with Missing Transverse Energy at the CERN anti-p p collider", Phys. Lett. B122, 476–485 (1983).

[39] G. Arnison et al., "Experimental Observation of Lepton Pairs of Invariant Mass around 95 GeV/c^2 at the CERN SPS Collider", Phys. Lett. B126, 398–410 (1983).

[40] P. Bagnaia et al., "Evidence for $Z^0 \to e^+ e^-$ at the CERN anti-p p Collider", Phys. Lett. B129, 130–140 (1983).

[41] W. Bartel et al., "Observation of Planar Three Jet Events in $e^+ e^-$ Annihilation and Evidence for Gluon Bremsstrahlung", Phys. Lett. B91, 142 (1980).

[42] D. P. Barber et al., "Discovery of Three Jet Events and a Test of Quantum Chromodynamics at PETRA Energies", Phys. Rev. Lett. 43, 830 (1979).

[43] C. Berger et al., "Evidence for Gluon Bremsstrahlung in $e^+ e^-$ Annihilations at High-Energies", Phys. Lett. B86, 418 (1979).

[44] R. Brandelik et al., "Evidence for Planar Events in $e^+ e^-$ Annihilation at High-Energies", Phys. Lett. B86, 243 (1979).

[45] W. Pauli, "The Connection Between Spin and Statistics", Phys. Rev. 58, 716–722 (1940).

[46] CDF and D0 Collaboration, "Combination of CDF and D0 Results on the Mass of the Top Quark", `arXiv:hep-ex/1007.3178` (2010).

[47] J. Goldstone, "Field Theories with Superconductor Solutions", Nuovo Cim. 19, 154–164 (1961).

[48] J. Goldstone, A. Salam, and S. Weinberg, "Broken Symmetries", Phys. Rev. 127 no. 3, 965–970 (1962).

[49] U. Nierste and F.-M. Stober, "Vorlesung zur Theoretischen Teilchenphysik I-III", Universität Karlsruhe (2006-2007).

[50] R. Barate et al., "Search for the Standard Model Higgs Boson at LEP", Phys. Lett. B565, 61–75 (2003).

[51] CDF and D0 Collaboration, "Combined CDF and D0 Upper Limits on Standard Model Higgs- Boson Production with up to 6.7 fb^{-1} of Data", `arXiv:hep-ex/1007.4587` (2010).

[52] J. Alcaraz, "Precision Electroweak Measurements and Constraints on the Standard Model", `arXiv:hep-ex/0911.2604` (2009).

[53] M. Kobayashi and T. Maskawa, "CP Violation in the Renormalizable Theory of Weak Interaction", Prog. Theor. Phys. 49, 652–657 (1973).

[54] E. Fermi, "Nuclear Physics", University of Chicago Press (1950).

[55] F. J. Dyson, "The S Matrix in Quantum Electrodynamics", Phys. Rev. 75, 1736–1755 (1949).

[56] Y. Fukuda et al., "Evidence for Oscillation of Atmospheric Neutrinos", Phys. Rev. Lett. 81, 1562–1567 (1998).

[57] Q. R. Ahmad et al., "Measurement of the Charged Current Interactions Produced by B-8 Solar Neutrinos at the Sudbury Neutrino Observatory", Phys. Rev. Lett. 87, 071301 (2001).

[58] F. Abe et al., "Observation of Top Quark Production in $\bar{p}p$ Collisions", Phys. Rev. Lett. 74, 2626–2631 (1995).

[59] S. Abachi et al., "Observation of the Top Quark", Phys. Rev. Lett. 74, 2632–2637 (1995).

[60] T. Aaltonen et al., "Observation of Electroweak Single Top Quark Production", Phys. Rev. Lett. 103, 092002 (2009).

[61] V. M. Abazov et al., "Observation of Single Top-Quark Production", Phys. Rev. Lett. 103, 092001 (2009).

[62] J. C. Collins, E. Soper, and G. F. Sterman, "Heavy Particle Production in High-Energy Hadron Collisions", Nucl. Phys. B263, 37 (1986).

[63] J. Pumplin et al., "New Generation of Parton Distributions with Uncertainties from Global QCD Analysis", JHEP 07, 012 (2002).

[64] P. M. Nadolsky et al., "Implications of CTEQ Global Analysis for Collider Observables", Phys. Rev. D78, 013004 (2008).

[65] N. Kidonakis, "Top Quark Pair and Single Top Production at Tevatron and LHC Energies", `arXiv:hep-ph/1008.2460` (2010).

[66] P. H. Frampton and S. L. Glashow, "Chiral Color: An Alternative to the Standard Model", Phys. Lett. B190, 157 (1987).

[67] C. T. Hill, "Topcolor: Top Quark Condensation in a Gauge Extension of the Standard Model", Phys. Lett. B266, 419–424 (1991).

[68] C. T. Hill and S. J. Parke, "Top Production: Sensitivity to New Physics", Phys. Rev. D49, 4454–4462 (1994).

[69] L. Randall and R. Sundrum, "A Large Mass Hierarchy from a Small Extra Dimension", Phys. Rev. Lett. 83, 3370–3373 (1999).

[70] N. Arkani-Hamed, S. Dimopoulos, and G. R. Dvali, "The Hierarchy Problem and New Dimensions at a Millimeter", Phys. Lett. B429, 263–272 (1998).

[71] K. Agashe, A. Belyaev, T. Krupovnickas, G. Perez, and J. Virzi, "LHC Signals from Warped Extra Dimensions", Phys. Rev. D77, 015003 (2008).

[72] D. Dicus, A. Stange, and S. Willenbrock, "Higgs Decay to Top Quarks at Hadron Colliders", Phys. Lett. B333, 126–131 (1994).

[73] J. L. Rosner, "Prominent Decay Modes of a Leptophobic Z′", Phys. Lett. B387, 113–117 (1996).

[74] R. Frederix and F. Maltoni, "Top Pair Invariant Mass Distribution: A Window on New Physics", JHEP 01, 047 (2009).

[75] Y. Kiyo, J. H. Kühn, S. Moch, M. Steinhauser, and P. Uwer, "Top Quark Pair Production near Threshold at LHC", Eur. Phys. J. C60, 375–386 (2009).

[76] M. Steinhauser, Private Communication (2010).

[77] T. Aaltonen et al., "Search for Resonant $t\bar{t}$ Production in p anti-p Collisions at $\sqrt{s} = 1.96$ TeV", Phys. Rev. Lett. 100, 231801 (2008).

[78] V. M. Abazov et al., "Search for $t\bar{t}$ Resonances in the Lepton plus Jets Final State in $p\bar{p}$ Collisions at $\sqrt{s} = 1.96$ TeV", D0 Note 5882-CONF (2009).

[79] S. Frixione and B. R. Webber, "Matching NLO QCD Computations and Parton Shower Simulations", JHEP 06, 029 (2002).

[80] S. Frixione, P. Nason, and B. R. Webber, "Matching NLO QCD and Parton Showers in Heavy Flavour Production", JHEP 08, 007 (2003).

[81] W. Bernreuther, A. Brandenburg, Z. G. Si, and P. Uwer, "Top Quark Pair Production and Decay at Hadron Colliders", Nucl. Phys. B690, 81–137 (2004).

[82] O. Antuñano, J. H. Kühn, and G. Rodrigo, "Top Quarks, Axigluons, and Charge Asymmetries at Hadron Colliders", Phys. Rev. D 77, 014003 (2008).

[83] J. H. Kühn and G. Rodrigo, "Charge Asymmetry of Heavy Quarks at Hadron Colliders", Phys. Rev. D59, 054017 (1999).

[84] J. H. Kühn and G. Rodrigo, "Charge Asymmetry in Hadroproduction of Heavy Quarks", Phys. Rev. Lett. 81, 49–52 (1998).

[85] P. H. Frampton, J. Shu, and K. Wang, "Axigluon as Possible Explanation for $p\bar{p} \to t\bar{t}$ Forward-Backward Asymmetry", Phys. Lett. B683, 294–297 (2010).

[86] Y. Bai, J. L. Hewett, J. Kaplan, and T. G. Rizzo, "LHC Predictions from a Tevatron Anomaly in the Top Quark Forward-Backward Asymmetry", `arXiv:hep-ph/1101.5203` (2011).

[87] G. Rodrigo and P. Ferrario, "Charge Asymmetry: a Theory Appraisal", `arXiv:hep-ph/1007.4328` (2010).

[88] P. Ferrario and G. Rodrigo, "Constraining Heavy Colored Resonances from Top-Antitop Quark Events", Phys. Rev. D80, 051701 (2009).

[89] I. Dorsner, S. Fajfer, J. F. Kamenik, and N. Kosnik, "Light Colored Scalars from Grand Unification and the Forward-Backward Asymmetry in Top Quark Pair Production", Phys. Rev. D81, 055009 (2010).

[90] R. S. Chivukula, E. H. Simmons, and C. P. Yuan, "Axigluons Cannot Explain the Observed Top Quark Forward- Backward Asymmetry", Phys. Rev. D82, 094009 (2010).

[91] M. V. Martynov and A. D. Smirnov, "On Mass Limit for Chiral Color Symmetry G′-Boson from Tevatron Data on $t\bar{t}$ Production", Mod. Phys. Lett. A25, 2637–2643 (2010).

[92] J. Shu, T. M. P. Tait, and K. Wang, "Explorations of the Top Quark Forward-Backward Asymmetry at the Tevatron", Phys. Rev. D81, 034012 (2010).

[93] K. Cheung, W. Y. Keung, and T. C. Yuan, "Top Quark Forward-Backward Asymmetry", Phys. Lett. B682, 287–290 (2009).

[94] S. Jung, H. Murayama, A. Pierce, and J. D. Wells, "Top Quark Forward-Backward Asymmetry from new t-Channel Physics", Phys. Rev. D81, 015004 (2010).

[95] V. Barger, W. Y. Keung, and C. T. Yu, "Asymmetric Left-Right Model and the Top Pair Forward- Backward Asymmetry", Phys. Rev. D81, 113009 (2010).

[96] M. Bauer, F. Goertz, U. Haisch, T. Pfoh, and S. Westhoff, "Top-Quark Forward-Backward Asymmetry in Randall-Sundrum Models Beyond the Leading Order", JHEP 11, 039 (2010).

[97] A. Djouadi, G. Moreau, F. Richard, and R. K. Singh, "The Forward-Backward Asymmetry of Top Quark Production at the Tevatron in Warped Extra Dimensional Models", Phys. Rev. D82, 071702 (2010).

[98] A. Arhrib, R. Benbrik, and C. H. Chen, "Forward-Backward Asymmetry of Top Quark in Diquark Models", Phys. Rev. D82, 034034 (2010).

[99] D. W. Jung, P. Ko, J. S. Lee, and S. H. Nam, "Model Independent Analysis of the Forward-Backward Asymmetry of Top Quark Production at the Tevatron", Phys. Lett. B691, 238–242 (2010).

[100] J. Cao, Z. Heng, L. Wu, and J. M. Yang, "Top Quark Forward-Backward Asymmetry at the Tevatron: a Comparative Study in Different New Physics Models", Phys. Rev. D81, 014016 (2010).

[101] P. Ferrario, "Recursive Methods in Quantum Field Theory and Top Quark Physics at the LHC", Tesis doctoral, Universitat de Valencia (2010).

[102] S. Myers and E. Picasso, "The Design, Construction and Commissioning of the CERN Large Electron Positron collider", Contemp. Phys. 31, 387–403 (1990).

[103] K. Aamodt et al., "The ALICE Experiment at the CERN LHC", JINST 3, S08002 (2008).

[104] H. Bohr and H. B. Nielsen, "Hadron Production from a Boiling Quark Soup", Nucl. Phys. B128, 275 (1977).

[105] A. A. Alves et al., "The LHCb Detector at the LHC", JINST 3, S08005 (2008).

[106] G. Aad et al., "The ATLAS Experiment at the CERN Large Hadron Collider", JINST 3, S08003 (2008).

[107] G. Anelli et al., "The TOTEM Experiment at the CERN Large Hadron Collider", JINST 3, S08007 (2008).

[108] O. Adriani et al., "The LHCf Detector at the CERN Large Hadron Collider", JINST 3, S08006 (2008).

[109] CERN Communication Group, "CERN FAQ – LHC the Guide", CERN-Brochure-2009-003-Eng (2009).

[110] C. E. Hill and M. O'Neil, "The High Voltage System for the High Intensity CERN Proton Source", Given at 19th International Linear Accelerator Conference (Linac 98), Chicago, IL, 23-28 Aug (1998).

[111] C. E. Hill, A. M. Lombardi, E. Tanke, and M. Vretenar, "Present Performance of the CERN Proton Linac", Given at 19th International Linear Accelerator Conference (Linac 98), Chicago, IL, 23-28 Aug (1998).

[112] K. Schindl, "The PS Booster as Pre-Injector for LHC", Part. Accel. 58, 63–78 (1997).

[113] R. Cappi, "The PS in the LHC Injector Chain", Part. Accel. 58, 79–89 (1997).

[114] T. Linnecar, "Preparing the SPS for LHC", Part. Accel. 58, 91–101 (1997).

[115] CMS Collaboration, "Measurement of CMS Luminosity", CMS Physics Analysis Summary EWK-10-004 (2010).

[116] CMS Collaboration, "Absolute Luminosity Normalization", CMS-DP-2011-002 (2011).

[117] S. van der Meer, "Stochastic Damping of Betatron Oscillations in the ISR", CERN-ISR-PO-72-31 (1972).

[118] `https://twiki.cern.ch/twiki/bin/view/CMSPublic/LumiPublicResults2010`, February 2011.

[119] G. L. Bayatian et al., "CMS Physics: Technical Design Report", CERN-LHCC-2006-001 (2006).

[120] `http://cms.web.cern.ch/cms/Media/Images/Detector/Detector Drawings/index.html`, February 2011.

[121] V. Karimäki, "The CMS Tracker System Project: Technical Design Report", CERN-LHCC-98-006 (1997).

[122] CMS Collaboration, "Addendum to the CMS Tracker TDR", CERN-LHCC-2000-016 (2000).

[123] CMS Collaboration, "The CMS Electromagnetic Calorimeter Project: Technical Design Report", CERN-LHCC-97-033 (1997).

[124] CMS Collaboration, "The CMS Hadron Calorimeter Project: Technical Design Report", CERN-LHCC-97-031 (1997).

[125] P. Adzic et al., "Energy Resolution of the Barrel of the CMS Electromagnetic Calorimeter", JINST 2, P04004 (2007).

[126] S. Chatrchyan et al., "Performance of the CMS Hadron Calorimeter with Cosmic Ray Muons and LHC Beam Data", JINST 5, T03012 (2010).

[127] CMS Collaboration, "CMS, the Compact Muon Solenoid. Muon Technical Design Report", CERN-LHCC-97-32 (1997).

[128] S. Dasu et al., "The TriDAS Project. Technical Design Report, Vol. 1: The Trigger Systems", CERN-LHCC-2000-038 (2000).

[129] P. Sphicas et al., "The TriDAS Project. Technical Design Report, Vol. 2: Data Acquisition and High-Level Trigger", CERN-LHCC-2002-026 (2002).

[130] CMS Collaboration, "CMS: The Computing Project. Technical Design Report", CERN-LHCC-2005-023 (2005).

[131] I. Bird et al., "LHC Computing Grid. Technical Design Report", CERN-LHCC-2005-024 (2005).

[132] J. Gruschke, "Nachweis von Top-Quarks und erste Messung des $t\bar{t}$-Wikungsquerschnitts bei einer Schwerpunktsenergie von 7 TeV mit dem CMS-Experiment am LHC", Doktorarbeit, Karlsruher Institut für Technologie, IEKP-KA/2011-4 (2011).

[133] S. Hoeche et al., "Matching Parton Showers and Matrix Elements", `arXiv:hep-ph/0602031` (2006).

[134] S. Catani, F. Krauss, R. Kuhn, and B. R. Webber, "QCD Matrix Elements + Parton Showers", JHEP 11, 063 (2001).

[135] Y. L. Dokshitzer, "Calculation of the Structure Functions for Deep Inelastic Scattering and e^+ e^- Annihilation by Perturbation Theory in Quantum Chromodynamics", Sov. Phys. JETP 46, 641–653 (1977).

[136] V. N. Gribov and L. N. Lipatov, "Deep Inelastic Electron Scattering in Perturbation Theory", Phys. Lett. B37, 78–80 (1971).

[137] G. Altarelli and G. Parisi, "Asymptotic Freedom in Parton Language", Nucl. Phys. B126, 298 (1977).

[138] T. Sjöstrand, S. Mrenna, and P. Z. Skands, "PYTHIA 6.4 Physics and Manual", JHEP 05, 026 (2006).

[139] B. Andersson, G. Gustafson, G. Ingelman, and T. Sjöstrand, "Parton Fragmentation and String Dynamics", Phys. Rept. 97, 31–145 (1983).

[140] S. Jadach, J. H. Kühn, and Z. Was, "TAUOLA: A Library of Monte Carlo Programs to Simulate Decays of Polarized Tau Leptons", Comput. Phys. Commun. 64, 275–299 (1990).

[141] J. Alwall et al., "MadGraph/MadEvent v4: The New Web Generation", JHEP 09, 028 (2007).

[142] J. Alwall et al., "A Standard Format for Les Houches Event Files", Comput. Phys. Commun. 176, 300–304 (2007).

[143] G. Corcella et al., "Herwig 6.5: An Event Generator for Hadron Emission Reactions With Interfering Gluons (Including Supersymmetric Processes)", JHEP 01, 010 (2001).

[144] M. Bahr et al., "Herwig++ Physics and Manual", Eur. Phys. J. C58, 639–707 (2008).

[145] R. Field, "Physics at the Tevatron", Acta Phys. Polon. B39, 2611–2672 (2008).

[146] R. Field, "Studying the 'Underlying Event' at CDF and the LHC", Proceedings of the First International Workshop on Multiple Partonic Interactions at the LHC, Perugia (2008).

[147] J. Bauer, "Perspektiven zur Beobachtung der elektroschwachen Produktion einzelner Top-Quarks mit dem CMS-Experiment", Doktorarbeit, Karlsruher Institut für Technologie, IEKP-KA/2010-8 (2010).

[148] R. Field, "Early LHC Underlying Event Data – Findings and Surprises", `arXiv:hep-ph/1010.3558` (2010).

[149] S. Agostinelli et al., "Geant4: A Simulation Toolkit", Nucl. Instrum. Meth. A506, 250–303 (2003).

[150] J. Allison et al., "Geant4: Developments and Applications", IEEE Trans. Nucl. Sci. 53, 270 (2006).

[151] W. Adam, B. Mangano, T. Speer, and T. Todorov, "Track Reconstruction in the CMS Tracker", CERN-CMS-NOTE-2006-041 (2006).

[152] T. Speer et al., "Track Reconstruction in the CMS Tracker", Nucl. Instrum. Meth. A559, 143–147 (2006).

[153] R. E. Kalman, "A New Approach to Linear Filtering and Prediction Problems", Transaction of the ASME, Journal of Basic Engineering 82, 35–45 (1960).

[154] R. Frühwirth, "Application of Kalman Filtering to Track and Vertex Fitting", Nucl. Instrum. Meth. A262, 444–450 (1987).

[155] R. Frühwirth, W. Waltenberger, and P. Vanlaer, "Adaptive Vertex Fitting", J. Phys. G34, N343 (2007).

[156] S. Chatrchyan et al., "Performance of CMS Muon Reconstruction in Cosmic-Ray Events", JINST 5, T03022 (2010).

[157] S. Baffioni et al., "Electron Reconstruction in CMS", Eur. Phys. J. C49, 1099–1116 (2007).

[158] W. Adam, R. Frühwirth, A. Strandlie, and T. Todorov, "Reconstruction of Electrons with the Gaussian-Sum Filter in the CMS Tracker at LHC", ECONF C0303241, TULT009 (2003).

[159] E. Meschi, T. Monteiro, C. Seez, and P. Vikas, "Electron Reconstruction in the CMS Electromagnetic Calorimeter", CERN-CMS-NOTE-2001-034 (2001).

[160] H. Bethe and W. Heitler, "On the Stopping of Fast Particles and on the Creation of Positive Electrons", Proc. Roy. Soc. Lond. A146, 83–112 (1934).

[161] G. P. Salam and G. Soyez, "A Practical Seedless Infrared-Safe Cone Jet Algorithm", JHEP 05, 086 (2007).

[162] G. C. Blazey et al., "Run II Jet Physics", `arXiv:hep-ex/0005012` (2000).

[163] S. Catani, Y. L. Dokshitzer, M. H. Seymour, and B. R. Webber, "Longitudinally Invariant k_{T} Clustering Algorithms for Hadron Hadron Collisions", Nucl. Phys. B406, 187–224 (1993).

[164] M. Cacciari, G. P. Salam, and G. Soyez, "The Anti-k_{T} Jet Clustering Algorithm", JHEP 04, 063 (2008).

[165] Y. L. Dokshitzer, G. D. Leder, S. Moretti, and B. R. Webber, "Better Jet Clustering Algorithms", JHEP 08, 001 (1997).

[166] CMS Collaboration, "Particle-Flow Event Reconstruction in CMS and Performance for Jets, Taus, and $\not\!\!E_{\mathrm{T}}$", CMS Physics Analysis Summary PFT-09-001 (2009).

[167] CMS Collaboration, "Plans for Jet Energy Corrections at CMS", CMS Physics Analysis Summary JME-07-002 (2008).

[168] CMS Collaboration, "Jet Performance in pp Collisions at $\sqrt{s} = 7$ TeV", CMS Physics Analysis Summary JME-10-003 (2010).

[169] CMS Collaboration, "Missing Transverse Energy Performance in Minimum-Bias and Jet Events from Proton-Proton Collisions at$\sqrt{s} = 7$ TeV", CMS Physics Analysis Summary JME-10-004 (2010).

[170] CMS Collaboration, "Jet Energy Corrections Determination at $\sqrt{s} = 7$ TeV", CMS Physics Analysis Summary JME-10-010 (2010).

[171] CMS Collaboration, "Algorithms for b-Jet Identification in CMS", CMS Physics Analysis Summary BTV-09-001 (2009).

[172] CMS Collaboration, "Commissioning of b-Jet Identification with pp Collisions at $\sqrt{s} = 7$ TeV", CMS Physics Analysis Summary BTV-10-001 (2010).

[173] CMS Collaboration, "$\not\!\!E_{\mathrm{T}}$ Performance in CMS", CMS Physics Analysis Summary JME-07-001 (2007).

[174] E. I. Fredholm, "Sur une Classe d'Equations Fonctionnelles", Acta Mathematica 27, 365–390 (1903).

[175] V. Blobel, "Unfolding Methods in High-Energy Physics Experiments", Lectures given at 1984 CERN School of Computing, Aiguablava, Spain, Sep 9-22 (1984).

[176] V. Blobel, "An Unfolding Method for High Energy Physics Experiments", `arXiv:hep-ex/0208022` (2002).

[177] G. Bohm and G. Zech, "Einführung in Statistik und Messwertanalyse für Physiker", DESY e-book, ISBN 3-935702-19-1 (2006).

[178] V. Blobel, "Unfolding – Linear Inverse Problems –", Notes for the Terascale Workshop on Unfolding and Data Correction at DESY (2010).

[179] A. Hocker and V. Kartvelishvili, "SVD Approach to Data Unfolding", Nucl. Instrum. Meth. A372, 469–481 (1996).

[180] A. Tikhonov, "Solution of Incorrectly Formulated Problems and the Regularization Method", Soviet Mathematics Doklady 4, 1035–1038 (1963).

[181] D. L. Phillips, "A Technique for the Numerical Solution of Certain Integral Equations of the First Kind", J. ACM 9 no. 1, 84–97 (1962).

[182] P. C. Hansen, "The L-Curve and its Use in the Numerical Treatment of Inverse Problems", Computational Inverse Problems in Electrocardiology, ed. P. Johnston, Advances in Computational Bioengineering, 119–142 (2000).

[183] T. Reginska, "A Regularization Parameter in Discrete Ill-Posed Problems", SIAM J. Sci. Comput. 17 no. 3, 740–749 (1996).

[184] G. D'Agostini, "A Multidimensional Unfolding Method based on Bayes' Theorem", Nucl. Instrum. Meth. A362, 487–498 (1995).

[185] T. Bayes, "An Essay toward Solving a Problem in the Doctrine of Chances", Phil. Trans. Roy. Soc. Lond. 53, 370–418 (1764).

[186] V. Blobel, "The RUN Manual: Regularized Unfolding for High-Energy Physics Experiments", OPAL Technical Note TN 361 (1996).

[187] `http://www.desy.de/~sschmitt/tunfold.html`, March 2011.

[188] N. Milke, "TRUEE: Time-dependent Regularized Unfolding for Economics and Engineerings", Talk at the Terascale Workshop on Unfolding and Data Correction at DESY (2010).

[189] R. Brun and F. Rademakers, "ROOT: An Object Oriented Data Analysis Framework", Nucl. Instrum. Meth. A389, 81–86 (1997).

[190] S. Baker and R. D. Cousins, "Clarification of the Use of χ^2 and Likelihood Functions in Fits to Histograms", Nucl. Instrum. Meth. 221, 437–442 (1984).

[191] T. Chwalek, "Messung der W-Boson-Helizitätsanteile in Top-Quark-Zerfällen mit dem CDF II Experiment und Studien zu einer frühen Messung des $t\bar{t}$-Wirkungsquerschnitts mit dem CMS Experiment", Doktorarbeit, Karlsruher Institut für Technologie, IEKP-KA/2010-5 (2010).

[192] CMS Collaboration, "Measurement of the W and Z Inclusive Production Cross Sections at $\sqrt{s} = 7$ TeV with the CMS Experiment at the LHC ", CMS Physics Analysis Summary EWK-10-005 (2011).

[193] CMS Collaboration, "Determination of the Jet Energy Scale in CMS with pp Collisions at $\sqrt{s} = 7$ TeV", CMS Physics Analysis Summary JME-10-010 (2010).

[194] CMS Collaboration, "Jet Energy Resolution in CMS at $\sqrt{s} = 7$ TeV", CMS Physics Analysis Summary JME-10-014 (2011).

[195] CMS Collaboration, "Measurement of the $\mathrm{t\bar{t}}$ Pair Production Cross Section at $\sqrt{s} = 7$ TeV using b-Quark Jet Identification Techniques in Lepton+Jets Events", to be published in Phys. Rev. D (2011).

[196] V. Khachatryan et al., "First Measurement of the Cross Section for Top-Quark Pair Production in Proton-Proton Collisions at $\sqrt{s} = 7$ TeV", Phys. Lett. B695, 424–443 (2011).

[197] CMS Collaboration, "Search for Narrow Resonances in Top-Pair Production close to Threshold in the Semileptonic Muon Channel at $\sqrt{s} = 10$ TeV", CMS Physics Analysis Summary TOP-09-009 (2009).

[198] K. Melnikov and F. Petriello, "Electroweak Gauge Boson Production at Hadron Colliders through $O(\alpha_s^2)$", Phys. Rev. D74, 114017 (2006).

[199] `http://mcfm.fnal.gov/mcfm.pdf`, "MCFM – Monte Carlo for FeMtobarn Processes", April 2011.

[200] `http://www.theta-framework.org`, April 2011.

[201] N. Metropolis, A. W. Rosenbluth, M. N. Rosenbluth, A. H. Teller, and E. Teller, "Equation of State Calculations by Fast Computing Machines", J. Chem. Phys. 21, 1087–1092 (1953).

[202] CMS Collaboration, "Search for Resonances in Semi-leptonic Top-pair Decays Close to Production Threshold", CMS Physics Analysis Summary TOP-10-007 (2011).

[203] D. E. Kaplan, K. Rehermann, M. D. Schwartz, and B. Tweedie, "Top Tagging: A Method for Identifying Boosted Hadronically Decaying Top Quarks", Phys. Rev. Lett. 101, 142001 (2008).

[204] CMS Collaboration, "Study of Jet Substructure in pp Collisions at 7 TeV in CMS", CMS Physics Analysis Summary JME-10-013 (2011).

[205] J. Ott, "Studien zur Suche nach schweren in Top-Quark-Paare zerfallenden Teilchen mit dem CMS-Detektor", Diplomarbeit, Universität Karlsruhe, IEKP-KA/2009-20 (2009).

Danksagung

Der Anfertigung dieser Arbeit wäre ohne die Hilfe einiger Personen nicht möglich gewesen. Diesen Personen sei daher an dieser Stelle mein Dank dafür ausgesprochen, dass sie mich in meiner Arbeit in den zurückliegenden Jahren unterstützt und zur Seite gestanden haben.

Zunächst danke ich Herrn Prof. Dr. Thomas Müller dafür, dass er es mir ermöglicht hat, in seiner Arbeitsgruppe, der ich schon seit meiner Diplomarbeit angehöre, als Doktorand tätig zu sein und die vorliegende Arbeit anfertigen konnte. Ebenso is es ihm zu verdanken, dass ich einen einjährigen Forschungsaufenthalt am CERN wahrnehmen konnte. Des Weiteren danke ich Herrn Prof. Dr. Günter Quast für die Übernahme des Korreferats dieser Arbeit.

Ein besonderer Dank gilt natürlich meinen Arbeitsgruppenkollegen. Hier sei besonders Frau Dr. Jeannine Wagner-Kuhr erwähnt, die immer ein offenes Ohr für Fragen hatte und mit vielen hilfreichen Ratschlägen maßgeblich zum gelingen dieser Arbeit beigetragen hat. Meinen Kollegen Dr. Thorsten Chwalek und Dr. Jasmin Gruschke möchte ich insbesondere für das Korrekturlesen dieser Arbeit danken. Bei Jochen Ott bedanke ich mich ebenfalls fürs Probelesen sowie für die gute Zusammenarbeit bei der Durchführung der Analyse zu schweren Resonanzen in der Top-Quark-Paarproduktion. Auch bei Manuel Renz möchte ich mich bedanken, vor allem für das gemeinsame Durchleiden der Prüfungsvorbereitung.

Allen weiteren Mitgliedern des Instituts für Experimentelle Kernphysik möchte ich für die angenehme Arbeitsathmosphäre danken. Dabei sei besonders den Mitglieder des Admin-Teams für die Aufrechterhaltung der Computing-Infrastruktur sowie Frau Bärbel Bräunling vom Sekretariat für die stets kompetente Hilfe gedankt.

Ich möchte mich an dieser Stelle auch bei Dr. Germán Rodrigo für die Ausarbeitung der Theorievorhesagen für die Ladungsasymmetrie sowie bei Natalie Milke für ihre Hilfe im Umgang mit dem von ihr geschriebenen Entfaltungsprogramm TRUEE bedanken.

Letzten Endes danke ich natürlich meiner Familie, die mich während der Zeit meiner Promotion stets unterstützt hat.